

# **Exploring new therapeutic properties from the encapsulation of pharmaceutical compounds within mesoporous silica particles**

By

**Michael Hui Ong Lau**

A thesis submitted to Macquarie University

For the degree of Doctor of Philosophy

Department of Molecular Sciences

2021

**Supervised by**

**Dr Alfonso Garcia-Bennett**



**MACQUARIE**  
University

Faculty of Science and Engineering

I hereby certify that the work presented in this thesis titled “Exploring new therapeutic properties from the encapsulation of pharmaceutical compounds within mesoporous silica particles” is original. Except where acknowledged in a customary manner, the material presented in this thesis is, to the best of my knowledge, original and has not been submitted in whole or part for a degree in any university. Several parts of this thesis have resulted from collaborative work with my supervisor, other researchers and research institutions. Their contributions are recognised and acknowledged respectively. No part of this thesis has been submitted to any other institution as a component of a degree or award.

Michael Hui Ong Lau

(Student Number: )

February 2021

# Table of Contents

<b>Abstract .....</b>	<b>vii</b>
<b><i>Publications arising from this thesis</i> .....</b>	<b>ix</b>
<b><i>Other relevant publications</i> .....</b>	<b>ix</b>
<b><i>Conference Presentations</i> .....</b>	<b>x</b>
<b><i>Awards</i> .....</b>	<b>x</b>
<b><i>Abbreviation</i> .....</b>	<b>xi</b>
<b><i>Thesis outline</i> .....</b>	<b>xiii</b>
<b><i>Aim of this thesis</i> .....</b>	<b>xiii</b>
<b>1 INTRODUCTION .....</b>	<b>1</b>
1.1 Free radicals play an important role in the pathogenesis of diseases.....	1
1.2 Reactive oxygen species.....	2
1.2.1 The superoxide anion .....	2
1.2.2 Hydrogen peroxide .....	2
1.2.3 The hydroxyl radical.....	3
1.3 Cellular mechanisms of ROS production.....	3
1.3.1 ROS in the mitochondria.....	3
1.3.2 Nicotinamide adenine dinucleotide phosphate oxidase .....	4
1.4 Reactive nitrogen species .....	4
1.4.1 Nitric oxide.....	4
1.4.2 Peroxynitrite anion .....	5
1.5 Antioxidants .....	6
1.5.1 Enzymatic antioxidants .....	6
1.5.2 Non-enzymatic antioxidants .....	7
1.5.3 Antioxidants, reactive species and the redox state .....	8
1.6 The blood brain barrier .....	10
1.6.1 Brain endothelial cells.....	10
1.6.2 Astrocytes .....	11
1.7 Disruption to BBB integrity by neuroinflammation .....	12
1.7.1 Lipopolysaccharide mediated neuroinflammation in brain endothelial cells .....	13
1.8 Therapeutic options for the treatment of neuroinflammation .....	15
1.8.1 Indomethacin.....	15
1.8.2 Ascorbic acid .....	16
1.8.3 Probucol.....	17

1.9	Bioavailability of pharmaceutical drug compounds.....	19
1.9.1	Drug solubility and dissolution .....	20
1.9.2	Biopharmaceutical classification system (BCS).....	21
1.9.3	Strategies to overcome poor solubility of drug compounds .....	22
1.9.4	Nanostructured materials as drug delivery systems .....	23
1.9.5	Porous nanostructured materials .....	25
1.10	Mesoporous silica .....	26
1.10.1	The synthesis of mesoporous silica .....	26
1.10.2	Mesoporous silica as drug delivery systems .....	28
1.10.3	Crystalline vs amorphous forms.....	28
1.10.4	Effect of textural properties of mesoporous silica on drug loading and release.....	29
1.10.5	Mechanisms of drug release from mesoporous silica .....	31
1.10.6	Effectiveness of drug compounds for the treatment of neuroinflammation are limited by their low aqueous solubility.....	32
1.11	References .....	35
<b>2</b>	<b>Materials and methodology.....</b>	<b>45</b>
2.1	Chemicals .....	45
2.2	Synthesis of mesoporous silica particles.....	45
2.2.1	AMS-6 synthesis.....	45
2.2.2	MCM-41 synthesis .....	46
2.2.3	SBA-15 synthesis .....	46
2.3	Drug compounds used in this thesis .....	46
2.4	Drug loading within mesoporous silica .....	47
2.5	Drug dissolution measurements .....	47
2.6	Characterisation techniques .....	47
2.6.1	X-ray diffraction (XRD) .....	47
2.6.2	High energy X-ray diffraction (HE-XRD) .....	49
2.6.3	Pair distribution function analysis (PDF).....	49
2.6.4	Scanning electron microscopy (SEM).....	50
2.6.5	Nitrogen sorption isotherm .....	50
2.6.6	Thermogravimetric analysis (TGA).....	52
2.6.7	Differential scanning calorimetry (DSC).....	52
2.7	Cell culture <i>in vitro</i> experiments.....	53
2.7.1	Cell viability assay .....	54
2.7.2	Muse® Oxidative stress kit.....	55



2.7.3	The 2',7'-Dichlorodihydrofluorescein diacetate (DCFDA) reactive oxygen stress dye	55
2.7.4	Nitric oxide assay .....	56
2.7.5	Peroxynitrite assay.....	57
2.7.6	COX enzyme activity assay.....	57
2.7.7	Prostaglandin E <sub>2</sub> Assay .....	59
2.8	<i>In vitro</i> BBB model.....	59
2.9	BBB permeability studies .....	60
2.9.1	Transendothelial electrical resistance (TEER).....	60
2.9.2	Method for calculating TEER for test compounds.....	62
2.9.3	Permeability of the BBB to tracer compounds .....	62
2.9.4	Method for calculating the permeability coefficient (P <sub>e</sub> ) .....	63
2.10	Cellular uptake of PB studies .....	63
2.10.1	Preparation of endothelial cells for cellular uptake studies.....	63
2.10.2	High performance liquid chromatography .....	64
2.11	Zebrafish experiments .....	65
2.11.1	General care.....	66
2.11.4	Screening antioxidant properties of test compounds in zebrafish model of oxidative stress.....	67
2.12	References .....	68
<b>3</b>	Using pair distribution function analysis to probe the local atomic order of drug compounds loaded within mesoporous silica. ....	72
3.1	Introduction .....	72
3.2	Author contribution .....	74
3.3	Full paper .....	75
3.4	Additional discussion .....	84
3.6	References .....	87
<b>4</b>	Unlocking the antioxidant properties of probucol by the encapsulation within mesoporous silica particles. ....	88
4.1	Introduction.....	88
4.2	Author contribution .....	91
4.3	Full paper .....	92
4.4	Additional discussion .....	100
4.5	Conclusion .....	104
4.6	References.....	105

<b>5</b>	Exploring the pharmacological properties of drug compounds released from mesoporous silica for the treatment of neuroinflammation. ....	108
5.1	Introduction .....	108
5.2	Materials and method.....	111
5.3	Results and discussion .....	114
5.3	Conclusion .....	122
5.4	References .....	124
<b>6</b>	Zebrafish as a biological model of oxidative stress for testing the therapeutic properties of drug compounds and mesoporous silica. ....	128
6.1	Introduction .....	128
6.2	Materials and methods .....	130
6.3	Results and discussion .....	133
6.4	Conclusion .....	139
6.5	References .....	140
<b>7</b>	<b>Overall conclusions and future directions.....</b>	<b>143</b>
7.1	References .....	145
<b>8</b>	<b>Appendices.....</b>	<b>146</b>
8.1	Appendix A: Supporting information of Chapter 3. ....	146
8.2	Appendix B: Supporting information of chapter 4.....	161
8.3	Appendix C: Supporting information of chapter 5.....	176
8.4	Appendix D: Supporting information of chapter 6. ....	181

# Abstract

Oxygen and nitrogen containing reactive species are biologically important molecules in a range of physiological systems. The heightened production of reactive species causes oxidative damage to key biomolecules that contribute to the pathogenesis of diseases such as diabetes, cardiovascular, cancer, and neurodegeneration. Disruption to the blood brain barrier integrity by oxidative stress and inflammation (neuroinflammation) is a key event that causes the infiltration of neurotoxins and the development of neurodegenerative diseases. Drug compounds with antioxidant/anti-inflammatory properties are ideal candidates for the treatment of neuroinflammation. However, the therapeutic effectiveness of these drug compounds are limited by their poor aqueous solubility.

The aim of this thesis is to explore the solubility and pharmacological properties of drug compounds released from mesoporous silica particle (MSP) for potentially new thereaputic applications. In chapter 3, the local molecular structure of the amorphous drug loaded within MSPs are explored through the use of pair distribution function (PDF) analysis of high energy X-ray diffraction (HE-XRD) scans in order to understand the effect of such differences on the *in vitro* drug release. While an enhancement in the dissolution rate was achieved for a range of poorly soluble drug compounds released from MSP, PDF analysis provided additional information on the local molecular ordering of the loaded drug, which other characterisation techniques such as differential scanning calorimetry (DSC), nitrogen sorption, and X-ray diffraction (XRD) could not.

In chapter 4, probucol (PB) a drug compound considered practically insoluble in biological media, was loaded within MSP to determine the effect of drug loading (wt%), textural properties of MSP and capsule dose on the solubility of PB as compared to crystalline PB. The encapsulation of PB in the amorphous form was achieved at an equivalent loading of 30 wt% in SBA-15, and AMS-6 with a significant enhancement in the solubility of PB released from MSP as compared to crystalline PB. Further *in vivo* studies in rats showed an enhancement in pharmacokinetic properties of PB released from AMS-6 was achieved compared to crystalline PB at the equivalent dose. Additional *in vitro* studies in cellular models of oxidative stress showed an enhancement in PB's antioxidant properties released from AMS-6 was achieved as compared to crystalline PB.

In chapter 5, the pharmacological properties of probucol and indomethacin released from AMS-6 was further explored in an *in vitro* blood brain barrier (BBB) model of neuroinflammation, using lipopolysaccharide (LPS) as the pro-inflammatory stimulus. An enhancement in the pharmacological properties of the drug released from AMS-6 was achieved as compared to the crystalline drug. Of the test compounds, ascorbic acid which is a potent water soluble antioxidant, and PB released from AMS-6 reduced LPS mediated increase in the permeability of the blood brain barrier compared to INDO and AMS-6INDO, suggesting drug compounds with antioxidant properties are superior in the treatment of neuroinflammation. In the final chapter, the antioxidant properties of PB released from AMS-6 was further explored *in vivo* in a zebrafish model of oxidative stress. PB released from AMS-6 reduced levels of reactive species at a lower dose in comparison to ascorbic acid and crystalline PB. Overall, this thesis suggest the encapsulation of poorly soluble drug compounds within MSP is a viable strategy to unlock the pharmacological properties of the drug compounds for new therapeutic applications.

## Acknowledgement

*The work and effort put into this thesis was made possible by the support and commitment of a great number of people. I would like to give my sincere thanks to my primary supervisor, Alfonso Garcia-Bennett, for taking me under his wings. Thanks for giving me the opportunity, and guidance to explore the many roles of a researcher. Without your support, both financial and motivational, I'm certain the work would have not been possible. Thank you to Tom Lawson, our lab manager/supervisor, for keeping us all safe and healthy in addition to the many resourceful advice, financial support, and laughs along the way. Thanks to our collaborators at UTS, Valery Coombes and Benjamin Sealy, for sharing their expertise in cell culture and helping me with the experiments. Thanks to Marco Morsch at the faculty of medicine, who provided me with the guidance and a helping hand in zebrafish experiments. Thank you to my research colleagues I have met along the way at Macquarie Uni. Special thanks goes to the members of the Nano biomaterials team for their support, and guidance along the journey. And of course, a big thanks to my parents and family who have, and continue to support me.*

Michael Hui Ong Lau

## ***Publications arising from this thesis***

1. Probing the amorphous state of pharmaceutical compounds within mesoporous material using pair distribution function analysis, *Journal of Pharmaceutical Sciences*, 2018, 107, 2216-2224.

A. Garcia-Bennett, **M. Lau**, N. Bedford

doi.org/10.1016/j.xphs.2018.03.029

2. Antioxidant properties of Probucol released from mesoporous silica, *European Journal of Pharmaceutical Sciences*, 2019, 138, 105038.

**M. Lau**, K. Giri, A. Garcia-Bennett

doi.org/ 10.1016/j.ejps.2019.105038

3. Antioxidant properties of probucol for the treatment of neuroinflammation, *In preparation*

**M. Lau**, B. Sealy, V. Coombes, A. Garcia-Bennett

4. Probucol released from mesoporous silica for the treatment of oxidative stress in zebrafish, *In preparation*

**M. Lau**, M. Morsch, A. Garcia-Bennett

## ***Other relevant publications***

1. Complexes and compositions comprising Probucol and uses thereof

International Patent Application, No. PCT/AU2020/050062, priority date 31<sup>st</sup> January 2019.

**M. Lau**, K. Giri, A. Garcia-Bennett

2. Pore structure and particle shape modulates the protein corona of mesoporous silica particles

K. Giri, I. Kushnerus, **M. Lau**, J. Ruan, A. Garcia-Bennett

*Materials Advances*, 2020, 1, 599-603.

doi.org/10.1039/D0MA00188K

3. A lysozyme corona complex for the controlled pharmacokinetic release of Probucol from mesoporous silica particles.

K. Giri, **M. Lau**, I. Kushnerus, I. Moroni, A. Garcia-Bennett, *Biomaterials Science*, 2020, 8, 3800-

3803. doi.org/10.1039/D0BM00445F

4. Effect of a protein corona on the fibrinogen induced cellular oxidative stress of gold nanoparticles,

I. Kuschnerus, **M. Lau**, K. Giri, N. Bedford, J. Biazik-Richmond, J. Ruan, A. Garcia-Bennett

*Nanoscale*, 2020, 12, 5898-5905.

[doi.org/10.1039/D0NR00371A](https://doi.org/10.1039/D0NR00371A)

## ***Conference Presentations***

1. **M. Lau**, N. Bedford, A. Garcia-Bennett. “Probing the amorphous state of pharmaceutical compounds within mesoporous material using pair distribution function analysis” at 10th International Mesostructured Materials Symposium (IMMS-10) held on 10th – 13th Sep 2018 in University of California Los Angeles, Los Angeles, CA, USA. (Poster)

2. **M. Lau**, A. Garcia-Bennett “Probing the amorphous state of pharmaceutical compounds within mesoporous material using pair distribution function analysis” at 1st annual Bionetwork research symposium on 13th Apr 2018, Macquarie University, Sydney, Australia. (Poster)

3. K. Giri, **M. Lau**, A. Garcia-Bennett “Understanding the effects of pore structure on drug release from mesoporous particles” at 8th International Nanomedicine Conference held on 3rd - 5th Jul 2017 in Sydney, Australia. (Poster)

## ***Awards***

1. 10<sup>th</sup> international mesostructured materials symposium (IMMS-10), winner of best poster, CA, USA, September 2018 (USD 500)

2. International Macquarie University Research Excellence Scholarship (iMQRES) availed from December 2016 to December 2019. (AUD 26,989/year)

## *Abbreviation*

AMS-6	Anionic surfactant templated mesoporous silica number 6
AA	Ascorbate
AR	Arachidonic acid
APTES	(3-Aminopropyl) triethoxysilane
AUC	Area under the curve
ATP	Adenosine triphosphate
BBB	Blood brain barrier
BCS	Biopharmaceutics classification system
CNS	Central nervous system
C <sub>max</sub>	Maximum concentration
CMC	Critical micelle concentration
COX	Cyclooxygenase
C <sub>s</sub>	Solubility of the solid in solvent
CSDS	Co-structure directing agent
CTAB	Cetyltrimethyl ammonium bromide
D	Diffusion coefficient
DMSO	Dimethyl sulfoxide
DMEM	Dulbecco/Vogt modified Eagle's minimal essential medium
DPF	Day post fertilisation
DSC	Differential scanning calorimetry
ELISA	Enzyme-linked immunosorbent assay
eNOS	Endothelial NOS
FBS	Fetal bovine serum
GIT	Gastrointestinal tract
GSH	Glutathione
INDO	Indomethacin
iNOS	inducible NOS
IUPAC	International union of pure and applied chemistry
LPS	Lipopolysaccharide
MSP	Mesoporous silica particles

MCM-41	Mobil composition of matter No.41
NADPH	Nicotinamide adenine dinucleotide phosphate oxidase
NVU	Neurovascular unit
NOS	nitric oxide synthases
NSAID	Non-steroidal anti-inflammatory drug
nNOS	Neuronal NOS
PB	Probucol
PGE <sub>2</sub>	Prostaglandin E <sub>2</sub>
RNS	Reactive nitrogen species
ROS	Reactive oxygen species
RT	Room temperature
SBA-15	Santa Barbara amorphous
SEM	Scanning electron microscope
SGF	Simulated gastric fluid
SIF	Simulated intestinal fluid
SLS	Sodium lauryl sulphate
SOD	Superoxide dismutase
TEER	Transendotehlial electrical resistance
TEOS	Tetraethyl orthosilicate
TGA	Thermogravimetric analysis
TEM	Transmission electron microscopy
TLR	Toll like receptors
TNF- $\alpha$	Tumour necrosis factor alpha
XRD	X-ray diffraction
WHO	World health organization



## ***Thesis outline***

The chapters of this thesis are arranged in the following order: **Chapter 1** provides a review of the topics explored in this thesis including the role of reactive oxygen species (ROS) in oxidative stress, ROS and inflammatory mediators of neuroinflammation, pharmaceutical and formulation science of drug compounds in their treatment of associated diseases, as well as the use of mesoporous silica particles in drug delivery. **Chapter 2** is a description of the synthesis, characterisation, biological assays, *in vitro* cellular and *in vivo* models utilised in the thesis. **Chapters 3-6** are written around the four scientific publications that I have co-authored, which form the core work of this thesis. Each of these chapters are introduced from a perspective that is broader than that of the introduction included in the manuscripts. Similarly, each chapter ends with a discussion of the results from a broader scope than included in the publications. **Chapter 7** provides a summary of the key findings of the research presented, and provides information of possible studies in the future.

## ***Aim of this thesis***

1. Probe the amorphous form of pharmaceutical drug compounds loaded within mesoporous silica (Chapter 3).
2. Study the impact of the textural properties of mesoporous silica on the rate of probucol release compared to crystalline probucol (Chapter 4).
3. Explore the therapeutic application of drug compounds released from mesoporous silica for the treatment of neuroinflammation in an *in vitro* model of the blood brain barrier (Chapter 5).
4. Explore the antioxidant properties of probucol in an *in vivo* model (Zebrafish) of oxidative stress (Chapter 6).

# 1 INTRODUCTION

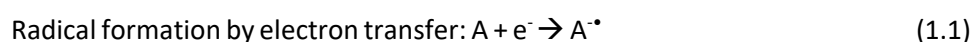
## 1.1 Free radicals play an important role in the pathogenesis of diseases

A free radical is defined as any atom or molecular species containing one or more unpaired electron(s) in an atomic or molecular orbital respectively [1, 2]. Free radicals produced in biological systems are highly reactive, and causes oxidative damage to a range of biomolecules that are vital for normal cell function and structure including: DNA, proteins, and lipids [3, 4]. The accumulation of cellular and tissue damage due to oxidative stress contributes to the pathogenesis of various diseases including diabetes, cardiovascular, and neurodegeneration (Table 1.1) [5].

Major organ	Diseases	Global total disease burden
Cardiovascular	Arteriosclerosis, hypertension, ischemia, heart failure	14.6%
Multi-organ	Cancer, diabetes, inflammation, infection, aging	9.4%
Neonatal	Pre-eclampsia, growth restriction	7.5%
Musculoskeletal	Arthritis, rheumatism	5.5%
Brain	Alzheimer's disease, Parkinson's, depression, stroke	4.9%
Lungs	Asthma, Chronic bronchitis	4.5%

**Table 1.1:** A summary of the major organs and diseases associated with oxidative stress, and the estimated global total disease burden (sum in cases of mortality and morbidity) in 2017 [6].

Oxygen and nitrogen free radicals, known as reactive oxygen species (ROS) and reactive nitrogen species (RNS), are considered the most important free radicals in biological systems as they are involved in various physiological processes including cell growth and apoptosis, immune function, and DNA replication [7, 8]. The production of free radicals occurs with the transfer of an electron, and are conventionally indicated with a superscript dot:



## 1.2 Reactive oxygen species

Reactive oxygen species (ROS), are oxygen containing molecules with one or more unpaired electron(s) [8]. As an example, the electronic configurations of the ROS superoxide anion ( $O_2^{\bullet -}$ ) and the hydroxyl radical ( $OH^{\bullet}$ ) are shown in Figure 1.1.

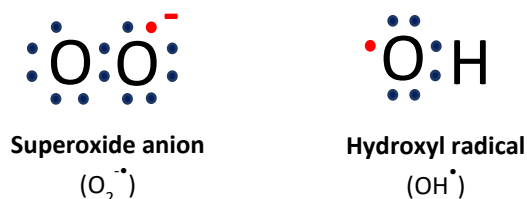
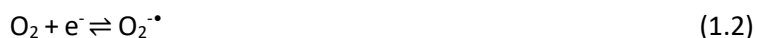


**Figure 1.1:** Octet electronic configurations of ROS  $O_2^{\bullet -}$  and  $OH^{\bullet}$ , where blue dots represent paired electrons and red dots represent an unpaired electron.

### 1.2.1 The superoxide anion

The superoxide anion ( $O_2^{\bullet -}$ ) is the primary ROS that leads to the production of secondary, more reactive species including hydrogen peroxide ( $H_2O_2$ ), and  $OH^{\bullet}$  [4]. The  $O_2^{\bullet -}$  is produced from the reduction of molecular  $O_2$ :



The molecule is unstable in aqueous solution, with a half-life of a few seconds, and is rapidly dismutated by the superoxide dismutase (SOD) enzyme to  $H_2O_2$  (rate constant,  $k \simeq 2 \times 10^9 \text{ mol} \cdot \text{l}^{-1} \cdot \text{s}^{-1}$ ) [4]. Furthermore, the  $O_2^{\bullet -}$  is poorly permeable across the cell membrane, and is generally restricted to the cell compartment in which it is produced [8].

### 1.2.2 Hydrogen peroxide

Compared to the  $O_2^{\bullet -}$ ,  $H_2O_2$  is a relatively more stable, diffusible, and cell membrane permeable reactive species, making it more biologically active in moving from the cell of origin to neighbouring cells [9].  $H_2O_2$  is typically produced from the reaction of two  $O_2^{\bullet -}$  to form  $H_2O_2$  and  $O_2$ :



This reaction can occur spontaneously or is catalysed by the SOD enzyme. The pathological effects of  $H_2O_2$  is considered to be mediated by the conversion of  $H_2O_2$  to the highly reactive  $OH^{\bullet}$  radical.

### 1.2.3 The hydroxyl radical

The hydroxyl radical ( $\text{OH}^\bullet$ ) is a highly unstable molecule, with an estimated half-life of 1 nano-seconds (ns) in biological systems [4]. It is produced from the addition of an electron to  $\text{H}_2\text{O}_2$  from the reduced metal ion ( $\text{Fe}^{2+}$ ), commonly referred to as the Fenton reaction [8, 10]:



In biological systems,  $\text{OH}^\bullet$  is mainly produced from the interaction between  $\text{O}_2^{\bullet-}$  and  $\text{H}_2\text{O}_2$  in the Haber-Weiss reaction [10]:

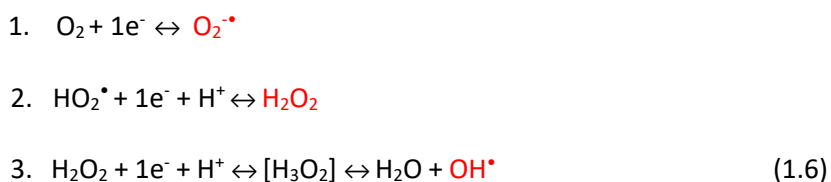


Furthermore, under oxidative stress,  $\text{O}_2^{\bullet-}$  can signal the release of  $\text{Fe}^{2+}$  from iron containing molecules such as ferritin (an intracellular protein that stores iron), increasing the levels of  $\text{Fe}^{2+}$  that are available for the production of  $\text{OH}^\bullet$  [8]. Most of the pathological effects of ROS is mediated by the production of the highly reactive  $\text{OH}^\bullet$  from the conversion of  $\text{O}_2^{\bullet-}$  and  $\text{H}_2\text{O}_2$ , as  $\text{OH}^\bullet$  reacts very rapidly with almost all of the biomolecules in living cells [8].

## 1.3 Cellular mechanisms of ROS production

### 1.3.1 ROS in the mitochondria

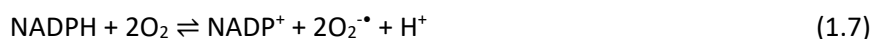
The electron transport chain of the mitochondria is the primary site for the production of energy in the form of adenosine triphosphate (ATP) molecules [10]. In aerobic organisms, cytochrome oxidase, a large multiprotein assembly complex, is responsible for catalysing the step by step reduction of molecular  $\text{O}_2$  to  $\text{H}_2\text{O}$  for the production of ATP in the mitochondria [10, 11]. During this process, the production of ROS as an intermediate product can occur through the following steps:



The reduction of molecular  $O_2$  generates the ROS  $O_2^{\cdot-}$ ,  $H_2O_2$ , and  $OH^{\cdot}$ . Mitochondria can consume approximately more than 95 % of  $O_2$  during the production of ATP [11]. The remaining 1-4 % of  $O_2$  molecules may be incompletely reduced and form  $O_2^{\cdot-}$  [11].

### 1.3.2 Nicotinamide adenine dinucleotide phosphate oxidase

Nicotinamide adenine dinucleotide phosphate oxidase (NADPH) is a transmembrane, multi-complex enzyme that serves to transport electrons for the reduction of molecular  $O_2$  to  $O_2^{\cdot-}$  [12]:



There are seven known isoforms of NADPH enzymes that are characterised by differences in protein composition, ROS expression, and tissue distribution [12].

## 1.4 Reactive nitrogen species

Reactive nitrogen species (RNS), are nitrogen containing molecules with one or more unpaired electron(s) [8, 9]. The main RNS in biological systems are nitric oxide ( $NO^{\cdot}$ ) and peroxynitrite anion ( $ONOO^-$ ) and their electron configurations are shown in Figure 1.2.

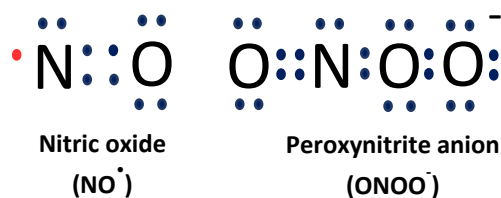
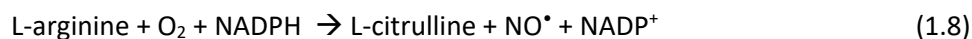


**Figure 1.2:** Electronic configurations of the RNS  $NO^{\cdot}$ , and  $ONOO^-$ , where blue dots represent paired electrons and red dots represent an unpaired electron.

### 1.4.1 Nitric oxide

Nitric oxide ( $NO^{\cdot}$ ) is a small molecule that regulates physiological functions involved in neurotransmission, vascular tone, immune function, and gene transcription [13]. It is generated by the enzyme nitric oxide synthases using L-arginine as the substrate, with  $O_2$  and NADPH as the co-substrates [14]. The oxidation of L-arginine follows the transfer of electrons from NADPH to form L-citrulline and  $NO^{\cdot}$  [14]:



In humans, NO• is produced by three different isoforms of the NOS enzyme: inducible NOS [15], endothelial NOS (*eNOS*), and neuronal NOS (*nNOS*) [16-18]. The *iNOS* expressed by macrophages is induced by microorganisms, parasites or other substances to produce a high amount of NO• within cytotoxic levels [16]. The *eNOS* is primarily expressed by endothelial cells and is an important regulator of cardiovascular function [17]. The *nNOS* expressed by neurons in the brain is responsible for the regulation of synaptic signalling in learning, memory, and neurogenesis [18].

#### 1.4.2 Peroxynitrite anion

Peroxynitrite anion (ONOO<sup>-</sup>) is a highly potent RNS that is produced from the interaction between NO• and O<sub>2</sub><sup>-•</sup>:



Compared to other reactive species, ONOO<sup>-</sup> is a highly reactive molecule that is capable of causing extensive damage to biological molecules. Furthermore, ONOO<sup>-</sup> is a relatively stable species, with a long biological half-life when compared to other ROS/RNS (Table 1.2).

ROS/RNS	Half-life (seconds)	Location	Reactivity	Diffusibility across plasma membrane
O <sub>2</sub> <sup>-•</sup>	10 <sup>-6</sup>	Mitochondria and cytosol	+++	++
H <sub>2</sub> O <sub>2</sub>	10 <sup>-3</sup>	Mitochondria and cytosol	++	+++++
OH•	10 <sup>-9</sup>	Mitochondria and cytosol	+++++	+
NO•	1-10	Mitochondria, cytosol, and plasma membrane	+	+++
ONOO <sup>-</sup>	1.9	Mitochondria	++++	+

**Table 1.2** Summary of the key properties of ROS/RNS. Data adapted from [4].

## 1.5 Antioxidants

Antioxidants are scavengers of reactive oxidative species. In this process antioxidants serve as either reducing or oxidising agents in the conversion of ROS/RNS into less reactive molecules with stable paired electrons (Figure 1.3) [19]. The antioxidant itself is converted to an unreactive metabolite. Other actions of antioxidants include the termination of free radical chain reactions, regeneration of antioxidants, and the regulation of enzymatic activities in the production of reactive species [20]. Antioxidants can be categorised into two main groups, enzymatic or non-enzymatic antioxidants.

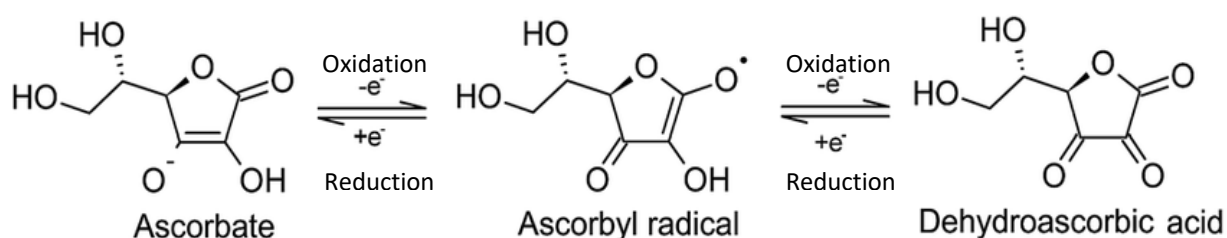


**Figure 1.3:** Antioxidants are scavengers of reactive species. In this example, the antioxidant ascorbate is the ionised form of ascorbic acid in biological media. The ascorbyl radical is the partially oxidised form of ascorbate and can act as an electron acceptor or donor (oxidant or reducer). The oxidation of ascorbyl radical generates dehydroascorbic acid which is unstable and has a half-life of approximately 6 minutes at physiological pH [21].

### 1.5.1 Enzymatic antioxidants

Enzymatic antioxidants, are enzymes that suppress or prevent the formation of ROS/RNS in cells. It does this by neutralising molecules that have the potential to develop into a free radical, or scavenging any free radicals that can induce the production of other radical species [20]. The main *enzymatic antioxidants* are:

#### (a) Superoxide dismutase

The superoxide dismutase (SOD) is considered the most powerful cellular antioxidant [8]. The enzyme catalyses the conversion of two molecules of  $O_2^{\bullet -}$  to  $H_2O_2$  and  $O_2$ . The  $H_2O_2$  is removed by either catalase or glutathione peroxidase enzyme [19].

### (b) Catalase

The enzyme catalase is found predominately in the peroxisomes of cells and promotes the reduction of  $\text{H}_2\text{O}_2$  into  $\text{H}_2\text{O}$  and  $\text{O}_2$  [19]:



The enzyme requires iron or manganese as a cofactor for enzyme activity [19].

### (c) Glutathione peroxidase

Glutathione peroxidase is primarily responsible for the reduction of  $\text{H}_2\text{O}_2$  to  $\text{H}_2\text{O}$  in the mitochondria, and the reduction of lipid peroxides to alcohols [8, 20]. The enzyme is important in protecting cells against lipid peroxidation by ROS/RNS [20].

## 1.5.2 Non-enzymatic antioxidants

Non-enzymatic antioxidants, are low molecular weight compounds that can be naturally produced by enzymes endogenously, or are acquired exogenously from the diet [20]. Non-enzymatic antioxidants can be further categorised as being either lipid soluble or water soluble antioxidants:

### (a) Vitamin E

Vitamin E is a lipid soluble antioxidant and plays a vital role in the protection of cell membranes from oxidative damage by reactive species [22]. Vitamin E is known to quench peroxyl radicals to stop it from propagating the chain reaction involved in lipid peroxidation [19].

### (b) Ascorbate

Ascorbate (AA) is a highly potent, water soluble antioxidant that can scavenge both intracellular and extracellular free radicals in biological systems (Figure 1.3) [23, 24]. AA is known to scavenge a range of ROS/RNS including peroxides,  $\text{ONOO}^-$ , and  $\text{O}_2^{\cdot -}$  [25].



### (c) Glutathione

Glutathione is a water soluble antioxidant that is produced in the cytosol by the enzyme glutathione synthetase [20]. The protective roles of the antioxidant include:

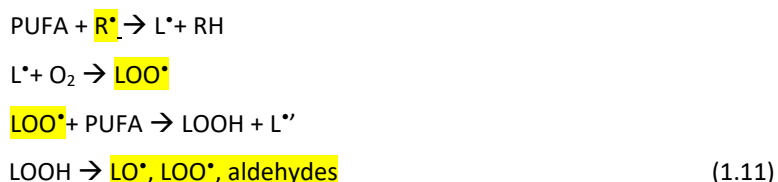
- As a cofactor of various detoxifying enzymes against oxidative stress [26].
- Scavenger of  $\text{OH}^\bullet$ ,  $\text{H}_2\text{O}_2$  and lipid peroxides [8].
- Regeneration of antioxidants AA and vitamin E to its active form [27].

#### 1.5.3 Antioxidants, reactive species and the redox state

It is the concentration of species (also known as the redox state) that determines whether ROS/RNS play a physiological or a pathological role in biological systems. The redox state is maintained within normal physiological levels when the production of ROS/RNS is balanced by antioxidant activity [8]. In this instance, the physiological functions of ROS/RNS includes:

- As signalling molecules associated with the surface receptor-ligand complex [29].
- Host defence mechanisms against pathogens and microbes [30].
- Regulation of cell differentiation and apoptosis [31, 32].

At high concentrations of species due to an imbalance between free radical production and antioxidant activity, ROS/RNS play a pathological role as they can oxidise biomolecules that are vital for cellular function and structure (Figure 1.4). All biomolecules can be oxidised by ROS/RNS, with lipids being particularly susceptible [33]. Cellular membranes are rich in polyunsaturated fatty acids (PUFAs). Oxidative destruction of PUFAs, also known as lipid peroxidation, is described below where the interaction between PUFA and an initiating radical ( $\text{R}^\bullet$ ) leads to a chain reaction sustained by the generation of free radicals (highlighted in yellow) [33]:



Oxidation of PUFA leads to the production of the fatty acid radical ( $L^{\bullet}$ ) which rapidly forms the fatty acid peroxy radical ( $LOO^{\bullet}$ ) in the presence of  $O_2$ . The  $LOO^{\bullet}$  initiates new chain reactions by oxidising other PUFA molecules, producing lipid hydroperoxides (LOOH) that break down to radical species including lipid peroxy ( $LO^{\bullet}$ ) and more lipid alkoxy radicals ( $LOO^{\bullet}$ ) [34]. Aldehydes are considered biologically active compounds that can diffuse and spread damage to neighbouring cells [33]. Other examples of oxidative damage include: single and or double strand DNA breaks, damage to the DNA backbone and oxidative modification to protein structure and function [3, 20]. Oxidation of biomolecules can lead to the development of DNA mutations, carcinogenesis, ageing and other diseases [3, 35]. Furthermore, ROS/RNS can activate molecular mechanisms that promote cell apoptosis, leading to loss in tissue structure and function [36-38].

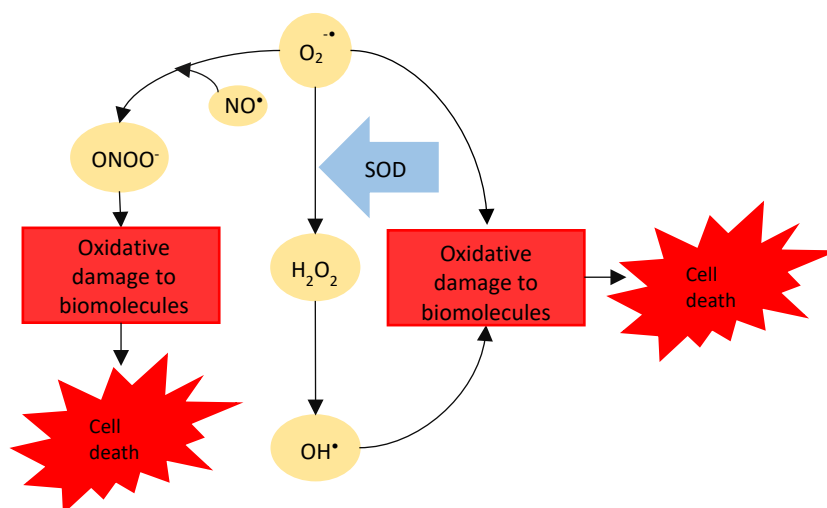


**Figure 1.4:** Schematic representation of the ROS/RNS mediated oxidative damage to biomolecules and cell death. The  $O_2^{\bullet-}$  is converted by the superoxide dismutase enzyme (SOD) to  $H_2O_2$ , which is converted to  $OH^{\bullet}$ . Additionally,  $O_2^{\bullet-}$  can react with  $NO^{\bullet}$  to produce the highly reactive  $ONOO^-$ .

While making up only a small fraction of the total body mass, the brain is the largest source of energy consumption, with estimates that it accounts for over 20 % of total body  $O_2$  metabolism in humans [39]. As the brain is rich in lipid content and weak in antioxidant capacity, it is highly susceptible to oxidative damage by ROS/RNS [39]. In particular, the brain is highly susceptible to the infiltration of proteins, immune cells, pathogens and other blood components that can activate molecular mechanisms to increase the production of reactive species [39, 40]. The brain is protected from these harmful compounds by the blood brain barrier (BBB), which is found at the interface between the blood capillaries and the brain [41]. The function of the BBB and the mechanisms that disrupt the integrity of the BBB is explored further in the next section.

## 1.6 The blood brain barrier

Blood vessels of the cardiovascular system serve to supply nutrient rich blood to vital organs, and also in the removal of waste from the body. In the central nervous system, the supply of blood to the brain is provided by a network of capillary blood vessels [42].

The brain endothelial cells lining the capillary blood vessels form the BBB against the entry of neurotoxins that are potentially harmful to the brain. Furthermore, the endothelial cells have specialised and diverse systems for the transport of essential nutrients into the brain including ions, amino acids, and glucose [41, 43]. The integrity of the BBB is supported by a network of cells including pericytes, and astrocytes (Figure 1.5).

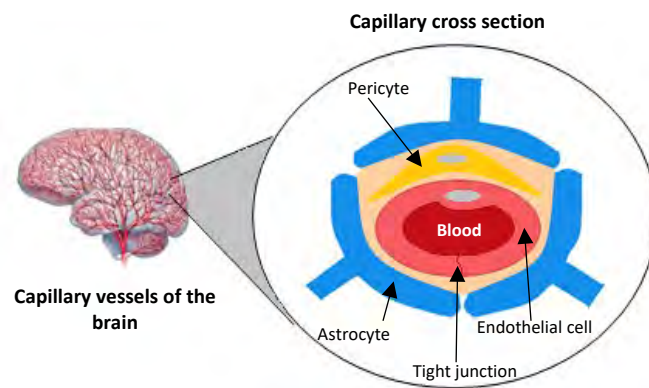


**Figure 1.5:** The cross sectional view of brain capillary blood vessels. The BBB is located in the vascular wall of the brain capillary vessels and is composed of endothelial cells, pericytes and astrocytes that are collectively known as the neurovascular unit (NVU) [44]. Endothelial cells form intercellular tight junctions against paracellular diffusion. Pericytes are found in the space between the capillary wall and astrocytes that coordinate in the function of the BBB [44]. Astrocytes play important roles in maintaining BBB integrity, ionic homeostasis and regulation of cerebral blood flow [45].

### 1.6.1 Brain endothelial cells

Brain endothelial cells form a tightly sealed, monolayer on the vascular wall of brain capillaries, functioning as the barrier between the blood and the brain [46]. The structural integrity of the BBB is maintained by tight junctions and adherens junction [41]. Tight junctions are transmembrane proteins that form between endothelial cells, maintaining low paracellular permeability and high electrical resistance of the BBB [41]. Adherens junction are proteins that maintain contact between tight junctions and endothelial cells [41, 44].

### (a) Tight junctions (TJs)

The three major transmembrane proteins that form TJs are:

- 1) *Claudin*, the major structural component and a transmembrane protein composed of 207-305 amino acids [47]. The main function of claudin is to generate a high electrical resistance that restricts access of ions through paracellular diffusion [47].
- 2) *Occludin*, the first integral membrane protein discovered within TJs of endothelial cells. Its main function is regulating selective diffusion of solutes across the BBB [48].
- 3) *Junctional adhesion molecules (JAMs)*, support the integrity of the BBB by forming the link between the cytoskeleton of endothelial cells and the tight junction proteins [44].

### (b) Adherens junction

Adherens junction (AJ) are glycoproteins that maintain the integrity of the tight junction-cell complex interaction. The transmembrane glycoproteins include the *cadherin* superfamily such as vascular endothelium cadherin (Ve-cadherin) which form adhesive complexes with adjacent cells [41]. The glycoproteins are linked to the cytoskeleton of endothelial cells by anchor proteins such as  $\alpha$ ,  $\beta$ ,  $\gamma$ -*catenin* [44].

#### 1.6.2 Astrocytes

Astrocytes play a supportive role in maintaining the structure and function of the BBB. The astrocyte end feet form a net like structure that are in direct contact with endothelial cells, and contain a high density of orthogonal arrays of particles (OAPs) [46, 49]. The OAPs contain the water channel aquaporin 4 (AQP4) that regulate BBB ion permeability and volume [45].

To summarise, each cell of the neurovascular unit play an important role in maintaining the structural integrity and function of the BBB (Figure 1.6). In the next section, disruption to the BBB integrity by mechanisms mediated by neuroinflammation are explored.

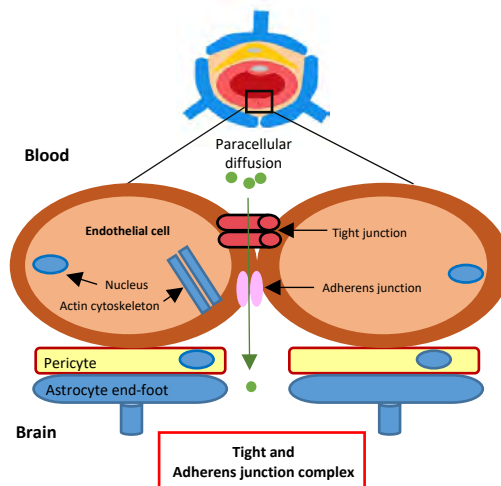


**Figure 1.6:** Tight and adherens junction protein complexes are formed between endothelial cells that restrict the paracellular permeability of molecules across the blood brain barrier.

## 1.7 Disruption to BBB integrity by neuroinflammation

Neuroinflammation is defined as the inflammatory response of the central nervous system (CNS) to pro-inflammatory stimuli such as pathogens, trauma, or UV radiation [50, 51]. The inflammatory response is mediated by the release of cytokines, inflammatory mediators, and ROS/RNS produced by brain endothelial cells, astrocytes, and peripheral immune cells [51, 52]. The release of ROS and pro-inflammatory mediators function to contain or eliminate the stimuli through the recruitment of immune cells or the activation of tissue repair responses at the site of injury. The intensity and duration of the neuroinflammation response is dependent on the severity, dose, and duration of the exposure (acute or chronic) to the pro-inflammatory stimuli [51].

For example, an acute and controlled neuroinflammatory response is considered beneficial in the containment and elimination of the pro-inflammatory stimuli. A chronic neuroinflammatory response occurs due to long term exposure to the stimuli. Specifically, the release of cytokines  $\text{TNF-}\alpha$ ,  $\text{IL-6}\beta$ , prostaglandin  $\text{E}_2$  ( $\text{PGE}_2$ ) and ROS/RNS during chronic neuroinflammation can cause disruption to the BBB integrity. This is a key event in the pathogenesis of neurodegenerative diseases [53-55]. Endothelial cells of the BBB are among the first cells to be exposed to pro-inflammatory stimuli, and are both a key target and source of the neuroinflammatory response [50]. One of the most important molecular mechanisms behind the neuroinflammatory pathways that disrupt the BBB integrity is the neuroinflammatory response of brain endothelial cells to the bacterial endotoxin, lipopolysaccharide.

### 1.7.1 Lipopolysaccharide mediated neuroinflammation in brain endothelial cells

Lipopolysaccharide (LPS) is a central component of gram negative bacteria, comprising of three structural elements including a core oligosaccharide, an O-specific chain made up of repeating sequences of polysaccharides, and the lipid A component that is key in eliciting the neuroinflammatory response [56].

Toll like receptors (TLR) are distributed on the cells of the innate immune system, functioning as sensors in the detection of pathogens, and the activation of the immune response [56, 57]. Brain endothelial cells express TLR 2,3,4 and 6 [58]. Binding of LPS to TLR4 of endothelial cells leads to an intracellular signalling cascade activating a host of signal transduction pathways, and the formation of the transcription factor, NF- $\kappa$ B, that mediate the transcription of cytokines, ROS/RNS production, activation of iNOS, and cyclooxygenase [59] enzyme (Figure 1.7) [57].

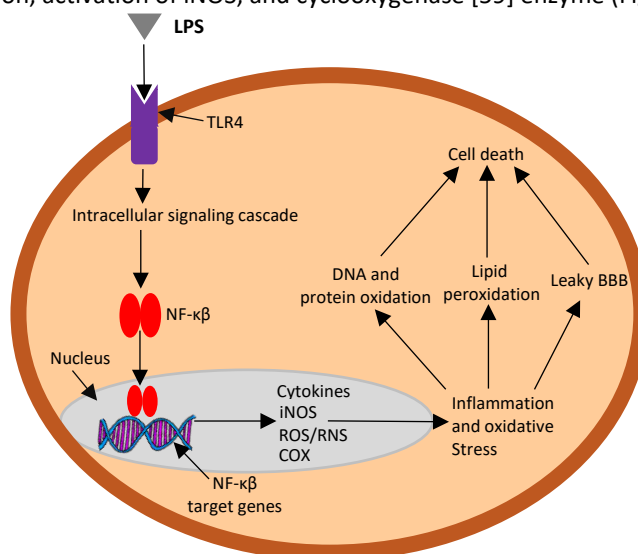


**Figure 1.7:** Schematic representation of the neuroinflammatory response in brain endothelial cells mediated by the LPS-NF- $\kappa$ B dependent signaling pathway. LPS binds to the TLR4 receptor on the endothelial cells, initiating downstream intracellular signaling cascades that leads to the activation and nuclear translocation of the transcription factor NF- $\kappa$ B. This leads to the transcription of genes that produce cytokines, ROS/RNS, iNOS and COX enzymes. The release of pro-inflammatory mediators and reactive species induce a neuroinflammatory response that cause the disruption to tight junction integrity (leaky BBB), lipid peroxidation and oxidative damage to proteins and DNA, resulting in cell apoptosis and death.

Cytokines are a group of polypeptides that activate the immune response to the pro-inflammatory stimuli. They are classified into different groups including the interleukins, tumor necrosis factors, chemokines, interferons, and growth factors. Cytokines can be synthesised by various cell types including microglia, astrocytes, endothelial cells, and macrophages [60]. Specifically, the increase in cytokine production of tumor necrosis factor (TNF- $\alpha$ ) and the interleukins (IL-1, IL-2, IL-6 and IL-8) during the neuroinflammatory state is known to cause significant changes in the permeability of the BBB [61-63]. Cytokine mediated BBB disruption is associated with the activation of the COX-

mediated production of prostaglandin, an increase in the production of ROS/RNS, and consequently an increase in vascular permeability [62, 64].

Oxidation of junctional proteins and biomolecules mediated by ROS/RNS are the key mechanisms that cause disruption to the integrity of the BBB [65-70]. For example, the oxidation of glutathione and thiol proteins of tight junctions by reactive species are associated with the increase in BBB permeability [69, 71-73]. Additionally, reactive species can disrupt the link between tight junction proteins with the cytoskeleton of endothelial cells that is crucial in maintaining the structure and function of the BBB [66, 67]. The rearrangement of the actin-cytoskeleton interaction is caused by ROS/RNS modifications to tight and adherens junction proteins that cause the increase in BBB permeability [73-75].

The iNOS enzyme can be activated by inflammatory mediators, LPS, and cytokines to produce unregulated concentrations of NO<sup>•</sup> [76]. High concentrations of NO<sup>•</sup> combine with the O<sub>2</sub><sup>•-</sup> to generate the highly reactive ONOO<sup>-</sup> radical which can oxidise a range of biomolecules and cause extensive damage to the structure and function of the BBB [76-78]. The nitration of actin and rearrangement of the actin-cytoskeleton interaction is the major mechanism of ONOO<sup>-</sup> mediated disruption to BBB integrity [77, 79].

Binding of LPS to the TLRs of endothelial cells initiates the biosynthesis of COX mediated prostaglandin E<sub>2</sub> (PGE<sub>2</sub>), which begins with the release of arachidonic acid (AR), an unsaturated fatty acid from the plasma membrane by phospholipases (PLA<sub>2</sub>) that is subsequently metabolised by the COX enzyme to prostaglandin H<sub>2</sub> (PGH<sub>2</sub>) [80]. PGH<sub>2</sub> is a substrate for synthase enzymes that convert it to bioactive prostaglandins including PGE<sub>2</sub>, PGI<sub>2</sub>, PGD<sub>2</sub>, and TXA<sub>2</sub> [80].

There are two isoforms of the COX enzyme: COX-1 is constitutively expressed in cells and produce prostaglandins to maintain normal physiological function, and the inducible COX-2, is activated by pro-inflammatory stimuli [81]. Both isoforms of the enzymes can contribute to the production of prostaglandins during neuroinflammation. Systemic exposure to high concentrations of LPS can activate a significant increase in COX-mediated PGE<sub>2</sub> production that cause brain tissue necrosis, breakdown of the blood brain barrier, and brain oedema *in vivo* [80, 82]. For example, an approximated 2-3 fold increase in BBB permeability was observed in rats within 6-12 hrs post injection of LPS compared to the negative control [82]. Correspondingly, levels of PGE<sub>2</sub> reached its peak 6 to 8 hr post injection of LPS, suggesting the increase in PGE<sub>2</sub> contributed to the significant disruption to BBB integrity [82-84].

## 1.8 Therapeutic options for the treatment of neuroinflammation

As the junctional proteins of the BBB are highly sensitive to the damage caused by ROS/RNS and pro-inflammatory mediators, therapeutic compounds containing antioxidant and/or anti-inflammatory properties are needed to protect the integrity of the BBB. Therapeutic options include: the non-steroidal anti-inflammatory drug (NSAID) indomethacin, which is an inhibitor of COX-mediated PGE<sub>2</sub> production, the antioxidant ascorbic acid that quench ROS/RNS, and probucol a compound with both anti-inflammatory and antioxidant properties. The pharmacological properties of these therapeutic options are dependent on solving formulation challenges associated with their oral delivery.

### 1.8.1 Indomethacin

Indomethacin (INDO) is a potent non-selective COX enzyme inhibitor (Figure 1.8) that has been shown to be more effective in the treatment of neuroinflammation compared to other drug compounds of the NSAID family. In an *in vitro* BBB model consisting of a monolayer of brain endothelial cells grown in culture, pre-treatment with INDO (1 µM) attenuated the LPS (50 ng/ml) mediated increase in BBB permeability [85]. In comparison, treatment with the selective COX-2 inhibitor, dexamethasone, was not as effective as INDO in maintaining the integrity of the BBB [85, 86]. Further *in vitro* studies of the BBB showed that treatment with INDO at 100 µM significantly reduced LPS induced increase in permeability to the small molecule sucrose (MW 342 Da) and to the protein, albumin (MW 65 KDa) [87]. The increase in permeability to both the small and large molecules in this instance is suggestive of major disruption to the BBB integrity involving both an increase in paracellular and transcellular permeability.

Disruption to BBB integrity by LPS can result in neurological damage, and cause physiological and behavioural changes that are similar to symptoms associated with neurodegenerative diseases including reduced activity, appetite, and decline in cognitive ability [83, 88, 89]. *In vivo* studies in mice treated with LPS showed significant cognitive decline and elevated levels of PGE<sub>2</sub> as compared to healthy mice [83]. Pre-treatment with INDO (15 mg/kg), or ibuprofen (30 mg/kg) prior to LPS injection was shown to reverse LPS induced behavioural changes, an effect that was not observed in mice pre-treated with COX-2 selective inhibitors nimesulide and dexamethasone [83]. Treatment with INDO led to a significant reduction in PGE<sub>2</sub> levels, and greater improvement in cognitive tests, which was not observed with other treatments including ibuprofen. From these studies, it can be concluded that



inhibition of COX-1 and COX-2 mediated production of PGE<sub>2</sub> play an important role in the treatment of neuroinflammation induced by LPS [86, 90, 91].

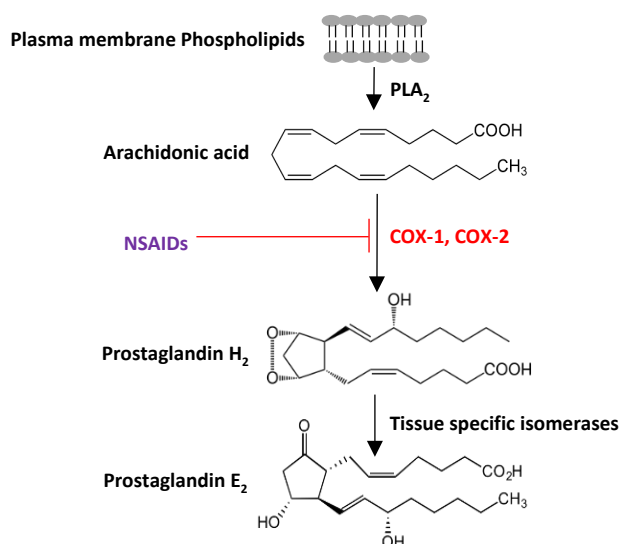


**Figure 1.8:** Schematic representation of the COX enzyme mediated production of PGE<sub>2</sub>. Nonsteroidal anti-inflammatories (NSAIDs) are drug compounds that inhibit COX enzyme activity. PLA<sub>2</sub> are phospholipases that hydrolyses lipids from the plasma membrane to arachidonic acid.

### 1.8.2 Ascorbic acid

In humans, ascorbic acid is an essential nutrient that is acquired from the diet. Ascorbic acid serve numerous physiological functions including the stimulation of endothelial cell proliferation, inhibition of cellular apoptosis, and a scavenger of ROS/RNS [92-94]. Ascorbic acid dissociates at physiological pH to form Ascorbate (AA), the redox state of ascorbic acid that is found abundantly in cells [95]. AA is a strong reducing agent, and as it is highly water soluble, has the ability to scavenge reactive species including O<sub>2</sub><sup>•</sup>, H<sub>2</sub>O<sub>2</sub> and OH<sup>•</sup> in aqueous media or intracellularly, therefore protecting against ROS/RNS mediated oxidation of biomolecules [23, 93, 96]. AA is taken up intracellularly via the sodium-dependent vitamin C transporter -2 (SVCT2) [95]. Endothelial cells maintain high levels of intracellular AA level by converting the oxidised form, dehydroascorbate (DHA), back to AA, and also through cellular uptake of DHA and AA (Figure 1.9) [93].

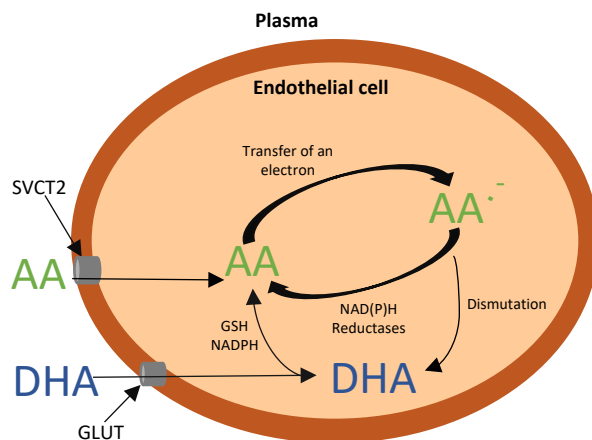


**Figure 1.9:** Schematic representation of the cellular uptake and regeneration of ascorbate (AA). AA enters the cells through the SVCT2 transporter, and intracellular AA can donate an electron to quench ROS/RNS to form an unreactive metabolite (AA<sup>•-</sup>) that is converted back to ascorbate by NADPH-dependent reductases. Furthermore, AA<sup>•-</sup> can undergo dismutation to DHA which is subsequently reduced by glutathione or nicotinamide adenine dinucleotide phosphate (NADPH) to AA. DHA from plasma can enter endothelial cells through the GLUT transporter.

Treatment with AA can preserve the structure and function of TJ proteins by mechanisms including inhibition of the iNOS enzyme, promotion of endothelial cell growth, and as a scavenger of reactive species [76, 96-104]. Furthermore, AA can preserve eNOS enzyme activity that is important in generating physiological levels of nitric oxide for normal vascular function and in maintaining BBB integrity [25, 105] .

### 1.8.3 Probucol

Probucol [106] is a pharmaceutical drug compound containing two butylated hydroxytoluenes connected by a sulfur carbon sulfur bond as the chemical structure (Figure 1.10) [107]. It was first introduced in the 1970s as a cholesterol lowering drug for the treatment of high cholesterol. Further studies have explored PB's antioxidant properties for the treatment of diseases caused by oxidative stress including atherosclerosis, xanthoma and neuroinflammation [108].

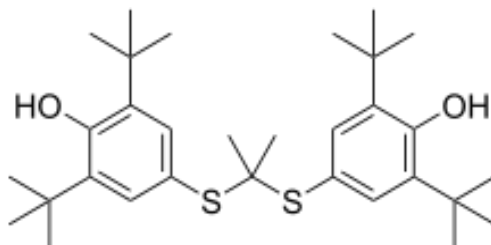


**Figure 1.10:** Chemical structure of probucol.

PB is a potent antioxidant capable of scavenging ROS/RNS involved in the oxidative modification of proteins and other biomolecules [109, 110]. In this process, PB is oxidised by ROS/RNS to unreactive intermediate products 3,3',5,5'-tetra-tert-butyl-4,4'-diphenoquinone (DPQ), with intermittent formation of 4,4'-dithiobis(2,6-di-tert-butyl-phenol) (DTBP) [111, 112]. The antioxidant property of PB is largely dependent on the rate of cellular uptake, and the intracellular concentration of the drug molecule.

As PB is a poorly soluble drug compound, a long pre-incubation of up to 8 to 12 hours is typically required to achieve a high intracellular drug concentration corresponding with the peak in antioxidant activity (Figure 1.11) [113]. This suggest PB is transported intracellularly where it is incorporated into the cellular membrane, or is further transported to intracellular compartments in quenching reactive species that have the potential to cause oxidative damage.

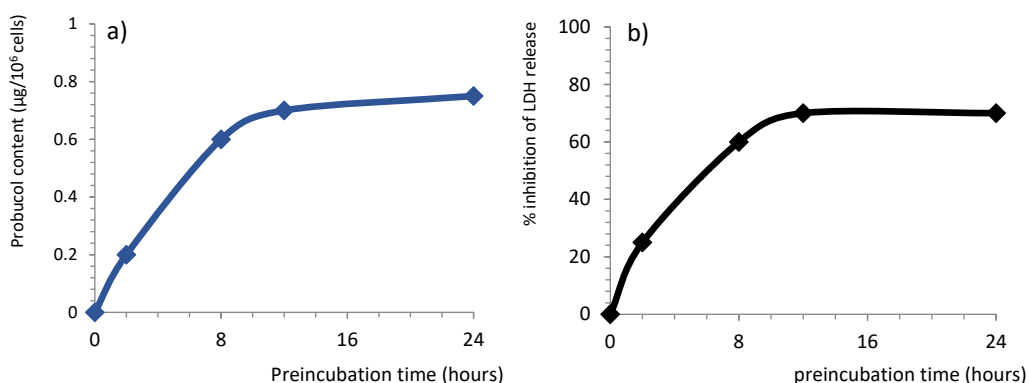


**Figure 1.11:** The intracellular concentration of probucol in (a) endothelial cells is related to (b) the peak inhibition of lactate dehydrogenase (LDH) release, a marker of tissue damage associated with oxidative stress. Figure adapted from [113].

The antioxidant and anti-inflammatory properties of PB has been explored in both *in vitro* and *in vivo* models of neuroinflammation [114, 115]. Pre-treatment with PB resulted in a dose dependent inhibition in the release of  $\text{NO}^*$ ,  $\text{PGE}_2$ ,  $\text{IL-1}\beta$  and  $\text{IL-6}$  from LPS treated microglia cells [115], and in *in vivo* neuroinflammatory models (mice) [114]. The anti-inflammatory properties of PB were associated with the downregulation of the  $\text{NF-}\kappa\beta$  signalling pathway [115].

*In vivo* models of neuroinflammation in mice fed a high fat diet was used to investigate the effectiveness of PB in maintaining BBB structure and function [116, 117]. Mice fed a high fat diet showed elevated blood glucose and cholesterol levels compared to mice fed a low fat diet. Furthermore, mice fed a high fat diet exhibited a significant reduction in cognitive ability corresponding with the disruption to TJ protein expression, brain inflammation, and

increased BBB permeability [116]. In mice fed a high fat diet supplemented with PB, levels of blood glucose and cholesterol were comparable to healthy mice fed a low fat diet [117]. Furthermore, performance in memory tests, and TJ protein expression was not significantly different between mice fed a high fat diet supplemented with PB and mice fed a low fat diet.

The disruption to BBB integrity caused by a diet high in fat is likely due to a combination of factors including elevated cholesterol and glucose levels that cause cellular damage associated with oxidative stress and inflammation. PB was shown to maintain BBB integrity via the suppression in the release of inflammatory cytokines, reactive species, cholesterol and blood glucose caused by a diet high in fat [117].

## 1.9 Bioavailability of pharmaceutical drug compounds

Oral drug administration remains the preferred route of administration as it is easy, and convenient for the patient to self-medicate [118]. The effectiveness of orally administered drugs are largely dependent on the drug's solubility in biological fluid and permeability across biological membranes in reaching its therapeutic target [119].

The bioavailability of the drug compound is highly complex and is dependent on both intrinsic (physiological) and extrinsic (drug formulation) factors. Intrinsic factors include pharmacokinetic considerations such as drug metabolism, distribution and elimination [120]. Extrinsic factors include the rate and extent of the drug's solubility in the gastrointestinal fluid, and permeability of the drug to diffuse across the plasma membrane of the cells lining the gastrointestinal tract [121].

In general, the processes that determine the pharmacological action of an orally administered drug can be summarised as: (i) disintegration in the GI tract, (ii) appropriate drug dissolution in GI fluids and drug permeation across the GI wall (Figure 1.12) [120, 122].

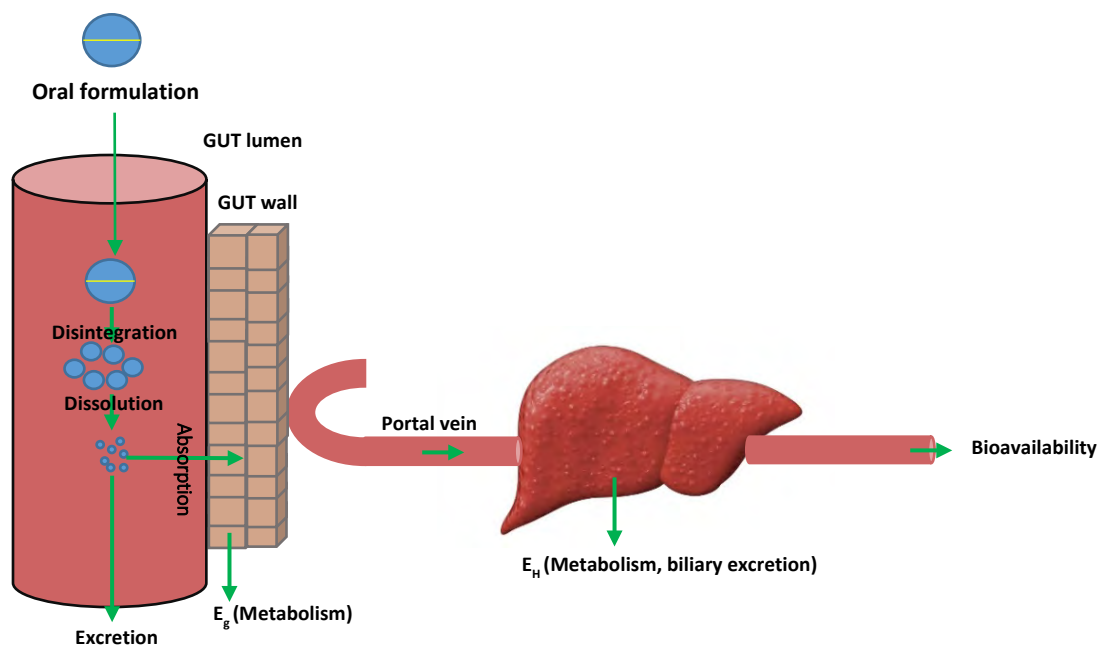


**Figure 1.12:** Schematic representation of the bioavailability of oral dosage formulations *in vivo*. Orally administered drug molecules undergo disintegration and dissolution in the biological media of the gastrointestinal tract. The dissolved drug molecules are absorbed across biological membranes and undergo metabolism by enzymes in the GUT wall ( $E_g$ ) or in the liver ( $E_H$ ) before reaching the systemic circulation.

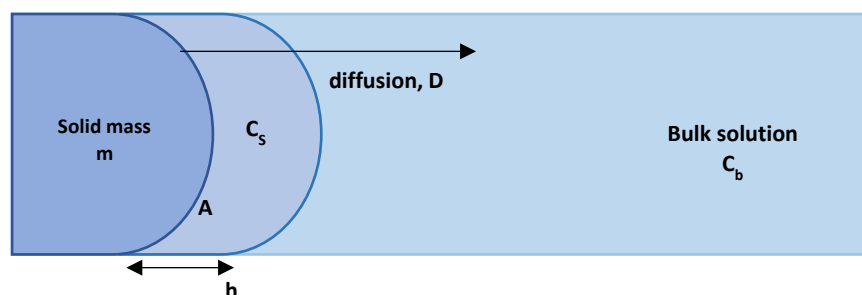
### 1.9.1 Drug solubility and dissolution

The solubility of a pharmaceutical drug is defined as the formation of a homogenous solution containing the solute (drug compound) in a particular solvent [123]. Solubility is generally expressed as mass per unit volume. Drug compounds can be classified as being highly soluble or as a practically insoluble material. As an example the United States and British pharmacopeia grades the solubility of a material in terms of quantification without regard to the solvent used (Table 1.3).

Solubility term	Approximate volume (ml) of solvent needed to dissolve 1 g of solute
Very soluble	Less than 1
Freely soluble	From 1 to 10
Soluble	From 10 to 30
Sparingly soluble	From 30 to 100
Slightly soluble	From 100 to 1000
Very slightly soluble	From 1000 to 10000
Practically insoluble	10000 and over

**Table 1.3:** United states and British pharmacopeia classification of solubility [124, 125].

Dissolution is defined as the rate in the mass transfer of the solute from the bulk solid state into the solution, and is a kinetic parameter expressed as mass per unit time. The Noyes-Whitney equation is used to describe the dissolution rate of a solid compound [126]:



$$\frac{dm}{dt} = \frac{AD (C_s - C_b)}{h}$$

Where  $dm/dt$  is the substance's dissolution rate (mass over time),  $m$  is the mass of the dissolved solute,  $A$  is the surface area of the solid exposed in solution,  $D$  is the diffusion coefficient of the particle in solvent,  $C_s$  is the solubility of the solid in solvent,  $C_b$  is the concentration of the solute in the bulk solution after time  $t$ , and  $h$  is the thickness of the diffusion layer surrounding the solid. The dissolution rate can be increased by a reduction in the particle size of the solid that increases the surface area available for the interaction between the solute and solvent. Based on the Noyes-Whitney equation, the dissolution rate is directly proportional to solubility of the drug compound.

### 1.9.2 Biopharmaceutical classification system (BCS)

The Biopharmaceutical classification system (BCS) was established to measure the solubility and permeability of drug compounds under standard conditions, which are the key rate limiting steps in oral absorption. Under the BCS, drug compounds are categorised into four classes based on their solubility and permeability profile (Figure 1.13). Permeability is the ability of the drug to cross lipid membranes and can be estimated from the lipid to water partition coefficient ( $\log P$ ), where  $P$  is the octanol to water concentration ratio of the drug [127, 128]. Another method is to measure the *in vitro* permeability of drug compounds across a monolayer of tissue cultured human colon adenocarcinoma (Caco-2) cells grown on a semi-permeable membrane [129]. Solubility is typically measured in aqueous media at controlled pH and temperature [129].

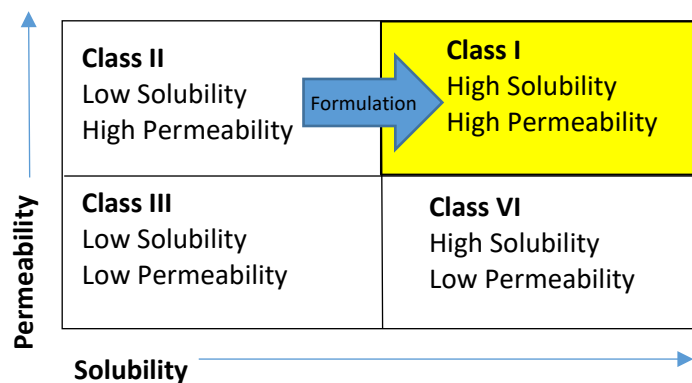


**Figure 1.13:** A representation of the BCS classification system. A class II drug compound can achieve an absorption profile similar to drug compounds in class I by formulation methods that enhances the drug's solubility. Examples of formulation design include particle micronisation, spray dry, or emulsion systems.

The BCS is a useful tool in guiding the design and development of pharmaceutical drug products. For example, a class I drug compound can be delivered effectively via oral administration to achieve high bioavailability, while a class II drug compound would face significant bioavailability issues due to its low solubility. The oral administration of drug compounds with low solubility will typically lead to erratic and incomplete drug absorption from the gastro-intestinal tract. Formulation strategies that enhance the drug's solubility/dissolution properties would need to be considered for class II compounds in order to improve its bioavailability [129].

### 1.9.3 Strategies to overcome poor solubility of drug compounds

A range of formulation strategies can be employed to enhance the solubility of class II drug compounds. Formulation with co-solvents that reduce the interfacial tension between aqueous solution and hydrophobic drug, thereby increasing the wettability and interaction between the solute and solvent is a common formulation strategy. Co-solvents typically used in drug formulations include ethanol, propylene glycol, glycerine and surfactants such as Tween, sodium lauryl sulphate, and alkylbenzene sulfonates [123].

The design of prodrugs, defined as inactive chemically modified drug molecules that undergo chemical or enzymatic transformation *in vivo* to the active drug, is an approach that can be used to improve the permeability and aqueous solubility of poorly soluble drug compounds [130]. Another formulation approach is the synthesis of the salt form of the active drug compound that retain the pharmacological activity and increase the aqueous solubility of the drug. Common salt forms include chlorides, carbonate, maleate and citrates [131].

Drug complexation with cyclodextrins, which are molecular donut-shaped structures consisting of glucose molecules with an interior diameter that typically measures between 0.6 nm to 0.8 nm, and the exterior surface consisting of hydrophilic surface groups can also be used to enhance the water solubility of drug compounds [132, 133].

Emulsions are defined as a biphasic system containing two immiscible liquids, one of which is dispersed finely as droplets in a second phase [134]. Examples include an oil in water emulsion (O/W) where the formation of oil droplets in water forms vehicles for the delivery of lipophilic drug compounds, and water in oil emulsion (W/O) typically used to prepare creams for external application [134]. Self-emulsifying drug delivery systems (SEDDS) are mixtures of oils, surfactants or a combination of hydrophilic solvents and co-solvents/surfactants [135]. These systems form O/W emulsions upon mild agitation or following oral administration where the intestine provide the necessary agitation for self-emulsification which can promote the wide distribution of the drug throughout the gastrointestinal tract [136]. Particle size reduction of the drug compound which increase the surface area available for solvation is also another common strategy to enhance the solubility of drug compounds [137].

These conventional formulation methods are summarised in Table 1.4 along with their key advantages and disadvantages.

Method	Advantages	Disadvantages
Cyclodextrin drug complex	Improvement in drug chemical stability	Higher cost. Limitation based on cavity size of cyclodextrins
Co-solvents	Simplicity and rapid	Possibility of drug precipitation <i>in vivo</i> Consideration of toxicity of the administered solvent
Prodrug drug design	Modification to increase drug solubility, chemical or metabolic stability and reduction in toxicity.	Difficulty in predicting <i>in vivo</i> response. Potential toxicity of the prodrug
Salt formation	Increase in solubility and dissolution	Not applicable to non-ionic compounds
Emulsions/SEDDS	Improved dissolution Formulation of a wide range of drugs.	Long term stability issues Drug precipitation <i>in vivo</i>
Particle size micronisation	Increase in drug dissolution	Particle agglomeration Difficulty in control of particle size uniformity

**Table 1.4:** summary of key formulation strategies and their main advantages and disadvantages [122, 138].

#### 1.9.4 Nanostructured materials as drug delivery systems

The broad applicability of conventional formulation strategies are restricted by issues of long term stability, toxicity, and precipitation that can result in altered pharmacological activity [139]. These disadvantages have led to intensive research in nanostructured materials as drug delivery systems (DDS) to address issues facing conventional



formulations. These materials are solid materials with length scale of a few nanometres (typically 1-100 nm) are commonly applied in the delivery of therapeutic agents including small molecules, genes, proteins, enzymes and pharmaceutical drug compounds [140, 141]. Ideal characteristics of nanostructured materials include biocompatibility, high physiochemical stability, and lack of immunogenicity. They are also easy to synthesise with a high degree of uniformity [141].

Nanostructured materials can be broadly categorised into two groups, the organic nanocarriers including liposomes, dendrimers, polymeric nanocarriers, micelles, carbon nanotubes, the inorganic nanocarriers including gold nanocarriers, magnetic nanocarriers, and porous nanostructured materials including porous silicon, metal-organic framework, and mesoporous silica. Their common properties and physicochemical properties are summarised in Table 1.5.

Organic nanostructured materials	Size of nanocarriers [52]	Properties	Applications
Liposome	50-100	Phospholipid bilayer carrier. Highly biocompatible, biodegradable.	Delivery of hydrophilic and hydrophobic drug compounds
Dendrimers	1-10	Branched macromolecules consisting a central core, symmetrical, homogenous carriers	Drug delivery, imaging, gene delivery, antiviral and vaccine delivery
Polymeric nanocarriers	10-100	Colloidal solid nanoparticles made from synthetic or natural polymers, highly biodegradable	Drug delivery, maintains drug stability.
Micelles	10-100	Colloidal aggregate of amphiphilic molecules, high bio-stability	Encapsulation of hydrophobic or hydrophilic drug compounds
Carbon nanotubes	0.4-3	Single or multi-layered carbon sheet with unique electrical and elastic property	Gene and drug delivery, peptide delivery
Inorganic nanostructured materials	Size of nanocarriers [52]	Properties	Applications
Gold nanocarriers	1-100	Highly biocompatible, low toxicity, multi surface functionality.	Bio-sensing, drug delivery, imaging
Magnetic nanocarriers	1-100	High chemical stability, high colloidal stability	Targeted drug delivery, imaging, bio-sensing
Porous silicon, metal organic framework and mesoporous silica materials	1-100	High loading capacity, chemical and thermal stability, biocompatibility	Drug delivery, peptide and protein delivery.

**Table 1.5:** Summary of the properties and applications of organic and inorganic nanostructured materials [142, 143].

### 1.9.5 Porous nanostructured materials

Porous silicon (Psi) are nanostructured materials with pore diameters in the mesoporous range of 2-50 nm, large surface area (up to 800 m<sup>2</sup>/g), and large pore volume (> 0.9 cm<sup>3</sup>/g) [144]. Porous silicon materials are produced by electrochemical etching via anodisation of semiconductor silicon wafers, where the silicon is present as the anode of an electrochemical cell and a hydrofluoric acid/ethanol mix is the electrolyte [144]. Having the silicon wafer as the electrode results in the development of porosity on the surface exposed to the electrolyte when current is applied [145, 146]. The porosity, porous layer thickness, pore size, pore-volume, and shape strongly depend on the fabrication conditions, including the hydrofluoric acid concentration, chemical composition of the electrolyte, current, and temperature [145]. The main disadvantage of Psi materials is the non-uniformity in both the porosity and thickness of the Psi layer. This has potential implications as the porosity determines its biological properties. For example, Psi with low porosity is generally bioinert compared to Psi materials with large pore size [147]. Porous silicon materials have been investigated for biomedical applications including biomedical imaging [59, 148] oral drug delivery of poorly soluble drugs [147, 149], controlled drug release [150, 151], or as permeation enhancers that enhance drug permeation across intestinal barriers [152].

Metal-organic framework (MOF) are crystalline porous materials constructed of metal ions and organic linkers and have been applied for industrial applications including gas storage [153, 154], chromatographic separation [155, 156], and catalysis [157, 158]. There is a growing interest in the use of MOF for biomedical applications, for example as MRI contrast agents for imaging [159, 160], and for the encapsulation of small drug molecules for intracellular drug delivery [161]. However further optimisation is required to generate optimal MOFs as a drug delivery vehicle: generally, MOFs are unstable under biological conditions which can result in premature release of drug or formation of large aggregates that reduce cellular uptake [162], biocompatibility where toxicity in biological systems need to be minimised [163], and issues of poor monodispersity and particle size (>100nm) that are not ideal for cellular uptake [164].

## 1.10 Mesoporous silica

Mesoporous silica particles (MSPs) are defined as ordered porous materials with pore sizes in the mesoporous range ( $\sim 2\text{-}50\text{ nm}$ ), with tuneable physicochemical properties including pore size, pore volume ( $\sim 0.6\text{-}1\text{ cm}^3/\text{g}$ ), surface area ( $\sim 700\text{-}1000\text{ m}^2/\text{g}$ ), pore structure, and particle size [144]. The well-defined porous structure allow MSPs to be optimised for the encapsulation and release of large biomolecules, therapeutic drug compounds, dyes and contrast agents for pharmaceutical applications and nanomedicine [145-147]. Since the first reported synthesis of MCM-41 (Mobil composition of Matter) reported in 1992 [148], the synthesis of various MSPs groups each with different physicochemical properties have been discovered including SBA-x, MSU-x, KIT-x, FDU-x and AMS-x, where the acronym refers to either the place of discovery (e.g. SBA- Santa Barbara Amorphous) or the mechanism of synthesis (e.g. FSM- Folded sheet mechanism) [144]. The MSPs used in this thesis are listed in the Table 1.6 below.

MSP	Surface area ( $\text{m}^2/\text{g}$ )	Pore Structure	Morphology	mesopores pore volume ( $\text{cm}^3/\text{g}^{-1}$ )	pore size [52]	Reference
MCM-41	800-1000	Ordered, 2-D hexagonal parallel arrangement of cylindrical mesoporous.	Spherical particles	0.5–1.5	1.5–10	[149]
SBA-15	400-1000	2-D, hexagonal, parallel cylindrical mesopores.	Rod shape	0.50– 1.3	5-10	[150]
AMS-6	520-667	3-D, bi-continuous cubic symmetry, cylindrical pore structure.	Spherical particles	0.5-0.6	3.2-4.8	[151]

**Table 1.6:** Summary of the textural properties of mesoporous silica particles used in this thesis.

### 1.10.1 The synthesis of mesoporous silica

Typically surfactants are used as templates in the synthesis of MSPs [144, 152, 153]. Surfactants consist of a hydrophilic head group and a linear hydrophobic tail, which characteristically accumulate at the water-air, or water-oil interface driven by the lowering of the interfacial free energy at the interphase boundary. Surfactants are classified as either anionic, cationic, non-ionic or zwitterionic depending on the polarity of the head group [152, 154]. Furthermore, surfactants in solution form aggregates called micelles, driven by the reduction in the free energy from the rearrangement of the respective hydrophobic and hydrophilic groups at the interphase boundary [155]. Micelle

formation is dependent on the concentration of the surfactant in solution, and the critical micellar concentration (CMC) is the limit at which the micelle formation start to occur [152, 155] .

The main components in the synthesis of MSPs include the surfactant, solvent, a catalyst (an acid or a base), and a source of silica. The surfactant is solubilised and may form the liquid crystal template prior to the addition of the silica source. When the concentration of the surfactant is above the CMC, surfactant molecules self-assemble into micelles of geometries dependent on the properties of the surfactant (e.g. hydrophobic chain length, head group area and total molecular volume) [144, 154]. Micelles can form either hexagonal, cubic, or lamellar mesophases depending on the type of surfactant used, concentration, pH, and temperature (Figure 1.14).

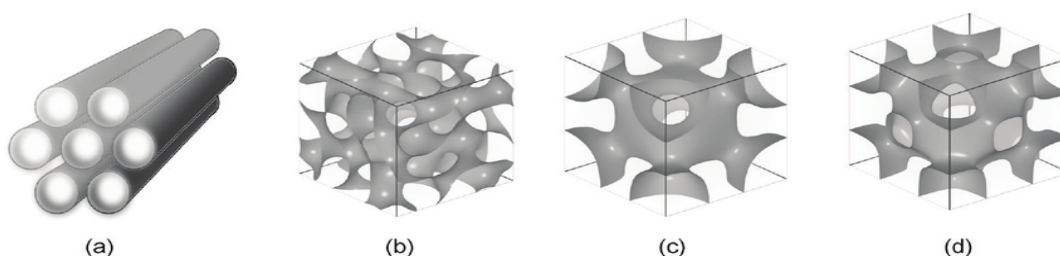


**Figure 1.14:** representation of common structures of MSPs: (a) hexagonal, (b) cubic (Ia3d), (c) cubic (Im3m), and (d) cubic (Pm3m) [156].

The polymerisation of silica precursors around the surfactant templates leads to the formation of an amorphous silica framework. Silica precursors include sodium silicate and alkoxysilanes, e.g. tetramethyl orthosilicate TMOS, tetraethyl orthosilicate TEOS, and tetrapropyl orthosilicate TPOS. Polymerisation occurs via hydrolysis and condensation reactions. Hydrolysis replaces the alkoxide groups (OR) with hydroxyl groups (OH) in the production of silanol groups ( $\equiv\text{Si-OH}$ ), followed by condensation reactions of the silanol groups in the production of siloxane bonds ( $\equiv\text{Si-O-Si}\equiv$ ) [153, 155]. The number of free hydroxyl groups (-OH) decreases when the formation of Si-O-Si bonds is maximised as the condensation reaction proceeds, resulting in the formation of ring structures that give form particles that act as nuclei [154, 155]. These particles can grow by Ostwald ripening, a process that is both pH and temperature dependent that allows for the growth of particles in size [152, 154]. Finally, the surfactant template can be removed by calcination or treatment with suitable solvents such as ethanol to form the final mesoporous silica particle (Figure 1.15).

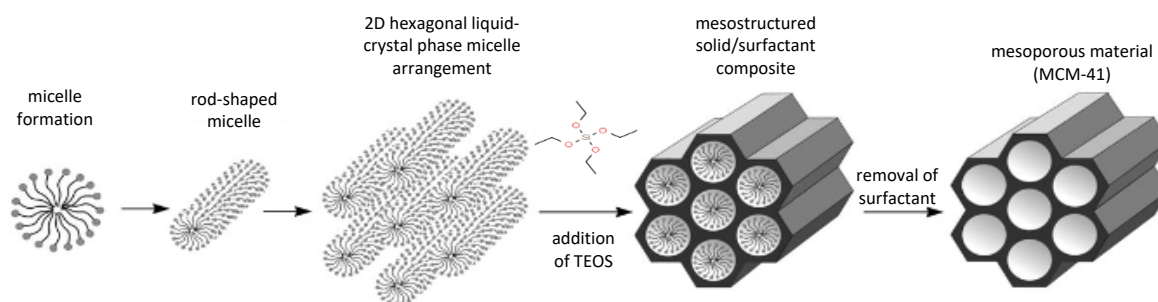


**Figure 1.15:** Schematic representation of the formation of mesoporous silica particle, MCM-41 [155].

### 1.10.2 Mesoporous silica as drug delivery systems

Loading of small drug compounds within MSPs can be used to overcome the limitations of current drug formulations including lack of drug specificity, poor drug stability, and low drug solubility. The following are examples of how nanostructured MSPs can be used to resolve formulation issues:

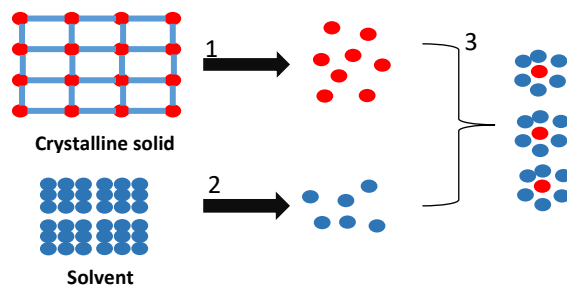
Functionalisation of target groups on the external surface of MSP allows for the selective interaction with specific receptors on the membrane of target cells, facilitating targeted drug delivery [157, 158].

Protection of the loaded drug molecule from oxidation, hydrolysis and other degradation processes by capping the mesoporous entrance with polymers, inorganic nanoparticles, or macromolecules that release the loaded drug compound in response to either internal or external stimuli [146, 159]. This can be achieved by anchoring pore-blocking caps with linkers that are cleaved when exposed to internal stimuli, such as pH, enzymes or external stimuli such as ultrasound, light or magnetic fields [146, 160].

Encapsulation of pharmaceutical drug compounds in the amorphous form enhances the solubility of drug compounds released from MSPs [161].

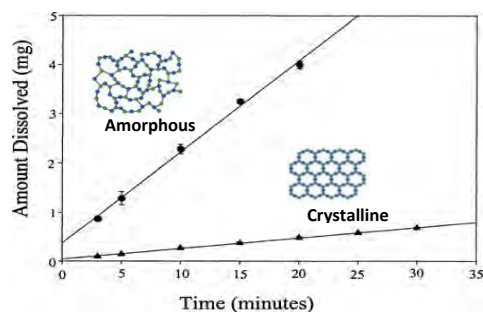
### 1.10.3 Crystalline vs amorphous forms

Solids in the crystalline form are characterised by long range order, and high thermodynamic stability. The dissolution profile of a crystalline material can be broadly defined into three processes. The first step is the disruption in the crystal lattice to expose individual molecules for solvation or hydration by solvent molecules. The next step is breaking of the solvent bonds in order to accommodate the solute molecules [162] (Figure 1.16).



**Figure 1.16:** Schematic of the general mechanisms in the solubility of a crystalline solid. 1) Disruption in the crystal lattice structure. 2) Cavitation of the solvent to host dissolved molecules. 3) Solvation of the solute molecules. Figure adapted from [162].

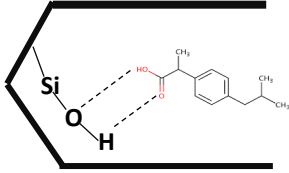
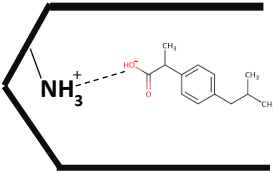
Unlike a crystalline solid, an amorphous material is characterised as having weaker short range order, and lacks long range molecular ordering [163]. A drug compound prepared in the amorphous form would in general have a higher solubility as less energy is required to break the weaker bonds in the amorphous system [163-165] (Figure 1.17). Furthermore, the amorphous material is characterised as having a higher energy state, with enhanced thermodynamic properties relative to the crystalline state (solubility, specific heat, vapour pressure) giving it greater molecular motion, chemical reactivity, and higher tendency to crystallise [163].



**Figure 1.17:** Representative release profile showing differences in local atomic ordering and dissolution rate of a drug compound prepared in the amorphous and crystalline forms [166]. The solubility of a crystalline material is dependent on the interactions between the discrete molecules. For example, a crystalline material with weak ionic interactions between discrete molecules has a higher solubility compared to crystalline materials with stronger covalent interactions between discrete molecules [167].

#### 1.10.4 Effect of textural properties of mesoporous silica on drug loading and release

The ability to synthesise MSPs with different textural properties make it a versatile material for the encapsulation of drug compounds for drug delivery. Specifically, the encapsulation of drug compounds in the amorphous form within the mesopores has been extensively investigated for the delivery of poorly soluble drug compounds [161, 168]. This is achieved by loading drug compounds within a critical pore diameter of the MSP that suppress the formation of nuclei and crystal growth [169, 170]. Other important textural properties that have an impact on the physical form of the loaded drug and release from MSP include pore structure, pore volume, surface area, and surface functionalisation (Table 1.7).

Textural property of MSP	Impact on drug loading	Impact on drug release	Relevant equation	References
Pore size	The pore size can affect the amount of drug adsorbed into the mesopores and the total drug loading capacity of the MSP.	Drug loaded in the amorphous form within MSP result in an enhancement in drug release as compared to the crystalline drug.  Pore size of MSP can be finely tuned to control rate of drug release.	The critical pore size of MSP to maintain amorphous form of the loaded drug:  $d^* = 4\sigma_{cl}T_m^{\infty}/[(T_m^{\infty} - T)\Delta H_{mPc}]$ Critical pore diameter $d^*$ , $\sigma_{cl}$ the surface energy between crystal and melt, $\Delta H_m$ the heat of melting, $T_m^{\infty}$ , the bulk melting temperature and $\rho_c$ the crystal density.	[170-179]
Pore structure	MSPs with 3-D arrangement of mesopores have in general a higher total loading capacity compared to 2-D pore structure.	Differences in pore structure can cause delay and incomplete drug release due to steric hindrance between silica wall and drug molecule.	$Q \equiv \sqrt{\frac{D\varepsilon}{\tau}} (2A - \varepsilon C_s) C_s t$ Where the release Q is related to the fractional porosity ( $\varepsilon$ ), tortuosity factor ( $\tau$ ), t is the immersion time, $C_s$ drug solubility, A is the initial drug amount, and D is the diffusion coefficient.	[180-185]
Surface area	The high surface area of MSP facilitate high drug adsorption into the mesopores.	High surface area of MSP facilitate rapid drug release from the absorption of solvent molecules into the mesopores.	$\frac{dm}{dt} = \frac{AD(C_s - C_b)}{h}$ $dm/dt$ is the dissolution rate, m is the solute mass, A is the surface area, D is the diffusion coefficient, $C_s$ is the solubility of the solid, $C_b$ concentration of the solute in bulk solution, h is the thickness of the diffusion layer.	[186-188]
Pore volume	MSP with high pore volume can achieve a higher drug loading capacity compared to MSP with smaller pore volume.	Re-crystallisation of excess drug on the surface of silica from complete pore filling can cause a delay in drug release.	Total drug loading capacity of MSP is determined by using thermal gravimetric analysis to determine drug loading amount (w/w%), nitrogen adsorption/desorption measurement to determine changes in textural properties of MSP, and differential scanning calorimetry or X-ray diffraction to determine the degree of crystallinity in drug loaded MSP sample.	[179, 187-190]
Surface silanols	The interaction between silanol (Si-OH) groups on the surface of MSP can interact with proton donor/acceptor groups of the drug molecule that can affect drug loading.	The interaction between silanol groups of MSP via hydrogen bonds with proton donor/acceptor groups of the drug compounds can be used to delay drug release from mesopores.	In this example, Ibuprofen is linked by hydrogen bonds between its carboxylic acid group and the silanol groups within the mesopores of MSP.  	[191-193]
Surface functionalisation	Surface functionalisation of MSP can facilitate greater interaction between drug molecules with the mesopores.	Surface functionalisation with amine ( $NH_2$ ), carboxylic acid ( $COOH$ ) can induce host-guest interaction with drug molecules that can be used to delay drug release from the mesopores.	In this example, the ionic bond between carboxylate group of ibuprofen and ammonium groups of amino functionalised within mesopores of MSP is shown.  	[194, 195]

**Table 1.7:** Summary of the textural properties of MSP on drug loading and release.

### 1.10.5 Mechanisms of drug release from mesoporous silica

Drug release from MSPs typically occur when the drug loaded material come in contact with solvent molecules in solution by the following mechanisms [175]:

- 1) absorption of solvent molecules into the mesopores occur by capillary force
- 2) The dissolution of drug molecules within the mesopores
- 3) Diffusion of the drug molecules from the mesopores into the bulk solvent

The kinetics of drug release from solid, inert matrix such as MSPs is commonly described by the Higuchi equation, where the penetration of solvent molecules into the mesopores lead to the subsequent drug release into the solution by Fickian diffusion [196]. Therefore, the rate of drug release is described as the square root of a time dependent process based on Fickian diffusion:

$$Q = k_h t^{1/2} \quad (1.15)$$

where  $Q$  is the amount of drug release,  $k_h$  is the release rate constant, and  $t$  is time. The release rate constant of the drug is proportional to the porosity of the MSPs, the solubility of the drug in the dissolution medium, the initial drug loading and the diffusion coefficient of the drug in the medium [196, 197]. A typical plot of the amount of drug release versus the square root of time will show a linear relationship for a diffusion controlled drug release process.

In a typical release experiment, the dissolution profile follows a bimodal release pattern, with an initial burst release of the drug likely from the surface or the mesopore entrances of the MSP, followed by a prolonged, slower drug release due to the diffusion of drug from the mesopores into the dissolution media [190]. The interaction between surface silanol groups or surface functionalised groups and the drug molecule may also play a role in the delay of the drug diffusion process from the mesopore [195].

An extension of the Higuchi model is the Korsmeyer-Peppas model:

$$Kt^n = M_t / M_{inf} \quad (1.16)$$

where  $M_t$  is the cumulative mass drug release at time  $t$  and  $M_{inf}$  is the cumulative drug release at infinite time. The drug release mechanism is represented by the proportional constant,  $k$ , and the release exponent  $n$ , where diffusion occurs when ( $n = 0.5$ ), non-fickian diffusion ( $n > 0.5$ ), and zero order release ( $n = 0$ ) [198, 199].



#### 1.10.6 Effectiveness of drug compounds for the treatment of neuroinflammation are limited by their low aqueous solubility

As discussed previously, disruption to the integrity of the BBB allows for the infiltration of cytotoxins and proteins that can cause neuronal cell damage and death [55]. This is caused by the exposure of BBB cells to stimuli that elicit a heightened neuroinflammatory response characterised by elevated levels of ROS, pro-inflammatory mediators and cytokines [51]. ROS mediated BBB disruption includes the decrease in tight junction expression, cellular apoptosis, and oxidative modification to tight junction proteins [51, 52]. High concentrations of PGE2 and cytokines are cytotoxic and are also known to mediate the disruption to tight junction integrity [52].

As neurodegenerative diseases is characterised by increased levels of ROS and pro-inflammatory mediators, pharmaceutical drug compounds with antioxidant and or anti-inflammatory properties are considered viable therapeutic strategies. Typically, pharmaceutical compounds with desirable antioxidant/anti-inflammatory properties are Class II compounds (BCS classification) which have high permeability but absorption is limited by the drug's low solubility. For example, NSAIDs like flurbiprofen, naproxen, and INDO are classified as Class II compounds, where it is estimated that only 1-2% of the drugs reach the cerebral spinal fluid of the brain after oral administration [200]. This low bioavailability is a significant limitation in the effectiveness of NSAID for the treatment of neurodegenerative diseases, such as Alzheimer's [200-202].

Furthermore, a range of Class II drug compounds with promising antioxidant and anti-inflammatory properties have their clinical effectiveness limited by poor solubility. This includes drug compounds in the treatment of diseases associated with oxidative stress such as diabetes, hypertension, and cardiovascular diseases. For example, drug compounds for the treatment of diabetes (e.g. metformin, pioglitazone), atherosclerosis (atorvastatin, rosuvastatin, simvastatin), and hypertension (carvedilol, amlodipine) have beneficial antioxidant and anti-inflammatory properties that are separate from their primary pharmacological effect [203-208]. The encapsulation of these drug compounds within MSPs have been shown to enhance the solubility of these poorly soluble drugs as compared to the crystalline drug, and are summarised in the Table 1.8 below.

Drug compound	MSP type	surface area (m <sup>2</sup> /g)	Pore size [52]	Pore volume (cm <sup>3</sup> /g), drug loading (% wt/wt)	<i>In vitro drug release</i>
Atorvastatin (AT)	SBA-15	641	6.18	0.85, 17%	SGF (pH =1.2). After 45 min, higher AT release was observed from SBA-15 (68%), vs crystalline AT (38%).
Carvedilol (CAR)	MCM-41	996	3.9	0.70, 25%	SIF (pH = 6.8), After 45 minutes, CAR release from MCM-41 was 41% vs Less than 20% release from crystalline CAR.
Celecoxib (CEL)	MCM-41 SBA-15	764 817	1.4 7.82	1.15, 25.1% 1.10, 25.3%	Phosphate buffer (pH = 7.4). CEL released from MCM-41 after 6 hours was 72.6 %, CEL released from SBA-15 was 95 %. Less than 60% released from crystalline CEL after 6 hours.
Flurbiprofen (FLU)	SBA-15	848.9	5.6	1.02, 27.1%	Phosphate buffer (pH = 7.2), FLU released from SBA-15 was 95 % after 6 hours.
Glibenclamide (GLB)	SBA-15	607	7.2	0.90, 22.5%	In SGF (pH = 1.2) GLB released from SBA-15 was ~ 100% after 60 minutes, GLB from commercial formulation (Daonil ®) released ~ 45% after 60 minutes.
Ibuprofen (IBU)	SBA-15 MCM-41	734.9 1363.7	6.0 2.3	1.05, 46.2% 1.0, 39.6%	In SGF (pH = 1.2), IBU released from SBA-15 was 95 % after 15 minutes, IBU released from MCM-41 was 88% after 15 minutes, and crystalline IBU was less than 16% after 15 minutes.
Indomethacin (INDO)	MCM-41 SBA-15	996 530	3.9 8.4	0.64, 0.70% 1.1, 0.9%	In Phosphate buffer (pH = 6.8), INDO released from SBA-15 was 95 % after 60 minutes, INDO released from MCM-41 was 70 % after 60 minutes, crystalline INDO release was 60 % after 60 minutes.
Naproxen (NAP)	SBA-15 MCM-41	923 1078	9.32 2.14	1.20,41.4% 0.97, 21.5%	Phosphate buffer (pH = 6.8), NAP released from SBA-15 was 100% after 30 minutes, NAP released from MCM-41 was 100% after 30 minutes, crystalline NAP release was < 5% after 30 minutes.
Piroxicam (PIR)	MCM-41 SBA-15	803 610	3.21 8.4	0.65, 14.1% 0.97, 12.0%	SGF (pH = 1.2) PIR released from MCM-41 was 88.4% after 30 minutes, PIR released from SBA-15 was 85 % after 30 minutes.  Crystalline PIR release was 53.3 % after 30 minutes.
Resveratrol (RES)	Mesoporous silica microspheres (MSM)	682	9.19	1.47, 41.3%	In 0.5% aqueous solution with Tween 80 as dissolution medium, RES released from MSM was 97.6% after 5 minutes, compared to crystalline RES of 60.7%.

**Table 1.8:** summary of the physicochemical properties of MSPs and class II drug compounds with known antioxidant/anti-inflammatory properties. SGF = simulated gastric fluid, SIF simulated intestinal fluid. Table modified from [161].

PB is an extreme example of a poorly soluble drug compound, with a reported solubility in water at 4-5 ng/l that makes it practically insoluble in biological media (Figure 1.18). Its poor solubility is a significant limitation in the effectiveness of its pharmacological properties in the treatment of diseases associated with oxidative stress and inflammation [107, 108, 209]. Furthermore, PBs low solubility makes it extremely challenging to achieve high oral bioavailability, as it is estimated only 2-8% of Probucol is absorbed from the gastrointestinal tract [210]. The overall aim of this thesis was to investigate how differences in the textural properties of MSP affect the physical

properties of the loaded drug including probucol and other insoluble drug compounds, and to identify how changes in the physical properties of the loaded drug affected its solubility. This is followed by in vivo studies to determine whether an enhancement in oral pharmacokinetics can be achieved in PB released from MSP following oral administration in rats. Furthermore the in vitro model of BBB and in vivo model of oxidative stress in zebrafish was used to evaluate the pharmacological properties of the drug compound released from MSP.

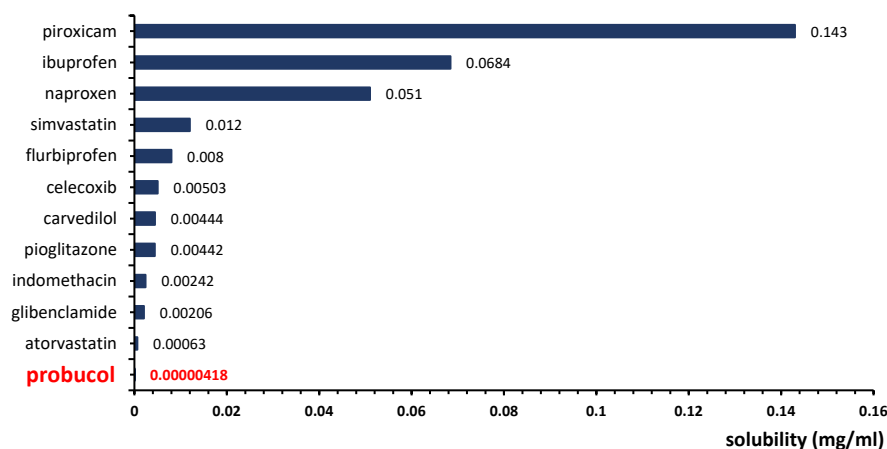


**Figure 1.18:** Summary of the solubility in water of pharmaceutical drug compounds with reported antioxidant and anti-inflammatory properties. These include NSAIDs (piroxicam, ibuprofen, naproxen, flurbiprofen, indomethacin), statins (simvastatin, atorvastatin), beta-blockers (carvedilol), thiazolidinediones (pioglitazone), and sulfonylureas (glibenclamide). Values taken from drugbank [211].

## 1.11 References

1. Zuo, L., et al., *Biological and physiological role of reactive oxygen species—the good, the bad and the ugly*. Acta physiologica, 2015. **214**(3): p. 329-348.
2. Halliwell, B. and J.M. Gutteridge, *Free radicals in biology and medicine*. 2015: Oxford University Press, USA.
3. Galli, F., et al., *Oxidative stress and reactive oxygen species*. Cardiovascular Disorders in Hemodialysis, 2005. **149**: p. 240-260.
4. Song, P. and M.H. Zou, *Roles of reactive oxygen species in physiology and pathology*. Atherosclerosis: Risks, mechanisms, and therapies, 2015: p. 379-392.
5. Halliwell, B., *Reactive oxygen species in living systems: source, biochemistry, and role in human disease*. The American journal of medicine, 1991. **91**(3): p. S14-S22.
6. Collaborators., G.D.a.I.I.a.P., *Global, regional, and national incidence, prevalence, and years lived with disability for 354 diseases and injuries for 195 countries and territories, 1990-2017: a systematic analysis for the Global Burden of Disease Study 2017*. . Lancet, 2018. **392**(10159): p. 1789-1858.
7. Alfadda, A.A. and R.M. Sallam, *Reactive oxygen species in health and disease*. Journal of Biomedicine and Biotechnology, 2012. **2012**.
8. Valko, M., et al., *Free radicals and antioxidants in normal physiological functions and human disease*. The international journal of biochemistry & cell biology, 2007. **39**(1): p. 44-84.
9. J.P. Kehrer, J.D.R., C.V. Smith,, *Comprehensive Toxicology* Second ed. 1.14 - Free Radicals and Reactive Oxygen Species,, ed. Charlene A. McQueen. 2010: Elsevier.
10. Turrens, J.F., *Mitochondrial formation of reactive oxygen species*. The Journal of physiology, 2003. **552**(2): p. 335-344.
11. Dröse, S. and U. Brandt, *Molecular mechanisms of superoxide production by the mitochondrial respiratory chain*, in *Mitochondrial Oxidative Phosphorylation*. 2012, Springer. p. 145-169.
12. Vignais, P., *The superoxide-generating NADPH oxidase: structural aspects and activation mechanism*. Cellular and Molecular Life Sciences CMLS, 2002. **59**(9): p. 1428-1459.
13. Butler, A.R. and D.L.H. Williams, *The physiological role of nitric oxide*. Chemical Society Reviews, 1993. **22**(4): p. 233-241.
14. Förstermann, U. and W.C. Sessa, *Nitric oxide synthases: regulation and function*. European heart journal, 2011. **33**(7): p. 829-837.
15. Thommes, M., et al., *Physisorption of gases, with special reference to the evaluation of surface area and pore size distribution (IUPAC Technical Report)*. Pure and Applied Chemistry, 2015. **87**(9-10): p. 1051-1069.
16. Nathan, C.F. and J.B. Hibbs Jr, *Role of nitric oxide synthesis in macrophage antimicrobial activity*. Current opinion in immunology, 1991. **3**(1): p. 65-70.
17. Forstermann, U. and T. Munzel, *Endothelial nitric oxide synthase in vascular disease: from marvel to menace*. Circulation, 2006. **113**(13): p. 1708-1714.
18. Zhou, L. and D.-Y. Zhu, *Neuronal nitric oxide synthase: structure, subcellular localization, regulation, and clinical implications*. Nitric oxide, 2009. **20**(4): p. 223-230.
19. Alkadi, H., *A review on free radicals and antioxidants*. Infectious Disorders-Drug Targets (Formerly Current Drug Targets-Infectious Disorders), 2020. **20**(1): p. 16-26.
20. Birben, E., et al., *Oxidative stress and antioxidant defense*. World Allergy Organization Journal, 2012. **5**(1): p. 9-19.

21. Lima, D.R., et al., *Determination of ascorbic acid in the retina during chicken embryo development using high performance liquid chromatography and UV detection*. Analytical Methods, 2016. **8**(27): p. 5441-5447.
22. Urano, S., et al., *Vitamin E: inhibition of retinol-induced hemolysis and membrane-stabilizing behavior*. Journal of Biological Chemistry, 1992. **267**(26): p. 18365-18370.
23. Frei, B., et al., *Ascorbate: the most effective antioxidant in human blood plasma*, in *Antioxidants in therapy and preventive medicine*. 1990, Springer. p. 155-163.
24. Beyer, R.E., *The role of ascorbate in antioxidant protection of biomembranes: interaction with vitamin E and coenzyme Q*. Journal of bioenergetics and biomembranes, 1994. **26**(4): p. 349-358.
25. Wilson, J.X., *Mechanism of action of vitamin C in sepsis: ascorbate modulates redox signaling in endothelium*. Biofactors, 2009. **35**(1): p. 5-13.
26. Irshad, M. and P. Chaudhuri, *Oxidant-antioxidant system: role and significance in human body*. 2002.
27. Dickinson, D.A., et al., *Cytoprotection against oxidative stress and the regulation of glutathione synthesis*. Biological chemistry, 2003. **384**(4): p. 527-537.
28. Wong, J.L., R. Cr  ton, and G.M. Wessel, *The oxidative burst at fertilization is dependent upon activation of the dual oxidase Udx1*. Developmental cell, 2004. **7**(6): p. 801-814.
29. Thannickal, V.J. and B.L. Fanburg, *Reactive oxygen species in cell signaling*. American Journal of Physiology-Lung Cellular and Molecular Physiology, 2000. **279**(6): p. L1005-L1028.
30. Yang, Y., et al., *Reactive oxygen species in the immune system*. International reviews of immunology, 2013. **32**(3): p. 249-270.
31. Verbon, E.H., J.A. Post, and J. Boonstra, *The influence of reactive oxygen species on cell cycle progression in mammalian cells*. Gene, 2012. **511**(1): p. 1-6.
32. Simon, H.-U., A. Haj-Yehia, and F. Levi-Schaffer, *Role of reactive oxygen species (ROS) in apoptosis induction*. Apoptosis, 2000. **5**(5): p. 415-418.
33. Cheeseman, K., *Mechanisms and effects of lipid peroxidation*. Molecular Aspects of Medicine, 1993. **14**(3): p. 191-197.
34. Girotti, A.W., *Mechanisms of lipid peroxidation*. Journal of free radicals in biology & medicine, 1985. **1**(2): p. 87-95.
35. Marnett, L.J., *Oxyl radicals and DNA damage*. carcinogenesis, 2000. **21**(3): p. 361-370.
36. Kobayashi, N., F.A. DeLano, and G.W. Schmid-Sch  nbein, *Oxidative stress promotes endothelial cell apoptosis and loss of microvessels in the spontaneously hypertensive rats*. Arteriosclerosis, thrombosis, and vascular biology, 2005. **25**(10): p. 2114-2121.
37. Buttke, T.M. and P.A. Sandstrom, *Oxidative stress as a mediator of apoptosis*. Immunology today, 1994. **15**(1): p. 7-10.
38. Kannan, K. and S.K. Jain, *Oxidative stress and apoptosis*. Pathophysiology, 2000. **7**(3): p. 153-163.
39. Salim, S., *Oxidative stress and the central nervous system*. Journal of Pharmacology and Experimental Therapeutics, 2017. **360**(1): p. 201-205.
40. Chen, Y., et al., *The role of astrocytes in oxidative stress of central nervous system: A mixed blessing*. Cell Proliferation, 2020. **53**(3): p. e12781.
41. Tajes, M., et al., *The blood-brain barrier: structure, function and therapeutic approaches to cross it*. Molecular membrane biology, 2014. **31**(5): p. 152-167.
42. Itoh, Y. and N. Suzuki, *Control of brain capillary blood flow*. Journal of Cerebral Blood Flow & Metabolism, 2012. **32**(7): p. 1167-1176.
43. Rubin, L. and J. Staddon, *The cell biology of the blood-brain barrier*. Annual review of neuroscience, 1999. **22**(1): p. 11-28.

44. Abbott, N.J., et al., *Structure and function of the blood–brain barrier*. Neurobiology of disease, 2010. **37**(1): p. 13-25.
45. Abbott, N.J., L. Rönnebeck, and E. Hansson, *Astrocyte–endothelial interactions at the blood–brain barrier*. Nature reviews neuroscience, 2006. **7**(1): p. 41-53.
46. Ballabh, P., A. Braun, and M. Nedergaard, *The blood–brain barrier: an overview: structure, regulation, and clinical implications*. Neurobiology of disease, 2004. **16**(1): p. 1-13.
47. Bolton, S., D. Anthony, and V. Perry, *Loss of the tight junction proteins occludin and zonula occludens-1 from cerebral vascular endothelium during neutrophil-induced blood–brain barrier breakdown in vivo*. Neuroscience, 1998. **86**(4): p. 1245-1257.
48. Kniesel, U. and H. Wolburg, *Tight junctions of the blood–brain barrier*. Cellular and molecular neurobiology, 2000. **20**(1): p. 57-76.
49. Cordiglieri, C. and C. Farina, *Astrocytes exert and control immune responses in the brain*. Current Immunology Reviews, 2010. **6**(3): p. 150-159.
50. Wu, F., L. Liu, and H. Zhou, *Endothelial cell activation in central nervous system inflammation*. Journal of Leukocyte Biology, 2017. **101**(5): p. 1119-1132.
51. DiSabato, D.J., N. Quan, and J.P. Godbout, *Neuroinflammation: the devil is in the details*. Journal of neurochemistry, 2016. **139**: p. 136-153.
52. Lyman, M., et al., *Neuroinflammation: the role and consequences*. Neuroscience research, 2014. **79**: p. 1-12.
53. Zlokovic, B.V., *Neurovascular pathways to neurodegeneration in Alzheimer's disease and other disorders*. Nature Reviews Neuroscience, 2011. **12**(12): p. 723-738.
54. Hensley, K., *Neuroinflammation in Alzheimer's disease: mechanisms, pathologic consequences, and potential for therapeutic manipulation*. Journal of Alzheimer's disease, 2010. **21**(1): p. 1-14.
55. Ransohoff, R.M., *How neuroinflammation contributes to neurodegeneration*. Science, 2016. **353**(6301): p. 777-783.
56. Bryant, C.E., et al., *The molecular basis of the host response to lipopolysaccharide*. Nature Reviews Microbiology, 2010. **8**(1): p. 8-14.
57. Dauphinee, S.M. and A. Karsan, *Lipopolysaccharide signaling in endothelial cells*. Laboratory investigation, 2006. **86**(1): p. 9-22.
58. Nagyórsi, P., et al., *Expression and regulation of toll-like receptors in cerebral endothelial cells*. Neurochemistry international, 2010. **57**(5): p. 556-564.
59. Ahire, J.H., et al., *Highly luminescent and nontoxic amine-capped nanoparticles from porous silicon: synthesis and their use in biomedical imaging*. ACS applied materials & interfaces, 2012. **4**(6): p. 3285-3292.
60. Hopkins, S.J. and N.J. Rothwell, *Cytokines and the nervous system I: expression and recognition*. Trends in neurosciences, 1995. **18**(2): p. 83-88.
61. de Vries, H.E., et al., *The influence of cytokines on the integrity of the blood-brain barrier in vitro*. Journal of neuroimmunology, 1996. **64**(1): p. 37-43.
62. Descamps, L., R. Cecchelli, and G. Torpier, *Effects of tumor necrosis factor on receptor-mediated endocytosis and barrier functions of bovine brain capillary endothelial cell monolayers*. Journal of neuroimmunology, 1997. **74**(1-2): p. 173-184.
63. Rochfort, K.D. and P.M. Cummins, *The blood–brain barrier endothelium: a target for pro-inflammatory cytokines*. Biochemical Society Transactions, 2015. **43**(4): p. 702-706.
64. Saija, A., et al., *Systemic cytokine administration can affect blood-brain barrier permeability in the rat*. Life sciences, 1995. **56**(10): p. 775-784.

65. Yokoo, H., et al., *Neurodegenerative evidence in mice brains with cecal ligation and puncture-induced sepsis: preventive effect of the free radical scavenger edaravone*. PLoS One, 2012. **7**(12): p. e51539.
66. Banan, A., et al., *Phospholipase C- $\gamma$  inhibition prevents EGF protection of intestinal cytoskeleton and barrier against oxidants*. American Journal of Physiology-Gastrointestinal and Liver Physiology, 2001. **281**(2): p. G412-G423.
67. Usatyuk, P.V., et al., *Redox regulation of reactive oxygen species-induced p38 MAP kinase activation and barrier dysfunction in lung microvascular endothelial cells*. Antioxidants and Redox Signaling, 2003. **5**(6): p. 723-730.
68. Lee, H.-S., et al., *Hydrogen peroxide-induced alterations of tight junction proteins in bovine brain microvascular endothelial cells*. Microvascular research, 2004. **68**(3): p. 231-238.
69. Rao, R.K., et al., *Tyrosine phosphorylation and dissociation of occludin-ZO-1 and E-cadherin- $\beta$ -catenin complexes from the cytoskeleton by oxidative stress*. Biochemical Journal, 2002. **368**(2): p. 471-481.
70. Haorah, J., et al., *Oxidative stress activates protein tyrosine kinase and matrix metalloproteinases leading to blood-brain barrier dysfunction*. Journal of neurochemistry, 2007. **101**(2): p. 566-576.
71. Staddon, J.M., et al., *Evidence that tyrosine phosphorylation may increase tight junction permeability*. Journal of cell science, 1995. **108**(2): p. 609-619.
72. Volberg, T., et al., *The effect of tyrosine-specific protein phosphorylation on the assembly of adherens-type junctions*. The EMBO Journal, 1992. **11**(5): p. 1733-1742.
73. Rao, R., et al., *Oxidant-induced disruption of intestinal epithelial barrier function: role of protein tyrosine phosphorylation*. American Journal of Physiology-Gastrointestinal and Liver Physiology, 1997. **273**(4): p. G812-G823.
74. Kevil, C.G., N. Okayama, and J.S. Alexander, *H<sub>2</sub>O<sub>2</sub>-mediated permeability II: importance of tyrosine phosphatase and kinase activity*. American Journal of Physiology-Cell Physiology, 2001. **281**(6): p. C1940-C1947.
75. Atkinson, K. and R. Rao, *Role of protein tyrosine phosphorylation in acetaldehyde-induced disruption of epithelial tight junctions*. American Journal of Physiology-Gastrointestinal and Liver Physiology, 2001. **280**(6): p. G1280-G1288.
76. Beckman, J.S. and W.H. Koppenol, *Nitric oxide, superoxide, and peroxynitrite: the good, the bad, and ugly*. American Journal of Physiology-cell physiology, 1996. **271**(5): p. C1424-C1437.
77. Tan, K.H., et al., *Peroxynitrite mediates nitric oxide-induced blood-brain barrier damage*. Neurochemical research, 2004. **29**(3): p. 579-587.
78. Torreilles, F., et al., *Neurodegenerative disorders: the role of peroxynitrite*. Brain Research Reviews, 1999. **30**(2): p. 153-163.
79. Freeman, B., *Free radical chemistry of nitric oxide: looking at the dark side*. Chest, 1994. **105**(3): p. 79S-84S.
80. Ricciotti, E. and G.A. FitzGerald, *Prostaglandins and inflammation*. Arteriosclerosis, thrombosis, and vascular biology, 2011. **31**(5): p. 986-1000.
81. Vane, J., Y. Bakhle, and R. Botting, *CYCLOOXYGENASES 1 AND 2*. Annual review of pharmacology and toxicology, 1998. **38**(1): p. 97-120.
82. De Vries, H.E., et al., *Eicosanoid production by rat cerebral endothelial cells: stimulation by lipopolysaccharide, interleukin-1 and interleukin-6*. Journal of neuroimmunology, 1995. **59**(1): p. 1-8.
83. Teeling, J., et al., *The effect of non-steroidal anti-inflammatory agents on behavioural changes and cytokine production following systemic inflammation: Implications for a role of COX-1*. Brain, behavior, and immunity, 2010. **24**(3): p. 409-419.
84. Matsumura, K., et al., *Mapping of prostaglandin E<sub>2</sub> binding sites in rat brain using quantitative autoradiography*. Brain research, 1992. **581**(2): p. 292-298.

85. Gaillard, P.J., A.B.G. de Boer, and D.D. Breimer, *Pharmacological investigations on lipopolysaccharide-induced permeability changes in the blood–brain barrier in vitro*. Microvascular research, 2003. **65**(1): p. 24-31.
86. Aïd, S. and F. Bosetti, *Targeting cyclooxygenases-1 and-2 in neuroinflammation: therapeutic implications*. Biochimie, 2011. **93**(1): p. 46-51.
87. Minami, T., et al., *Roles of nitric oxide and prostaglandins in the increased permeability of the blood-brain barrier caused by lipopolysaccharide*. Environmental toxicology and pharmacology, 1998. **5**(1): p. 35-41.
88. Qin, L., et al., *Systemic LPS causes chronic neuroinflammation and progressive neurodegeneration*. Glia, 2007. **55**(5): p. 453-462.
89. Brown, G.C., *The endotoxin hypothesis of neurodegeneration*. Journal of neuroinflammation, 2019. **16**(1): p. 1-10.
90. Yang, W., G. Xiong, and B. Lin, *Cyclooxygenase-1 mediates neuroinflammation and neurotoxicity in a mouse model of retinitis pigmentosa*. Journal of neuroinflammation, 2020. **17**(1): p. 1-17.
91. Choi, S.-H., S. Aid, and F. Bosetti, *The distinct roles of cyclooxygenase-1 and-2 in neuroinflammation: implications for translational research*. Trends in pharmacological sciences, 2009. **30**(4): p. 174-181.
92. Kuzkaya, N., et al., *Interactions of peroxynitrite, tetrahydrobiopterin, ascorbic acid, and thiols implications for uncoupling endothelial nitric-oxide synthase*. Journal of Biological Chemistry, 2003. **278**(25): p. 22546-22554.
93. Bendich, A., et al., *The antioxidant role of vitamin C*. Advances in Free Radical Biology & Medicine, 1986. **2**(2): p. 419-444.
94. Arrigoni, O. and M.C. De Tullio, *Ascorbic acid: much more than just an antioxidant*. Biochimica et Biophysica Acta (BBA)-General Subjects, 2002. **1569**(1-3): p. 1-9.
95. Wilson, J.X., *Regulation of vitamin C transport*. Annu. Rev. Nutr., 2005. **25**: p. 105-125.
96. Jackson, T.S., et al., *Ascorbate prevents the interaction of superoxide and nitric oxide only at very high physiological concentrations*. Circulation research, 1998. **83**(9): p. 916-922.
97. Wu, F., J.X. Wilson, and K. Tyml, *Ascorbate protects against impaired arteriolar constriction in sepsis by inhibiting inducible nitric oxide synthase expression*. Free Radical Biology and Medicine, 2004. **37**(8): p. 1282-1289.
98. Han, M., et al., *Ascorbate protects endothelial barrier function during septic insult: Role of protein phosphatase type 2A*. Free Radical Biology and Medicine, 2010. **48**(1): p. 128-135.
99. Heller, R., et al., *L-Ascorbic acid potentiates nitric oxide synthesis in endothelial cells*. Journal of Biological Chemistry, 1999. **274**(12): p. 8254-8260.
100. Saeed, R.W., T. Peng, and C.N. Metz, *Ascorbic acid blocks the growth inhibitory effect of tumor necrosis factor- $\alpha$  on endothelial cells*. Experimental Biology and Medicine, 2003. **228**(7): p. 855-865.
101. Wu, F., et al., *Ascorbate inhibits NADPH oxidase subunit p47phox expression in microvascular endothelial cells*. Free Radical Biology and Medicine, 2007. **42**(1): p. 124-131.
102. Wu, F., K. Tyml, and J.X. Wilson, *Ascorbate inhibits iNOS expression in endotoxin-and IFN $\gamma$ -stimulated rat skeletal muscle endothelial cells*. FEBS letters, 2002. **520**(1-3): p. 122-126.
103. Shekhonin, B., et al., *Relative distribution of fibronectin and type I, III, IV, V collagens in normal and atherosclerotic intima of human arteries*. Atherosclerosis, 1987. **67**(1): p. 9-16.
104. Schor, A.M., S.L. Schor, and T.D. Allen, *Effects of culture conditions on the proliferation, morphology and migration of bovine aortic endothelial cells*. Journal of cell science, 1983. **62**(1): p. 267-285.
105. May, J.M. and Z.-c. Qu, *Nitric oxide mediates tightening of the endothelial barrier by ascorbic acid*. Biochemical and biophysical research communications, 2011. **404**(2): p. 701-705.



106. Pereira, C., et al., *Designing novel hybrid materials by one-pot co-condensation: from hydrophobic mesoporous silica nanoparticles to superamphiphobic cotton textiles*. ACS applied materials & interfaces, 2011. **3**(7): p. 2289-2299.
107. Zimetbaum, P., H. Eder, and W. Frishman, *Probucol: pharmacology and clinical application*. The Journal of Clinical Pharmacology, 1990. **30**(1): p. 3-9.
108. Yamashita, S., D. Masuda, and Y. Matsuzawa, *Did we abandon probucol too soon? Current opinion in lipidology*, 2015. **26**(4): p. 304-316.
109. Iqbal, M., S.D. Sharma, and S. Okada, *Probucol as a potent inhibitor of oxygen radical-induced lipid peroxidation and DNA damage: in vitro studies*. Redox report, 2004. **9**(3): p. 167-172.
110. Bridges, A., N. Scott, and J. Belch, *Probucol, a superoxide free radical scavenger in vitro*. Atherosclerosis, 1991. **89**(2): p. 263-265.
111. Barnhart, R.L., S.J. Busch, and R.L. Jackson, *Concentration-dependent antioxidant activity of probucol in low density lipoproteins in vitro: probucol degradation precedes lipoprotein oxidation*. Journal of lipid research, 1989. **30**(11): p. 1703-1710.
112. Witting, P.K., et al., *Probucol protects against hypochlorite-induced endothelial dysfunction identification of a novel pathway of probucol oxidation to a biologically active intermediate*. Journal of Biological Chemistry, 2005. **280**(16): p. 15612-15618.
113. Kuzuya, M., et al., *Probucol prevents oxidative injury to endothelial cells*. Journal of lipid research, 1991. **32**(2): p. 197-204.
114. Zucoloto, A.Z., et al., *Probucol attenuates lipopolysaccharide-induced leukocyte recruitment and inflammatory hyperalgesia: Effect on NF- $\kappa$ B activation and cytokine production*. European journal of pharmacology, 2017. **809**: p. 52-63.
115. Jung, Y.S., et al., *Probucol inhibits LPS-induced microglia activation and ameliorates brain ischemic injury in normal and hyperlipidemic mice*. Acta Pharmacologica Sinica, 2016. **37**(8): p. 1031-1044.
116. Mamo, J.C., et al., *Probucol prevents blood-brain barrier dysfunction and cognitive decline in mice maintained on pro-diabetic diet*. Diabetes and Vascular Disease Research, 2019. **16**(1): p. 87-97.
117. Mooranian, A., et al., *The biological effects of the hypolipidaemic drug probucol microcapsules fed daily for 4 weeks, to an insulin-resistant mouse model: potential hypoglycaemic and anti-inflammatory effects*. Drug delivery and translational research, 2018. **8**(3): p. 543-551.
118. Homayun, B., X. Lin, and H.-J. Choi, *Challenges and recent progress in oral drug delivery systems for biopharmaceuticals*. Pharmaceutics, 2019. **11**(3): p. 129.
119. Song, N.-N., S.-Y. Zhang, and C.-X. Liu, *Overview of factors affecting oral drug absorption*. Asian J Drug Metab Pharmacokinet, 2004. **4**(3): p. 167-176.
120. Allam, A.N., S. El Gamal, and V. Naggar, *Bioavailability: A pharmaceutical review*. Int J Novel Drug Deliv Tech, 2011. **1**(1): p. 77-93.
121. Schanker, L.S., *On the mechanism of absorption of drugs from the gastrointestinal tract*. Journal of Medicinal Chemistry, 2002. **2**(4): p. 343-359.
122. Williams III, R.O., A.B. Watts, and D.A. Miller, *Formulating poorly water soluble drugs*. Vol. 22. 2016: Springer.
123. Savjani, K.T., A.K. Gajjar, and J.K. Savjani, *Drug solubility: importance and enhancement techniques*. International Scholarly Research Notices, 2012. **2012**.
124. USP, U. 30, NF 25. in *The United States Pharmacopeia and The National Formulary, The United States Pharmacopoeial Convention, INC*. 2007.
125. Pharmacopoeia, B., *British Pharmacopoeia, Volume I & II*. London: Medicines and Healthcare Products Regulatory Agency (MHRA), 2009: p. 4788.

126. Noyes, A.A. and W.R. Whitney, *The rate of solution of solid substances in their own solutions*. Journal of the American Chemical Society, 1897. **19**(12): p. 930-934.
127. Fagerholm, U., *The role of permeability in drug ADME/PK, interactions and toxicity—presentation of a permeability-based classification system (PCS) for prediction of ADME/PK in humans*. Pharmaceutical research, 2008. **25**(3): p. 625-638.
128. Moriguchi, I., et al., *Simple method of calculating octanol/water partition coefficient*. Chemical and pharmaceutical bulletin, 1992. **40**(1): p. 127-130.
129. Ku, M.S., *Use of the biopharmaceutical classification system in early drug development*. The AAPS journal, 2008. **10**(1): p. 208-212.
130. Sanches, B.M. and E.I. Ferreira, *Is prodrug design an approach to increase water solubility?* International journal of pharmaceutics, 2019. **568**: p. 118498.
131. Gupta, D., et al., *Salts of therapeutic agents: chemical, physicochemical, and biological considerations*. Molecules, 2018. **23**(7): p. 1719.
132. Loftsson, T. and M.E. Brewster, *Pharmaceutical applications of cyclodextrins. 1. Drug solubilization and stabilization*. Journal of pharmaceutical sciences, 1996. **85**(10): p. 1017-1025.
133. Saokham, P., et al., *Solubility of cyclodextrins and drug/cyclodextrin complexes*. Molecules, 2018. **23**(5): p. 1161.
134. Khan, B.A., et al., *Basics of pharmaceutical emulsions: A review*. African Journal of Pharmacy and Pharmacology, 2011. **5**(25): p. 2715-2725.
135. Gursoy, R.N. and S. Benita, *Self-emulsifying drug delivery systems (SEDDS) for improved oral delivery of lipophilic drugs*. Biomedicine & pharmacotherapy, 2004. **58**(3): p. 173-182.
136. Shah, N., et al., *Self-emulsifying drug delivery systems (SEDDS) with polyglycolized glycerides for improving in vitro dissolution and oral absorption of lipophilic drugs*. International journal of pharmaceutics, 1994. **106**(1): p. 15-23.
137. Chaumeil, J., *Micronization: a method of improving the bioavailability of poorly soluble drugs*. Methods and findings in experimental and clinical pharmacology, 1998. **20**(3): p. 211-216.
138. Pinnamaneni, S., N. Das, and S. Das, *Formulation approaches for orally administered poorly soluble drugs*. Pharmazie, 2002. **57**(5): p. 291-300.
139. Chi Lip Kwok, P. and H.-K. Chan, *Nanotechnology versus other techniques in improving drug dissolution*. Current pharmaceutical design, 2014. **20**(3): p. 474-482.
140. Patra, J.K., et al., *Nano based drug delivery systems: recent developments and future prospects*. Journal of nanobiotechnology, 2018. **16**(1): p. 71.
141. Hassan, S., et al., *Evolution and clinical translation of drug delivery nanomaterials*. Nano Today, 2017. **15**: p. 91-106.
142. Wilde, G., *Nanostructured materials*. 2009: Elsevier.
143. Wilczewska, A.Z., et al., *Nanoparticles as drug delivery systems*. Pharmacological reports, 2012. **64**(5): p. 1020-1037.
144. Narayan, R., et al., *Mesoporous silica nanoparticles: A comprehensive review on synthesis and recent advances*. Pharmaceutics, 2018. **10**(3): p. 118.
145. Cha, W., et al., *Mesoporous silica nanoparticles as carriers for intracellular delivery of nucleic acids and subsequent therapeutic applications*. Molecules, 2017. **22**(5): p. 782.
146. Argyo, C., et al., *Multifunctional mesoporous silica nanoparticles as a universal platform for drug delivery*. Chemistry of Materials, 2014. **26**(1): p. 435-451.
147. Deodhar, G.V., M.L. Adams, and B.G. Trewyn, *Controlled release and intracellular protein delivery from mesoporous silica nanoparticles*. Biotechnology journal, 2017. **12**(1): p. 1600408.

148. Kresge, C., et al., *Ordered mesoporous molecular sieves synthesized by a liquid-crystal template mechanism*. nature, 1992. **359**(6397): p. 710-712.
149. Grün, M., et al., *Novel pathways for the preparation of mesoporous MCM-41 materials: control of porosity and morphology*. Microporous and mesoporous materials, 1999. **27**(2-3): p. 207-216.
150. Zhao, D., et al., *Triblock co polymer syntheses of mesoporous silica with periodic 50 to 300 angstrom pores*. Science, 1998. **279**(548): p. 548-552.
151. Atluri, R., N. Hedin, and A.E.G. Bennett, *Hydrothermal phase transformation of bicontinuous cubic mesoporous material AMS-6*. Chem Mater, 2008. **20**: p. 3857-3866.
152. Huo, Q., D.I. Margolese, and G.D. Stucky, *Surfactant control of phases in the synthesis of mesoporous silica-based materials*. Chemistry of Materials, 1996. **8**(5): p. 1147-1160.
153. Wan, Y. and D. Zhao, *On the controllable soft-templating approach to mesoporous silicates*. Chemical reviews, 2007. **107**(7): p. 2821-2860.
154. Stucky, G.D., et al., *Directed synthesis of organic/inorganic composite structures*. Studies in Surface Science and Catalysis, 1997. **105**: p. 3-28.
155. Hoffmann, F., et al., *Silica-based mesoporous organic-inorganic hybrid materials*. Angewandte Chemie International Edition, 2006. **45**(20): p. 3216-3251.
156. Lee, U., M.-H. Kim, and Y.-U. Kwon, *Mesoporous thin films with accessible pores from surfaces*. Bulletin of the Korean Chemical Society, 2006. **27**(6): p. 808-816.
157. Heidegger, S., et al., *Immune response to functionalized mesoporous silica nanoparticles for targeted drug delivery*. Nanoscale, 2016. **8**(2): p. 938-948.
158. Bharti, C., et al., *Mesoporous silica nanoparticles in target drug delivery system: A review*. International journal of pharmaceutical investigation, 2015. **5**(3): p. 124.
159. Yang, P., S. Gai, and J. Lin, *Functionalized mesoporous silica materials for controlled drug delivery*. Chemical Society Reviews, 2012. **41**(9): p. 3679-3698.
160. Vallet-Regí, M., et al., *Mesoporous silica nanoparticles for drug delivery: current insights*. Molecules, 2018. **23**(1): p. 47.
161. Maleki, A., et al., *Mesoporous silica materials: From physico-chemical properties to enhanced dissolution of poorly water-soluble drugs*. Journal of Controlled Release, 2017. **262**: p. 329-347.
162. Van den Mooter, G., *The use of amorphous solid dispersions: A formulation strategy to overcome poor solubility and dissolution rate*. Drug Discovery Today: Technologies, 2012. **9**(2): p. e79-e85.
163. Hancock, B.C. and G. Zografi, *Characteristics and significance of the amorphous state in pharmaceutical systems*. J Pharm Sci, 1997. **86**(1): p. 1-12.
164. Hancock, B.C., S.L. Shamblin, and G. Zografi, *Molecular mobility of amorphous pharmaceutical solids below their glass transition temperatures*. Pharmaceutical research, 1995. **12**(6): p. 799-806.
165. Murdande, S.B., et al., *Solubility advantage of amorphous pharmaceuticals: I. A thermodynamic analysis*. Journal of pharmaceutical sciences, 2010. **99**(3): p. 1254-1264.
166. Law, D., et al., *Ritonavir-PEG 8000 amorphous solid dispersions: in vitro and in vivo evaluations*. Journal of pharmaceutical sciences, 2004. **93**(3): p. 563-570.
167. Fahlman, B., *Materials Chemistry*. 2 ed. 2011, Netherlands: Springer. 736.
168. Riikonen, J., W. Xu, and V.-P. Lehto, *Mesoporous systems for poorly soluble drugs-recent trends*. International journal of pharmaceutics, 2018. **536**(1): p. 178-186.
169. Hamilton, B.D., et al., *Manipulating crystal growth and polymorphism by confinement in nanoscale crystallization chambers*. Accounts of Chemical Research, 2012. **45**(3): p. 414-423.

170. Rengarajan, G., et al., *Stabilization of the amorphous state of pharmaceuticals in nanopores*. Journal of Materials Chemistry, 2008. **18**(22): p. 2537-2539.
171. Shen, S.C., et al., *Stabilized amorphous state of ibuprofen by co-spray drying with mesoporous SBA-15 to enhance dissolution properties*. Journal of pharmaceutical sciences, 2010. **99**(4): p. 1997-2007.
172. Shen, S.C., et al., *Physical state and dissolution of ibuprofen formulated by co-spray drying with mesoporous silica: effect of pore and particle size*. Int J Pharm, 2011. **410**: p. 188-195.
173. Heikkilä, T., et al., *Evaluation of mesoporous TCPSi, MCM-41, SBA-15, and TUD-1 materials as API carriers for oral drug delivery*. Drug delivery, 2007. **14**(6): p. 337-347.
174. Zhang, Y., et al., *Spherical mesoporous silica nanoparticles for loading and release of the poorly water-soluble drug telmisartan*. J Control Release, 2010. **145**: p. 257-263.
175. Mellaerts, R., et al., *Enhanced release of itraconazole from ordered mesoporous SBA-15 silica materials*. Chem Commun, 2007: p. 1375-1377.
176. Horcajada, P., et al., *Influence of pore size of MCM-41 matrices on drug delivery rate*. Micropor Mesopor Mat, 2004. **68**: p. 105-109.
177. Jia, L., et al., *Successfully tailoring the pore size of mesoporous silica nanoparticles: Exploitation of delivery systems for poorly water-soluble drugs*. Int J Pharm, 2012. **439**: p. 81-91.
178. Van Speybroeck, M., et al., *Enhanced absorption of the poorly soluble drug fenofibrate by tuning its release rate from ordered mesoporous silica*. European Journal of Pharmaceutical Sciences, 2010. **41**(5): p. 623-630.
179. Van Speybroeck, M., et al., *Ordered mesoporous silica material SBA-15: a broad-spectrum formulation platform for poorly soluble drugs*. Journal of pharmaceutical sciences, 2009. **98**(8): p. 2648-2658.
180. Zhu, Y.F., et al., *Hollow mesoporous spheres with cubic pore network as a potential carrier for drug storage and its in vitro release kinetics*. J Mater Res, 2005. **20**(1): p. 54-61.
181. Izquierdo-Barba, I.I., et al., *Release evaluation of drugs from ordered three-dimensional silica structures*. Eur J Pharm Sci, 2005. **26**(5): p. 365-373.
182. Qu, F., et al., *A controlled release of ibuprofen by systematically tailoring the morphology of mesoporous silica materials*. J Solid State Chem, 2006. **179**(7): p. 2027-2035.
183. Heikkilä, T., et al., *Mesoporous silica material TUD-1 as a drug delivery system*. Int J Pharm, 2007. **331**: p. 133-138.
184. Hu, Y., et al., *3D cubic mesoporous silica microsphere as a carrier for poorly soluble drug carvedilol*. Microporous and Mesoporous Materials, 2012. **147**(1): p. 94-101.
185. Zhu, W., et al., *Exploitation of 3D face-centered cubic mesoporous silica as a carrier for a poorly water soluble drug: influence of pore size on release rate*. Materials Science and Engineering: C, 2014. **34**: p. 78-85.
186. Friedrich, H., B. Fussnegger, and K. Kolter, *Dissolution rate improvement of poorly water-soluble drugs obtained by adsorbing solutions of drugs in hydrophilic solvents onto high surface area carriers*. Eur J Pharm Biopharm, 2006. **62**(2): p. 171-177.
187. Andersson, J., J. Rosenholm, and S. Areva, *Influences of material characteristics on ibuprofen drug loading and release profiles from ordered micro-and mesoporous silica matrices*. Chem Mater, 2004. **16**(21): p. 4160-4167.
188. Bavnhoj, C.G., et al., *The role interplay between mesoporous silica pore volume and surface area and their effect on drug loading capacity*. International Journal of Pharmaceutics: X, 2019. **1**: p. 100008.
189. Limnell, T., et al., *Drug delivery formulations of ordered and nonordered mesoporous silica: comparison of three drug loading methods*. Journal of pharmaceutical sciences, 2011. **100**(8): p. 3294-3306.
190. Xu, W., J. Riikonen, and V.-P. Lehto, *Mesoporous systems for poorly soluble drugs*. International journal of pharmaceutics, 2013. **453**(1): p. 181-197.

191. Horcajada, P., et al., *Influence of superficial organic modification of MCM-41 matrices on drug delivery rate*. Solid State Sciences, 2006. **8**(10): p. 1243-1249.
192. Vallet-Regí, M., F. Balas, and D. Arcos, *Mesoporous materials for drug delivery*. Angewandte Chemie International Edition, 2007. **46**(40): p. 7548-7558.
193. Babonneau, F., et al., *Encapsulation of ibuprofen in mesoporous silica: solid state NMR characterization*. MRS Online Proceedings Library, 2003. **775**(1): p. 3261-3266.
194. Munoz, B., et al., *MCM-41 organic modification as drug delivery rate regulator*. Chemistry of Materials, 2003. **15**(2): p. 500-503.
195. Song, S.-W., K. Hidajat, and S. Kawi, *Functionalized SBA-15 materials as carriers for controlled drug delivery: Influence of surface properties on matrix– drug interactions*. Langmuir, 2005. **21**(21): p. 9568-9575.
196. Higuchi, T., *Mechanism of sustained-action medication. Theoretical analysis of rate of release of solid drugs dispersed in solid matrices*. Journal of pharmaceutical sciences, 1963. **52**(12): p. 1145-1149.
197. Xue, J.M. and M. Shi, *PLGA/Mesoporous silica hybrid structure for controlled drug release*. J Control Release, 2004. **98**(2): p. 209-217.
198. Siepmann, J. and F. Siepmann, *Mathematical modeling of drug delivery*. International journal of pharmaceutics, 2008. **364**(2): p. 328-343.
199. Dash, S., et al., *Kinetic modeling on drug release from controlled drug delivery systems*. Acta Pol Pharm, 2010. **67**(3): p. 217-223.
200. Imbimbo, B.P., V. Solfrizzi, and F. Panza, *Are NSAIDs useful to treat Alzheimer's disease or mild cognitive impairment?* Frontiers in aging neuroscience, 2010. **2**.
201. Deardorff, W.J. and G.T. Grossberg, *Targeting neuroinflammation in Alzheimer's disease: evidence for NSAIDs and novel therapeutics*. Expert Review of Neurotherapeutics, 2017. **17**(1): p. 17-32.
202. Rogers, J., et al., *Clinical trial of indomethacin in Alzheimer's disease*. Neurology, 1993. **43**(8): p. 1609-1609.
203. Hasanpour Dehkordi, A., et al., *Metformin and its anti-inflammatory and anti-oxidative effects; new concepts*. Journal of Renal Injury Prevention, 2019.
204. Zhang, W.-Y., et al., *Pioglitazone inhibits the expression of inflammatory cytokines from both monocytes and lymphocytes in patients with impaired glucose tolerance*. Arteriosclerosis, thrombosis, and vascular biology, 2008. **28**(12): p. 2312-2318.
205. Tu, Q., et al., *Atorvastatin protects against cerebral ischemia/reperfusion injury through anti-inflammatory and antioxidant effects*. Neural regeneration research, 2014. **9**(3): p. 268.
206. Ghaisas, M.M., et al., *Antioxidant, antinociceptive and anti-inflammatory activities of atorvastatin and rosuvastatin in various experimental models*. Inflammopharmacology, 2010. **18**(4): p. 169-177.
207. Calò, L.A., A. Semplicini, and P.A. Davis, *Antioxidant and antiinflammatory effect of carvedilol in mononuclear cells of hypertensive patients*. The American journal of medicine, 2005. **118**(2): p. 201-202.
208. Toma, L., et al., *Anti-oxidant and anti-inflammatory mechanisms of amlodipine action to improve endothelial cell dysfunction induced by irreversibly glycated LDL*. Biochemical and Biophysical Research Communications, 2011. **411**(1): p. 202-207.
209. Betge, S., et al., *Oral treatment with probucol in a pharmacological dose has no beneficial effects on mortality in chronic ischemic heart failure after large myocardial infarction in rats*. European journal of pharmacology, 2007. **558**(1-3): p. 119-127.
210. Zaitseva, T., et al., *Pharmacokinetics of probucol dosage forms in clinical tests*. Pharmaceutical Chemistry Journal, 1995. **29**(4): p. 245-247.
211. Analytics, O.P.H. *Drugbank*. 2020 07/2020]; Available from: <https://go.drugbank.com/>.

# 2 Materials and methodology

## 2.1 Chemicals

Unless stated, all chemicals were purchased from Sigma Aldrich (Sydney, Australia) and used as received without further purification. Biological assay kits were purchased from Sigma Aldrich (Sydney, Australia), and Abcam (Melbourne, Australia).

## 2.2 Synthesis of mesoporous silica particles

In this thesis, MSPs with different structural and textural properties were synthesised. The MSPs used in this thesis and their structural and textural properties are listed in Table 2.1:

Material	Particle shape	Pore structure	a (Å) <sup>a</sup>	Pore size <sup>b</sup> (nm)	Pore volume <sup>b</sup> (cm <sup>3</sup> /g)	Surface area <sup>c</sup> (m <sup>2</sup> /g)
MCM-41	Spherical	2D-hexagonal	86.7	3.2	0.5	975.5
AMS-6	Spherical	3D-bicontinuous	113.2	4.7	0.7	777.3
SBA-15	Rod	2D-hexagonal	205.5	10.5	0.9	646.9

<sup>a</sup>Unit cell from powder XRD

<sup>b</sup>Pore size, pore volume from nitrogen isotherm analysis of samples (see section 2.6 for details)

<sup>c</sup>Specific surface area from nitrogen isotherm.

**Table 2.1** Structural and textural properties of MSPs used in this thesis.

### 2.2.1 AMS-6 synthesis

The synthesis of AMS-6 follows the protocol reported previously [1]. 1.875 g C<sub>12</sub> Alanine (C<sub>12</sub>Ala) was added to 375 ml Milli-Q® water and stirred (300 rpm) overnight at 80 °C, in a closed polypropylene (PPE) bottle. 1.875 g of (3-Aminopropyl) triethoxysilane (APTES) was added to the mixture and allowed to stir for one minute at 1000 rpm, 80 °C. 9.375 g of tetraethyl orthosilicate (TEOS) was added and allowed to stir at 1000 rpm, at 80 °C for one hour. The synthesis bottle was stirred at 500 rpm, 80 °C for 24 hours. The synthesis bottle was allowed to cool at room temperature for 12 hours. The sample was filtered without further washing. The material was calcined in a furnace

set at 550°C for 3 hours. The molar composition of the reaction mixture was C<sub>12</sub>Ala: APTES: TEOS: H<sub>2</sub>O 0.15: 0.19: 1: 46.13.

### 2.2.2 MCM-41 synthesis

The synthesis of MCM-41 followed the protocol reported previously [2]. 50 g of Milli-Q® water was added to 2.5 g of n-hexadecyltrimethylammonium bromide (C<sub>16</sub>TMABr) surfactant, 13.5 g aqueous ammonia (28 %) and 60 g ethanol at room temperature, in a closed PPE bottle stirring at 300 rpm for 20 minutes. 4.7 g of TEOS was added, and the solution was allowed to stir at 300 rpm for a further 2 hours in room temperature. The synthesis bottle was kept in the synthesis oven set at 100°C for 24 hours. Samples were filtered and washed with the mother liquor and allowed to dry overnight. The material was calcined at 550°C for 3 hours to remove the organic surfactant. The final molar composition of the reaction mixture was CTAB: NH<sub>3</sub>:H<sub>2</sub>O: TEOS: EtOH 0.3: 11: 144: 1: 58.

### 2.2.3 SBA-15 synthesis

The synthesis of SBA-15 followed the protocol reported previously [3]. 135 g of Milli-Q® water, 9.8 g of hydrochloric acid (37%), and 3.85 g of Pluronic P123 was added and kept at 40°C in a closed PPE bottle stirred at 500 rpm for one hour. TEOS (8.19 g) was added and the mixture was stirred at 300 rpm, 40°C for 24 hours. The synthesis bottle was kept inside the synthesis oven at 100°C for 48 hours. The samples were filtered without washing, and dried at room temperature overnight. The material was calcined at 550°C for 3 hours. The molar composition of the reaction mixture was P123: H<sub>2</sub>O: HCl: TEOS 0.48: 16.67: 1.21: 1.

## 2.3 Drug compounds used in this thesis

The drug compounds used in this thesis are Albendazole, Indomethacin, Hydrocortisone, and Probuco. Their physical properties are listed in Table 2.2. All drug compounds are commercially available from Sigma and were used as received without further purification.

Drug compound	MW (g/mol)	Water solubility (mg/L)	Clog P	Melting point (°C)	Therapeutic indication
Albendazole	265.3	0.02	3.1	202	Anti-fungal
Indomethacin	357.8	0.9	3.2	159	Anti-inflammatory
Hydrocortisone	362.4	0.2	10.5	211	Anti-inflammatory
Probucol	516.8	$4.1 \times 10^{-5}$	8.9	125	Anti-inflammatory/antioxidant

**Table 2.2** Physical properties of drug compounds used in this thesis. All values were taken from drug bank [4]

## 2.4 Drug loading within mesoporous silica

Calcined MSP (1 g) was dispersed in 250 ml ethanol and sonicated for 30 minutes. 100 mg (10 wt%), 200 mg (20 wt%) or 300 mg (30 wt%) of the drug compound was dispersed in the above MSP ethanol solution and stirred at 300 rpm, in room temperature for 30 minutes. The solvent was evaporated using a rotary evaporator (stirring rate 100 rpm, bath temperature 40 °C) connected to a programmable vacuum pump. The pressure ramp was 800 mbar for 30 minutes, 500 mbar for 30 minutes, and 30 mbar for 30 minutes, to ensure full removal of the solvent.

## 2.5 Drug dissolution measurements

Dissolution profiles of pharmaceutical drug compounds from mesoporous silica were measured in simulated intestinal fluid (SIF, pH 6.8) under sink conditions. The chemical composition of SIF was 0.896 g NaOH, 6.80 g  $\text{KH}_2\text{PO}_4$  in 1 L Milli-Q® water [5]. Drug loaded mesoporous materials (30 mg) was loaded in size 3 gelatine capsules and added to a dissolution vessel containing 900 ml of SIF. Commercially available pharmaceutical drug compounds unloaded in mesoporous silica were used as standards for comparison. Dissolution vessels were placed in a dissolution bath maintained at 37 °C and under constant stirring at 50 rpm. A USP II dissolution apparatus (708-DS dissolution apparatus, Agilent Technologies) equipped with a peristaltic pump and Cary 60 UV-Vis spectrophotometer was used to measure the rate of drug release at regular intervals over a period of 24 hours.

## 2.6 Characterisation techniques

### 2.6.1 X-ray diffraction (XRD)

Powder XRD is a crystallographic technique used to determine the atomic and molecular structure of crystalline or periodic materials [6]. The material to be analysed is irradiated with incident X-rays. The constructive



interference between the incident rays with planes of atoms arranged symmetrically with a separation distance,  $d$ , is measured. A diffraction peak is obtained when conditions of the Bragg's law are met [7, 8]. The Bragg's law relates the wavelength of the electromagnetic radiation to the x-ray incident angle, diffraction angle and the lattice spacing in the material:

$$2d\sin\theta = n\lambda \quad (2.1)$$

where  $d$  is the interplanar spacing  $d_{hkl}$  ( $hkl$  = miller indices),  $\theta$  is the bragg angle ( $2\theta$  is the angle between incident and reflected beam),  $n$  is the order of the interference (normally  $n = 1$ ) and  $\lambda$  is the wavelength [8]. Scanning the material through a range of  $2\theta$  angles allows for the detection of all possible diffraction directions of the crystal lattice.

The diffraction peaks in XRD scans of mesoporous materials provide information of the porous structure of the material [9-11]. For example, the diffraction pattern of MCM-41 mesoporous material typically includes three to five reflections of between  $1$ - $10^\circ$   $2\theta$  (Figure 2.1). The reflections are due to ordered hexagonal array of parallel silica pores and can be indexed assuming a hexagonal unit cell as (100), (110), (200), (210), and (300) reflections [2]. As the materials are not crystalline at the atomic level, no ordered reflections are observed at higher angles except for a broad peak between  $20$  - $26^\circ$   $2\theta$  due to disordered Si-O-Si bonds in the silica wall.

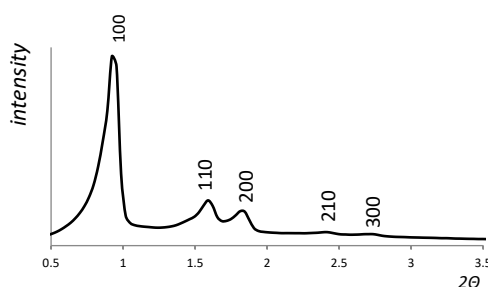


**Figure 2.1:** XRD scan of a MCM-41 mesoporous silica particle.

The XRD of crystalline pharmaceutical drug compounds are characterised by sharp diffraction peaks between  $10$ - $60^\circ$   $2\theta$ . In drug loaded mesoporous silica, drug loading results in an amorphous form characterised by XRD patterns showing broad, diffuse scattering band containing no sharp diffraction peaks. The presence of crystalline material on the external surface of silica particles of drug loaded samples is identified by diffraction peaks between  $10^\circ$ -  $60^\circ$   $2\theta$ .

All XRD analysis was performed using a Bruker D8 Discover diffractometer equipped with Cu-K $\alpha$  radiation as X-Ray source ( $\lambda = 1.5406\text{\AA}$ ). Data were collected and analysed with the DIFFRAC.SUITE™ software (Bruker).

## 2.6.2 High energy X-ray diffraction (HE-XRD)

HE-XRD uses X-rays with electromagnetic energies of 60-150 keV or approximately one order of magnitude higher than conventional X-rays [12, 13]. The main advantages of using HE-XRD are:

- 1) The high penetration of the X-ray allow for experiments to be conducted in air with minimal polarisation effects [14].
- 2) Damage to biological samples from radiation are minimised, as high resolution data can be obtained with very short exposures to the X-ray beam [14, 15].

In this thesis, HE-XRD experiments were performed at the 11-ID-C beam line of the Advanced Photon Source, Argonne National Laboratory. Samples were loaded into 1mm Kapton capillaries for diffraction measurements performed at 115keV.

## 2.6.3 Pair distribution function analysis (PDF)

PDF, also known as total scattering analysis, is an analytical technique used to acquire structural information on amorphous materials by using the complete (Bragg and non-Bragg) scattering XRD pattern [16]. The local atomic structure of disordered materials can be described quantitatively using the PDF. The HE-XRD scan of the material is corrected by data reduction steps including the removal of the background scattering (air or vacuum) for the extraction of a total X-ray structure factor,  $S(Q)$ . This function is fourier transformed to provide an average probability function of all the atomic positions in the material, i.e. called the radial or pair distribution function  $G_x(r)$  [17]. The PDF describes the probability of finding two atoms separated at a certain distance in a lattice [17]. Other information that can be acquired include average bond angles, co-ordination numbers, and development of a structural model that fits the PDF function [14].

Background corrected HE-XRD patterns are first converted into scattering functions  $S(Q)$  via:

$$S(Q) = 1 + \frac{I^{\text{coh}}(Q) - \sum c_i |f_i(Q)|^2}{|\sum c_i f_i(Q)|^2} \quad (2.2)$$

Where  $c_i$  and  $f_i$  are the atomic concentration within the sample and X-ray scattering factors respectively,  $Q$  is the magnitude of the wave vector [17]. The Fourier transformation of  $Q[S(Q) - 1]$  was used to obtain atomic pair distribution function:

$$G(r) = \left(\frac{2}{\pi}\right) \int_{Q=0}^{Q_{\max}} Q[S(Q) - 1] \sin(Qr) dQ \quad (2.3)$$

Conversion of HE-XRD data into atomic PDFs was done with the program RAD [18].

#### 2.6.4 Scanning electron microscopy (SEM)

SEM was used for the visual inspection of the shape and particle size of mesoporous silica. SEM was also used to observe for the presence of crystalline drug material in drug loaded silica materials.

An electron source, commonly a tungsten filament, generates an electron beam that interacts with the surface of the sample. This results in the emission of different signals from the sample surface, including secondary electrons, backscattered electrons, and X-rays [19]. The signals are captured by detectors in order to produce images of the particle morphology. SEM imaging is typically performed under vacuum. In this thesis, SEM images were captured with a JEOL 7100F field emission SEM hot Schottky electron gun (1.2 nm resolution). Samples were prepared without gold coatings and imaged at magnifications between x1000-x30000, at 1.5 kV using gentle beam mode.

#### 2.6.5 Nitrogen sorption isotherm

Nitrogen ( $N_2$ ) sorption isotherms were used to determine the changes in textural properties of mesoporous silica, before and after loading pharmaceutical drug compounds, including surface area, pore volume, and pore size. A  $N_2$  sorption isotherm plot is the amount of gas adsorbed on the surface at a fixed temperature that is plotted as a function of pressure.

In a typical  $N_2$  sorption isotherm experiment, the process of adsorption begins with the formation of a monolayer of  $N_2$  adsorbed onto the surface of the material, followed by a multilayer formation [20]. The adsorption process takes place at a temperature below the critical point of nitrogen, as under this temperature the amount of gas adsorbed on the material increases with the increase in pressure [21]. There are six different types of adsorption isotherm plots based on the IUPAC recommendation (Figure 2.2) [22]. Mesoporous materials is categorised as type IV isotherm curve based on the adsorption and desorption of  $N_2$  from the surface and pores.

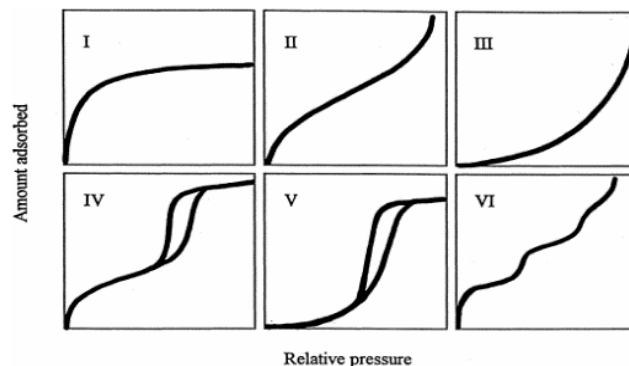


**Figure 2.2:** Six isotherm types as classified by IUPAC [22]

Different mathematical models can be used to describe the adsorption and desorption process. In this thesis, the surface area was determined by using the BET (Brunauer-Emmett-Teller) model of multilayer adsorption [23]. This is based on the following hypotheses:

- 1) Gas molecules undergo physical adsorption on the solids and can form multiple layers;
- 2) Gas molecules interact with adjacent layers;
- 3) Langmuir theory can be applied to each adsorbed layer

The BET equation thus follows:

$$\frac{P}{V(P_0 - P)} = \frac{1}{cV_m} + \frac{(c-1)P}{cV_m P_0} \quad (2.4)$$

where  $P$  and  $P_0$  are the equilibrium and saturation pressure of the adsorbate at the temperature of adsorption,  $V$  is the adsorbed gas quantity,  $V_m$  is the monolayer adsorbed gas quantity and  $c$  is the BET constant [23].

The density functional theory (DFT) method was used in the calculation of the pore size distribution (PSD) of mesoporous silica assuming a cylindrical pores geometry [24].

$N_2$  adsorption isotherm measurements were performed with a Micromeritics TriStar II Surface Area and Porosity instrument and the data were analysed with the TriStar II 3020 software (Micromeritics). Prior to the experiments, samples were degassed to remove adsorbed gas or vapor. This was achieved by heating the sample under vacuum. A micromeritics VacPrep 061 sample Degas System was used to degas MSP samples at  $60^\circ\text{C}$ , and at  $40^\circ\text{C}$  for drug loaded MSP samples overnight prior to  $N_2$  adsorption desorption experiments.

## 2.6.6 Thermogravimetric analysis (TGA)

TGA was used to determine the loading amount of pharmaceutical drug compounds in mesoporous silica. Generally, this is based on heating the sample at a set heating rate from 20 to 900 °C in air or oxygen. The amount of drug loaded in mesoporous silica is calculated from the weight loss from the decomposition of drug molecules between 150 °C - 650 °C.

TGA was performed on a TGA 2050 Thermogravimetric Analyser by TA Instrument (Delaware, USA). The data were collected and analysed by the TA instrument (Universal Analysis 2000, 3.0 G) software. The mass of the samples analysed varied between 5 and 10 mg, the heating rate was 10 °C/min, the temperature was increased from 25 °C to 1000 °C and the gas flow rate was 50 ml/min.

## 2.6.7 Differential scanning calorimetry (DSC)

A DSC records the change in the heat flow as the sample is heated at a linear rate to a specific temperature. Changes in heat flow provide information regarding the physical properties of the material [25]. In the first example (Figure 2.3 a), an increase in heat flow is required to increase the temperature of the sample, which is indicative of a change in the sample's heat capacity ( $\Delta C_p$ ). The temperature associated with the  $\Delta C_p$  can be used to determine the glass transition temperature of some drug compounds [26, 27], where the material changes from a glassy, solid form to a more viscous state [27].

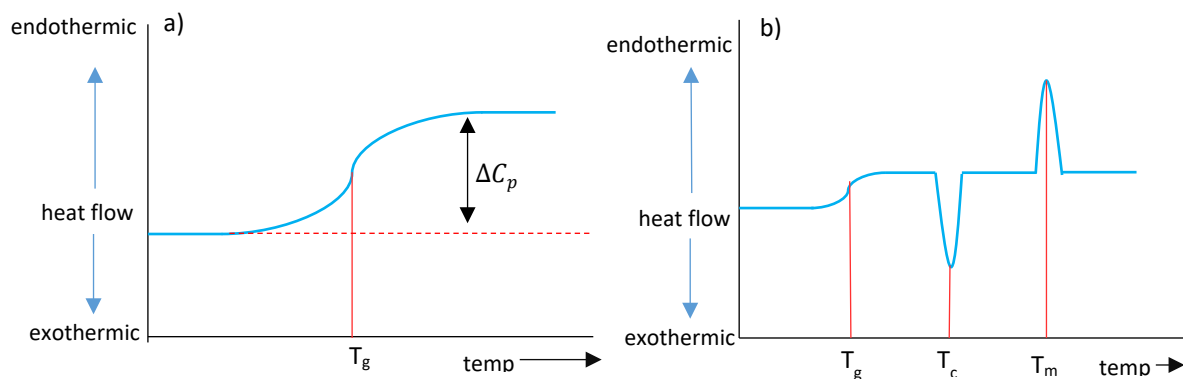


**Figure 2.3:** Representative DSC scans and important parameters,  $T_g$  is glass transition of temperature,  $\Delta C_p$  change in heat capacity,  $T_c$  crystallization temperature,  $T_m$  melting temperature.

In the case of the crystallisation temperature ( $T_c$ ), the material is experiencing an exothermic phase transition, characterised by a reduction in heat flow as the material transitions from the amorphous to crystalline form (Figure

2.3b) [28]. The melting temperature indicates the material is experiencing an endothermic phase transition, characterised by the increase in heat flow required to melt the crystalline material. The amorphous or crystalline content in a given sample can be estimated from the enthalpy of fusion in the given equation below.

$$X_c (\%) = (\Delta H / \Delta H_0) / 100 \quad (2.5)$$

where  $\Delta H$ , is the enthalpy of fusion of the sample and  $\Delta H_0$  is the enthalpy of fusion of the crystalline material, both of which can be derived experimentally from the DSC trace of the sample [28, 29].

In this thesis, DSC measurements were performed with a DSC 2010 Differential Scanning Calorimeter by TA Instruments (Delaware, USA). Data were collected and analysed with Advantage Software. The mass of the samples analysed varied between 3 and 5 mg and the nitrogen flow rate was 50 ml/min. The method used to heat the samples was the following: the temperature was increased from 20°C to 200°C (heating rate= 10°C/min), then maintained at 200°C for 15 minutes; subsequently, the temperature was decrease to 20°C (cooling rate = 10°C/min) and maintained at 20°C for 15 minutes; a second heating/cooling run was performed in the same way.

## 2.7 Cell culture *in vitro* experiments

*In vitro* cell experiments were conducted using BV2 (brain microglial cell line from C57BL/6 mice) and hCMEC/D3 (human brain endothelial) cell lines. Cells were seeded on 24 or 96 well plates and incubated at 37 °C with 5% CO<sub>2</sub>, 95% fresh air, until ~ 95% cell confluency was reached. Initial experiments investigated the effect of H<sub>2</sub>O<sub>2</sub> and LPS at different concentrations on cellular viability, ROS production and inflammation. Further studies were conducted to investigate the antioxidant and anti-inflammatory properties of the test compounds released from mesoporous silica as compared to the crystalline drug. The test compounds used for the *in vitro* experiments are represented in Figure 2.4:

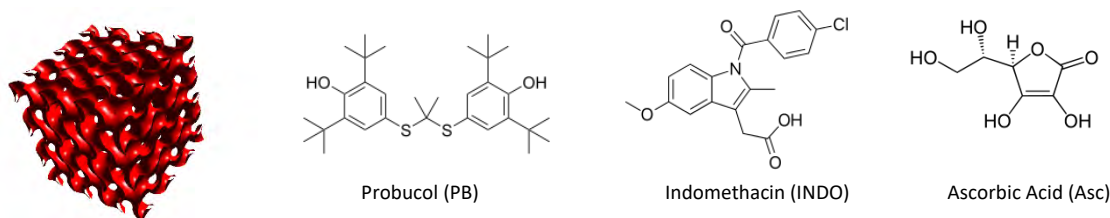


**Figure 2.4:** Test compounds used for *in vitro* analysis loaded into mesoporous silica AMS-6 and in their crystalline form. A model of the mesostructure of AMS-6 is shown on the left.

Test compounds at 1, 10, 50, and 100  $\mu\text{M}$  of the active ingredient were used for the *in vitro* experiments. Drug loaded within mesoporous silica AMS-6 is denoted by the drug loaded amount (e.g. 30 wt/wt%). The general method for seeding cells on a 24 or 96 well plate for the *in vitro* cell experiments were as follows:

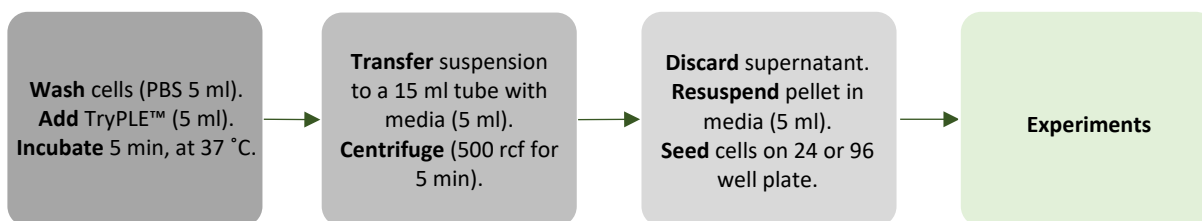


**Figure 2.5:** General method used to seed cells on 24 or 96 well plates.

### 2.7.1 Cell viability assay

The Muse® Count and Viability Assay (abacus dx, Meadowbrook, QLD) utilises a mixture of two fluorescent DNA intercalating dyes in a single reagent that differentially stains viable and non-viable cells [30]. A DNA binding dye stains the nucleus of dead and dying cells (non-viable) that have lost their membrane integrity, while viable cells with an intact membrane are not stained by the dye. A second, membrane permeable DNA staining dye stains all cells with a nucleus, allowing for the differentiation between nucleated cells and debris or non-nucleated cells [30]. The Muse® cell system analyser counts all stained events, and differentiates between free nuclei and cellular debris from viable nucleated cells based on cell size properties. Samples are analysed on the Muse® Cell Analyser using a guided touchscreen user interface. Results are displayed on the Muse® cell analyser screen as a plot of two cell populations; percentage of viable nucleated cells and percentage of nucleated non-viable cells.

Cell viability was measured at different time points following the incubation of cells in media containing LPS or  $\text{H}_2\text{O}_2$  together with different concentrations of the test compounds. The following method was used to conduct cell viability experiments using a confluent 24 well plate:

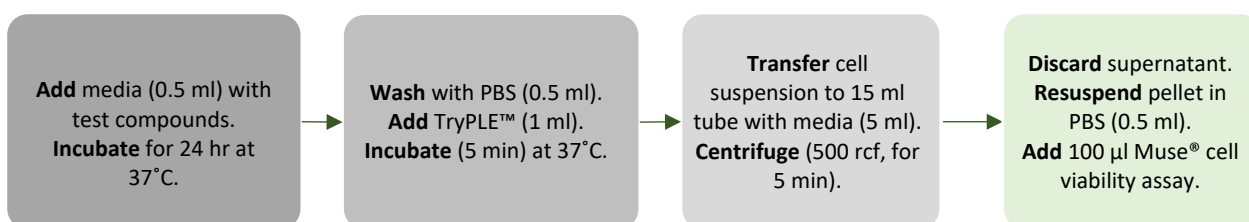


**Figure 2.6:** Method for sample preparation and analysis using the Muse® cell viability assay.

### 2.7.2 Muse® Oxidative stress kit

The Muse® Oxidative stress kit (abacus dx, Meadowbrook, QLD) allows for the quantitative measurement of cellular populations undergoing oxidative stress based on the intracellular detection of  $O_2^{\bullet-}$ . The Muse® oxidative stress reagent is based on the cell permeable dye dihydroethidium [31]. The dye is oxidised in the presence of  $O_2^{\bullet-}$ , forming the DNA-binding fluorophore ethidium bromide, staining the nucleus of cells under oxidative stress with red fluorescence [31]. With this assay, it is possible to differentiate between the percentage of cells that are not under oxidative stress (%ROS - cells), against cells that are under oxidative stress (%ROS + cells).

Oxidative stress was measured at different time points following the incubation of cells in media containing LPS or  $H_2O_2$  together with different concentrations of the test compounds. The following method was used to measure levels of cellular oxidative stress using a confluent 24 well plate:

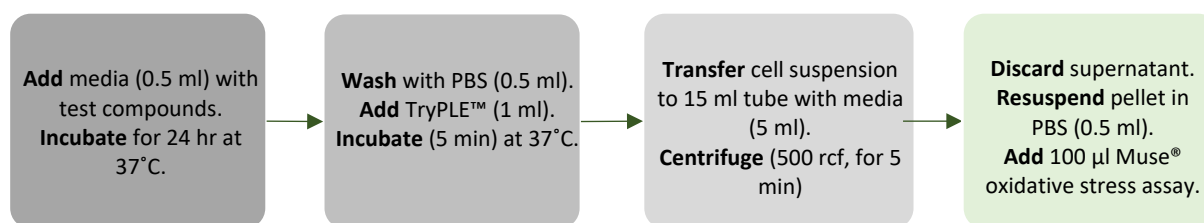


**Figure 2.7:** Method for sample preparation using the Muse® oxidative stress kit. Samples were run in the Muse® cell analyser.

### 2.7.3 The 2',7'-Dichlorodihydrofluorescein diacetate (DCFDA) reactive oxygen stress dye

The cell permeable, non-fluorescent molecular probe 2',7'-Dichlorodihydrofluorescein diacetate (DCFDA) was used for the detection of intracellular ROS including  $O_2^{\bullet-}$ ,  $H_2O_2$ ,  $OH^{\bullet}$  and  $NO^{\bullet}$  [32]. DCFDA diffuses into cells and is deacetylated by cellular esterases to the non-fluorescent, 2',7'-dichlorodihydrofluorescein ( $H_2DCF$ ) product that remains in the cell (Figure 2.8) [32]. The presence of intracellular ROS oxidises  $H_2DCF$  to the fluorescent 2',7'-dichlorofluorescein (DCF), which can be detected using a fluorescence plate reader at 485 nm excitation (Ex) and 535 nm emission (Em) wavelength respectively [32].



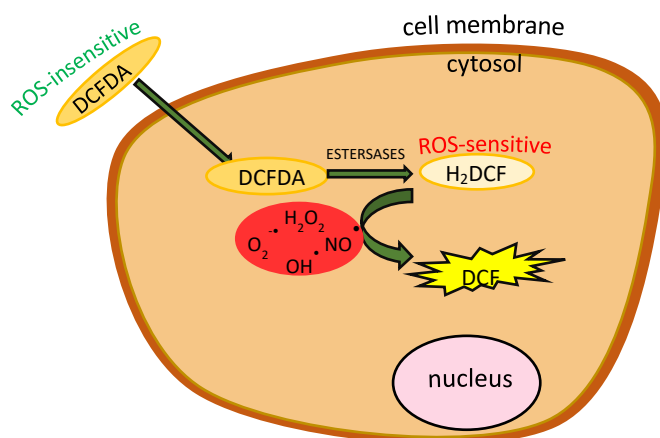


**Figure 2.8:** Schematic of ROS detection by the DCFDA. Diffusion of the DCFDA probe across the plasma membrane of cells occurs where it is converted to H<sub>2</sub>DCF by intracellular esterase enzyme. H<sub>2</sub>DCF is oxidised by cellular ROS molecules to form the highly fluorescent DCF compound.

The following method was used to measure ROS/RNS production in a confluent 96 well plate:

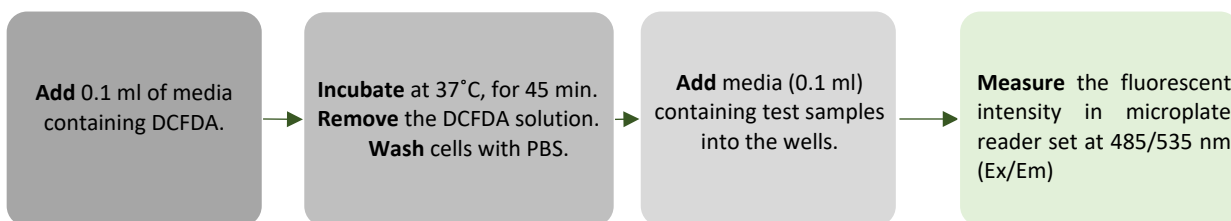


**Figure 2.9:** Method for sample preparation and analysis using the DCFDA probe.

#### 2.7.4 Nitric oxide assay

As NO<sup>•</sup> has an extremely short half-life of a few seconds, the stable decomposition products nitrite (NO<sub>2</sub><sup>-</sup>) and nitrate (NO<sub>3</sub><sup>-</sup>) are typically measured to determine the total NO<sup>•</sup> levels in biological fluids [33]. Levels of NO<sub>2</sub><sup>-</sup> are typically low, as it is rapidly oxidised *in vivo* to NO<sub>3</sub><sup>-</sup> which has a longer half-life of between 5-8 hours [34, 35]. The nitric oxide assay kit (ab65328, abcam, Melbourne) was used to measure total NO<sub>2</sub><sup>-</sup> and NO<sub>3</sub><sup>-</sup> levels, which provides an indirect measurement of NO<sup>•</sup>. Using the reagents provided by the assay kit, NO<sub>3</sub><sup>-</sup> is reduced to NO<sub>2</sub><sup>-</sup> by the nitrate reductase enzyme. The addition of Griess reagents result in the generation of dinitrogen trioxide (N<sub>2</sub>O<sub>3</sub>), from acidified NO<sub>2</sub><sup>-</sup>, and the reaction between N<sub>2</sub>O<sub>3</sub> with sulphanilamide to produce a diazonium ion that is coupled to N-(1-naphthyl)ethylene diamine in the formation of the chromatic azo product. The chromatic azo product is measured in a microplate reader at the absorption wavelength of 540 nm [36].

The following method was used to prepare samples for analysis of total NO<sup>•</sup> levels from a confluent 24 well plate:

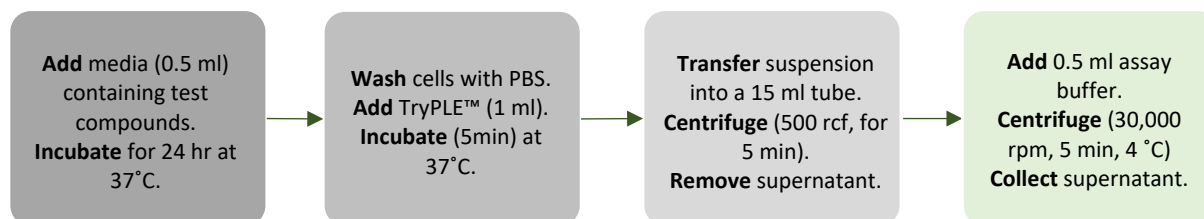


**Figure 2.10:** Method for the sample preparation.

The following method was used to analyse levels of total NO<sup>•</sup> as recommended by the supplier:

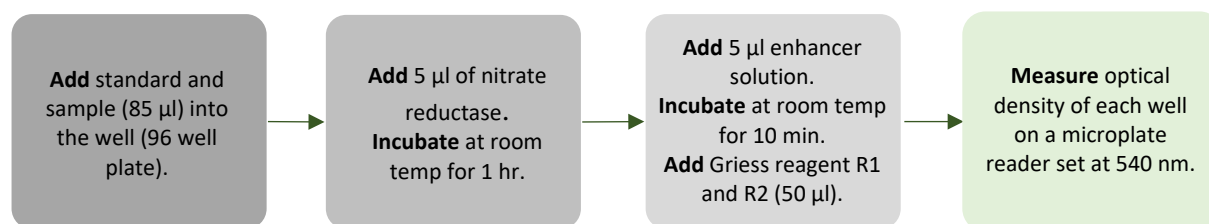


**Figure 2.11:** Method for the analysis of NO<sup>•</sup> levels in samples.

### 2.7.5 Peroxynitrite assay

The peroxynitrite assay kit (ab233469, abcam, Melbourne) contains the peroxynitrite sensor green, which specifically reacts with peroxynitrite (ONOO<sup>-</sup>) in solution to form a bright green fluorescent product, and the fluorescent intensity can be measured on a microplate reader at Ex/Em wavelength of 490/530 nm. The following method was used to measure levels of ONOO<sup>-</sup> in a confluent 24 well plate:

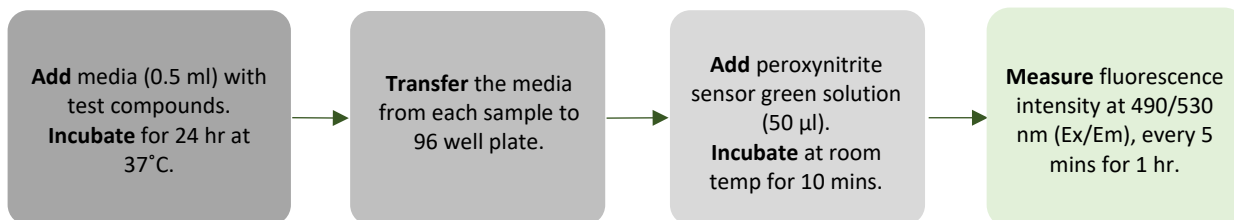


**Figure 2.12:** Method for the analysis of peroxynitrite in samples

### 2.7.6 COX enzyme activity assay

Arachidonic acid, together with phospholipids, is an integral part of the cellular membrane and is released into the intracellular compartment by the hydrolytic action of phospholipases [37]. Using arachidonic acid as the substrate, the COX enzyme catalyses two sequential enzymatic reactions; the first is the addition of molecular oxygen

at carbon 11 of arachidonic acid to form prostaglandin G<sub>2</sub> (PGG<sub>2</sub>; the cyclooxygenase reaction), and the reduction of PGG<sub>2</sub> to prostaglandin H<sub>2</sub> (PGH<sub>2</sub>; the peroxidase reaction) by the addition of molecular oxygen at carbon 15 [38]. PGH<sub>2</sub> is subsequently converted to biological active eicosanoids such as prostaglandin E<sub>2</sub> (PGE<sub>2</sub>) by the synthase enzymes [37]. There are two isoforms of the COX enzyme, COX-1 and COX-2. Both isoforms are membrane glycoproteins located in the membranes of the nucleus and endoplasmic reticulum. Both COX-1 and COX-2 have similar molecular weights (70 and 72 kDa respectively), tertiary structures, and perform the same catalytic reactions [37] [39].

The COX activity assay kit (ab204699, abcam, Melbourne) measures the peroxidase activity of the COX enzyme; the addition of 10-acetyl-3,7-dihydroxyphenoxazine (ADHP) is oxidised by the COX peroxidase to generate resorufin, a highly fluorescein compound [38]. The fluorescent intensity of resorufin is analysed by a microplate reader set at 530/585 nm (Ex/Em) wavelength (Figure 2.13) [38].

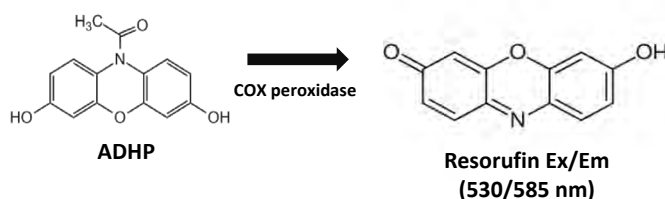


**Figure 2.13:** The molecule 10-acetyl-3,7-dihydroxyphenoxazine (ADHP) is oxidised by COX peroxidase to the fluorescent molecule resorufin.

The following method was used to prepare samples from a confluent 24 well plate:

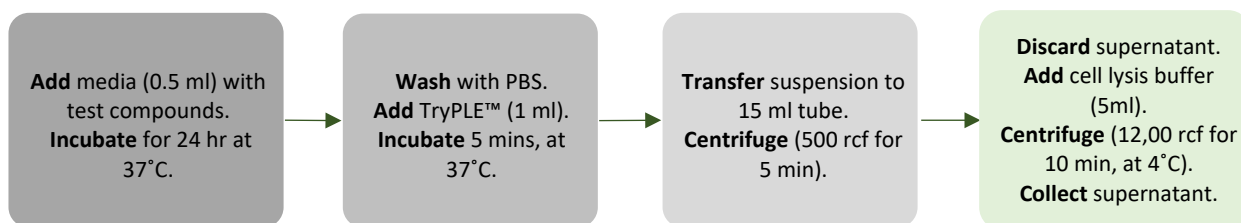


**Figure 2.14:** Method for collecting samples for COX enzyme analysis

The following method was used to analyse levels of COX enzyme activity:

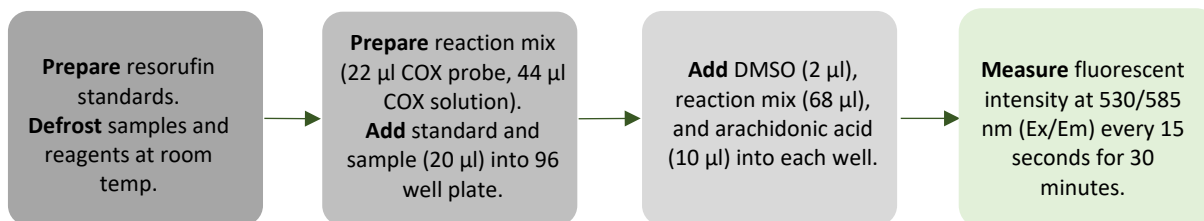


**Figure 2.15:** Preparation of standards and samples for COX enzyme analysis

### 2.7.7 Prostaglandin E<sub>2</sub> Assay

The PGE<sub>2</sub> ELISA (enzyme-linked immunosorbent assay) kit (ab136948, abcam, Melbourne) was used to quantify levels of PGE<sub>2</sub> in the cell culture media from test samples. This method follows the basic principles of ELISA, where a monoclonal PGE<sub>2</sub> antibody binds in a competitive manner to PGE<sub>2</sub> present in the cell culture media, or to a PGE<sub>2</sub> covalently linked with an alkaline phosphatase molecule [40, 41]. The monoclonal antibody then binds to a goat anti-mouse IgG antibody (capture antibody) pre-coated onto 96 well plate. Excess reagents are washed away, and a chemiluminescent (Lumiphos 530™ CLIA substrate) substrate is added that reacts with the bound PGE<sub>2</sub>-alkaline phosphatase conjugate to produce light emission at 530 nm. The intensity of the emitted light is inversely proportional to the concentration of PGE<sub>2</sub> in the samples.

The following method was used to prepare samples from a confluent 24 well plate:

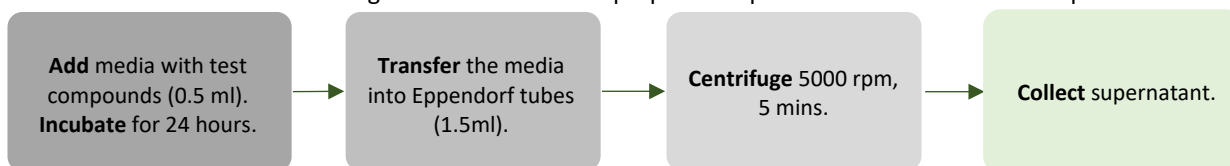


**Figure 2.16:** Method for collecting samples for PGE<sub>2</sub> analysis

The following method as recommended by the supplier was used to analyse PGE<sub>2</sub> levels:

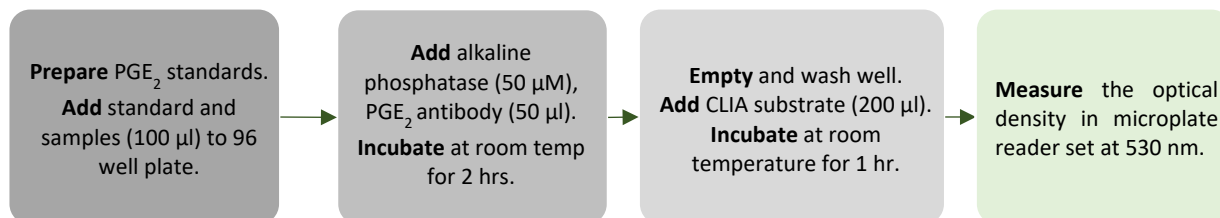


**Figure 2.17:** Preparation of samples and standards for PGE<sub>2</sub> analysis

## 2.8 *In vitro* BBB model

A transwell® cell culture plate (Corning® Transwell® Polyester membrane cell culture inserts, 24 well, 6.5 mm Transwell® with 0.4 µm pore polyester membrane insert, Sigma, Australia) was used to establish an *in vitro* BBB model consisting of a monolayer of human brain endothelial cells seeded on the membrane of the transwell® insert (Figure 2.18). When cells on the transwell® membrane were approximately 90 % confluency (~ 5-6 days post seeding), test samples can be introduced in the upper compartment of the insert, and the integrity of the BBB can be investigated by measuring transendothelial electrical resistance (TEER) or permeability to tracer compounds [42-

44]. Initial experiments were conducted to develop a neuroinflammatory model of the BBB using LPS as the pro-inflammatory stimulus. Subsequent studies were conducted to investigate the effectiveness of the test compounds with antioxidant and/or anti-inflammatory properties in maintaining the integrity of the BBB.

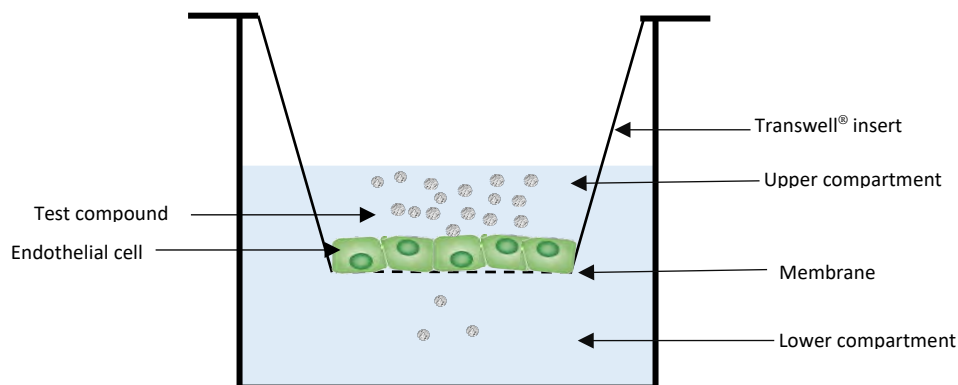


**Figure 2.18:** The *in vitro* model of the blood brain barrier. Brain endothelial cells were grown on the membrane of the transwell® insert. Cell culture media was added to the upper and lower compartment of the transwell® insert.

The following method was used to prepare the *in vitro* BBB model following protocols reported previously with slight modifications [45, 46]:

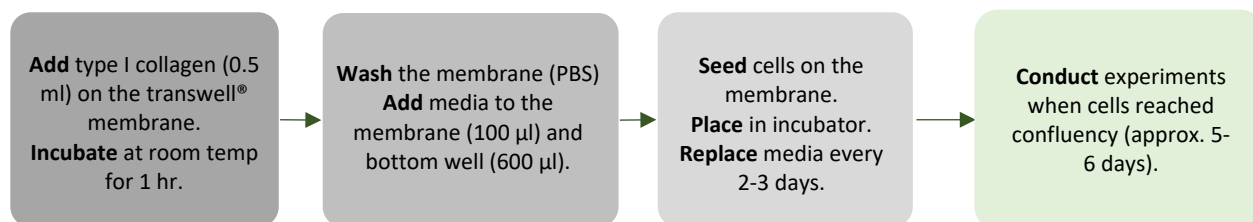


**Figure 2.19:** method for the development of the *in vitro* BBB model.

## 2.9 BBB permeability studies

### 2.9.1 Transendothelial electrical resistance (TEER)

In this thesis, the integrity of the BBB was measured by two methods: 1) Measure of the TEER across the BBB, and 2) the permeability of the BBB to tracer compounds. The key difference between the two methods is TEER is a measure of the integrity of tight junctions by ionic conductance, whereas the permeability coefficient calculated from the flux of tracer compounds across the BBB is an indication of the pore size of the tight junction [47, 48].

The Millicell® ERS-2 voltohmmeter (Merck Millipore, Bayswater, Australia) was used to measure the TEER of the *in vitro* BBB. In a typical experiment, one electrode is placed in the upper and lower compartment of the transwell® insert (Figure 2.20). The pair of electrodes are 4 mm wide by 1 mm in thickness, and contains a silver/silver chloride pellet for the measurement of voltage. Resistance in ohms ( $\Omega$ ) is calculated based on the ratio of the applied alternating current (AC) and the measured current, as per Ohm's law [49].

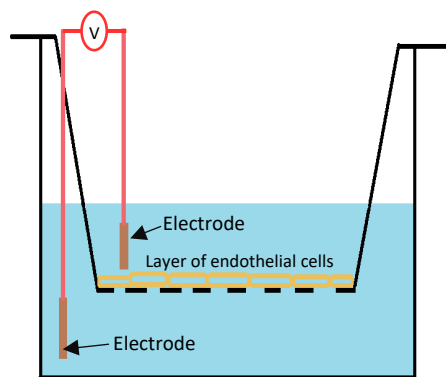


**Figure 2.20:** Representation of the TEER apparatus to measure the permeability of the *in vitro* BBB. Voltage is applied across the two electrodes, and the resistance is calculated based on the applied voltage and the measured current. TEER values are recorded in ohms ( $\Omega$ ).

The TEER measurements were conducted to measure the effect of LPS on the integrity of the BBB. This was followed by TEER measurements of the test compounds added together with LPS in the BBB model. The test compounds used in this thesis were indomethacin, ascorbic acid, and probucol with or without loading in mesoporous silica at 1, 10, 50, and 100  $\mu$ M of the active ingredient.

The TEER measurements were taken at time points of 2, 4, 6, and 24 hours for each sample. After 24 hours, permeability of the BBB to tracer compounds were performed.

The following method for taking TEER measurements was used on a confluent transwell® plate:

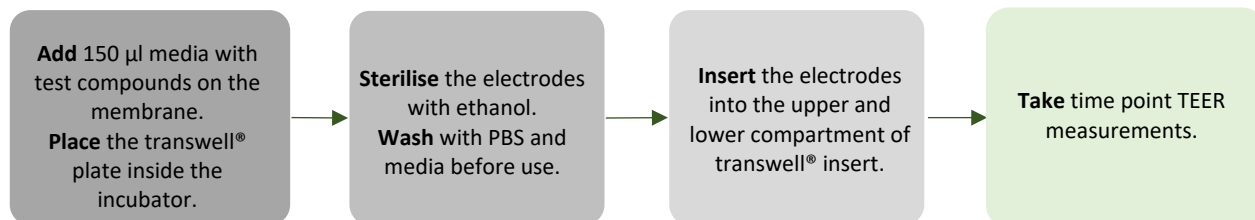


**Figure 2.21:** Taking TEER measurements on a transwell® plate.

## 2.9.2 Method for calculating TEER for test compounds

The following method was used to calculate the TEER of each test compound used in the *in vitro* BBB permeability studies. A TEER reading across the transwell® membrane without cells was measured ( $R_{\text{blank membrane}}$ ), and a TEER measurement across the transwell® membrane with cells was taken ( $R_{\text{total}}$ ). The sample specific resistance ( $R_{\text{sample}}$ ) in ohms, is calculated as:

$$R_{\text{sample}} = R_{\text{total}} - R_{\text{blank membrane}} \quad (2.6)$$

This  $R_{\text{sample}}$  value is multiplied by the effective surface area ( $M_{\text{area}}$ ) of the transwell® membrane [42] [50] ( $6.5 \text{ cm}^2$  is the surface area of the transwell® membrane used in this thesis):

$$\text{TEER}_{\text{sample}} = R_{\text{sample}} (\text{ohms}) \times M_{\text{area}} (\text{cm}^2) \quad (2.7)$$

The  $\text{TEER}_{\text{sample}}$  value for each sample is reported in  $\Omega \cdot \text{cm}^2$ .

## 2.9.3 Permeability of the BBB to tracer compounds

FITC-dextrans are polysaccharides varying in lengths of branched glucose molecules, and are commercially available in molecular weights from 4 – 70 kD (Figure 2.22). Advantages of FITC dextrans compared to other tracer compounds are: it is an inert compound that does not affect cellular function, are non-reactive with serum proteins, and are retained within cells of the BBB under normal conditions [51].

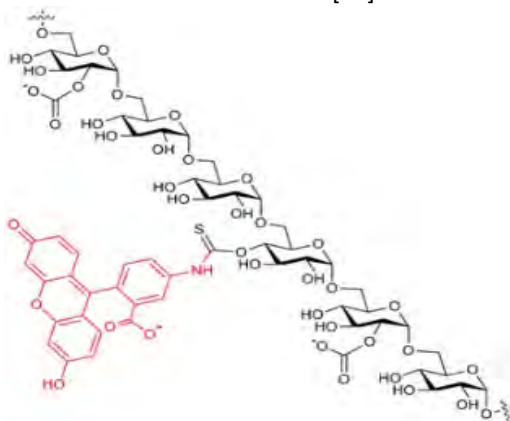


**Figure 2.22:** FITC labelled dextran molecule. FITC molecule is represented in red.

In this thesis, FITC dextran of two sizes, a smaller 3-5 kDa, and a larger 59-77 kDa was used to determine the effect of LPS with or without test compounds on the integrity of the BBB. The smaller FITC dextran size is representative of small molecules and electrolytes, while the larger FITC dextran is the typical size of larger biomolecules including proteins, such as albumin which has a molecular weight of 66.5 kDa [52, 53].

The following method was used to conduct permeability measurements following the protocol reported previously

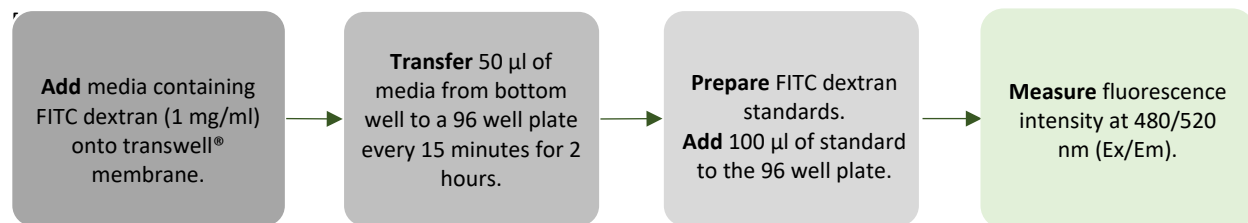


**Figure 2.23:** Method for taking permeability measurements of FITC dextran.

#### 2.9.4 Method for calculating the permeability coefficient ( $P_e$ )

Permeability coefficients take into account the difference in the permeability of FITC dextran across the transwell® membrane with and without cells. The concentration of the FITC dextran added to the top (abluminal) of the transwell® membrane and collected from the bottom (luminal) well of the transwell® plate was calculated for each time point based on the standard calibration curve of FITC dextran. The cleared volume across the transwell® membrane was calculated for each time point using the following equation [55]:

$$\text{Cleared volume } (\mu\text{L}) = \text{FITC concentration}_{\text{abluminal}} \times \text{Volume}_{\text{abluminal}} / \text{FITC Concentration}_{\text{luminal}} \quad (2.8)$$

The average cleared volumes were plotted versus time in minutes for each sample. Clearance slopes for the empty transwell® membrane ( $PS_{\text{insert}}$ ) and the transwell® membrane with endothelial cells following treatment with LPS and the test compounds ( $PS_{\text{test+cells+insert}}$ ) were calculated using linear regression analysis, and used to obtain the permeability product of the test compound ( $PS_{\text{test+cells}}$ ) [55]:

$$1/PS_{\text{test+cells}} = 1/PS_{\text{test+cells+insert}} - 1/PS_{\text{insert}} \quad (2.9)$$

Permeability coefficients ( $P_e$ ) for each test compound was derived by dividing the  $PS_{\text{test+cells}}$  value by the surface area of the cell culture insert. Data are presented with units of  $\times 10^{-6} \text{ cm/sec}$ .

#### 2.10 Cellular uptake of PB studies

##### 2.10.1 Preparation of endothelial cells for cellular uptake studies

Cellular uptake of PB released from AMS-6 compared to crystalline PB were conducted to relate differences in the pharmacological properties of the drug compound with the intracellular drug concentration as determined by



high performance liquid chromatography (HPLC). This was conducted in an *in vitro* experiment with endothelial cells grown on 24 well plate.

The following method was used to prepare samples for the analysis of PB cellular uptake using a confluent 24 well plate:

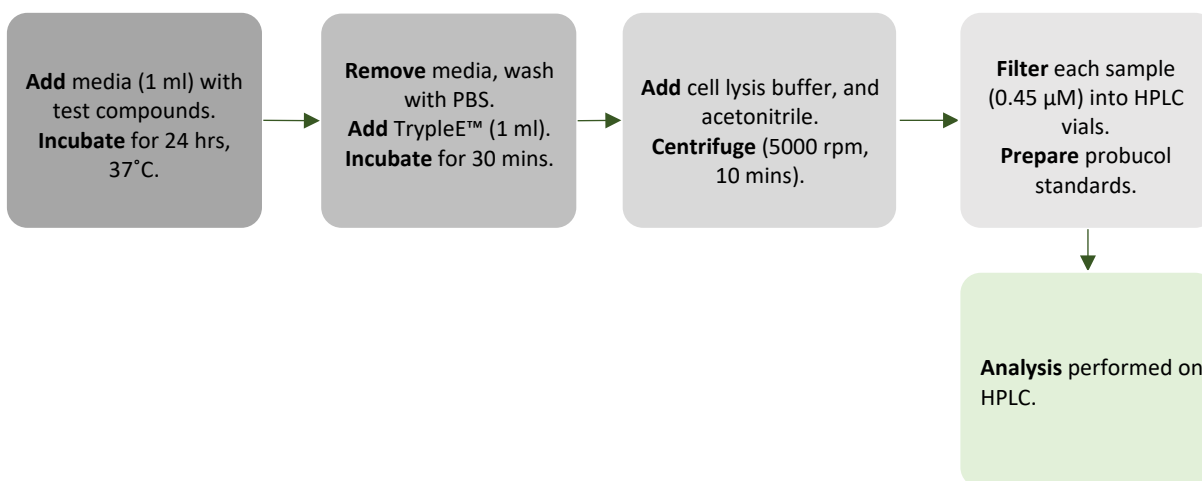


**Figure 2.24:** Method for the *in vitro* cellular uptake of PB experiments.

### 2.10.2 High performance liquid chromatography

The HPLC was used in this thesis for the detection, and quantification of PB in samples from *in vitro* cellular uptake studies [56]. The basic principle of the HPLC is the separation and detection of the compound of interest in a sample by a mobile and stationary phase. The mobile phase is a mixture containing Milli-Q® water with the addition of polar or non-polar organic solvents maintained at a specified flow rate through the HPLC by a high pressure pump.

The stationary phase is the HPLC column. A typical example is a C18 HPLC column packed with silica particles with long hydrocarbon chains that make it non-polar [57] [58]. If a polar solvent is used with a non-polar stationary phase, polar compounds in the sample will have a stronger attraction to the solvent and will pass through the column quicker as compared to a non-polar compound. This is known as the retention time of the compound, which is the time it takes the compound to travel through the column to the detector. The retention time can be used to separate compounds in the sample and is dependent on the solvent flow rate, the composition of the HPLC column, the composition of the solvent, and the temperature of the column [57].

The detector unit detects the compound of interest after leaving the HPLC column. This is based on the absorption of UV light at different wavelengths by the organic compound [57]. UV light is shone through the liquid, and a UV detector detects the amount of light that is absorbed, which will depend on the amount of the compound passing through the column. This will be displayed as a series of peaks on the plot of absorbance and retention time, and the area of the peak can be used to determine the concentration of the compound in the sample [59].

In this thesis, the following HPLC (Agilent Technologies Inc., Santa Clara, CA, USA) settings was used to quantify the amount of PB in samples collected from *in vitro* cellular uptake studies: The mobile phase was delivered at a flow rate of 1.0 ml/min through a C18 column (Zobrax SB-C18, 5  $\mu$ m, 4.6 x 150 mm, Agilent Technologies Inc, Santa Clara, CA, USA) at 40 °C and the detection wavelength was 241 nm. The injection volume was 1  $\mu$ l. Mobile phase consisted of acetonitrile (solvent A) and distilled water (solvent B) delivered at a gradient: Solvent A was 80% at 0 minutes, and changed from 80% to 85 % at 3 minutes, and changed from 85% to 90% at 7 minutes for a total run time of 10 minutes [60, 61]. An autosampler injection volume of 5  $\mu$ l was used for sample analysis. Analysis was carried out using Agilent Chem station software (V. A. 09. 01, Agilent Technologies Inc., Santa Clara, CA, U.S.A.). The concentrations of probucol in the samples were determined by the linear equation obtained from the standard curve ( $R^2=0.99$ ).

## 2.11 Zebrafish experiments

Zebrafish (*Danio rerio*) are tropical freshwater fish originating in the Ganges river of northern india [62]. Each male/female pair can mate and reproduce approximately 200-300 fertilised eggs per week. Unlike other animal species, zebrafish embryos are transparent and develop externally from a fertilised egg, outside of the mother (figure 2.22) [63, 64]. Embryos develop inside an outer shell, called a chorion, and hatch approximately 2 days post fertilization (dpf). The chorion can be dechorinated for experimental work at any time post fertilisation. By day 5-6th post fertilization (dpf) zebrafish have consumed their yolk nutrients and begin free feeding [65]. Zebrafish is a useful *in vivo* model to study basic cellular biology, embryo development, and the pathogenesis of diseases [66, 67]. In this thesis, an established *in vivo* model of oxidative stress in zebrafish [68] was used to screen the pharmacological and toxicological profile of the test compounds. Specifically, the antioxidant properties of PB released from AMS-6 was compared to crystalline PB and ascorbic acid in embryonic zebrafish (3dpf). Experimental protocols were

approved by Macquarie University Animal Ethics Committee (Zebrafish models of neural disorders; protocol no. 2012/050; using zebrafish to understand how the central nervous system responds to neuronal stress and death caused by neurodegenerative diseases, 2015/033).

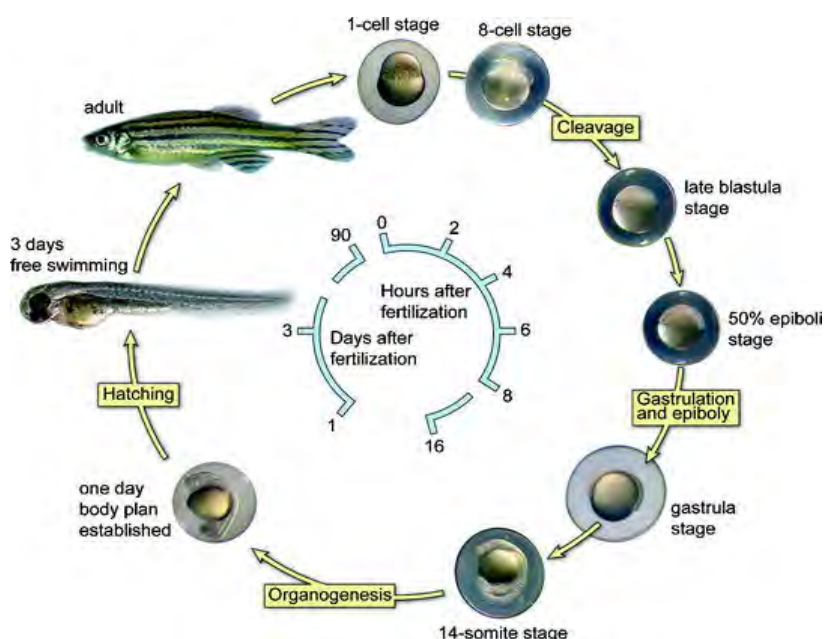


**Figure 2.25:** Embryonic zebrafish develop as a single cell from a fertilised egg (top of the cycle). The cell undergo rapid division as the embryo grows and progresses through important stages of development. Organ development begins approximately 16 hpf (hour post fertilisation), and after 24 hpf the complete body plan of the embryo and organs are developed. Larvae hatch after approximately 2 dpf. Zebrafish reach sexual maturity in around 3 months and can live up to 5 years [69].

### 2.11.1 General care

All experiments involving zebrafish were conducted at the faculty of medicine and health sciences at Macquarie University. Live zebrafish were maintained by lab technicians in a water tank heated to 28.5 °C with approximately 25 fish per tank, in distilled filtered water. Fish were fed 1-2 times per day, and water was replaced at least once a week.

Zebrafish were maintained at a controlled daily day night cycle (14 hr light/ 10 hr dark). An equal number of male and female zebrafish were maintained in the fish tank and were well fed with food such as liver paste and brine shrimp. Embryos were collected in the morning from the bottom of the fish tank and transferred to petri dish containing buffer free-E3 media (E3 media).

Embryos (25-50 per 100 ml) were maintained in E3 media in a petri dish at 28.5 °C. In this thesis, zebrafish 3 days post fertilization (3dpf) was used for the experiments.

#### 2.11.4 Screening antioxidant properties of test compounds in zebrafish model of oxidative stress

The toxicological profile and antioxidant property of AMS-6PB, crystalline PB, and ascorbic acid were tested in the zebrafish model at the following concentrations of the active ingredient: 25, 50, 100, 200 µM. ROS production in zebrafish was measured by using the DCFDA probe.

The following method was used to conduct the experiments:

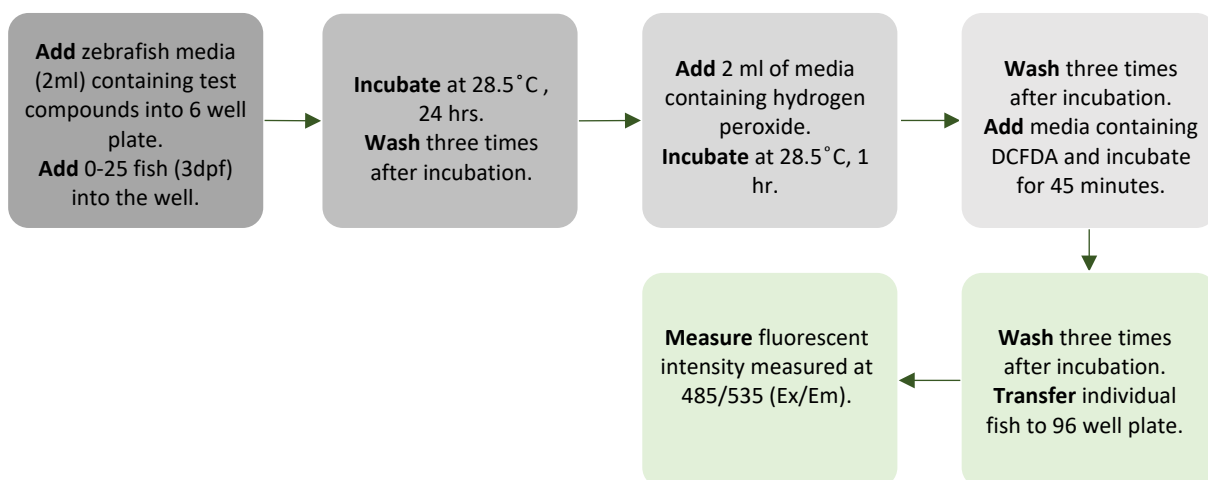


**Figure 2.26:** Method for measuring ROS in zebrafish.

## 2.12 References

1. Atluri, R., N. Hedin, and A.E.G. Bennett, *Hydrothermal phase transformation of bicontinuous cubic mesoporous material AMS-6*. Chem Mater, 2008. **20**: p. 3857-3866.
2. Grün, M., et al., *Novel pathways for the preparation of mesoporous MCM-41 materials: control of porosity and morphology*. Microporous and mesoporous materials, 1999. **27**(2-3): p. 207-216.
3. Kruk, M., et al., *Characterization of the porous structure of SBA-15*. Chemistry of materials, 2000. **12**(7): p. 1961-1968.
4. Analytics, O.P.H. *Drugbank*. 2020 07/2020]; Available from: <https://go.drugbank.com/>.
5. Stippler, E., S. Kopp, and J. Dressman, *Comparison of US Pharmacopeia simulated intestinal fluid TS (without pancreatin) and phosphate standard buffer pH 6.8, TS of the International Pharmacopoeia with respect to their use in in vitro dissolution testing*. Dissolution Technologies, 2004. **11**(2): p. 6-11.
6. Bunaciu, A.A., E.G. Udrişţoiu, and H.Y. Aboul-Enein, *X-ray diffraction: instrumentation and applications*. Critical reviews in analytical chemistry, 2015. **45**(4): p. 289-299.
7. Epp, J., *X-ray diffraction (XRD) techniques for materials characterization*, in *Materials characterization using nondestructive evaluation (NDE) methods*. 2016, Elsevier. p. 81-124.
8. Jauncey, G., *The scattering of x-rays and Bragg's law*. Proceedings of the National Academy of Sciences of the United States of America, 1924. **10**(2): p. 57.
9. Kruk, M., et al., *Characterization of highly ordered MCM-41 silicas using X-ray diffraction and nitrogen adsorption*. Langmuir, 1999. **15**(16): p. 5279-5284.
10. Kumar, D., et al., *MCM-41, MCM-48 and related mesoporous adsorbents: their synthesis and characterisation*. Colloids and Surfaces A: Physicochemical and Engineering Aspects, 2001. **187**: p. 109-116.
11. Zhao, D., et al., *Triblock copolymer syntheses of mesoporous silica with periodic 50 to 300 angstrom pores*. science, 1998. **279**(5350): p. 548-552.
12. Petkov, V., *Nanostructure by high-energy X-ray diffraction*. Materials Today, 2008. **11**(11): p. 28-38.
13. Hejral, U., et al., *High-energy x-ray diffraction from surfaces and nanoparticles*. Physical Review B, 2017. **96**(19): p. 195433.
14. Benmore, C., *A review of high-energy X-ray diffraction from glasses and liquids*. ISRN Materials Science, 2012. **2012**.
15. Chen, E.Y., et al., *Understanding and utilizing the biomolecule/nanosystems interface*, in *Nanotechnologies in Preventive and Regenerative Medicine*. 2018, Elsevier. p. 207-297.
16. Toby, B. and T. Egami, *Accuracy of pair distribution function analysis applied to crystalline and non-crystalline materials*. Acta Crystallographica Section A: Foundations of Crystallography, 1992. **48**(3): p. 336-346.
17. Petkov, V., *Pair distribution functions analysis*. Characterization of Materials, 2002: p. 1-14.
18. Petkov, V., *RAD, a program for analysis of X-ray diffraction data from amorphous materials for personal computers*. Journal of applied crystallography, 1989. **22**(4): p. 387-389.
19. Singh, A.K., *Experimental methodologies for the characterization of nanoparticles*. Engineered nanoparticles, 2016. **2**: p. 125-170.
20. Sing, K.S., *Physisorption of nitrogen by porous materials*. Journal of Porous Materials, 1995. **2**(1): p. 5-8.
21. Sing, K., *The use of nitrogen adsorption for the characterisation of porous materials*. Colloids and Surfaces A: Physicochemical and Engineering Aspects, 2001. **187**: p. 3-9.

22. Thommes, M., et al., *Physisorption of gases, with special reference to the evaluation of surface area and pore size distribution (IUPAC Technical Report)*. Pure and Applied Chemistry, 2015. **87**(9-10): p. 1051-1069.
23. Naderi, M., *Surface Area: Brunauer–Emmett–Teller (BET)*, in *Progress in filtration and separation*. 2015, Elsevier. p. 585-608.
24. Ravikovitch, P.I., G.L. Haller, and A.V. Neimark, *Density functional theory model for calculating pore size distributions: pore structure of nanoporous catalysts*. Advances in colloid and interface science, 1998. **76**: p. 203-226.
25. Höhne, G., W.F. Hemminger, and H.-J. Flammersheim, *Differential scanning calorimetry*. 2013: Springer Science & Business Media.
26. Hancock, B.C., S.L. Shamblin, and G. Zografi, *Molecular mobility of amorphous pharmaceutical solids below their glass transition temperatures*. Pharmaceutical research, 1995. **12**(6): p. 799-806.
27. Hancock, B.C. and G. Zografi, *The relationship between the glass transition temperature and the water content of amorphous pharmaceutical solids*. Pharmaceutical research, 1994. **11**(4): p. 471-477.
28. Clas, S.-D., C.R. Dalton, and B.C. Hancock, *Differential scanning calorimetry: applications in drug development*. Pharmaceutical science & technology today, 1999. **2**(8): p. 311-320.
29. Vitez, I., *Utilization of DSC for pharmaceutical crystal form quantitation*. Journal of thermal analysis and calorimetry, 2004. **78**(1): p. 33-45.
30. Millipore, E., *Precise and accurate counts and viability measurements across multiple cell lines using the Muse™ cell count & viability assay*. BioTechniques, 2012. **52**(3): p. 200-203.
31. Peshavariya, H.M., G.J. Dusting, and S. Selemidis, *Analysis of dihydroethidium fluorescence for the detection of intracellular and extracellular superoxide produced by NADPH oxidase*. Free radical research, 2007. **41**(6): p. 699-712.
32. Chen, X., et al., *2', 7'-Dichlorodihydrofluorescein as a fluorescent probe for reactive oxygen species measurement: forty years of application and controversy*. Free radical research, 2010. **44**(6): p. 587-604.
33. Tsikas, D., *Review Methods of quantitative analysis of the nitric oxide metabolites nitrite and nitrate in human biological fluids*. Free radical research, 2005. **39**(8): p. 797-815.
34. Yoshida, K., et al., *Biotransformation of nitric oxide, nitrite and nitrate*. International archives of occupational and environmental health, 1983. **52**(2): p. 103-115.
35. Bryan, N.S. and M.B. Grisham, *Methods to detect nitric oxide and its metabolites in biological samples*. Free Radical Biology and Medicine, 2007. **43**(5): p. 645-657.
36. Grisham, M.B., G.G. Johnson, and J.R. Lancaster Jr, *Quantitation of nitrate and nitrite in extracellular fluids*, in *Methods in enzymology*. 1996, Elsevier. p. 237-246.
37. Blobaum, A.L. and L.J. Marnett, *Structural and functional basis of cyclooxygenase inhibition*. Journal of medicinal chemistry, 2007. **50**(7): p. 1425-1441.
38. Petrovic, N. and M. Murray, *Using N, N, N', N'-tetramethyl-p-phenylenediamine (TMPD) to assay cyclooxygenase activity in vitro*, in *Advanced Protocols in Oxidative Stress II*. 2010, Springer. p. 129-140.
39. Vane, J., Y. Bakhle, and R. Botting, *CYCLOOXYGENASES 1 AND 2*. Annual review of pharmacology and toxicology, 1998. **38**(1): p. 97-120.
40. Lequin, R.M., *Enzyme immunoassay (EIA)/enzyme-linked immunosorbent assay (ELISA)*. Clinical chemistry, 2005. **51**(12): p. 2415-2418.
41. Avrameas, S. and R.M. Lequin, *Historical Background of the Invention of EIA and ELISA/The author of the article cited above responds*. Clinical chemistry, 2006. **52**(7): p. 1430.
42. Srinivasan, B., et al., *TEER measurement techniques for in vitro barrier model systems*. Journal of laboratory automation, 2015. **20**(2): p. 107-126.

43. Naik, P. and L. Cucullo, *In vitro blood–brain barrier models: current and perspective technologies*. Journal of pharmaceutical sciences, 2012. **101**(4): p. 1337-1354.
44. Nozohouri, S., et al., *Estimating Brain Permeability Using In Vitro Blood-Brain Barrier Models*. 2020.
45. Monaghan-Benson, E. and E.S. Wittchen, *In vitro analyses of endothelial cell permeability*, in *Permeability Barrier*. 2011, Springer. p. 281-290.
46. Poller, B., et al., *The human brain endothelial cell line hCMEC/D3 as a human blood-brain barrier model for drug transport studies*. Journal of neurochemistry, 2008. **107**(5): p. 1358-1368.
47. Yeste, J., et al., *Engineering and monitoring cellular barrier models*. Journal of biological engineering, 2018. **12**(1): p. 1-19.
48. Wegener, J. and J. Seebach, *Experimental tools to monitor the dynamics of endothelial barrier function: a survey of in vitro approaches*. Cell and tissue research, 2014. **355**(3): p. 485-514.
49. Srinivasan, B. and A.R. Kolli, *Transepithelial/Transendothelial Electrical Resistance (TEER) to Measure the Integrity of Blood-Brain Barrier*, in *Blood-Brain Barrier*. 2019, Springer. p. 99-114.
50. Wang, Y. and J.S. Alexander, *Analysis of endothelial barrier function in vitro*, in *Permeability Barrier*. 2011, Springer. p. 253-264.
51. Lampugnani, M.G. and E. Dejana, *Endothelial Cell Permeability Assays in Culture*, in *Methods in Endothelial Cell Biology*. 2004, Springer. p. 103-113.
52. Mayhan, W.G. and D.D. Heistad, *Permeability of blood-brain barrier to various sized molecules*. American Journal of Physiology-Heart and Circulatory Physiology, 1985. **248**(5): p. H712-H718.
53. Ziylan, Y.Z., P.J. Robinson, and S.I. Rapoport, *Blood-brain barrier permeability to sucrose and dextran after osmotic opening*. American Journal of Physiology-Regulatory, Integrative and Comparative Physiology, 1984. **247**(4): p. R634-R638.
54. Deli, M.A., et al., *Permeability studies on in vitro blood–brain barrier models: physiology, pathology, and pharmacology*. Cellular and molecular neurobiology, 2005. **25**(1): p. 59-127.
55. Watson, P.M.D., et al., *Modelling the endothelial blood-CNS barriers: a method for the production of robust in vitro models of the rat blood-brain barrier and blood-spinal cord barrier*. BMC neuroscience, 2013. **14**(1): p. 1-21.
56. Thammana, M., *A review on high performance liquid chromatography (HPLC)*. Res Rev J Pharm Anal RRJPA, 2016. **5**(2): p. 22-28.
57. Bhardwaj, S.K., K. Dwivedia, and D. Agarwala, *A review: HPLC method development and validation*. International Journal of Analytical and Bioanalytical Chemistry, 2015. **5**(4): p. 76-81.
58. Neue, U.D. and M.Z. El Fallah, *HPLC columns: theory, technology, and practice*. Vol. 415. 1997: Wiley-Vch New York.
59. Bélanger, J.M., J.J. Paré, and M. Sigouin, *High performance liquid chromatography (HPLC): principles and applications*, in *Techniques and Instrumentation in Analytical Chemistry*. 1997, Elsevier. p. 37-59.
60. Nourooz-Zadeh, J., et al., *Measurement of plasma probucol levels by high-performance liquid chromatography*. Journal of Chromatography B: Biomedical Sciences and Applications, 1994. **654**(1): p. 55-60.
61. Moorianian, A., et al., *The biological effects of the hypolipidaemic drug probucol microcapsules fed daily for 4 weeks, to an insulin-resistant mouse model: potential hypoglycaemic and anti-inflammatory effects*. Drug delivery and translational research, 2018. **8**(3): p. 543-551.
62. Tavares, B. and S.S. Lopes, *The importance of Zebrafish in biomedical research*. Acta medica portuguesa, 2013. **26**(5): p. 583-592.
63. Kimmel, C.B., et al., *Stages of embryonic development of the zebrafish*. Developmental dynamics, 1995. **203**(3): p. 253-310.

64. D'Costa, A. and I.T. Shepherd, *Zebrafish development and genetics: introducing undergraduates to developmental biology and genetics in a large introductory laboratory class*. Zebrafish, 2009. **6**(2): p. 169-177.
65. Westerfield, M., *The Zebrafish Book: A Guide for the Laboratory Use of Zebrafish Danio ("Brachydanio Rerio")*. 2007: University of Oregon.
66. Teame, T., et al., *The use of zebrafish (Danio rerio) as biomedical models*. Animal Frontiers, 2019. **9**(3): p. 68-77.
67. Lieschke, G.J. and P.D. Currie, *Animal models of human disease: zebrafish swim into view*. Nature Reviews Genetics, 2007. **8**(5): p. 353-367.
68. Formella, I., et al., *Real-time visualization of oxidative stress-mediated neurodegeneration of individual spinal motor neurons in vivo*. Redox biology, 2018. **19**: p. 226-234.
69. Willemsen, R., et al., *Zebrafish (Danio rerio) as a model organism for dementia*, in *Animal Models of Dementia*. 2011, Springer. p. 255-269.



# 3

## Using pair distribution function analysis to probe the local atomic order of drug compounds loaded within mesoporous silica.

### 3.1 Introduction

The aqueous solubility of drug compounds is a key parameter in determining the bioavailability of orally administered drugs. Advances in the fields of drug design and high throughput screening has led to the discovery of new drug compounds that whilst potent, are highly hydrophobic, and low in solubility [1, 2]. Furthermore, the discovery of new molecular targets with lipophilic ligands translates to the increasing need of drug molecules that have a high degree of lipophilicity [3]. It is estimated that poorly soluble compounds account for 90 % of new chemical entities, 75 % of compounds under development and 40 % of the top 200 oral drugs available in the USA and Europe (Figure 3.1) [4, 5].

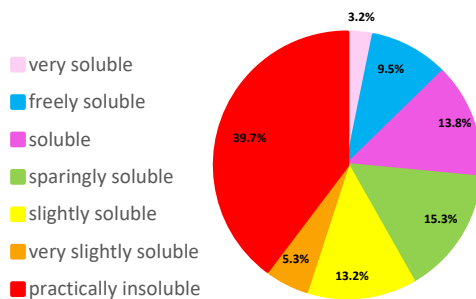


**Figure 3.1:** Solubility of the top 200 oral drugs marketed in the US and Europe. Figure modified from [5].

An enhancement in solubility can be achieved by the preparation of poorly soluble drug compounds in their amorphous form [6]. This include the preparation of the drug in the amorphous form as solid dispersions with polymers by techniques such as co-milling, spray drying, and hot melt extrusion [7, 8]. Drugs loaded within MSPs can stabilise the amorphous form of a wide range of poorly soluble drug compounds [9, 10]. The thermodynamic

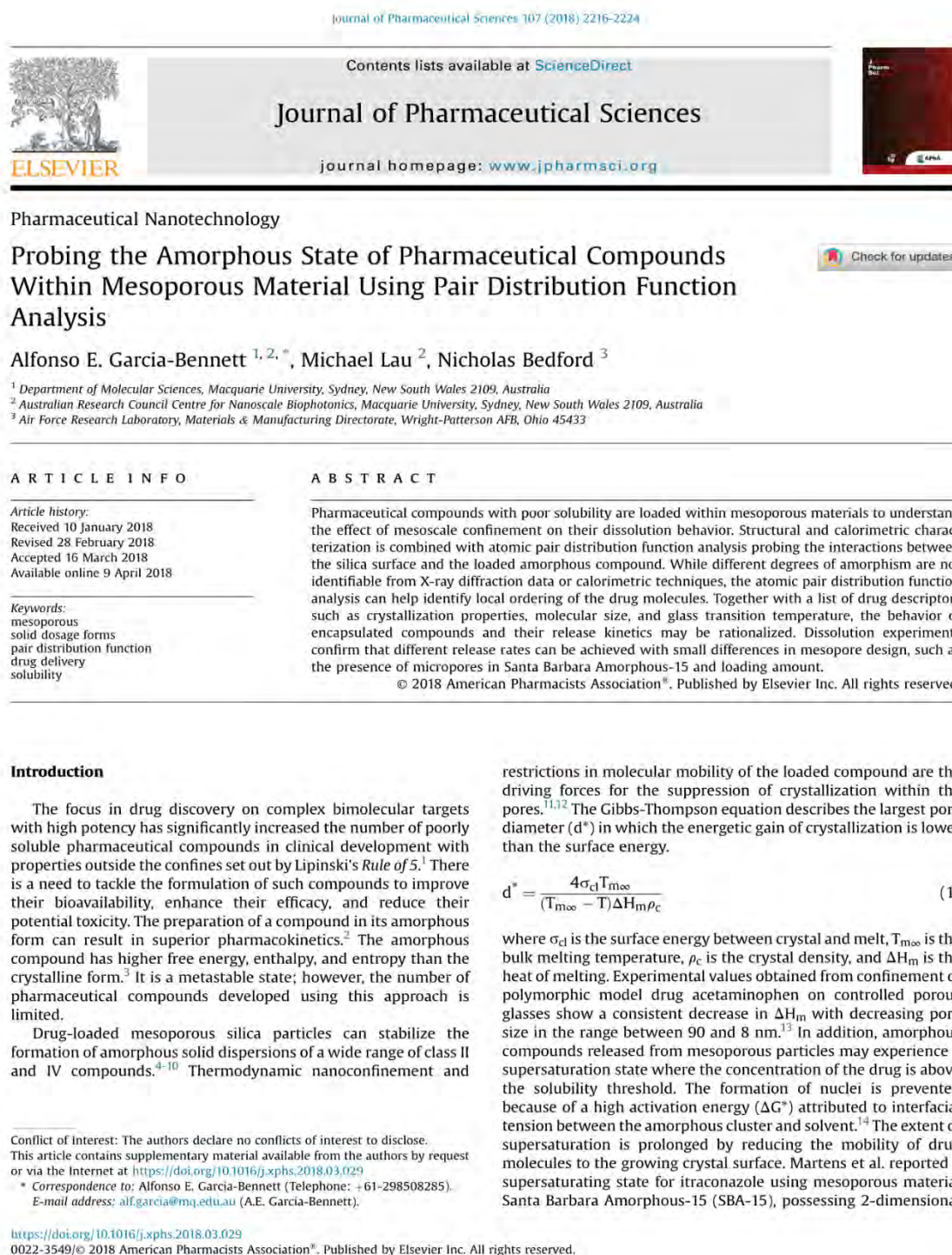
nanoconfinement, and restrictions in molecular mobility of the loaded drug compound are the key driving forces for the suppression of crystallisation within the mesopores. However, characterisation of the amorphous drug loaded within mesopores is difficult, with the amorphous content generally being inferred from the degree of crystallinity (or lack of) based on XRD and DSC analysis of the drug loaded materials [11, 12]. Therefore, characterisation techniques that can provide information on discrete changes in the molecular ordering of amorphous materials, and how such changes affect the solubility of the drug compound are needed, irrespective of the technique used to create the amorphous form of the drug.

The aim of this work is to probe the local atomic ordering of an amorphous drug loaded within mesoporous silica using pair distribution function analysis (PDF). The PDF takes into account both diffracted and diffuse scattering from HE-XRD scattering data, providing information on the local atomic ordering of the amorphous form. A range of mesoporous materials MCM-41 (2d-hexagonal), MCM-48 (3d-cubic) and SBA-15 with different textural properties were chosen to load the drug compounds albendazole, indomethacin, and hydrocortisone at different loadings (wt%), and the drug loaded materials were characterised using XRD, DSC, and HE-XRD. *In vitro* dissolution experiments were conducted to compare the release profiles of the drugs, in order to relate how subtle changes in local atomic ordering of the amorphous form affected the drug release kinetics from mesoporous silica.

### 3.2 Author contribution

Name	Conception of the study	Design experiment and methodology	Data collection	Data analysis and interpretation	Drafting and writing the manuscript
<b>Alfonso E. Garcia-Bennett</b>	√	√	√	√	√
<b>Michael Lau</b>	√	√	√	√	√
<b>Nicholas Bedford</b>		√	√	√	

### 3.3 Full paper



Garcia-Bennett, A., Lau, M., & Bedford, N. (2018). Probing the amorphous state of pharmaceutical compounds within mesoporous material using pair distribution function analysis. *Journal of Pharmaceutical Sciences*, 107(8), 2216–2224. <https://doi.org/10.1016/j.xphs.2018.03.029>



(2d) cylindrical 7.9-nm pores, with 80% release of the drug within a 5-min period for drug loadings of 32.1 wt%.<sup>15</sup> A similar SBA-15 material was used to create a supersaturation state for the anti-cancer agent dasatinib, which is prone to rapid crystallization and possesses a polymorph-dependent solubility.<sup>16,17</sup>

Characterization of the amorphous state inside mesopores is challenging because of the lack of long-range order needed to satisfy the Bragg condition in traditional powder diffraction. In this work, we use atomic pair distribution function analysis (PDF)<sup>18</sup> to study the local structure of amorphous phases. The PDF is a sine Fourier transform of the total scattering structure function,  $S(Q)$ . It results in the number of atoms in a spherical shell at a distance  $r$  from the reference atom, where  $Q$  is the magnitude of the scattering vector. Both diffracted and diffuse scattering are taken into account, allowing to probe signals from crystalline and disordered domains of the sample. As such, atomic PDF analysis is ideal to assess structure and function relationships of materials with limited long-range order. For example, the approach was recently shown to distinguish the degree of disorder of hydrate and anhydrate drug forms.<sup>19</sup>

In this work, mesoporous materials MCM-41 (2d-hexagonal),<sup>20</sup> MCM-48 (3d-cubic), and SBA-15<sup>21</sup> were loaded at different concentrations with pharmaceutical compounds such as albendazole (ABZ), indomethacin (INDO), and hydrocortisone (HYD). These were selected for their low solubility and ability to form amorphous phases or so called glass formers.<sup>22</sup>

The glass transition temperature,  $T_g$ , is indicative of molecular mobility and has an influence in drug nucleation and growth (Table 1). Good glass formers, with higher  $T_m/T_g$  ratio readily form stable amorphous phases and should thus be suitable for encapsulation within mesoporous silica. The aim of this work is to characterize different molecular ordering of the encapsulated compounds using advanced X-ray diffraction analysis in combination with differential scanning calorimetry (DSC). The novel use of PDF may identify different types of amorphism that can be used to better understand drug release kinetics from porous excipients.

## Materials and Methods

### Synthesis of Mesoporous Materials

All chemicals, including pharmaceutical drug compounds, were purchased from Sigma-Aldrich (Sydney, Australia) unless stated and used as received without further purification. The *Synthesis of Mesoporous Material SBA-15* has already been described and is based on the self-assembly of the polymeric surfactant P123 ( $\text{EO}_{20}\text{PO}_{70}\text{EO}_{20}$ ,  $M_{av} = 5800$ ) in aqueous acidic conditions.<sup>16</sup> In a typical synthesis, tetraethyl orthosilicate (8.19 g) was added to a mixture of P123 (4.0 g), HCl (8.0 g, 35 wt%), and deionized water (100 mL) at 40°C. After the mixture was stirred for 24 h, the mesostructured product was cured at 100°C for an additional 48 h. The product

was filtered without washing and dried at ambient temperature. The surfactant was removed by exhaustive solid–liquid extraction using an HCl (35%)/ethanol solution (ratio 2:8) at 70°C for 24 h before calcination to remove any remaining surfactant and at 550°C (1 h in flowing air) to give the final porous material. The *Synthesis of Mesoporous Material MCM-41* has been reported previously.<sup>23</sup> In this preparation, cetyltrimethylammonium bromide (CTAB, 9.4 g) was dissolved in 65 g of deionized water under stirring before the addition of trimethyl ammonium hydroxide (7.0 g). The resulting gel with molar ratio is  $1\text{SiO}_2: 0.27\text{CTAB}: 0.19\text{trimethyl ammonium hydroxide}: 40\text{H}_2\text{O}$ , was heated in a sealed stainless steel autoclave at 100°C for hydrothermal treatment for 24 h. The product was recovered by filtration, washed thoroughly with distilled water, and then dried in air. The surfactant was removed by calcination as described previously. The *Synthesis of Mesoporous Material MCM-48* has been reported previously.<sup>21</sup> In this case, sodium silicate is used as the silica source, CTAB as the surfactant, and ethanol as a structure-directing additive. Briefly, distilled water and surfactant are stirred at room temperature for 1 h followed by addition of ethanol. After 30 min of further stirring at room temperature, the desired amount of sodium silicate is added, and hydrothermal treatment is conducted in a Teflon autoclave at 100°C for 4 days. The synthesis gel had a molar ratio of  $1\text{SiO}_2: 0.25\text{Na}_2\text{O}: 0.65\text{C}_{16}\text{TMABr}: 5\text{CH}_3\text{CH}_2\text{OH}: 100\text{H}_2\text{O}$ . The filtered product was dried in air and calcined as described previously.

### Characterization Equipment and Protocols

#### Material Characterization

Scanning electron microscopy images were obtained using a JSM-7401F scanning electron microscope (JEOL Ltd., Tokyo, Japan) operating at 1–2 kV with no gold coating. Transmission electron microscopy of calcined and extracted samples was conducted with a JEOL 3000F microscope (JEOL Ltd.) operating at 300 kV (spherical aberration: 0.6 mm; resolution: 1.7 Å). Images were recorded using a Gatan SC1000 11-megapixel charge coupled device camera model, at 30,000–100,000 $\times$  magnification using low-dose conditions on calcined and drug-loaded samples. Nitrogen adsorption isotherms were measured at liquid nitrogen temperature ( $-196^\circ\text{C}$ ) using a Micromeritics TriStar II volumetric adsorption analyser (Micromeritics Instrument Corporation, Norcross, GA). Before the measurements, the samples were outgassed for 3 h at 200°C. The Brunauer–Emmett–Teller (BET) equation was used to calculate the surface area from the adsorption data obtained in the relative pressure ( $P/P_0$ ) range of 0.05 and 0.3. The total pore volume was calculated from the amount of gas adsorbed at  $P/P_0 = 0.95$ . Pore size distribution (PSD) curves were derived using the density functional theory method, assuming a cylindrical pore model for all samples. Values from the  $t$ -plot analysis are obtained at a thickness range from 3 to 5 Å. A thermogravimetric analysis instrument (TGA-2050; TA Instruments, New Castle, DE) was used to determine the loading amount. Analysis was conducted at a heating rate of  $20^\circ\text{C min}^{-1}$  from 20°C to 800°C in air. The sample weights varied from 5 to 10 mg. The derivative weight loss calculation was performed using TA instruments software (Universal analysis 2000, version 3.0 G; TA Instruments). The amount of drug loaded was derived from the weight lost between 120°C and 650°C. Thermal analysis was conducted using a DSC instrument (DSC-2010; TA instruments, DE) at a heating rate of  $10^\circ\text{C min}^{-1}$  from 20°C to 350°C in a nitrogen atmosphere using aluminum-crimped pans. The sample weight varied from 5 to 10 mg. Analysis was performed using TA Instruments software (Universal analysis 2000, version 3.0 G; TA Instruments).

High-energy X-ray diffraction (HE-XRD) experiments were performed at 11-ID-C of the Advanced Photon Source, Argonne National Laboratory. Samples were loaded into ~1-mm OD Kapton capillaries for diffraction measurements, which were performed at

**Table 1**

Chemical Properties of Compounds ABZ, INDO, and HYD, Including the Molecular Weight (Mw), Pol.SA, the Logarithmic Partition Concentration (ClogP), and the Glass Transition and Melting Temperatures,  $T_g$  and  $T_m$ , Respectively

Compound	Mw, g/mol	Pol.SA ( $\text{\AA}^{23}$ )	ClogP <sup>b</sup>	$T_g$ ( $^\circ\text{C}$ ) <sup>c</sup>	$T_m$ ( $^\circ\text{C}$ ) <sup>c</sup>	$T_m/T_g$
ABZ	265.3	67.01	3.1	60	202	3.36
INDO	357.8	68.53	4.2	44	159	3.61
HYD	362.4	94.83	1.2	86	211	2.45

The  $T_m/T_g$  ratio is additionally included.

<sup>a</sup> Values obtained from DrugBank.<sup>22</sup>

<sup>b</sup> Values obtained from reference.<sup>27</sup>

<sup>c</sup> Values from the Merck Index.<sup>30</sup>

**Table 2**

Physical Characterization of Calcined and Drug-Loaded Mesoporous MCM-41, MCM-48, and SBA-15 Particles, Including Unit Cell Parameters, BET Surface Area ( $S_{\text{BET}}$ ), Microporous Surface Area as Derived From t-Plot Analysis ( $t_{\text{microp}}$ ), the Total Pore Volume ( $T_{\text{vol}}$ ), the PSD, the Drug Loading Amount, and the Drug Decomposition Temperature From TGA (DT)

Material	$^a$ Unit Cell, Å	$^b$ $S_{\text{BET}}$ , m <sup>2</sup> /g	$^c$ $t_{\text{microp}}$ , m <sup>2</sup> /g	$^d$ $T_{\text{vol}}$ , cm <sup>3</sup> /g	$^e$ PSD (Å)	Load (%wt)	$^f$ DT (°C)
SBA-15	120.8	871.1	280.8	1.00	118.0	—	192.2 <sup>a</sup>
MCM-48	98.6	1117.4	—	1.10	36.5	—	173.5
MCM-41	42.8	922.6	—	0.61	42.6	—	172.9
ABZ							
SBA-15 ABZ	120.9	551.5	201.3	0.66	117.8	18.3	173.5
	120.9	404.8	—	0.53	117.8	29.8	172.9
	120.9	229.0	—	0.33	117.8	50.4	181.3
MCM-48 ABZ	97.3	936.5	—	0.90	41.6	13.5	171.5
	97.3	821.3	—	0.80	41.6	26.4	174.0
	97.3	741.8	—	0.71	40.9	29.2	175.4
MCM-41 ABZ	43.6	731.7	—	0.49	36.0	12.0	172.2
	43.6	638.4	—	0.41	35.9	15.9	174.1
	43.6	516.2	—	0.32	35.9	32.4	173.4
HYD							420.7 <sup>d</sup>
SBA-15 HYD	120.1	421.4	84.6	0.57	101.0	7.3	377.9
	119.8	366.7	56.4	0.54	101.3	24.5	362.1
	120.4	163.7	13.0	0.27	96.1	35.6	356.1
MCM-48 HYD	98.9	943.5	—	0.89	40.3	8.1	362.4
	96.3	843.5	—	0.71	38.1	14.7	364.1
	97.5	717.4	—	0.59	35.4	19.7	378.7
MCM-41 HYD	43.8	808.9	—	0.47	33.4	9.4	370.6
	43.7	691.7	—	0.41	32.7	13.6	370.2
	43.2	303.1	—	0.16	31.0	29.8	352.8
INDO							288.7
SBA-15 INDO	119.5	465.1	65.3	0.66	102	10.5	293.5
	119.7	384.8	23.7	0.60	101	15.1	303.6
	120.0	87.4	—	0.15	84.7	40.1	315.7
MCM-48 INDO	98.2	872.3	—	0.84	40.2	10.4	301.6
	97.7	851.7	—	0.78	40.2	16.7	299.6
	97.2	635.7	—	0.62	40.1	34.3	325.8
MCM-41 INDO	43.0	720.1	—	0.57	34.3	8.0	298.0
	42.9	621.5	—	0.49	33.8	12.0	300.2
	42.9	267.5	—	0.20	32.9	24.4	324.0

<sup>a</sup> Value from powder XRD.

<sup>b</sup> Specific surface area.

<sup>c</sup> Microporous surface area.

<sup>d</sup> Total pore volume and pore size distribution.

<sup>e</sup> Decomposition temperature for the largest TGA weight loss peak.

115 keV. Diffraction data were collected on an area detector, integrated into 1D diffraction patterns, and background corrected for subsequent PDF analysis. Background-corrected HE-XRD patterns  $I^{\text{coh}}(Q)$  were first converted into scattering functions  $S(Q)$  via the following equation:

$$S(Q) = 1 + \frac{I^{\text{coh}}(Q) - \sum c_i |f_i(Q)|^2}{|\sum c_i f_i(Q)|^2}$$

where  $c_i$  and  $f_i$  are the atomic concentration within the sample and X-ray scattering factors, respectively. Atomic PDFs were obtained from the Fourier transform of  $Q [S(Q) - 1]$  via the following equation:

$$G(r) = \left(\frac{2}{\pi}\right) \int_{Q=0}^{Q_{\text{max}}} Q[S(Q) - 1] \sin(Qr) dQ$$

Conversion of HE-XRD data into atomic PDFs was done with the program radial distribution.<sup>24</sup>

#### Drug Loading and Kinetic Release Experiments

Drug loading was achieved via a wetness impregnation method. In brief, a concentrated drug solution in ethanol was mixed with a sample of mesoporous silica (200 mg) and briefly sonicated. The solvent was removed by rotary evaporation at 40°C. Samples were

left to dry and stored in a desiccator until further use. Drug release was conducted as follows: simulated intestinal fluid (SIF) was prepared by dissolving NaOH (0.896 g) and KH<sub>2</sub>PO<sub>4</sub> (6.805 g) in purified water (1 L) to give a solution with a pH of 6.8. Release measurements were conducted twice and averaged. All chemicals used were purchased from Sigma-Aldrich, and purified water (Millipore Reference, Sydney, Australia) was used for the experiment. Size-1 gelatin capsules (Batch: RL042; ProSciTech, Queensland, Australia) were used for both pure drug and drug-loaded mesoporous silica samples.

Drug release was assessed under sink conditions (900 mL SIF, pH 6.8) by UV/Vis absorbance scan (Cary 60 UV-Vis; Agilent, Sydney, Australia) using 20 mg of drug-loaded silica for all measurements. UV/VIS spectra were collected at each time point at a wavelength of 295 nm, 248 nm, and 320 nm for ABZ, HYD, and INDO, respectively. The release was carried out in a dissolution bath (708-DS; Agilent) at a stirring rate of 50 rpm at 37°C, and data were collected for 24 h.

#### Results

Table 2 and Figure S1 summarize the structural and physical properties of mesoporous materials prepared. Calcined materials are highly ordered as confirmed from transmission electron microscopy images and show sharp XRD peaks between 0.5 and 6° 2θ. The morphologies of MCM-41 and MCM-48 are characterized by agglomerated nanoparticles, whereas SBA-15 shows rod-shaped



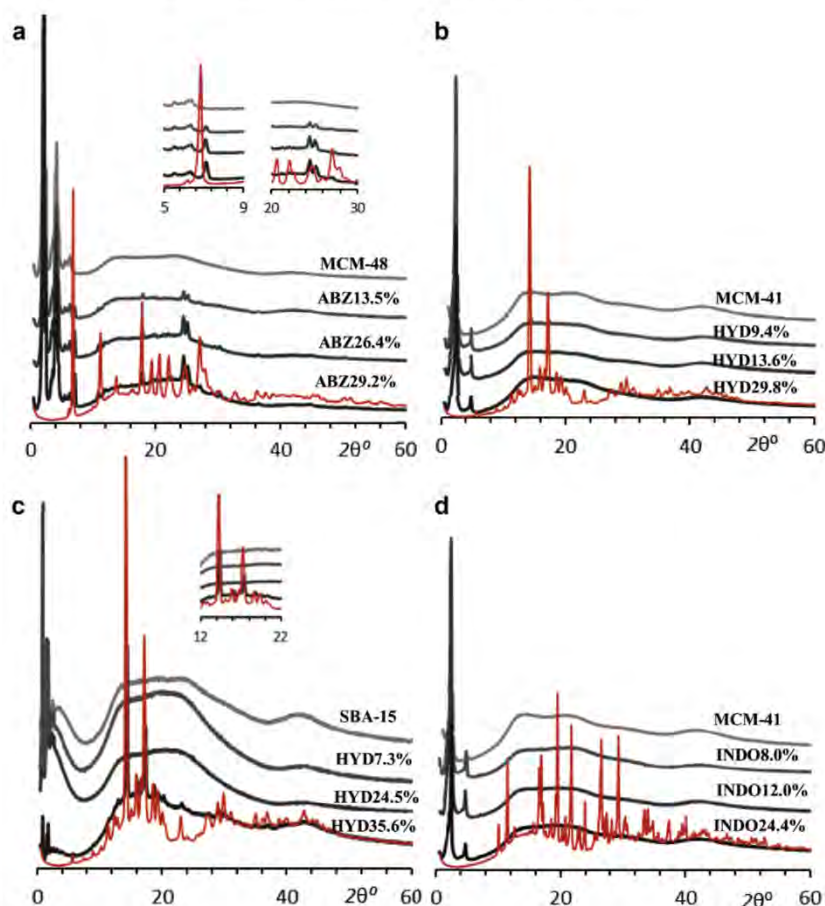


**Figure 1.** X-ray diffractograms of selected mesoporous silica materials loaded with (a) ABZ, (b and c) HYD, and (d) INDO. The respective crystalline drugs are in red. Insets show peaks associated with crystalline material after drug loading. Unlabeled y-axis corresponds to intensity in arbitrary units.

micrometer-sized particles. Drug compounds were loaded via a wetness impregnation using ethanol followed by solvent evaporation. Loading amounts between 9 and 50 wt% were confirmed by TGA. Samples are denoted in their loaded drug and weight percent, for example, MCM-41INDO10%.

Loading of ABZ resulted in a decrease in the decomposition temperature ( $D_T$ ) for all mesoporous materials (Table 2). The decomposition of ABZ occurs in a 3-step process for crystalline ABZ (Fig. S2) with the first step at 192.2°C. Three steps are also observed for the loaded samples with a shift to lower temperatures, as low as 171°C. A similar trend with an even more pronounced decrease in  $D_T$  in comparison to the crystalline form is observed for HYD. The single-peak decomposition for INDO-loaded samples shifts toward higher temperature, increasing with loading amount, with MCM-48INDO34.3% measuring an increase as high as 36°C.

A consistent decrease in the total mesopore volume (Tvol) is measured from N<sub>2</sub> sorption isotherms upon drug loading (Fig. S3 and Table 2). The pore size of MCM-41HYD29.8 wt% is reduced from 42 to 31 Å, accompanied with a decrease in Tvol of 73%. A

preferential filling of the micropores of SBA-15 occurs for ABZ loading but only partially for HYD and INDO. Despite a high loading, SBA-15HYD35.6% retains 13 m<sup>2</sup>/g of microporosity. In contrast, micropores in SBA-15 are filled after a 29-wt% loading of ABZ. The micropore diameter in SBA-15 is estimated at 18.9 Å (Fig. S1c).

X-ray diffraction patterns show no differences in unit cell values of loaded and calcined mesoporous materials (Table 2). The high angle region (10–70° 2θ; Figure 1 and Fig. S3) reveals the presence of crystalline domains for all ABZ-loaded materials. The peak positions for MCM-48ABZ samples do not match those of the unloaded crystalline drug, indicating the formation of ABZ crystalline polymorphs outside of the mesoporous materials during the loading procedure.<sup>25</sup> Furthermore, scanning electron microscopy (SEM) images (Fig. 2a) show the presence of thin platelet crystals outside the particles. For HYD-loaded samples, the lower pore size materials (MCM-41 and MCM-48) show no evidence of recrystallization, even above 30 wt% loading. The higher pore size of SBA-15 does not prevent recrystallization above loading amounts of 35 wt% (Fig. 1c). No diffraction peaks are observed for

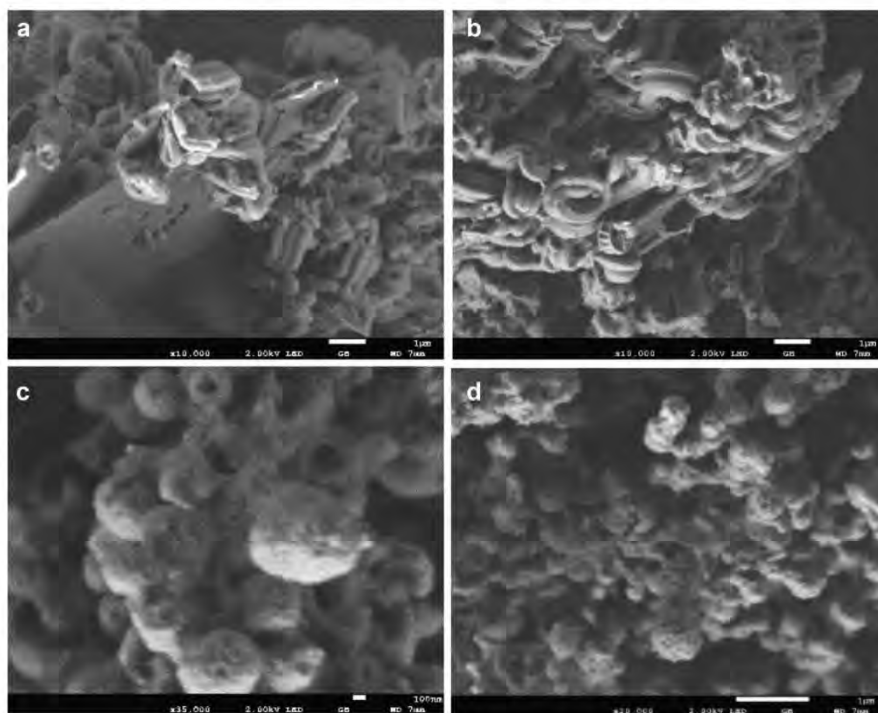


**Figure 2.** Scanning electron microscopy images of (a) SBA-15ABZ50.4% and (b) SBA-15HYD35.6% showing the presence of crystalline material on the external surface and images of (c) MCM-48INDO34.3% and (d) MCM-41ABZ24.4% showing a surface layer on the external surface.

INDO-loaded samples, except for MCM-48INDO34.3%, which only fills 44% of the mesopore volume (Fig. S4). SEM images do not reveal the presence of large crystals of HYD (Fig. 2b), even on the external surface of MCM-41ABZ and MCM-48INDO particles (Figs. 2c–2d).

Figures 3a and 3b show DSC traces for selected samples loaded with ABZ. A melting endotherm is observed at lower temperatures for the crystalline compound ( $T_m = 203.1^\circ\text{C}$ ) from a small amount of a crystalline polymorph, in agreement with XRD observations. The thermal parameters,  $T_m$  ( $\Delta H_m$ ) for SBA-15ABZ29.4%, MCM-41ABZ32.4%, and MCM-48ABZ26.4%, are  $173.3^\circ\text{C}$  (24.9 J/g),  $173.9^\circ\text{C}$  (30.7 J/g), and  $169.1^\circ\text{C}$  (18.0 J/g), respectively. Sample SBA-15ABZ50.4% shows additional melting endotherms with peaks at  $180^\circ\text{C}$ ,  $215^\circ\text{C}$ , and  $230^\circ\text{C}$ . The amount of crystalline drug in loaded samples can be estimated from the ratio of melting enthalpies of the loaded and the unloaded drug ( $\Delta H_{\text{loaded}}/\Delta H_{\text{crystalline}}$ ). This equals to 10.2% for MCM-41ABZ32.4% and 34.3% for SBA-15ABZ50.4%. Figures 3c and 3d show DSC traces for INDO-loaded samples where a sharp melting endotherm ( $T_m = 157^\circ\text{C}$ ) associated with the crystalline phase is observed at high loadings. The amount of crystalline INDO corresponds to 6% in MCM-48INDO34%, 4.3% in SBA-15INDO40.1%, and 3% for MCM-41INDO24%. No significant features are observed in traces of HYD-loaded samples except for d24.5% where a small melting endotherm is observed (Fig. 3d). To better understand the local structure of the amorphous drug compounds within mesoporous silica, HE-XRD patterns were converted into atomic PDFs (Fig. 4; Figs. S6–S7).

Atomic PDFs are ideal in probing atomic scale order of disordered materials as they represent intuitive atomic pair distances that scale with all contributions from the XRD pattern (both Bragg and diffuse features).<sup>25</sup> All PDFs exhibit a first peak at  $r = 1.6 \text{ \AA}$  which corresponds to the Si–O bond length and feature longer atomic pair distances expected in amorphous silica.<sup>26</sup> Notably, the PDFs of the drug-loaded samples have different features and increases in overall relative intensity, depending on the silica and drug combination in question. For example, HE-XRD patterns of ABZ loaded into the SBA-15 silica show a moderate amount of Bragg peaks in the crystalline drug compound (Fig. S6). The corresponding atomic PDFs reflect this observation by showcasing additional structural features not found in the amorphous silica, indicating intermolecular drug ordering (Fig. 4a). Conversely, ABZ loaded into MCM-48 silica materials shows a lack of crystalline features and thus exhibit PDFs very similar to those of the amorphous silica template (Figs. 4b and S6a). Similar comparisons can be made across various drugs' template in the same material. Using SBA-15 as an example, HYD and INDO exhibit minimal Bragg scattering in their corresponding HE-XRD patterns compared with ABZ. Once converted into atomic PDFs, the local structural distances become more pronounced. INDO-loaded SBA-15 only shows an analogous feature at the highest loading (Fig. 4c). For SBA-15 HYD samples (Fig. 4d), a strong atomic pair distance is observed at  $2.62 \text{ \AA}$  at 7.3 wt% and  $24.5 \text{ wt\%}$ , which shifts to smaller distances at 35.6% ( $2.58 \text{ \AA}$ ). This feature is not contributed to the SBA-1515 material and is likely an evidence of localized ordering of HYD within the template at higher loadings. All drug-loaded silica samples exhibit vastly



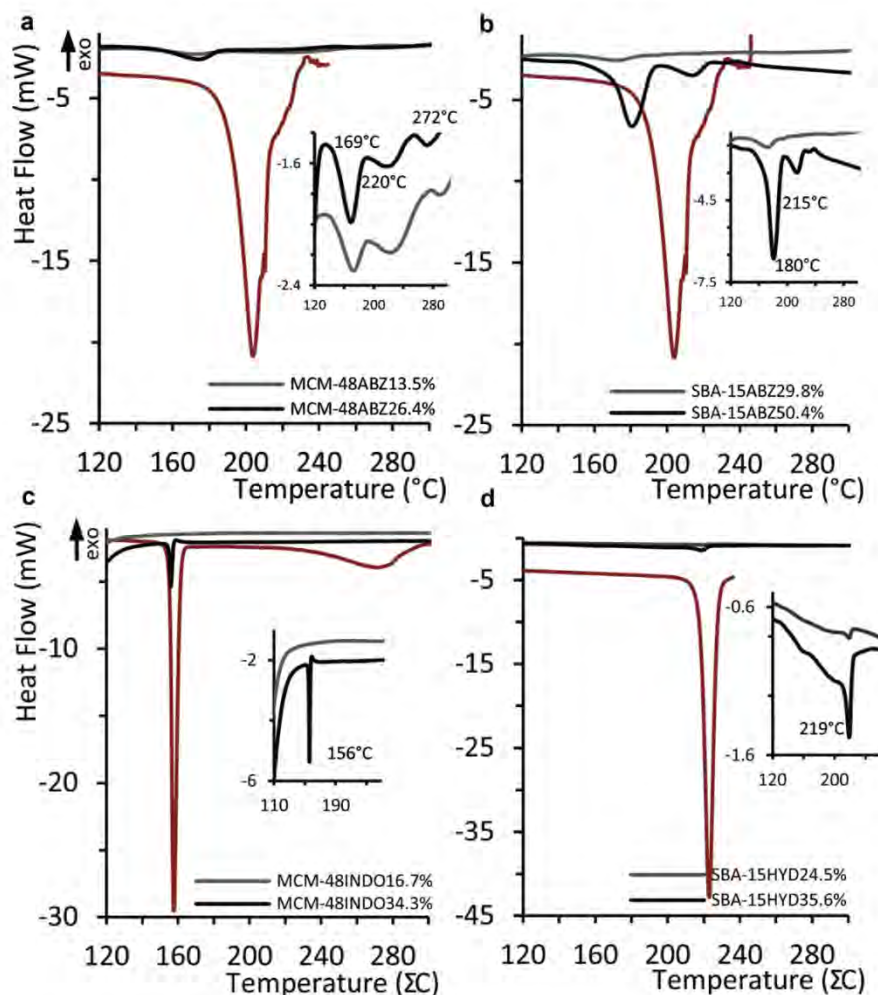


**Figure 3.** DSC traces of selected samples of (a) MCM-48ABZ, (b) SBA-15ABZ, (c) MCM-48INDO, and (d) SBA-15HYD as well as free crystalline drugs (red curves). Insets show enlarged areas of the curves shown.

different PDFs compared with the crystalline drug itself, which is attributed to the comparative lack of long-range order found in the loaded compounds. To better reconcile these differences, atomic PDFs of the drug-loaded samples were obtained by background subtracting the HE-XRD pattern of the silica from the drug-loaded material. For SBA-15ABZ (Fig. S7), a strong atomic pair distance is observed at 2.60 Å for 18.3-wt% samples and 2.20 Å for the 29.8-wt% samples. This peak disappears at the 50.4-wt% ABZ loading (2.58 Å), which shows different ordering due to the presence of a crystalline material. Nonetheless, it is still significantly different to the free crystalline drug. A main feature is observed around 1.55 Å which corresponds to the bond lengths associated with C–C, C–N, and C–O around the aromatic portion of each molecule.

The pattern of atomic pair distances of drug compounds within the silica template is notably different from that of the crystalline

counterparts. Hydrogen-containing distance are largely absent from the PDFs of drug-loaded silica samples, probably lost in background subtraction of a large amount of silica scattering from the HE-XRD. Selected features from the drug molecules within the silica materials are more pronounced. This may arise from oversampling of short-range versus long-range order intramolecular atomic pair distances in the crystalline drug compound. The degree of disorder of the drug compound will have a large impact on its kinetic release properties. Figure 5 and Figure S8 show dissolution curves conducted in SIF under sink conditions. All ABZ-loaded samples show a significant enhancement in dissolution compared with the crystalline drug, including SBA-15ABZ50.4% which possesses ~34% of a crystalline polymorph according to calorimetric data.

Release curves could be fitted using the Higuchi kinetic model of diffusion-controlled release (Table S9). At a similar ABZ loading of

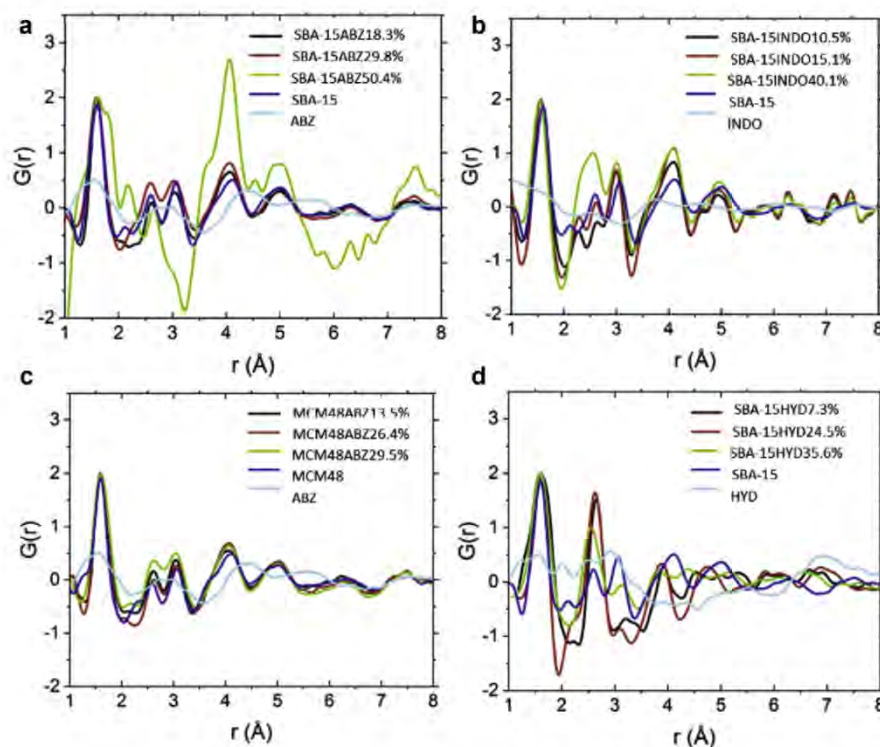


**Figure 4.** Atomic PDFs for (a) SBA-15ABZ, (c) MCM-48ABZ, (b) SBA-15INDO, and (d) SBA-15HYD samples loaded at different drug concentrations compared with those of the crystalline compounds (light blue) and the calcined silica mesoporous materials (dark blue).

30 wt%, SBA-15 results in a more rapid release rate in comparison to MCM-41 and MCM-48 accompanied by a lower time for the dissolution of 50% of the total released drug,  $t_{50\%}$  (Fig. 5b). Mesoporous materials loaded with ABZ show zero order release kinetics at  $t \leq 3$  h. Only for MCM-41ABZ samples does the total ABZ released increases with loading amount (Fig. 58). An enhancement in dissolution is also observed when INDIGO is released from mesoporous materials, with the exception of MCM-48INDO34.4%. This is the only INDIGO sample to show significant formation of crystalline drug from XRD and calorimetry. The release curve for this sample is similar to the free crystalline drug. All mesoporous silica structures enhanced the dissolution of HYD, with samples releasing more than 65% of loaded drug within a 2-h period (Fig. 5d) and SBA-15 samples resulting in faster rates. When low HYD loadings are compared, where the amorphous drug resides solely within the pores, both Higuchi and Korsmeyer-Peppas models accurately fit the curves as indicated by  $R^2$  values  $\geq 0.98$  (Table S9). Rate constants,  $k_H$  and  $k_{K-P}$ , increase with decreasing pore size for HYD samples loaded below 10 wt% with the release exponent,  $n$ , for  $k_{K-P}$  suggesting a burst effect ( $0.45 \leq n \leq 0.8$ ).

## Discussion

These results highlight the interplay between fundamental drug physical properties such as “glassy” behavior, the mesopore size, drug loading amount, and release kinetics. A decrease in the release

rate for ABZ with smaller mesopore sizes is observed, a trend reversed for HYD and INDIGO. One notable difference between the compounds is their crystallization temperature, which vary in the order ABZ (56°C), INDIGO (104°C), and HYD (123°C).<sup>27</sup> This may explain the observation of crystalline material after loading of ABZ. Even in the presence of a certain amount of crystalline drug compound, the dissolution behavior of ABZ is significantly improved.

Calorimetry shows that INDIGO (with lower  $T_g$  values) has similar or higher DT than its crystalline counterpart, whereas drug compounds ABZ and HYD with higher  $T_g$  show lower DT when loaded. This correlates well with a higher molecular mobility and a more pronounced enhancement in dissolution even at high drug loadings for ABZ and HYD (e.g., SBA-15ABZ50%).

Loading of HYD into SBA-15 does not fill the micropores fully at higher drug loadings. Considering that HYD has a larger polar surface area (Pol.SA) than ABZ (95 vs. 67 Å<sup>2</sup>) but a significant lower  $\log P$  (1.2 vs. 3.1), we can conclude that because of its size, HYD molecules preferentially resides in the larger mesopores of SBA-15. This leads to a concentration-independent release rate for HYD, where  $k_H$  remains almost constant. The smaller Pol.SA of INDIGO (68 Å<sup>2</sup>) fills the micropores completely with 15% of the original  $T_{vol}$  remaining after 40 wt% loading. This sample shows no traces of crystalline material from either XRD or DSC, but the PDFs show small difference as a function of increased loading in SBA-15INDIGO samples (Fig. 4d). As expected, this sample shows the largest enhancement in dissolution of all INDIGO loadings within SBA-15



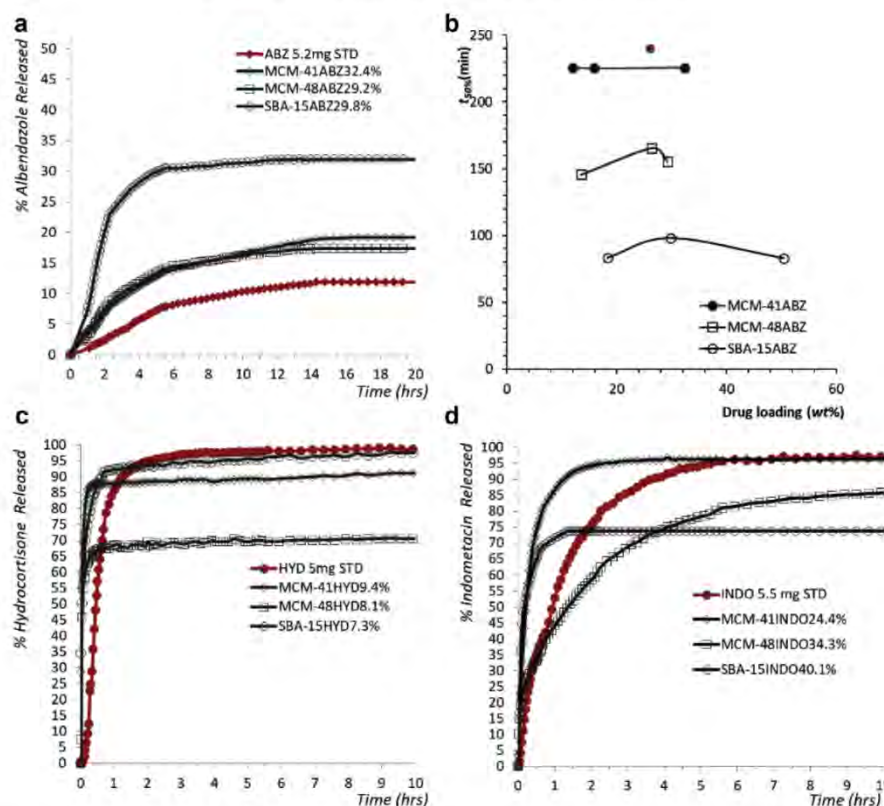


**Figure 5.** Dissolution curves for the drug load of mesoporous silica samples conducted under sink conditions in SIF at a dose of 20 mg of loaded mesoporous sample. Data are shown as a percentage of the total drug released. (a) A comparison for ABZ-loaded materials at approximately 30 wt% loading to a standard crystalline drug sample (red curve). (b) Plot of the time taken for 50% of the total released drug,  $t_{50\%}$ , versus loading amount for ABZ-loaded samples, where the red spot is the value of the free crystalline drug (5.2 mg dose). A comparison for (c) HYD and (d) INDO release from loaded mesoporous materials.

(Fig. 5d, Table S9, Fig. S10). In contrast to INDO and HYD, no decrease in pore size is observed for samples of ABZ loaded into SBA-15 (Fig. S11), whereas a considerable decrease in pore volume and surface area is observed. This, seemingly contradictory result, can be explained by considering a preferential filling of the micropore space of SBA-15 and a dispersed distribution of ABZ molecules within the hexagonal porous structure of SBA-15.

The general enhancements in solubility obtained in this work agree well with previous reports. Van Speybroeck et al. showed an enhancement in solubility for a single loading of INDO (18 wt%) within an SBA-15 sample possessing a micropore volume of  $0.10 \text{ cm}^3/\text{g}$ . Almost 100% of drug release was achieved after approximately 15 min.<sup>7</sup> Mesoporous SBA-15 samples presented here, having a similar micropore volume ( $0.12 \text{ cm}^3/\text{g}$ ), show similar release rates, albeit with slower release kinetics at higher loading amounts. There are no available data to compare the release of ABZ from mesoporous materials. However, when ABZ crystals were milled to sizes below 700 nm and significant enhancement in dissolution was observed under acidic media, 63% of dissolution of the drug occurred within 30 min.<sup>28</sup> This result constitutes a much faster release kinetics than that observed here, presumably because of the acidic conditions. Nonetheless, the SBA-15-ABZ18.3% sample

is in the same order of magnitude, with 15% of the total amount loaded released within 30 min in simulated intestine media. Lopez et al. have loaded and released HYD from a variety of SBA-15 samples with varying pore size at a loading of 40 wt%. In this study, the degree of microporosity was unfortunately not measured, and released experiments were conducted in distilled water.<sup>29</sup> The observed release kinetics was dependent on pore size, with the largest pore material (6.9 nm) releasing 61% of the HYD in 26 h. Kinetic release experiments for SBA-15HYD35% prepared here with a pore size of 11 nm showed significantly faster release with 100% of the loaded HYD released within 1 h.

Incomplete release of INDO and ABZ occurs over the time points studied (Figs. 5 and S9). This is less significant in HYD-loaded samples. This has been previously observed for mesoporous particles. It is thought to be caused by incomplete penetration of the medium within the intricate mesopore structure and because of strong interactions between the silica (silanol) surface and drug molecules.<sup>31</sup> As HYD-loaded samples were released over 90% and 65% of the total loaded drug for SBA-15, MCM-41, and MCM-48, it is likely that incomplete release in our study is due to a strong interaction of ABZ and INDO with the porous surfaces. Further work should be centered in understanding if there is a structural

component in the nature of the interaction and how the degree of amorphism plays a role, in this context.

## Conclusions

Atomic PDFs provide a means to assess atomic scale structural information which can be correlated to the molecular packing of the encapsulated drug, especially when scattering from the silica materials is background subtracted from the HE-XRD. Small differences in the intramolecular atomic pair distances are identified with increasing loading amount signaling a departure from complete disorder, for example, as in the case of INDO and HYD loaded within SBA-15. This should allow to determine a loading threshold before external crystallization occurs, for a given drug and solvent combination. The decomposition thermogravimetric peaks give information about the extent of disorder of a loaded compound with significant shifts as a result of drug loading. As demonstrated with ABZ compounds with low  $T_C$  and high  $T_m/T_g$  ratio, the development of alternative drug-loading protocols to ensure no crystalline polymorphs are formed is required. Large effects in terms of dissolution enhancement are nonetheless obtained by mesopore confinement. Although the relation between pore size and molecular size is clearly important, the degree of mesopore and micropore filling is shown to be a determining factor. Molecular modeling simulations from PDF data and further sampling with a more diverse drug range will be required to determine an accurate and predictive kinetic release model under nanopore confinement.

## Acknowledgments

This work was financed through support from the ARC Centre of Excellence for Nanoscale BioPhotonics (CE140100003), an ARC Future Fellowship (A.E.G.-B., FT150100342), and a Macquarie University Infrastructure grant (MQRIBG9201501951). This research used 11-ID-C of the Advanced Photon Source, a U.S. Department of Energy (DOE) Office of Science User Facility operated for the DOE Office of Science by Argonne National Laboratory under Contract No. DE-AC02-06CH11357. HE-XRD measurements were performed at the Advanced Photon Source, a US Department of Energy (DOE) Office of Science User Facility operated for the DOE Office of Science by Argonne National Laboratory under Contract No. DE-AC02-06CH11357. The authors thank Yang Ren for assistance with HE-XRD experiments. A.E.G.-B. thanks Macquarie University's Microscopy Unit for access to SEM facilities.

## References

- Paul SM, Mytelka DS, Dunwiddie CT, et al. How to improve R&D productivity: the pharmaceutical industry's grand challenge. *Nat Rev Drug Discov*. 2010;9(3):203–214.
- Cuatrecasas P. Drug discovery in jeopardy. *J Clin Invest*. 2006;116(11):2837–2842.
- Huang Y, Dai WG. Fundamental aspects of solid dispersion technology for poorly soluble drugs. *Acta Pharm Sin B*. 2014;4(1):18–25.
- Savjani KT, Gajjar AK, Savjani JK. Drug solubility: importance and enhancement techniques. *ISRN Pharm*. 2012;2012:195727.
- Xu W, Riikonen J, Lehto VP. Mesoporous systems for poorly soluble drugs. *Int J Pharm*. 2013;453(1):181–197.
- Mellaerts R, Fayad EJ, Van den Mooter G, et al. In situ FT-IR investigation of etravirine speciation in pores of SBA-15 ordered mesoporous silica material upon contact with water. *Mol Pharm*. 2013;10(2):567–573.
- Van Speybroeck M, Barillaro V, Thi TD, et al. Ordered mesoporous silica material SBA-15: a broad-spectrum formulation platform for poorly soluble drugs. *J Pharm Sci*. 2009;98(8):2648–2658.
- Van Speybroeck M, Mellaerts R, Mols R, et al. Enhanced absorption of the poorly soluble drug fenofibrate by tuning its release rate from ordered mesoporous silica. *Eur J Pharm Sci*. 2010;41(5):623–630.
- Xia X, Zhou C, Ballell L, Garcia-Bennett AE. In vivo enhancement in bioavailability of atazanavir in the presence of proton-pump inhibitors using mesoporous materials. *ChemMedChem*. 2012;7(1):43–48.
- Butler JM, Dressman JB. The developability classification system: application of biopharmaceutics concepts to formulation development. *J Pharm Sci*. 2010;99(12):4940–4954.
- Rengarajan GT, Enke D, Steinhart M, Beiner M. Stabilization of the amorphous state of pharmaceuticals in nanopores. *J Mater Chem*. 2008;18(22):2537.
- Prasad BR, Lele S. Stabilization of the amorphous phase inside carbon nanotubes: solidification in a constrained geometry. *Philos Mag Lett*. 1994;70(6):357–361.
- Sonnenberger N, Anders N, Golitsyn Y, et al. Pharmaceutical nanocrystals confined in porous host systems—interfacial effects and amorphous interphases. *Chem Commun (Camb)*. 2016;52(24):4466–4469.
- Kashchiev D, van Rosmalen GM. Review: nucleation in solutions revisited. *Cryst Res Technol*. 2003;38(7–8):555–574.
- Mellaerts R, Aerts CA, Van Humbeeck J, Augustijns P, Van den Mooter G, Martens JA. Enhanced release of itraconazole from ordered mesoporous SBA-15 silica materials. *Chem Commun (Camb)*. 2007;(13):1375–1377.
- Kjellman T, Xia X, Alfredsson V, Garcia-Bennett AE. Influence of microporosity in SBA-15 on the release properties of anticancer drug dasatinib. *J Mater Chem B*. 2014;2(32):5265.
- Roy S, Quinones R, Matzger AJ. Structural and physicochemical aspects of dasatinib hydrate and anhydrate phases. *Cryst Growth Des*. 2012;12(4):2122–2126.
- Young CA, Goodwin AL. Applications of pair distribution function methods to contemporary problems in materials chemistry. *J Mater Chem*. 2011;21(18):6464.
- Boetker JP, Koradia V, Rades T, Rantanen J, Savolainen M. Atomic pairwise distribution function analysis of the amorphous phase prepared by different manufacturing routes. *Pharmaceutics*. 2012;4(1):93–103.
- Tuysuz H, Lehmann CW, Bongard H, Tesche B, Schmidt R, Schuth F. Direct imaging of surface topology and pore system of ordered mesoporous silica (MCM-41, SBA-15, and KIT-6) and nanocast metal oxides by high resolution scanning electron microscopy. *J Am Chem Soc*. 2008;130(34):11510–11517.
- Kruk M, Jaroniec M, Ryoo R, Kim JM. Characterization of high-quality MCM-48 and SBA-1 mesoporous silicas. *Chem Mater*. 1999;11(9):2568–2572.
- Wishart DS, Knox C, Guo AC, et al. DrugBank: a comprehensive resource for in silico drug discovery and exploration. *Nucleic Acids Res*. 2006;34(Database issue):D668–D672.
- Manzano M, Aina V, Areán CO, et al. Studies on MCM-41 mesoporous silica for drug delivery: effect of particle morphology and amine functionalization. *Chem Eng J*. 2008;137(1):30–37.
- Petkov V. Rad, a program for analysis of x-ray-diffraction data from amorphous materials for personal computers. *J Appl Crystallogr*. 1989;22:387–389.
- Billinge SJ, Kanatzidis MG. Beyond crystallography: the study of disorder, nanocrystallinity and crystallographically challenged materials with pair distribution functions. *Chem Commun (Camb)*. 2004;(7):749–760.
- Shatnawi M, Paglia G, Dye JL, Cram KC, Lefenfeld M, Billinge SJL. Structures of alkali metals in silica gel nanopores: new materials for chemical reductions and hydrogen production. *J Am Chem Soc*. 2007;129(5):1386–1392.
- Mahlin D, Bergstrom CA. Early drug development predictions of glass-forming ability and physical stability of drugs. *Eur J Pharm Sci*. 2013;49(2):323–332.
- Koradia DK, Parikh HR. Dissolution enhancement of alendazole through nanocrystal formulation. *J Pharm Biomed Sci*. 2012;4(Suppl 1):S62–S63.
- Lopez T, Ortiz E, Alexander-Katz R, Basaldella E, Bokhimi X. Cortisol controlled release by mesoporous silica. *Nanomedicine*. 2009;5(2):170–177.
- Windholz M. The merck index online. *Science*. 1984;226(4680):1250.
- McCarthy CA, Atherton JA, Devine KJ, Crean AB. Role of drug adsorption onto the silica silica surface in drug release from mesoporous silica systems. *Mol Pharmaceutics*. 2018;15:141–149.

### 3.4 Additional discussion

In this work, PDF analysis provided an insight into the subtle changes of the local molecular order of drug compounds loaded within mesoporous silica. This knowledge can be incorporated with other characterisation techniques such as DSC, XRD, and N<sub>2</sub> sorption isotherms to understand the local molecular properties of amorphous drug molecules within the pores. Various factors are known to play a role in the drug release properties of mesoporous silica, including the physical and chemical properties of the drug compound, textural properties of mesoporous silica, drug loading (wt%) and amount of crystallinity in the drug loaded silica material.

The glass forming ability of a compound is related to the ratio between  $T_m/T_g$  and can be used to determine whether it is a good or poor glass former. Typically, drug compounds with higher  $T_m/T_g$  ratio are good glass formers and have a low tendency for crystallisation, form highly stable amorphous forms, and are good candidates for loading into mesoporous silica [13, 14]. The polar surface area of the drug compound (effective size) may affect its ability to penetrate and remain within the porous silica matrix. The larger polar surface area of HYD molecules showed a preference for the larger mesopores of SBA-15. Microporosity in SBA-15 silica was measureable even at the highest dose loading of 35.6%. In comparison, drug compounds with smaller polar surface area filled the micropores of SBA-15 silica at high drug loadings. This can have implications in regards to the drug release from SBA-15, as the microporosity may cause a delay in the rate of drug release due to steric hindrance between the drug and silica wall [15].

The confinement of the loaded drug within the porous structure is known to maintain the drug in a stable amorphous form. Complete mesopore filling at higher drug loadings caused crystallisation of the drug on the exterior surface of the silica particle. It is perhaps surprising to observe the presence of crystallinity at low ABZ loadings of 10 wt% in MSPs from XRD and DSC scans, where complete saturation of the pores was not observed. The PDF profile of the loaded ABZ was different to crystalline ABZ, and differences in atomic distances increased with the increase in loading amount showing a departure from complete disorder. This may have occurred where the unloaded drug re-crystallised on the surface of the particle, an effect observed from SEM images of ABZ loaded in SBA-15, at the highest loading amount. The low crystallisation temperature of ABZ at 56 °C relative to the other drug compounds used in the study may have facilitated the crystallisation of the unloaded drug, suggesting a washing step to remove



the unloaded drug material should have been made. Even in the presence of crystalline material, drugs loaded in SBA-15 showed an enhancement in dissolution as compared to crystalline drug (Figure 3.2).

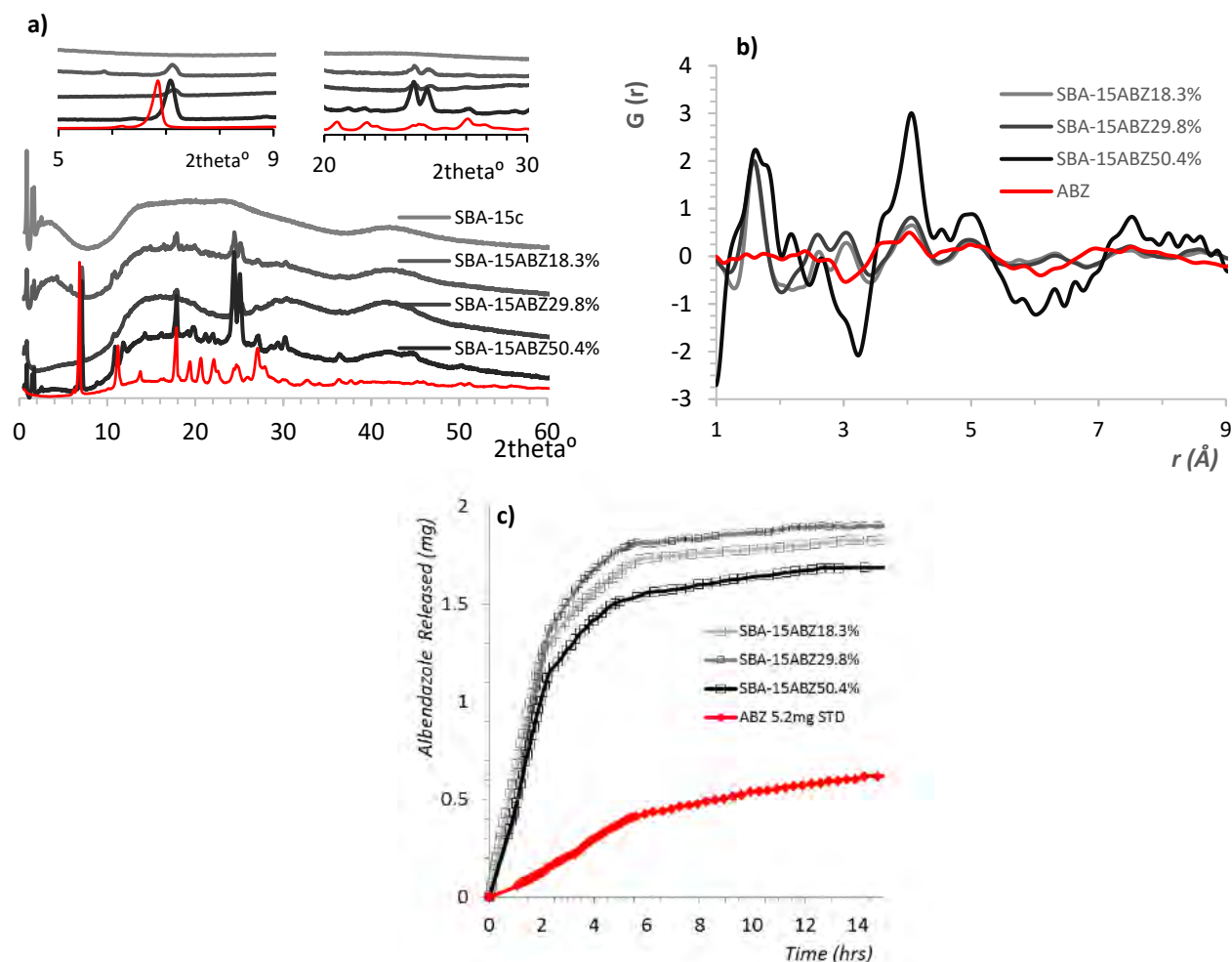


**Figure 3.2:** Characterisation of crystalline ABZ, and ABZ loaded in mesoporous silica SBA-15. a) XRD scans showed the presence of crystalline material at the lowest loading amount of 18.3% and the intensity of diffraction peaks increased with the loading amount up to 50.4%. y-axis is arbitrary units b). PDF analysis of HE-XRD patterns was able to detect changes in the local atomic ordering of drug loaded samples, suggesting a move from complete disorder in ABZ occurred with the increase in drug loading. c) in vitro drug release measurements showed an enhancement in drug release was achieved in ABZ loaded in SBA-15. Changes in the local atomic ordering associated with loading amount played a role in the reduction in rate of drug release, likely associated with the increase in crystallinity of the sample.

In the case of HYD and INDO, XRD diffraction peaks were detected at the highest loadings (SBA-15HYD 35.6% and MCM-48INDO 34.3%). A change in local molecular distances become more pronounced with the increase loading amount, as observed from the PDF patterns of SBA-15HYD and MCM-48INDO samples, suggesting a move from complete disorder to a higher degree of order. No observable crystalline material was observed from SEM for these samples, which suggest that changes in the local molecular ordering of drug loaded material may have

occurred with the recrystallisation of the drug compound on the surface of the MSP that was not observed under SEM. The presence of a very small amount of crystalline material, with a calculated % crystallinity for MCM-48INDO 34.3% at 6 % and SBA-15HYD 35.6% at 4.3 %, was observed by DSC. Thus, the subtle changes in the local molecular ordering was likely due to the presence of crystallinity in these samples and accounted for the calculated delay in drug release kinetics observed in in vitro dissolution experiments. For example, the difference in  $t_{50\%}$  release between MCM-48INDO 10.4% and 34.3 % was 150 vs 390 minutes respectively, more than 2 fold difference in release kinetics.

### 3.5 Conclusion

PDF provided additional information regarding changes in the local molecular ordering of the drug compound likely associated with the recrystallisation of the drug outside the mesopores. In particular, PDF was able to detect subtle changes in local molecular distances correlated with the presence of crystallinity in SBA-15HYD and MCM-48INDO samples. XRD analysis and DSC was unable to provide information about these changes except at high loadings. These changes are related to conformational rearrangements of the drug molecules within the mesopores as the drug loading increases. Further work would be needed to evaluate how the subtle changes in local molecular ordering could be used as a tool in developing a model that can be used to predict the suitability of a drug compound for loading in mesoporous silica.

### 3.6 References

1. Macarron, R., et al., *Impact of high-throughput screening in biomedical research*. Nature reviews Drug discovery, 2011. **10**(3): p. 188-195.
2. Liu, R., X. Li, and K.S. Lam, *Combinatorial chemistry in drug discovery*. Current opinion in chemical biology, 2017. **38**: p. 117-126.
3. Keserü, G.M. and G.M. Makara, *The influence of lead discovery strategies on the properties of drug candidates*. nature reviews Drug Discovery, 2009. **8**(3): p. 203-212.
4. Takagi, T., et al., *A provisional biopharmaceutical classification of the top 200 oral drug products in the United States, Great Britain, Spain, and Japan*. Molecular pharmaceutics, 2006. **3**(6): p. 631-643.
5. Rodriguez-Aller, M., et al., *Strategies for formulating and delivering poorly water-soluble drugs*. Journal of Drug Delivery Science and Technology, 2015. **30**: p. 342-351.
6. Knopp, M.M., et al., *Effect of amorphous phase separation and crystallization on the in vitro and in vivo performance of an amorphous solid dispersion*. European Journal of Pharmaceutics and Biopharmaceutics, 2018. **130**: p. 290-295.
7. He, Y. and C. Ho, *Amorphous solid dispersions: utilization and challenges in drug discovery and development*. Journal of Pharmaceutical Sciences, 2015. **104**(10): p. 3237-3258.
8. Newman, A., K. Nagapudi, and R. Wenslow, *Amorphous solid dispersions: a robust platform to address bioavailability challenges*. Therapeutic delivery, 2015. **6**(2): p. 247-261.
9. Maleki, A., et al., *Mesoporous silica materials: From physico-chemical properties to enhanced dissolution of poorly water-soluble drugs*. Journal of Controlled Release, 2017. **262**: p. 329-347.
10. Xu, W., J. Riikonen, and V.-P. Lehto, *Mesoporous systems for poorly soluble drugs*. International journal of pharmaceutics, 2013. **453**(1): p. 181-197.
11. Ma, X. and R.O. Williams III, *Characterization of amorphous solid dispersions: An update*. Journal of Drug Delivery Science and Technology, 2019. **50**: p. 113-124.
12. Liu, X., et al., *Characterization of amorphous solid dispersions*. Journal of Pharmaceutical Investigation, 2018. **48**(1): p. 19-41.
13. Mahlin, D. and C.A. Bergström, *Early drug development predictions of glass-forming ability and physical stability of drugs*. European Journal of Pharmaceutical Sciences, 2013. **49**(2): p. 323-332.
14. Alhalaweh, A., et al., *Physical stability of drugs after storage above and below the glass transition temperature: Relationship to glass-forming ability*. International journal of pharmaceutics, 2015. **495**(1): p. 312-317.
15. Kjellman, T., et al., *Influence of microporosity in SBA-15 on the release properties of anticancer drug dasatinib*. Journal of Materials Chemistry B, 2014. **2**(32): p. 5265-5271.



# 4

## Unlocking the antioxidant properties of probucol by the encapsulation within mesoporous silica particles.

### 4.1 Introduction

Probucol (PB), a compound originally synthesised as an antioxidant containing two butylated hydroxytoluenes, was approved in the early 1970s for the treatment of high cholesterol [1]. PB lowers plasma low density lipoproteins (LDL) by increasing LDL uptake in the liver and converting it to bile acids for excretion [2, 3]. This reduces cholesterol absorption [2], and increases LDL removal in a receptor independent pathway [2]. A daily dose of PB at 1 g/day was found to decrease plasma cholesterol by 11 %, and LDL levels by approximately 10-15% in humans [4-6]. However, PB also lowers plasma high density lipoprotein (HDL) levels by approximately 10-20%, which raised concerns that the compound may increase the risk of developing coronary heart disease [4, 5]. Since 1995, a number of factors have led to the withdrawal of PB from most western countries including the development of statins in the 1980s, concerns regarding PB's lowering of HDL, and reports of adverse effects including irregular heart rate and ventricular arrhythmias [7, 8].

There has been renewed interest in the application of PB's antioxidant and anti-inflammatory properties for the treatment of oxidative stress in coronary artery restenosis [9], diabetes [10] and neurodegeneration [11]. This interest was inspired by the discovery that PB protects LDL from oxidative modification, a key event in the pathogenesis of atherosclerosis [12, 13]. However, results from clinical studies of PB in the prevention of atherosclerosis and coronary artery restenosis have been mixed [14-17] due to its limited oral bioavailability (2-8 % bioavailability) [18], as it is practically insoluble in water (solubility at 25 °C, 2-5 ng/ml). To further enhance the beneficial properties of PB, there is a need for new drug formulations that address its poor solubility. A range of lipid/surfactant based, and co-milled formulations have achieved significant improvement in the solubility and

bioavailability of PB as summarised in Table 4.1.

Formulation	<i>In vitro</i> solubility/dissolution	<i>In vivo</i> pharmacokinetics			Reference
		C <sub>max</sub> (µg/mL)	T <sub>max</sub> (h)	AUC <sub>(0-t)</sub> (µg h/mL)	
Nanoemulsion	Solubility (pH = 6.8) = 20 mg/ml vs 8-10 ng/ml (PB standard).	0.5 ± 0.007 (0.07 ± 0.01)	7.0 ± 1.4 (7.5 ± 1.0)	7.6 ± 0.8 (0.8 ± 0.09)	[19]
Co milled	30 % drug release after 2 hr compared to 0.68% from PB standard.	2.5 ± 1.09 (0.4 ± 0.3)	2.5 ± 0.76 (2.3 ± 1.07)	21.4 ± 6.3 (7.4 ± 3.3)	[20]
Self-assembled nanoparticles	Aqueous solubility ~ 20 mg/ml, increase of (~ 2 x10 <sup>6</sup> times) compared to PB standard.	0.5 ± 0.02 (0.05 ± 0.005)	3.0 ± 0.1 (7.3 ± 1.0)	13.1 ± 0.2 (1.3 ± 0.1)	[21]
Co milled with vitamin E	Solubility ~ 760 ng/ml over 20 minutes in simulated intestinal fluid (pH = 6.5).	0.11 ± 0.03 (0.05 ± 0.03)	8 ± 0.1 (16 ± 1.0)	1.4 ± 0.3 (0.5 ± 0.04)	[22]

**Table 4.1:** Summary of PB formulations including *in vitro* solubility/dissolution results, pharmacokinetic parameters of the PB formulations as compared to PB standard (data in brackets) from *in vivo* studies conducted in rats or mice. C<sub>max</sub>, maximum plasma concentration; T<sub>max</sub>, time to achieve maximum plasma concentration, AUC<sub>0-t</sub>, area under the plasma concentration time curve from zero to time point t hr observation period.

The encapsulation of PB in porous materials has been investigated in the development of self-emulsifying drug delivery systems (SEDDS) (Table 4.2). In such systems, PB in a solution containing surfactant and lipid, is loaded within the porous material to facilitate the formation of an oil in water emulsions upon contact with the dissolution medium. Complete PB release (~ 95 %) was achieved from large macroporous materials (5 µM pore size) as compared to less than 3 % drug release from commercially available MSP (2-15 nm pore size) [23]. Release from materials with larger pore size was enhanced by easier diffusion of the solvent molecules into the porous matrix as compared to materials with smaller pore sizes in MSPs, as drug molecules remained trapped within the mesopores [23].

Formulation	Porous material	pore size	<i>In vitro</i> dissolution	Reference
SEDDS	Porous silica particles and Commercially available MSPs (Aeroperl® 300, Aerosil® 200, SBA-15).	Three porous silica particles with pore size of 5 µM, 500 nm, and 150 nm respectively were synthesised. Pore size of commercially available MSPs between 8 to 30 nm were used for comparison.	Complete drug release (~100%) over 15 minutes was achieved from large pore 5 µM silica in dissolution medium (pH ~2). <3% of PB released from mesoporous silica over 120 minutes in dissolution medium (pH ~2)	[23]
SEDDS	Neusilin® US2	5 nm to 3 µM, majority (> 30%) between 500 to 700 nm.	~ 80% PB released in dissolution medium (pH ~2) within 15 minutes.	[24]
SEDDS	Neusilin® US2	5 nm to 3 µM, majority (> 30%) between 500 to 700 nm.	PB released from neusilin® US2 was ~80% within 15 minutes, in purified water as dissolution medium.	[25]

**Table 4.2:** Summary of PB SEDDS formulations loaded in porous materials with different pore sizes (nm) and measured (%) drug release from *in vitro* dissolution experiment.

The development of amorphous formulations using MSPs has been shown to be a viable strategy to enhance the solubility of a range of poorly soluble drug compounds [26, 27], but it has not been explored for PB. A review of patents shows PB is listed as an example of a practically insoluble pharmaceutical drug compound that would likely benefit from loading within mesopores [28-30]. In this work, PB was loaded within MSPs AMS-6, MCM-41, and SBA-15 with different textural properties to explore the effect of such differences on the physical properties of the loaded drug. *In vitro* drug release measurements, and *in vivo* pharmacokinetic studies were conducted in rats to compare the release of PB from MSPs and crystalline PB. The antioxidant properties of PB released from MSP were evaluated in the context of two *in vitro* cellular models of oxidative stress; (a) in human brain endothelial cells challenged with hydrogen peroxide, and (b) in lipopolysaccharide (LPS) activated mouse microglial cells. LPS was chosen in this *in vitro* model as it is a potent pro-inflammatory stimulus that induces microglial activation and a subsequent increase in the release of pro-inflammatory cytokines and ROS production [31].

## 4.2 Author contribution

Name	Conception of the study	Design experiment and methodology	Data collection	Data analysis and interpretation	Drafting and writing the manuscript
Michael Lau	√	√	√	√	√
Kalpeshkumar Giri			√		√
Alfonso E. Garcia-Bennett	√	√		√	√

## 4.3 Full paper



### Antioxidant properties of probucol released from mesoporous silica

Michael Lau<sup>a</sup>, Kalpeshkumar Giri<sup>a,b</sup>, Alfonso E. Garcia-Bennett<sup>a,b,\*</sup>

<sup>a</sup> Department of Molecular Sciences, Macquarie University, Sydney, NSW 2109, Australia

<sup>b</sup> Australian Research Council Centre for Nanoscale Biophotonics, Macquarie University, Sydney, NSW 2109, Australia.

#### ARTICLE INFO

##### Keywords:

Drug delivery  
Pharmaceutical excipients  
Antioxidant properties  
Probucol  
Mesoporous silica

#### ABSTRACT

Antioxidants play a vital role in scavenging reactive oxygen species (ROS) produced by the reduction of molecular oxygen from various cellular mechanisms. Under oxidative stress, an increase in the levels of ROS overwhelms the antioxidant response, causing oxidative damage to biological molecules, and leading to the development of various diseases. Drug compounds with potent antioxidant properties are typically poorly water soluble and highly hydrophobic. An extreme case is Probucol (PB), a potent antioxidant with reported water solubility of 5 ng/ml, and oral bioavailability of < 10%. In this study, PB was loaded in mesoporous silica at various drug loadings to understand the changes to the physical properties of the loaded drug, and its *in vitro* drug release. Further *in vitro* studies were conducted in endothelial and microglia cell models to compare the free radical scavenging efficiency of ascorbic acid, PB, and PB release from mesoporous silica particles.

Out of the three different mesostructured particles studied, the maximum loading of PB was achieved for large pore mesoporous particles (SBA-15) at 50 wt% drug loading, before complete pore filling was observed. For all materials, loadings above complete pore filling resulted in the recrystallization of PB on the external surface. *In vitro* drug release measurements showed a rapid dissolution rate at low drug loadings compared to a bimodal release profile of amorphous and crystalline drug at higher drug loadings. PB loaded in mesoporous particle was shown to enhance the antioxidant response to extracellular ROS in the endothelial cell line model, and to intracellular ROS in the microglia cell model.

Our results indicate that the antioxidant properties of PB can be significantly improved by using mesoporous silica as a delivery vehicle.

#### 1. Introduction

Reactive oxygen species (ROS) are highly unstable oxygen carrying free radicals that cause oxidative damage to biological molecules including DNA, proteins, and lipids (Di Meo et al., 2016). The reduction of molecular oxygen by intracellular mechanisms results in the production of endogenous ROS (Di Meo et al., 2016). Examples include peroxyl, superoxide anion, and hydroxyl radicals (Pourova et al., 2010). Exogenous sources of ROS include exposure to xenobiotics, radiation, and toxic chemicals (Pourova et al., 2010). Furthermore, ROS are involved in important cellular processing and signaling pathways which are vital for normal cell functioning (Pourova et al., 2010). A steady state concentration of ROS is maintained by antioxidant defense mechanisms that act as free radical scavengers in protecting biological molecules against oxidative damage.

Antioxidant defense mechanisms can be classified into two categories: antioxidant enzymes, and chain-breaking antioxidants. Antioxidant enzymes are produced endogenously and include the

superoxide dismutase (SOD), catalase, and glutathione peroxidases (Birben et al., 2012). These enzymes catalyze the conversion of ROS into a more stable, unreactive molecule. Chain-breaking antioxidants are free radical scavengers that convert ROS into a more stable unreactive molecule (Padayatty et al., 2003). These antioxidants can be further classified as water or fat soluble. Ascorbic acid is a highly potent water soluble antioxidant that can scavenge a range of intracellular and extracellular ROS, including superoxide, hydroxyl and hydrogen peroxide (Padayatty et al., 2003). Vitamin E is the most important fat soluble antioxidant that is found in cellular membranes, protecting it from oxidative damage by ROS (Padayatty et al., 2003).

Under oxidative stress, increased concentrations of ROS overwhelms the antioxidant defense mechanisms, causing oxidative damage to cells and the development in pathological conditions such as diabetes, cancer, and cardiovascular diseases (Birben et al., 2012; Day, 2004). In diabetes, increasing evidence implicate oxidative stress in impaired glucose metabolism, and the development of complications including hypertension, atherosclerosis, and nephropathy (Baynes, 1991). Despite

\* Corresponding author at: Department of Molecular Sciences, Macquarie University, Sydney, NSW 2109, Australia.  
E-mail address: alf.garcia@mq.edu.au (A.E. Garcia-Bennett).

<https://doi.org/10.1016/j.ejps.2019.105038>

Received 23 April 2019; Received in revised form 15 July 2019; Accepted 5 August 2019

Available online 06 August 2019

0928-0987/ © 2019 Published by Elsevier B.V.



the evidence on the role of oxidative stress in these diseases, the effectiveness of treatment with antioxidant supplementation such as ascorbic acid or vitamin E has been inconclusive (Balbi et al., 2018; Kizhakekuttu and Widlansky, 2010).

Instead, drug compounds with antioxidant properties are being investigated for the treatment of diseases caused by oxidative stress. The statins rosuvastatin (Holvoet, 2008), atorvastatin (Wassmann et al., 2002), and simvastatin (Chartoumpekis et al., 2010) have antioxidant properties that inhibit LDL (low density lipoprotein) oxidation independent of the drug's effect in lowering LDL levels. Oral hypoglycemic medications including gliclazide (O'Brien et al., 2000), metformin and pioglitazone were shown to have antioxidant activities, inhibit LDL oxidation, and increase antioxidant levels from *in vivo* studies in diabetic patients (O'Brien et al., 2000; Singh et al., 2016). In patients with hypertension, production of ROS and markers of lipid oxidation are increased, and levels of the antioxidant SOD and glutathione are decreased (Rodrigo et al., 2007; Redón et al., 2003). Anti-hypertensive medications metoprolol and carvedilol was shown in an *in vivo* human study to reduce thiobarbituric acid reactive substances considered a marker of oxidative stress (Kukin et al., 1999), amlodipine was shown to increase levels of SOD and reduce oxidative stress in patients with hypertension (Mahajan et al., 2007), and enalapril was shown to reduce oxidative stress markers, and increase antioxidant enzyme levels in diabetic rats (de Cavanagh et al., 2001).

Probucol is an antioxidant containing two butylated hydroxytoluene moieties (Kuzuya and Kuzuya, 1993). It is a potent free radical scavenger, and is used to inhibit lipid oxidation in the treatment of atherosclerosis, xanthoma, and cardiovascular diseases (Barnhart et al., 1989; Kuzuya and Kuzuya, 1993). Due to its potent antioxidant properties, there has been renewed interest in expanding the clinical use of PB in diseases such as type II diabetes, restenosis after angioplasty, and diabetic nephropathy (Yamashita et al., 2015). However, PB's extreme physicochemical properties make it highly challenging in achieving favorable pharmacokinetics from oral administration. It is a non-ionizable, highly lipophilic drug compound with a partition coefficient of 8.9, water solubility of 2–5 ng/ml, and reported oral bioavailability of < 10% (Nielsen et al., 2008) ranking it among the most poorly soluble, and hydrophobic drug compound with known antioxidant activity (Fig. 1).

Various formulation strategies have been used to improve the

dissolution rate of PB including dry/wet milling, spray drying, and nanoemulsions (Thybo et al., 2008; Li et al., 2017; Zhang et al., 2014). The enhancement in % PB release of 30% at 2 h was achieved from a co-milled formulation containing surfactant and polymer, compared to the release of 0.68% at 2 h in a commercial PB formulation (Li et al., 2017). A spray dried formulation of PB with polymer PVP-K30 achieved a 60% of drug release after 1 h (Thybo et al., 2008). Wet milling of PB with dispersing agents gelucire, vitamin E, and pluronic F-108 was investigated by Tanaka et al. (2012). Results from *in vitro* dissolution experiments indicated the highest apparent solubility and % PB release was achieved by wet milling with vitamin E (Tanaka et al., 2012). However, concerns regarding the potential toxicity of the surfactants and polymers used in these formulations, low drug loading, and incomplete drug release highlight the extreme challenge in formulating PB for oral administration.

Mesoporous silica are ordered porous materials characterized by pore sizes between 2 and 50 nm, large surface area (up to 1000 m<sup>2</sup>/g), and adjustable pore volume (up to 1 cm<sup>3</sup>/g) (Wu et al., 2013). The porous properties and high surface area of mesoporous silica make it an attractive drug carrier for the delivery of high drug payloads (up to ~30%w/w) (Xu et al., 2013). Drug loaded in mesoporous silica are stabilized within the nano-confines of the mesopores in the amorphous state, due to the restriction in molecular mobility that limit the recrystallization of the loaded drug (Rengarajan et al., 2008; Prasad and Lele, 1994). The release of the amorphous drug from the mesopores has higher dissolution rate compared to its crystalline state, as demonstrated in a range of poorly soluble drug compounds (Jangra et al., 2016; Xu et al., 2013; Maleki et al., 2017). For example, a faster atorvastatin dissolution rate was achieved from the drug loaded in 2-dimensional (2d) ordered mesoporous silica SBA-15 (68% over 45 min) compared to the crystalline drug (40% over 45 min) (Maleki and Hamidi, 2016), and (Hu et al., 2012) demonstrated an enhancement in carvedilol dissolution rate of 60% over 45 min was achieved from drug loaded in 3d ordered mesoporous silica SBA-16, compared to 20% in crystalline drug. Both atorvastatin and carvedilol have very low solubility in the same range as PB, however the latter has a considerably higher Clog P (Fig. 1) making it harder to formulate in a soluble bioavailable form.

In this work, our aim is to demonstrate the enhancement in dissolution rate, and antioxidant properties of PB can be achieved by

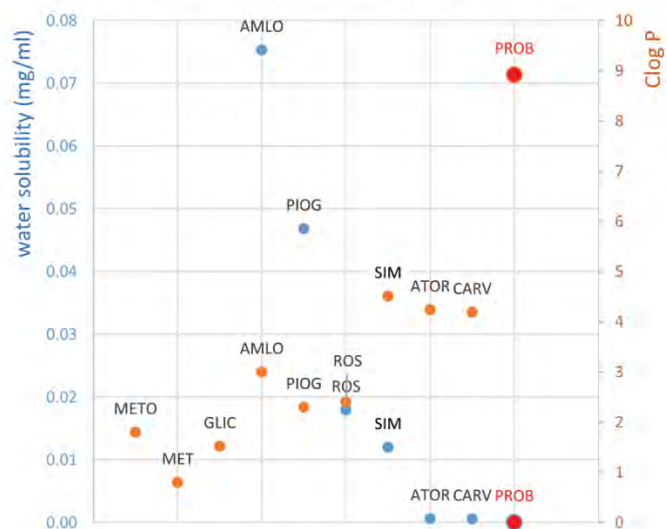


Fig. 1. Solubility in water (blue) and Clog P (orange) of poorly soluble drug compounds. Probucol (PB) has the highest calculated partition coefficient of 8.9 (Clog P) and lowest solubility in water of 2–5 ng/ml compared to the other poorly soluble drug compounds: metoprolol (METO), metformin (MET), gliclazide (GLIC), amlodipine (AMLO), pioglitazone (PIOG), rosuvastatin (ROS), simvastatin (SIM), atorvastatin (ATOR), carvedilol (CARV). (For interpretation of the references to colour in this figure legend, the reader is referred to the web version of this article.)



loading the drug in mesoporous silica. Changes in the physical properties of drug loaded samples in terms of crystallinity, surface textural properties of mesoporous silica, and drug dissolution are investigated at different drug loading amounts wt% and capsule dose. Additionally, two *in vitro* cellular models are used to investigate the antioxidant response of PB and ascorbic acid to extracellular ROS in the endothelial cell line, and to intracellular ROS in the microglia cell line.

## 2. Materials and methods

### 2.1. Chemicals and reagents

Tetraethylorthosilicate (TEOS), cetyltrimethylammonium bromide (CTAB), (3-aminopropyl)triethoxysilane (APTES), aqueous ammonia (32 wt%), pluronic p123 (p123), hydrochloric acid, ethanol, propylene bottles, hydrogen peroxide ( $H_2O_2$ ), lipopolysaccharides (LPS), dimethyl sulfoxide (DMSO), probucol, ascorbic acid, Dulbecco's Modified Eagle Media (DMEM) were purchased from Sigma Aldrich (Sydney, Australia). N-lauroyl-L-alanine ( $C_{12}$ Ala) was purchased from BOC sciences (New York, USA). Fetal bovine serum (FBS), penicillin-streptomycin (10,000 U/ml), TrypLE express enzyme (TrypLE), were purchased from Thermo Fisher scientific (Victoria, Australia). Muse™ count and viability assay kit, and Muse® oxidative stress kit were purchased from Merck Millipore (Victoria, Australia). All chemicals were of reagent grade and used without further purification. Milli-Q® water was used throughout the experiments.

### 2.2. Synthesis of mesoporous particles

#### 2.2.1. Synthesis of AMS-6

The synthesis of AMS-6 follows the protocol reported previously (Aturi et al., 2008). Briefly,  $C_{12}$ Ala was used as the surfactant, APTES as the co-structure directing agent (CSDA), and TEOS the silica source. A homogenous solution of  $C_{12}$ Ala (0.10 g) in Milli-Q® water (20 g) was kept at 80 °C for 24 h under static conditions. The surfactant solution was stirred for 10 min before the addition of APTES (0.10 g). After stirring for 3 min, TEOS (0.51 g) was added and the solution was stirred for 10 min at 80 °C in a closed bottle. The synthesis gel was heated at 80 °C under static conditions for 24 h. The silica product was filtered and dried at room temperature, followed by calcination at 550 °C for 3 h to remove the surfactant template.

#### 2.2.2. Synthesis of MCM-41

The synthesis of MCM-41 followed the protocol reported previously (Grün et al., 1999). Briefly, CTAB (2.5 g) was added to Milli-Q® water (50 g), 13.2 g aqueous ammonia (32 wt%) and 60.0 g of absolute ethanol in a propylene bottle. The solution was stirred at room temperature for a period of 1 h. Subsequently, 4.7 g of TEOS was added, and the mixture was stirred for a further of 2 h. The closed propylene bottle was placed inside an oven set to 100 °C for a period of 24 h. The sample was filtered, washed with ethanol and left to dry at room temperature for 12 h. The sample was calcined in a furnace at 550 °C for 3 h.

#### 2.2.3. Synthesis of SBA-15

The synthesis of SBA-15 followed the protocol reported previously (Kruk et al., 2000). 4 g of p123 was dispersed in 30 g water and stirred for 4 h. 120 g of 2 M hydrochloric acid solution was added and stirred for 2 h. 8.54 g of TEOS was added to the solution under stirring at 100 rpm for 20 min. The resulting gel was aged at 40 °C for 24 h and the bottle was placed inside the oven at 100 °C for 48 h. After synthesis, the solution was filtered, washed with distilled water and dried at room temperature, followed by calcination at 600 °C for 5 h.

### 2.3. Scanning electron microscopy (SEM)

Images were obtained using a JSM-7401F scanning electron microscope (JEOL Ltd., Tokyo, Japan) operating at 1–2 kV with no gold coating, using gentle beam mode at magnifications between 100 and 10,000.

### 2.4. Nitrogen adsorption/desorption isotherm

Nitrogen adsorption/desorption isotherm were measured at liquid nitrogen temperature (–196 °C) using a Micromeritics TriStar II volumetric adsorption analyzer (Micromeritics Instrument Corporation, GA, USA) for calcined and drug loaded mesoporous particle samples. Before the measurements, the samples were degassed for 3 h at 80 °C. The surface area of the samples was calculated by using the Brunauer–Emmett–Teller (BET) equation in the relative pressure ( $P/P_0$ ) range of 0.05 and 0.3 (Brunauer et al., 1938). The total pore volume was calculated from the amount of gas adsorbed at  $P/P_0 = 0.95$ . The pore size distribution curves were derived using the density functional theory (DFT) assuming a cylindrical pore model for all samples. All calcined mesoporous materials exhibited a type IV isotherm profile, with SBA-15 displaying a type  $H_1$  hysteresis in desorption branch. No hysteresis is observed in mesoporous AMS-6 nor MCM-41 due to the smaller pore size distribution (Ravikovitch et al., 2006).

### 2.5. Drug loading

PB was loaded into mesoporous silica via a wetness impregnation method. Briefly, the drug was dissolved in a glass beaker with ethanol. In a round bottom flask, calcined mesoporous silica was mixed with ethanol and sonicated for 10 min. The solution containing dissolved drug was added to the round bottom flask with mesoporous silica, and the mixture was mixed for 20 min. The solvent was removed by rotary evaporation at 40 °C, 150 rpm rotation at a pressure of 66 Pa. Samples were left to dry, and stored in a desiccator until further use. Samples were labelled according to the drug loading percentage. For example, AMS-6PB30% was labelled for samples containing 30% (w/w) PB loaded in mesoporous silica AMS-6.

### 2.6. Thermogravimetric analysis (TGA)

A Thermogravimetric Analysis instrument (TA instruments, TGA-2050, Delaware, USA) was used to determine the drug loading amount in the mesoporous particle. Analysis was conducted at a heating rate of 20 °C min<sup>–1</sup> from 20 to 800 °C. The sample weights varied from 5 mg to 10 mg. The derivative weight loss calculation was performed using TA instruments software (TA instruments, Universal analysis 2000, version 3.0 G).

### 2.7. Differential scanning calorimetry (DSC)

Differential scanning calorimetry instrument (TA instruments, DSC-2010, Delaware, USA) was used to determine the crystallinity of the sample at a heating rate of 10 °C min<sup>–1</sup> from 20 to 350 °C. The sample weights varied from 5 mg to 10 mg. Analysis was performed using TA instruments software (TA instruments, Universal analysis 2000, version 3.0 G).

### 2.8. Powder X-ray diffraction (XRD)

Powder XRD was performed on free drug and drug loaded samples to determine the presence of crystalline drug (Bruker D8 Discover XRD) using CuK $\alpha$  radiation ( $\lambda = 1.5418 \text{ \AA}$ ). The diffraction patterns were recorded between 0.5 and 70° (2 $\theta$ ) for drug loaded samples and 1 to 8° (2 $\theta$ ) for unloaded calcined mesoporous samples.



### 2.9. Drug release

Drug release studies were conducted in simulated intestinal fluid (SIF) containing 0.25% (w/v) CTAB as a wetting agent. Size 1 gelatin capsules (ProSciTech, Batch: RL042, Queensland, Australia) were used to encapsulate both the pure drug and drug loaded mesoporous silica samples. Drug release was assessed under sink conditions (900 ml SIF, pH 6.8) using a UV/Vis spectrometer (Agilent, Cary 60 UV-Vis, Sydney, Australia) at  $\lambda_{\text{max}}$  of 242 nm. The release was carried out in an Apparatus II dissolution bath (Agilent, 708-DS, Sydney, Australia) at a stirring rate of 50 rpm, 37 °C, and data collected approximately every 5 min for 24 h.

### 2.10. Cell culture

Immortalized human cerebral microvascular endothelial cells (hCMEC/D3) were kindly donated by Mr. Guoying Wang (Macquarie University, Centre for Nanoscale Biophotonics, Australia). Immortalized murine microglia cells were kindly donated by Dr. Lindsay Parker (Macquarie University, Centre for Nanoscale Biophotonics, Australia). hCMEC/D3 Cells were cultured in DMEM supplemented with 10% FBS and 1% Penicillin/Streptomycin at 37 °C with 5% CO<sub>2</sub>, 95% fresh air, and were passaged every 5 to 7 days. Cells of passage length between 25 and 35 days were used for the *in vitro* experiments.

Microglia cells were cultured in DMEM supplemented with 10% FBS and 1% Penicillin/Streptomycin at 37 °C with 5% CO<sub>2</sub>, 95% fresh air, and were passaged every 3 to 4 days. Cells of passage between 10 and 15 days were used for the *in vitro* experiments.

### 2.11. *In vitro* cell experiments

hCMEC/D3 Cells were seeded onto 6 well plates at a density of  $2 \times 10^6$  to  $4 \times 10^6$  containing 2 ml media and cultured for 5 to 7 days. On the day of the experiment, media in each of the wells was discarded. The test compound (ascorbic acid, AMS-6PB, and PB) was added together with hydrogen peroxide into each of the six well plates. Hydrogen peroxide, AMS-6 PB, and ascorbic acid was prepared in fresh media and sonicated briefly for 5 min. PB was dissolved in DMSO and was further diluted in media to a final concentration of < 0.01% (v/v). The 6 well plates were left inside the incubator for the duration of the experiment. Percentage of cells under oxidative stress, and cell viability were analyzed by the Muse® Oxidative stress kit, and Muse™ count and viability kit, respectively.

Microglia cells were seeded onto 6 well plates at a density of  $2 \times 10^6$  to  $3 \times 10^6$  containing 2 ml media and cultured for 1 day. 10 µg/ml LPS was added to activate microglia cells, and incubated at 37 °C with 5% CO<sub>2</sub>, 95% fresh air for 48 h. The test compounds PB, ascorbic acid, and AMS-6 PB were incubated between 2 and 24 h. The percentage of cells under oxidative stress, and cell viability were analyzed by the Muse® Oxidative stress kit, and Muse™ count and viability kit, respectively.

### 2.12. Muse® oxidative stress kit

The Muse® oxidative stress kit quantitatively determines the count and percentage of cells that are under oxidative stress (%ROS +) based on intracellular detection of superoxide radicals, from cells that are not under oxidative stress (%ROS -). The Muse® oxidative stress reagent is based on dihydroethidium which is cell membrane permeable and oxidizes with intracellular free radicals to form the fluorophore ethidium bromide.

Each sample was analyzed according to the protocol provided by the manufacturer. Briefly, media was removed from the six well plates, and TrypLE was used as the dissociation agent to recover the cells. Approximately 1 ml of fresh media was added to stop the TrypLE

reaction and the cell suspension was added into 15 ml falcon tubes for centrifugation at 300 g for 3 min. Media was removed, and PBS was added to re-suspend the cell pellet. 100 µl of cell suspension was added to 190 µl of Muse® oxidative stress reagent and incubated for 30 min. Data analysis was performed on the MUSE cell analyzer®.

### 2.13. Muse™ count and viability kit

The Muse™ count and viability reagent contain a DNA-binding dye that stains the nucleus of dead and dying cells. The dye does not stain the live cells, allowing for the discrimination between dead and viable (live) cells. Samples were analyzed following the protocols provided by the manufacturer. Briefly, media was removed from the six well plates, and TrypLE was used as the dissociation agent. Approximately 1 ml of fresh media was added to stop the TrypLE reaction and the cell suspension was added into 15 ml falcon tubes for centrifugation at 300 g for 3 min. Media was removed, and PBS was added to re-suspend the cell pellet. 10 µl of cell suspension was added to 400 µl of Muse™ count and viability reagent and incubated for 10 min. Data analysis was performed on the MUSE cell analyzer® containing the Muse™ count and viability software module that performs the calculations to determine the percentage of viable and dead cells.

## 3. Results and discussion

Probuco was loaded into mesoporous silica material AMS-6, with a 3d cubic mesostructure; and into MCM-41 and SBA-15, with 2d hexagonal arrangement of mesopores (Manzano et al., 2008; Atluri et al., 2008). A wetness impregnation method using ethanol as a solvent was utilized to load PB. Detailed synthetic and characterization results are included in the Electronic Supporting Information (Fig. S1). Table 1 shows a summary of structural and textural properties of PB loaded mesoporous materials. Approximately 50, 40, and 30 wt% of PB could be loaded within SBA-15, AMS-6, and MCM-41 respectively, before complete pore filling was determined from nitrogen adsorption measurements. The larger pore size of calcined SBA-15 (104.5 Å) and AMS-6 (46.7 Å) versus MCM-41 (31.7 Å) allowed for a larger loading amount of PB before complete pore filling was attained. To study the nature of PB adsorbed onto the external particle surface, samples were also loaded up to 60 wt%. Samples are denoted with their loading amount, e.g. AMS-6PB13.2% as determined from TGA analysis (Fig. S2).

The crystalline state of the drug before and after loading into mesoporous silica was investigated by XRD and DSC. There was no loss of mesoscale order as a function of drug loading < 30 wt% of PB (Figs. 2a and S3). XRD patterns at drug loadings above complete pore filling resulted in the presence of crystalline drug, likely on the surface of the silica particle (Fig. 2b). The scattering peaks from XRD do not completely correspond with those of the original crystalline polymorph (form I) but also contain another PB polymorph (form II, see also Fig. S3b), suggesting recrystallization of PB was likely to have occurred (Gerber et al., 1993). DSC scans of PB loaded mesoporous materials further confirm the presence of crystalline drug at loadings above complete pore filling, compared to the confinement within the mesopores of amorphous PB at lower drug loadings (Fig. S4). The presence of two endothermic peaks from DSC scans in high drug loaded samples (> 40 wt%) indicate a mixture of polymorphic crystals was likely present (Fig. S4). The amount of crystalline material in the samples can be estimated from the ratio in the enthalpy of melting of crystalline PB to the drug loaded mesoporous materials (Fig. 2c).

Drug loadings ≤ 40 wt% resulted in < 5% crystalline drug for the larger pore materials of SBA-15 and AMS-6; and < 10% for MCM-41. Loadings above 40 wt% resulted in a rapid increase in the %crystallinity (Fig. 2c). This was likely caused by the recrystallization of PB outside of the mesopores due to the saturation in surface area (Fig. 2d) and pore volume (Fig. S5). Furthermore, the broad endothermic peak above 50 °C, observed from the DSC thermograph at low drug loading was



**Table 1**

Summary of structural, porosity, and loading properties of PB within mesoporous silica particles AMS-6, MCM-41, and SBA-15; including unit cell parameters ( $a^*$ ), BET surface area ( $S_{\text{BET}}$ ), the total pore volume ( $T_{\text{vol}}$ ), the pore size distribution (PSD), the drug loading amount and the drug decomposition temperature from TGA ( $D_T$ ). The melting endotherm ( $T_m$ ) and enthalpy ( $\Delta H_m$ ) are derived from DSC scans. Note that only calcined SBA-15 has 119.9 m/g of additional microporosity.

	$a$ (Å) <sup>a</sup>	$S_{\text{BET}}$ (m <sup>2</sup> /g) <sup>b</sup>	$T_{\text{vol}}$ (cm <sup>3</sup> /g) <sup>c</sup>	PSD <sup>d</sup> (Å)	Load (%wt)	$D_T$ (°C)	$T_m$ (°C)	$\Delta H_m$ (J/g)
MCM-41	43.3	975.5	0.5	31.7				
AMS-6	51.8	777.3	0.7	46.7				
SBA-15	118.6	646.9	0.9	104.5				
PB						210.4	124.2	54.5
MCM-41PB	44.2	764.9	0.4	31.4	13.1	263.3		
	44.2	432.5	0.2	31.0	18.5	252.8	112.8	0.05
	44.2	273.7	0.1	30.4	31.8	269.7	112.6	1.0
					42.1	221.3	113.0	4.3
							122.8	0.6
					47.8	231.5	113.7	12.4
					60.4	246.2	113.6	17.2
							123.4	6.3
AMS-6PB	56.9	379.6	0.4	43.8	13.1	245.1		
	56.9	330.1	0.3	43.6	22.5	255.8		
	56.9	197.7	0.2	40.3	28.4	256.5	112.7	0.04
					41.2	261.1	113.1	1.7
					51.9	228.1	113.1	7.6
							122.9	0.07
					60.3	243.7	113.7	15.1
							123.2	0.7
SBA-15PB	109.7	271.9	0.5	97.5	12.1	229.8		
	109.7	245.9	0.4	90.2	19.1	232.2		
	109.7	145.9	0.3	87.9	29.9	238.9	112.2	0.3
		68.8	0.1	87.8	41.5	237.5	113.1	2.3
		12.5	0.03	87.2	49.5	227.0	113.6	12.3
							122.8	1.8
					56.4	238.8	113.7	18.1
							123.1	3.2

<sup>a</sup> Unit cell from powder XRD.

<sup>b</sup> Specific surface area.

<sup>c</sup> Total pore volume and pore size distribution.

<sup>d</sup> Decomposition temperature for the largest TGA weight loss peak.

likely due to the evaporation of water, as silica has been demonstrated to be highly hydrophilic (Fig. S4 insert) (Cordeiro et al., 2016). With the increase in drug loading, a shift in the water desorption endotherm to a lower temperature suggested the adsorption of crystalline PB increased the hydrophobicity of the sample. Therefore, drug loadings above complete pore filling were likely to cause a reduction in drug release kinetics, due to the increase in the amount of recrystallized, hydrophobic PB in these samples.

*In vitro* dissolution experiments were conducted under sink conditions in simulated intestine fluid (SIF). They generally follow a bimodal drug release pattern consisting of an initial burst, followed by the slower release of PB (Figs. 3a, S6). The burst release at drug loadings < 30 wt% was due to the release of amorphous PB from the mesopores. Drug loadings above complete pore filling caused the reduction in drug release kinetics (Table S1), likely due to the presence of recrystallized PB on the silica surface. Full release of PB was achieved below this loading level except for MCM-41, where only MCM-41 PB13.1% releases the full amount of the drug loaded (Fig. S6). This may indicate a strong dependency of release kinetics on the diffusion properties of the dissolution media for the smaller pore material (McCarthy et al., 2017). The optimal loading amount of PB in SBA-15 and AMS-6 is 30 wt%, and 20 wt% for MCM-41 (Fig. 3b).

In order to better understand the dissolution kinetics of PB, dose dependent release profiles were measured between 30 and 100 mg. These are shown in the ESI Figs. S7 and S8. Only a small increase in the total amount of PB released is observed at higher doses. This is

accompanied by a reduction in the overall percentage of drug released and a loss of sink conditions. Thus, at a dose of 100 mg the formulation of SBA-15PB29.9%, only releases 67% of the loaded PB after 24 h. This trend is observed for all mesoporous materials in this work irrespective of pore size and indicates that PB reaches its saturation state > 30 wt% within the dissolution media (Kjellman et al., 2014).

The mechanism of free radical termination by PB is based on the reaction of its two phenolic hydrogens with ROS to form spiroquinone or diphenoquinone (Barnhart et al., 1989). However, the antioxidant response of PB is limited by its low solubility (Colle et al., 2013). In an *in vivo* study (Betge et al., 2007), oral administration of PB in rats was not effective in scavenging ROS mediated cardiac remodeling after myocardial infarction, as therapeutic concentrations of the drug was not achieved. In comparison to PB, ascorbic acid is a water soluble antioxidant. Upon interaction with a ROS, ascorbic acid acts as an electron donor to quench unstable free radicals, protecting biological molecules from oxidative damage (Padayatty et al., 2003). Ascorbic acid was chosen as an example of a highly potent water soluble compound to compare its antioxidant properties to that of the poorly soluble drug PB.

The antioxidant properties of the test compounds at 100  $\mu\text{M}$  concentration were initially tested in the hCMEC/D3 cell line. In this cell model, the ROS  $\text{H}_2\text{O}_2$  and the test compound were incubated together with the endothelial cells, and the extracellular scavenging efficacy of the antioxidants was determined by analyzing the percentage of cells under oxidative stress (%ROS +) compared to cells that were not (%ROS -) using the Muse® oxidative stress kit. Fig. 4a shows the %ROS + cells after 24 h incubation with  $\text{H}_2\text{O}_2$  at different concentrations with or without PB, AMS-6 PB28.4% or ascorbic acid. %ROS - cells are shown in Fig. S9a. In comparison to the positive control, PB released from AMS-6 resulted in higher scavenging response evidenced by a decrease in %ROS + cells when incubated together with  $\text{H}_2\text{O}_2$  at concentrations below 1000  $\mu\text{M}$ . At the higher concentration of 1500  $\mu\text{M}$  only limited improvement in antioxidant effect was observed. In a subsequent time dependent study, hCMEC/D3 cells were incubated with the test compound and 1000  $\mu\text{M}$   $\text{H}_2\text{O}_2$ . AMS-6PB28.4% consistently resulted in a decreased number of %ROS + cells (Fig. 4b), in comparison to ascorbic acid or PB alone.

Hydrogen peroxide is a potent ROS that causes degradation to DNA, peroxidation of lipid membranes, and cell death (Shaji et al., 2019). At concentrations > 100  $\mu\text{M}$ ,  $\text{H}_2\text{O}_2$  is known to cause a significant increase in endothelial cell permeability, disruption to cellular membrane protein expression, and decrease in cell viability (Shaji et al., 2019). This is consistent with results from this study as the incubation of endothelial cells with 1000  $\mu\text{M}$   $\text{H}_2\text{O}_2$  from 2 to 24 h (positive control) caused the increase in %ROS + cells, and reduction in %viable cells (Fig. S10). The increase in cell death was likely associated with the oxidation of cellular membranes by  $\text{H}_2\text{O}_2$ . Treatment with AMS-6 PB28.4% was shown to delay the increase in %ROS + and cell death, suggesting the release of the amorphous PB from mesoporous silica was more efficient in free radical scavenging, and protecting the hCMEC/D3 cells from oxidative damage by  $\text{H}_2\text{O}_2$ .

In the second cellular model, microglia cells were used to further investigate the antioxidant properties of ascorbic acid, PB, and AMS-6PB28.4%. In the activated state, microglia releases proinflammatory cytokines, and ROS that are part of the immune response to neurotoxins (Thameem Dheen et al., 2007). Oxidative damage by the chronic release of ROS superoxide and nitric oxide cause neuronal cell death, and the development of brain diseases such as depression, Alzheimer's and Parkinson's (Papa-Wagner et al., 2013; Cobourne-Duval et al., 2016). Microglia cells were activated by incubation with 10  $\mu\text{g}/\text{ml}$  LPS for 48 h to induce intracellular production of ROS, and were subsequently treated with the test compounds at 1  $\mu\text{M}$  concentration. In the positive control, incubation with LPS without test compounds resulted in the significant increase in %ROS + cells to 75% after 24 h (Fig. 5a). Furthermore, a significant increase in cell death was observed from the

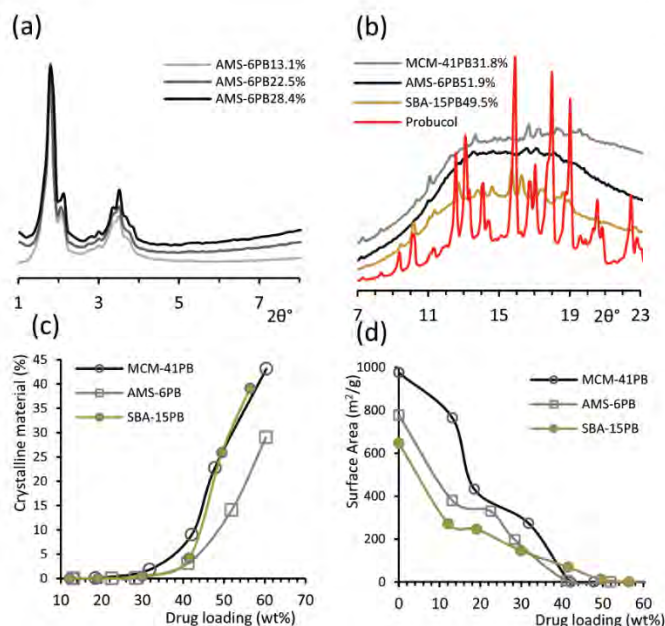


**Fig. 2.** (a) Diffractograms for drug loaded mesoporous AMS-6 normalized to the most intense peaks. See ESI (Fig. S3) for other materials. No changes to mesoscale order are observed. (b) X-ray diffractograms of drug loaded mesoporous samples at high loading showing the presence of crystalline PB on the external particle surface. These are absent at lower loadings. (c) Percentage amount of crystalline material estimated from differential scanning calorimetry. (d) Decrease in surface area as a function of loading amount as measured by nitrogen adsorption isotherms.

positive control compared to the other samples (Fig. S11a). Treatment with AMS-6PB28.4%, and ascorbic acid resulted in a significant reduction in %ROS + cells compared to PB, and positive control after 6 h (Fig. 5a). No statistical significance was observed between treatment with ascorbic acid or AMS-6 PB28.4% in terms of %ROS + or cell viability. A significant enhancement in antioxidant response was observed in AMS-6PB28.4% compared to PB after 6 h incubation.

The antioxidant response of PB was limited by its low solubility in aqueous media, a result consistent with previous findings (Horwitz

et al., 1996; Betge et al., 2007). The release of PB from its amorphous state with superior solubility, and release kinetics led to the enhancement in  $H_2O_2$  scavenging efficiency, protecting hCMEC/D3 cells against oxidative stress, and cell death in an extracellular ROS model. Treatment with either PB or ascorbic acid did not result in an overall reversal of %ROS + hCMEC/D3 cells, likely due to the high concentration of  $H_2O_2$  used in this study. In the second cell model, activation of microglia cells by LPS was used to determine the efficacy of the test compounds in scavenging intracellular ROS levels. The antioxidant

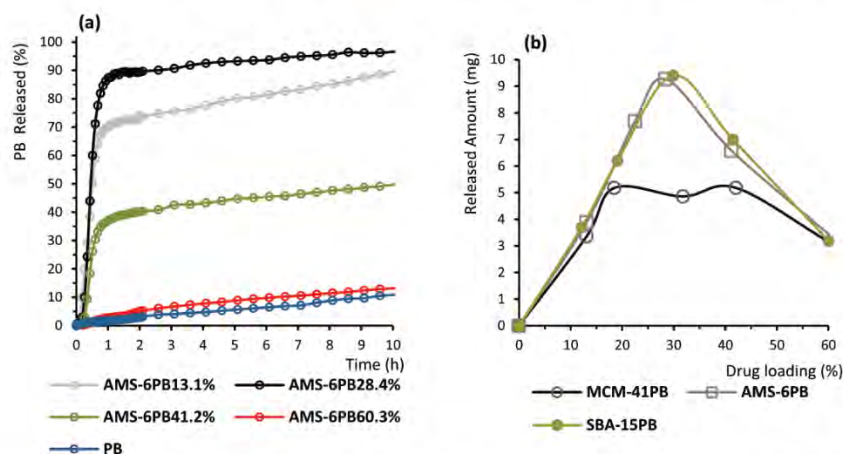


**Fig. 3.** Results from *in vitro* dissolution studies (a) Kinetic release profile of AMS-6 PB at different loading amounts, showing the initial burst release is followed by a slower rate of drug release. A reduction in % release of PB was observed at high drug loadings. See ESI (Fig. S6) for other materials. (b) Total amount of PB released from a 30 mg capsule dose of drug loaded mesoporous silica particles. Complete drug release was achieved up to 30 wt% drug loading in AMS-6 and SBA-15 mesoporous silica particles.



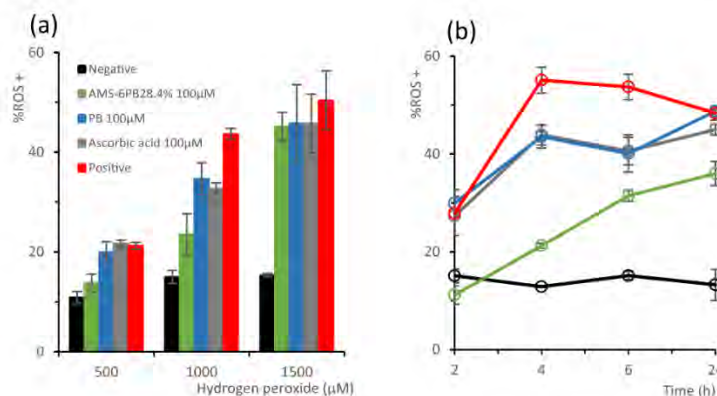


Fig. 4. (a) %ROS + cells (hCMEC/D3) after 24 h incubation with different concentrations of hydrogen peroxide (500 μM to 1500 μM) together with the test compounds. The positive control is hydrogen peroxide alone whilst the negative control represents normal cell growth with no hydrogen peroxide. (b) Evolution of antioxidant activity of test samples between 2 and 24 h incubation with 1000 μM hydrogen peroxide plotted as a function of %ROS + cells (hCMEC/D3). See Fig. S9 for %ROS - data.

response is shown to be dependent on the dissolution rate of PB in aqueous media, with a faster effect observed for PB released from mesoporous silica. The scavenging of intracellular ROS is likely to be enhanced by silica particle uptake across the cell membrane of the macrophages, which has been found to be rapid and favorable for mesoporous AMS-6 particles (Witaspl et al., 2009). Therefore, results from the *in vitro* work in the two cellular models indicate the release of amorphous PB from mesoporous AMS-6 can enhance the antioxidant response to extracellular or intracellular ROS. This can potentially open new therapeutic applications for mesoporous silica loaded PB in the treatment of diseases associated with oxidative stress, where rapid quenching of free radicals are required such as in treatment of cardiovascular diseases (Moris et al., 2017).

#### 4. Conclusion

The enhancement of dissolution of extremely lipophilic pharmaceutical compounds is demonstrated using PB as a model drug. Whilst the dissolution improvement is significant, the maximum loading capacity of PB within the pores of mesoporous materials is optimal at 30 wt%, above which the compound crystallizes primarily as the form II polymorph on the external surface. Release kinetics is fastest in the absence of crystalline material and at doses below 40 mg. In comparison to the excipient polyvinylpyrrolidone K-30 (Thybo et al., 2008) or co-milling techniques (Li et al., 2017), a faster release kinetics is observed here with > 80% of the loaded amount released within the first hour for SBA-15 and AMS-6 mesoporous silica formulations. At high loadings above 30 wt% and 40 mg doses the solubilized compound

quickly reaches saturation. The released PB has improved antioxidant behavior in comparison to the crystalline form, which may enable its use in new therapeutic areas where solubility and rapid therapeutic kinetics are required such as for the treatment of cardiovascular diseases.

#### Declaration of competing interest

AEGB is the co-founder of Nanologica AB (Stockholm, Sweden) a company commercializing nanoporous materials for biomedical applications. No other co-authors report any potential conflict of interest.

#### Acknowledgements

This work was partly financed through support from the ARC Centre of Excellence for Nanoscale BioPhotonics (CE140100003), an ARC Future Fellowship (AEGB, FT150100342) as well as a Macquarie University Infrastructure grant (MQRIBG 9201501951). AEGB would like to thank Macquarie University's Microscopy Unit for access to SEM facilities.

#### Appendix A. Supplementary data

Supplementary data to this article can be found online at <https://doi.org/10.1016/j.ejps.2019.105038>.

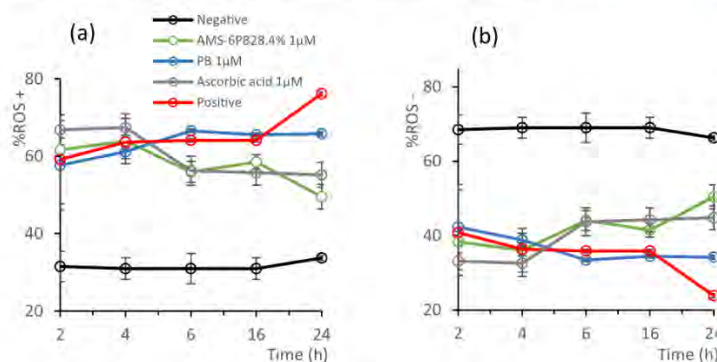


Fig. 5. (a) %ROS + microglia cells and (b) %ROS - microglia cells after incubation with test compounds for 2 to 24 h. Microglia cells were activated by incubation with 10 μg/ml LPS for 48 h, after which cells were incubated with test compounds for 2 to 24 h. Positive was activated microglia cells without incubation with test compounds, and negative was microglia cells without activation with LPS.

## References

- Atluri, R., Hedin, N., Garcia-Bennett, A.E., 2008. Hydrothermal phase transformation of bicontinuous cubic mesoporous material AMS-6. *Chem. Mater.* 20, 3857–3866.
- Balbi, M.E., Tonin, F.S., Mendes, A.M., Borba, H.H., Wiens, A., Fernandez-Llmos, F., Pontarolo, R., 2018. Antioxidant effects of vitamins in type 2 diabetes: a meta-analysis of randomized controlled trials. *Diabetol. Metab. Syndr.* 10, 18.
- Barnhart, R.L., Busch, S.J., Jackson, R.L., 1989. Concentration-dependent antioxidant activity of probucol in low density lipoproteins in vitro: probucol degradation precedes lipoprotein oxidation. *J. Lipid Res.* 30, 1703–1710.
- Baynes, J.W., 1991. Role of oxidative stress in development of complications in diabetes. *Diabetes* 40, 405–412.
- Betge, S., Lutz, K., Roskos, M., Figulla, H.-R., 2007. Oral treatment with probucol in a pharmacological dose has no beneficial effects on mortality in chronic ischemic heart failure after large myocardial infarction in rats. *Eur. J. Pharmacol.* 558, 119–127.
- Birben, E., Sahiner, U.M., Sackesen, C., Erzurum, S., Kalayci, O., 2012. Oxidative stress and antioxidant defense. *World Allergy Organ. J.* 5, 9.
- Brunauer, S., Emmett, P.H., Teller, E., 1938. Adsorption of gases in multimolecular layers. *J. Am. Chem. Soc.* 60, 309–319.
- Chartoumpakis, D., Ziros, P.G., Psyrriannis, A., Kyriazopoulou, V., Papavassiliou, A.G., Habeos, I.G., 2010. Simvastatin lowers reactive oxygen species level by Nrf2 activation via PI3K/Akt pathway. *Biochem. Biophys. Res. Commun.* 396, 463–466.
- Cobourne-Duval, M.K., Taka, E., Mendonca, P., Bauer, D., Soliman, K.F., 2016. The antioxidant effects of thymoquinone in activated BV-2 murine microglial cells. *Neurochem. Res.* 41, 3227–3238.
- Colle, D., Santos, D.B., Moreira, E.L.G., Hartwig, J.M., dos Santos, A.A., Zimmermann, L.T., Hort, M.A., Farina, M., 2013. Probuco increases striatal glutathione peroxidase activity and protects against 3-nitropropionic acid-induced pro-oxidative damage in rats. *PLoS One* 8, e67658.
- Cordeiro, T., Santos, A.F., Nunes, G., Cunha, G., Sotomayor, J., Fonseca, I.M., Danêde, F., Dias, C., Cardoso, M.M., Correia, N., 2016. Accessing the physical state and molecular mobility of naproxen confined to nanoporous silica matrices. *J. Phys. Chem. C* 120, 14390–14401.
- Day, B.J., 2004. Catalytic antioxidants: a radical approach to new therapeutics. *Drug Discov. Today* 9, 557–566.
- de Cavanagh, E.M., Inseera, F., Toblli, J., Stella, I., Fraga, C.G., Ferder, L., 2001. Enalapril attenuates oxidative stress in diabetic rats. *Hypertension* 38, 1130–1136.
- Di Meo, S., Reed, T.T., Venditti, P., Victor, V.M., 2016. Role of ROS and RNS sources in physiological and pathological conditions. *Oxidative Med. Cell. Longev.* 2016.
- Gerber, J.J., Cairn, M.R., Lötter, A.P., 1993. Structures of two conformational polymorphs of the cholesterol-lowering drug probucol. *J. Crystallogr. Spectrosc. Res.* 23, 863–869.
- Grün, M., Unger, K.K., Matsumoto, A., Tsutsumi, K., 1999. Novel pathways for the preparation of mesoporous MCM-41 materials: control of porosity and morphology. *Microporous Mesoporous Mater.* 27, 207–216.
- Holvoet, P., 2008. Relations between metabolic syndrome, oxidative stress and inflammation and cardiovascular disease. *Verh. K. Acad. Geneesk. Belg.* 70, 193–219.
- Horwitz, L.D., Wallner, J.S., Decker, D.E., Buxser, S.E., 1996. Efficacy of lipid soluble, membrane-protective agents against hydrogen peroxide cytotoxicity in cardiac myocytes. *Free Radic. Biol. Med.* 21, 743–753.
- Hu, Y., Zhi, Z., Zhao, Q., Wu, C., Zhao, P., Jiang, H., Jiang, T., Wang, S., 2012. 3D cubic mesoporous silica microsphere as a carrier for poorly soluble drug carvedilol. *Microporous Mesoporous Mater.* 147, 94–101.
- Jangra, S., Girotra, P., Chhokar, V., Tomer, V., Sharma, A., Duhan, S., 2016. In-vitro drug release kinetics studies of mesoporous SBA-15-azathioprine composite.
- Kizhakekuttu, T.J., Widlansky, M.E., 2010. Natural antioxidants and hypertension: promise and challenges. *Cardiovasc. Ther.* 28, e20–e32.
- Kjellman, T., Xia, X., Alfredsson, V., Garcia-Bennett, A.E., 2014. Influence of microporosity in SBA-15 on the release properties of anticancer drug dasatinib. *J. Mater. Chem. B* 2, 5265–5271.
- Kruk, M., Jaroniec, M., Ko, C.H., Ryoo, R., 2000. Characterization of the porous structure of SBA-15. *Chem. Mater.* 12, 1961–1968.
- Kukin, M.L., Kalman, J., Charney, R.H., Levy, D.K., Buchholz-Varley, C., Ocampo, O.N., Eng, C., 1999. Prospective, randomized comparison of effect of long-term treatment with metoprolol or carvedilol on symptoms, exercise, ejection fraction, and oxidative stress in heart failure. *Circulation* 99, 2645–2651.
- Kuzuya, M., Kuzuya, F., 1993. Probuco as an antioxidant and antiatherogenic drug. *Free Radic. Biol. Med.* 14, 67–77.
- Li, J., Yang, Y., Zhao, M., Xu, H., Ma, J., Wang, S., 2017. Improved oral bioavailability of probucol by dry media-milling. *Mater. Sci. Eng. C* 78, 780–786.
- Mahajan, A.S., Babbar, R., Kansal, N., Agarwal, S.K., Ray, P.C., 2007. Antihypertensive and antioxidant action of amlodipine and vitamin C in patients of essential hypertension. *J. Clin. Biochem. Nutr.* 40, 141–147.
- Maleki, A., Hamidi, M., 2016. Dissolution enhancement of a model poorly water-soluble drug, atorvastatin, with ordered mesoporous silica: comparison of MSF with SBA-15 as drug carriers. *Expert Opin. Drug Deliv.* 13, 171–181.
- Maleki, A., Kettiger, H., Schoubben, A., Rosenholm, J.M., Ambrogio, V., Hamidi, M., 2017. Mesoporous silica materials: from physico-chemical properties to enhanced dissolution of poorly water-soluble drugs. *J. Control. Release* 262, 329–347.
- Manzano, M., Aina, V., Arcan, C., Balas, F., Cauda, V., Colilla, M., Delgado, M., Vallet-Regi, M., 2008. Studies on MCM-41 mesoporous silica for drug delivery: effect of particle morphology and amine functionalization. *Chem. Eng. J.* 137, 30–37.
- McCarthy, C.A., Ahern, R.J., Devine, K.J., Crean, A.M., 2017. Role of drug adsorption onto the silica surface in drug release from mesoporous silica systems. *Mol. Pharm.* 15, 141–149.
- Moris, D., Spartalis, M., Spartalis, E., Karachaliou, G.-S., Karaolanis, G.I., Tsuroufils, G., Tsilimigras, D.I., Tzatzaki, E., Theocharis, S., 2017. The role of reactive oxygen species in the pathophysiology of cardiovascular diseases and the clinical significance of myocardial redox. *Ann. Transl. Med.* 5.
- Nielsen, F.S., Petersen, K.B., Müllertz, A., 2008. Bioavailability of probucol from lipid and surfactant based formulations in minipigs: influence of droplet size and dietary state. *Eur. J. Pharm. Biopharm.* 69, 553–562.
- O'Brien, R.C., Luo, M., Balazs, N., Mercuri, J., 2000. In vitro and in vivo antioxidant properties of gliclazide. *J. Diabetes Complicat.* 14, 201–206.
- Padayatty, S.J., Katz, A., Wang, Y., Eck, P., Kwon, O., Lee, J.-H., Chen, S., Corpe, C., Dutta, A., Dutta, S.K., 2003. Vitamin C as an antioxidant: evaluation of its role in disease prevention. *J. Am. Coll. Nutr.* 22, 18–35.
- Popa-Wagner, A., Mitran, S., Sivanesan, S., Chang, E., Buga, A.-M., 2013. ROS and brain diseases: the good, the bad, and the ugly. *Oxidative Med. Cell. Longev.* 2013.
- Pourova, J., Kottova, M., Voprsalova, M., Pour, M., 2010. Reactive oxygen and nitrogen species in normal physiological processes. *Acta Physiol.* 198, 15–35.
- Prasad, B.R., Lele, S., 1994. Stabilization of the amorphous phase inside carbon nanotubes: solidification in a constrained geometry. *Philos. Mag. Lett.* 70, 357–361.
- Ravikovich, P.I., Vishnyakov, A., Neimark, A.V., Ribeiro Carrott, M.M.L., Russo, P.A., Carrott, P.J., 2006. Characterization of micro-mesoporous materials from nitrogen and toluene adsorption: experiment and modeling. *Langmuir* 22, 513–516.
- Redón, J., Oliva, M.R., Tormos, C., Giner, V., Chaves, J., Iradi, A., Sáez, G.T., 2003. Antioxidant activities and oxidative stress byproducts in human hypertension. *Hypertension* 41, 1096–1101.
- Rengarajan, G., Enke, D., Steinhart, M., Beiner, M., 2008. Stabilization of the amorphous state of pharmaceuticals in nanopores. *J. Mater. Chem.* 18, 2537–2539.
- Rodrigo, R., Prat, H., Passalacqua, W., Araya, J., Guichard, C., Bächler, J.P., 2007. Relationship between oxidative stress and essential hypertension. *Hypertens. Res.* 30, 1159.
- Shaji, C.A., Robinson, B.D., Yeager, A., Beeram, M.R., Davis, M.L., Isbell, C.L., Huang, J.H., Tharakan, B., 2019. The tri-phasic role of hydrogen peroxide in blood-brain barrier endothelial cells. *Sci. Rep.* 9, 133.
- Singh, R., Gupta, B., Tripathi, K., Singh, S., 2016. Anti oxidant potential of metformin and pioglitazone in type 2 diabetes mellitus: beyond their anti glycaemic effect. *Diabetes Metab. Syndr. Clin. Res. Rev.* 10, 102–104.
- Tanaka, Y., Inkyo, M., Yumoto, R., Nagai, J., Takano, M., Nagata, S., 2012. Nanoparticulation of probucol, a poorly water-soluble drug, using a novel wet-milling process to improve in vitro dissolution and in vivo oral absorption. *Drug Dev. Ind. Pharm.* 38, 1015–1023.
- Thameem Dheen, S., Kaur, C., Ling, E.-A., 2007. Microglial activation and its implications in the brain diseases. *Curr. Med. Chem.* 14, 1189–1197.
- Thybo, P., Pedersen, B.L., Hovgaard, L., Holm, R., Müllertz, A., 2008. Characterization and physical stability of spray dried solid dispersions of probucol and PVP-K30. *Pharm. Dev. Technol.* 13, 375–386.
- Wassmann, S., Laufs, U., Müller, K., Konkol, C., Ahlborn, K., Bäumer, A.T., Linz, W., Böhm, M., Nickenig, G., 2002. Cellular antioxidant effects of atorvastatin in vitro and in vivo. *Arterioscler. Thromb. Vasc. Biol.* 22, 300–305.
- Witasz, E., Kupferschmidt, N., Bengtsson, L., Hultenby, K., Smedman, C., Paulie, S., Garcia-Bennett, A.E., Fadeel, B., 2009. Efficient internalization of mesoporous silica particles of different sizes by primary human macrophages without impairment of macrophage clearance of apoptotic or antibody-opsonized target cells. *Toxicol. Appl. Pharmacol.* 239, 306–319.
- Wu, S.-H., Mou, C.-Y., Lin, H.-P., 2013. Synthesis of mesoporous silica nanoparticles. *Chem. Soc. Rev.* 42, 3862–3875.
- Xu, W., Riikonen, J., Lehto, V.-P., 2013. Mesoporous systems for poorly soluble drugs. *Int. J. Pharm.* 453, 181–197.
- Yamashita, S., Masuda, D., Matsuzawa, Y., 2015. Did we abandon probucol too soon? *Curr. Opin. Lipidol.* 26, 304–316.
- Zhang, Z., Jiang, S., Liu, Z., Niu, B., Gu, W., Li, Y., Cui, J., 2014. Directed self-assembled nanoparticles of probucol improve oral delivery: fabrication, performance and correlation. *Pharm. Res.* 31, 2266–2275.

## 4.4 Additional discussion

In this study, PB was loaded as an amorphous form within MSPs with key differences in their pore diameters ( $\phi$ ). At the equivalent loading amount of 20 wt%, no melting endotherm was observed from drug loaded samples in MCM-41 ( $\phi$  3.2 nm), AMS-6 ( $\phi$  4.7 nm) and SBA-15 ( $\phi$  10.5 nm). Loading of the drug compound in the amorphous form within MSPs is based on the principles of equilibrium thermodynamics, where suppression of crystallisation is achieved by the critical pore diameter of the carrier [32]. Specifically, a pore diameter that is below the critical nucleation size of a drug compound is required to suppress the formation of nuclei and crystal growth [32]. The critical pore diameter has been previously calculated for a range of drug compounds, and can be used as a guide in selecting a MSP with the suitable pore size for the loading of the drug in the amorphous form (Table 4.3) [33].

Pharmaceutical drug	Molecular weight (g/mol) *	Log P *	Aqueous solubility (mg/ml)*	Calculated critical pore diameter (nm)	Mesoporous silica, pore diameter (nm)	Key finding	Reference
Haloperidol	375.9	3.7	0.004	8.4	Parateck SLC 500 – 6.10	Drug loaded in amorphous form within MSP with pore diameter < calculated critical pore diameter.	[33]
Carbamazepine	236.3	2.8	0.15	17.6	Syloid XDP 3050 – 17.90		
Benzamide	317.8	0.85	0.06	29.5	Neusilin US2 – 18.76 Aeroperl 300- 30.12		
Ezetimibe	409.4	4.6	0.008	4.5	Neusilin US2 – 5 Aeroperl 300- 30	Neusilin US2 maintained drug in amorphous form due to restriction in molecular mobility.	[34]
Nifedipine	346.3	2.20	0.018	18	Xerogel- 2.5	Critical nucleation size was below the pore diameter of the MSP.	[35]
Acetaminophen	151.1	0.51	4.2	3.6	Controlled porous glasses (CPG) – 4.6	Reduction in molecular mobility of drug loaded within CPG prevented drug re-crystallisation.	[36]

\*values taken from drugbank [37].

**Table 4.3:** Studies that have investigated the effect of pore diameter and the physical form of the loaded drug within MSPs. In general, drug compounds were loaded in the amorphous form within MSPs with pore size diameter less than the calculated critical pore diameter of the drug compound.

At higher loadings of PB, complete pore filling of mesopores resulted in the crystallisation of the drug on the external surface of all the MSPs. In silica particles with a lower pore volume such as MCM-41 (0.5 cm<sup>3</sup>/g) mesopore filling occurred at a lower drug loading (~20 wt %) compared to 30 wt% for SBA-15 (0.9 cm<sup>3</sup>/g) and AMS-6 (0.7 cm<sup>3</sup>/g). DSC scans of the drug loaded samples are shown below (Figure 4.1).



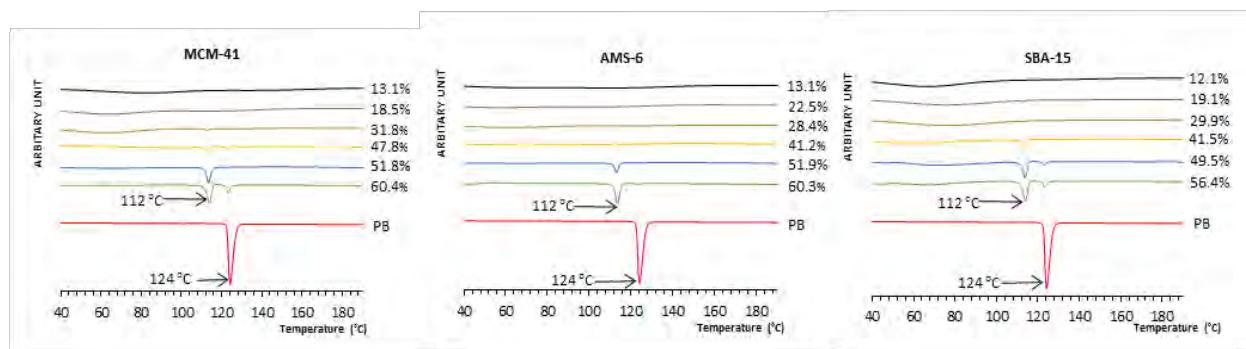


**Figure 4.1:** DSC scans of PB loaded within mesoporous silica MCM-41, AMS-6, and SBA-15 showing the shift to a lower melting point (~ 112 °C) compared to the commercially available crystalline PB (~124 °C). This suggest PB crystallised to polymorph II crystals in drug loaded MSP samples compared to form I polymorph of crystalline PB [38]. The presence of two melting point temperatures in high drug loaded samples > 50 wt% suggest the presence of both PB crystal polymorphs in the sample.

In vitro drug release measurements of PB showed a rapid initial burst release, followed by the slower rate of diffusion of the remaining drug. The initial burst release suggests the amorphous drug is likely to be located near the surface of the mesopores where it is easily accessible to the dissolution medium. In samples where PB was loaded above the critical loading amount of the MSP, a reduction in the % PB released in dissolution medium was observed due to the presence of crystalline drug on the exterior particle surface (Figure 4.2). At the higher drug loadings, the release profile follows a zero order release similar to crystalline PB. This finding is consistent with other encapsulations, where the crystallisation of the compound above MSP pore capacity leads to a reduction in the release kinetics [39-41].

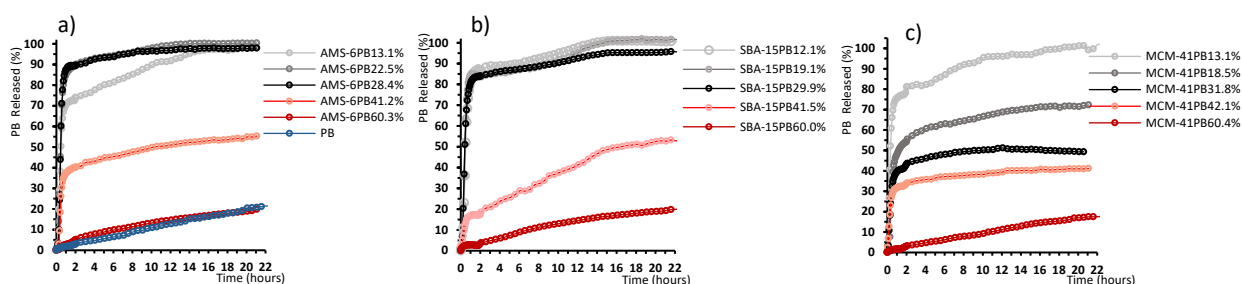


**Figure 4.2:** Drug release curves of PB released from AMS-6 (a), SBA-15 (b), and MCM-41 (c) mesoporous silica particles as compared to crystalline PB.

Further experiments were conducted to determine whether PB can be loaded in an amorphous form within a larger pore size MSP, such as the commercially available MSP Syloid® (W.R. Grace – Surface area 274.8 m<sup>2</sup>/g, pore size 40 nm, pore volume 1.6 cm<sup>3</sup>/g) (Table 4.4). At a similar loading amount of 28.5 wt%, the recrystallisation of PB was evident from diffraction peaks in the XRD of the loaded sample (Figure 4.3a). PB released from Syloid followed a zero order release kinetics similar to the crystalline drug, in contrast to the burst release of PB from AMS-6 and SBA-15 (Figure 4.3b). No saturation in pore volume and surface area was observed from nitrogen sorption analysis

of the SyloidPB28.5% loading. The critical pore size needed to suppress crystallisation of PB is not met by Syloid ( $\phi$  40 nm), and is likely to be between 10-40 nm.

MSP	Surface area (m <sup>2</sup> /g)	Pore size (nm)	Pore volume (cm <sup>3</sup> /g)
Syloid	274.8	40	1.6
SyloidPB28.5%	139.3	38	0.9

**Table 4.4** Textural properties of Syloid before and after loading PB at 28.5 wt% as measured by nitrogen adsorption/desorption isotherm.

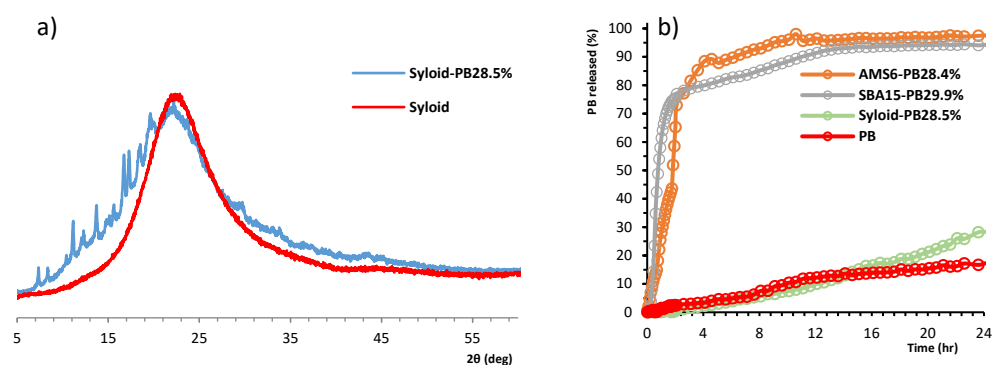


**Figure 4.3:** a) XRD scans of syloid and syloidPB28.5%. PB was loaded within the MSP in the crystalline form as observed by the presence of bragg diffraction peaks. b) Drug release measurements comparing the release of PB from AMS-6, SBA-15, and syloid at the equivalent loading amount of 30 wt%. The release of crystalline PB is shown in red.

From these results, different formulations of PB could be developed based on the pore size of MSP, for example a slower sustained release of PB from MSP with a large pore size (e.g. 20-30 nm) as compared to a rapid burst release profile from MSP with smaller pore size (5-10 nm). Further studies would be needed to calculate the critical pore size of MSP for the loading of PB more precisely, along with characterisation and dissolution experiments in the development of formulations for oral administration with controlled drug release properties.

*In vivo* bioavailability studies were conducted in rats to determine the pharmacokinetic properties of PB released from MSP [42]. AMS-6PB 34.8% was chosen as the drug was loaded in the amorphous form and results from *in vitro* dissolution experiments showed an enhancement in drug release was achieved compared to crystalline PB. The  $C_{max}$  for AMS-6PB 34.8% and for crystalline PB were 229.71 ng/ml and 30.89 ng/ml respectively, which represented a 7 times increase in bioavailability (Figure 4.4). The reduction in  $t_{max}$ , and  $t_{1/2}$  in PB released from AMS-6 indicate a rapid dissolution, adsorption and distribution of the drug compared to crystalline PB. This finding is consistent with an enhancement in dissolution and oral bioavailability of a range of poorly soluble drug compounds released from

MSPs, showing good correlation between in vitro and in vivo results [43, 44]. For example, a recent study demonstrated an enhancement in drug release and oral bioavailability of a practically insoluble antiviral drug compound, velpatasvir (0.00585 mg/ml), with an approximate 2 fold increase in bioavailability of the drug released from MSP compared to the crystalline drug [44]. While the pharmacokinetic properties of PB released from AMS-6 was lower than the reported values of different PB formulations listed in Table 4.1, encapsulation of PB within the mesopores offer a key advantage as it requires a simple, single drug loading procedure in the preparation of the oral formulation that avoids the need for multiple preparation steps.

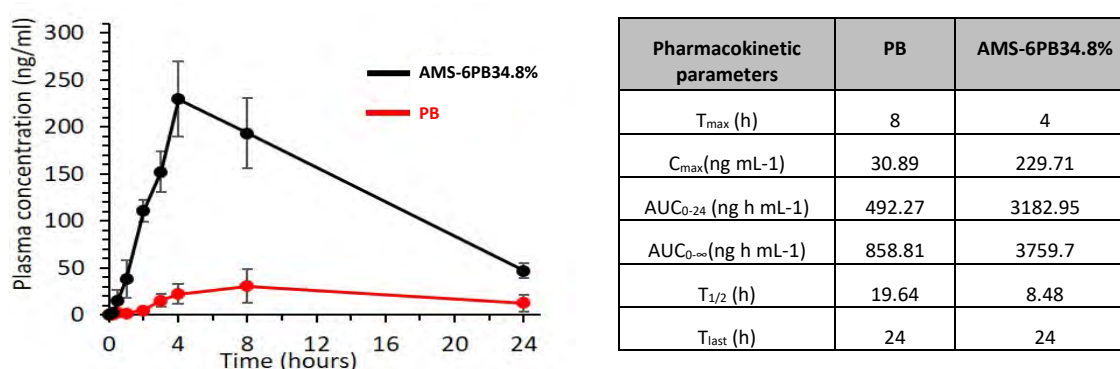


**Figure 4.4:** Plasma PB concentration for crystalline PB (10 mg) and PB released from MSP, AMS-6 (equivalent 10 mg dose) after a single-dose oral administration to Sprague dawley rats.  $C_{max}$ , maximum plasma concentration;  $T_{max}$ , time to achieve maximum plasma concentration,  $t_{1/2}$ , terminal half-life;  $AUC_{0-24h}$ , area under the plasma concentration time curve from zero to 24 hr observation period;  $AUC_{0-\infty}$ , area under the plasma concentration time curve from time zero to extrapolated infinity;  $t_{last}$ , last time point.

The antioxidant properties of PB released from AMS-6 were compared to crystalline PB in two in vitro models of cellular oxidative. In the first model, levels oxidative stress in human brain endothelial cells were measured with the treatment of hydrogen peroxide and test compounds, and in the second in vitro model LPS was used to generate oxidative stress in microglia cells. In both models PB released from AMS-6 was more effective in reducing the percentage of cells under oxidative stress as compared to crystalline PB. Previous studies have shown PB is a scavenger of ROS including the superoxide anion [45], hydrogen peroxide [46] and the hydroxyl radical [47]. In those studies, PB was typically dissolved in organic solvents ethanol, DMSO or lipids [47-49]. Furthermore, a long pre-incubation time of up to 12 hours was required in some cases to observe a positive antioxidant effect, likely due to rapid crystallisation of PB in cell culture media [49]. The results from this study show that PB released from AMS-6 protected against cellular oxidative stress in both cellular models of oxidative stress, a promising result that led us to further study the antioxidant properties of PB in an in vitro neuroinflammation model of the BBB.



## 4.5 Conclusion

PB was loaded in the amorphous form within MSPs with well-defined pore sizes in MCM-41 (3.2 nm) AMS-6 (4.7 nm) and SBA-15 (10.5 nm) at approximate drug loading of 30 wt%. The release of PB was significantly enhanced from MSP as compared to crystalline PB. The larger pore size Syloid material (40nm) resulted in a loading of PB as a crystalline polymorph at the drug loading of 28.5%. The drug release profile of SyloidPB-28.5% followed a linear zero-order kinetics similar to the crystalline drug. Oral formulations of PB can be developed with different drug release kinetics by loading PB in MSP with different pore sizes. A significant 7-fold enhancement in oral pharmacokinetic properties *in vivo* was observed for PB released from AMS-6 as compared to crystalline PB. Furthermore, the enhancement in antioxidant property of PB released from AMS-6 was observed from *in vitro* models of cellular oxidative stress as compared to crystalline PB.

## 4.6 References

1. Zimetbaum, P., H. Eder, and W. Frishman, *Probucol: pharmacology and clinical application*. The Journal of Clinical Pharmacology, 1990. **30**(1): p. 3-9.
2. Beynen, A., *Mode of hypocholesterolemic action of probucol in animals and man*. Artery, 1987. **14**(2): p. 113-126.
3. Nestel, P.J. and T. Billington, *Effects of probucol on low density lipoprotein removal and high density lipoprotein synthesis*. Atherosclerosis, 1981. **38**(1-2): p. 203-209.
4. Atmeh, R.F., et al., *The hypolipidemic action of probucol: a study of its effects on high and low density lipoproteins*. Journal of lipid research, 1983. **24**(5): p. 588-595.
5. Kesäniemi, Y. and S.M. Grundy, *Influence of probucol on cholesterol and lipoprotein metabolism in man*. Journal of Lipid Research, 1984. **25**(8): p. 780-790.
6. Mellies, M.J., et al., *Effects of probucol on plasma cholesterol, high and low density lipoprotein cholesterol, and apolipoproteins A1 and A2 in adults with primary familial hypercholesterolemia*. Metabolism, 1980. **29**(10): p. 956-964.
7. Yamashita, S. and Y. Matsuzawa, *Where are we with probucol: a new life for an old drug?* Atherosclerosis, 2009. **207**(1): p. 16-23.
8. McCaughan, D., *Nine years of treatment with probucol*. Artery, 1982. **10**(1): p. 56-70.
9. Liu, J., et al., *Effects of probucol on restenosis after percutaneous coronary intervention: a systematic review and meta-analysis*. PloS one, 2015. **10**(4): p. e0124021.
10. Yang, S., et al., *Probucol ameliorates renal injury in diabetic nephropathy by inhibiting the expression of the redox enzyme p66Shc*. Redox biology, 2017. **13**: p. 482-497.
11. Mamo, J.C., et al., *Probucol prevents blood-brain barrier dysfunction and cognitive decline in mice maintained on pro-diabetic diet*. Diabetes and Vascular Disease Research, 2019. **16**(1): p. 87-97.
12. Steinberg, D., S. Parthasarathy, and T.E. Carew, *In vivo inhibition of foam cell development by probucol in Watanabe rabbits*. The American Journal of Cardiology, 1988. **62**(3): p. B6-B12.
13. Sasahara, M., et al., *Inhibition of hypercholesterolemia-induced atherosclerosis in the nonhuman primate by probucol. I. Is the extent of atherosclerosis related to resistance of LDL to oxidation?* The Journal of clinical investigation, 1994. **94**(1): p. 155-164.
14. Tardif, J.-C., et al., *Effects of AGI-1067 and probucol after percutaneous coronary interventions*. Circulation, 2003. **107**(4): p. 552-558.
15. Stocker, R., *Molecular mechanisms underlying the antiatherosclerotic and antidiabetic effects of probucol, succinobucol, and other probucol analogues*. Current opinion in lipidology, 2009. **20**(3): p. 227-235.
16. Betge, S., et al., *Oral treatment with probucol in a pharmacological dose has no beneficial effects on mortality in chronic ischemic heart failure after large myocardial infarction in rats*. European journal of pharmacology, 2007. **558**(1-3): p. 119-127.
17. Yamashita, S., D. Masuda, and Y. Matsuzawa, *Did we abandon probucol too soon?* Current opinion in lipidology, 2015. **26**(4): p. 304-316.
18. Marshall, F., *Pharmacology and toxicology of probucol*. Artery, 1982. **10**(1): p. 7-21.
19. Zhang, Z., et al., *A high-drug-loading self-assembled nanoemulsion enhances the oral absorption of probucol in rats*. Journal of Pharmaceutical Sciences, 2013. **102**(4): p. 1301-1306.
20. Li, J., et al., *Improved oral bioavailability of probucol by dry media-milling*. Materials Science and Engineering: C, 2017. **78**: p. 780-786.

21. Zhang, Z., et al., *Directed self-assembled nanoparticles of probucol improve oral delivery: fabrication, performance and correlation*. Pharmaceutical research, 2014. **31**(9): p. 2266-2275.
22. Tanaka, Y., et al., *Nanoparticulation of probucol, a poorly water-soluble drug, using a novel wet-milling process to improve in vitro dissolution and in vivo oral absorption*. Drug development and industrial pharmacy, 2012. **38**(8): p. 1015-1023.
23. Gumaste, S.G. and A.T. Serajuddin, *Development of solid SEDDS, VII: Effect of pore size of silica on drug release from adsorbed self-emulsifying lipid-based formulations*. European Journal of Pharmaceutical Sciences, 2017. **110**: p. 134-147.
24. Gumaste, S.G., B.O. Freire, and A.T. Serajuddin, *Development of solid SEDDS, VI: Effect of precoat of Neusilin® US2 with PVP on drug release from adsorbed self-emulsifying lipid-based formulations*. European Journal of Pharmaceutical Sciences, 2017. **110**: p. 124-133.
25. Nowak, R., Z. Iqbal, and N. Chavan, *Extended release formulations of cannabinoids*. 2020, Google Patents.
26. Maleki, A., et al., *Mesoporous silica materials: From physico-chemical properties to enhanced dissolution of poorly water-soluble drugs*. Journal of Controlled Release, 2017. **262**: p. 329-347.
27. Van Speybroeck, M., et al., *Ordered mesoporous silica material SBA-15: a broad-spectrum formulation platform for poorly soluble drugs*. Journal of pharmaceutical sciences, 2009. **98**(8): p. 2648-2658.
28. Shen, S.-C., W.K. Ng, and L. Chia, *Mesoporous material excipients for poorly aqueous soluble ingredients*. 2014, Google Patents.
29. Li, Y., Z. Zhang, and Z. Liu, *Use of probucol and derivatives thereof for anti-tumour metastasis* 2014.
30. Zhou, C., X. Xia, and A.E. Garcia-Bennett, *Super-saturating delivery vehicles for poorly water-soluble pharmaceutical and cosmetic active ingredients and suppression of crystallization of pharmaceutical active ingredients*. 2017, Google Patents.
31. Lively, S. and L.C. Schlichter, *Microglia responses to pro-inflammatory stimuli (LPS, IFN $\gamma$ + TNF $\alpha$ ) and reprogramming by resolving cytokines (IL-4, IL-10)*. Frontiers in Cellular Neuroscience, 2018. **12**: p. 215.
32. Hamilton, B.D., et al., *Manipulating crystal growth and polymorphism by confinement in nanoscale crystallization chambers*. Accounts of Chemical Research, 2012. **45**(3): p. 414-423.
33. Vraníková, B., et al., *Relevance of the theoretical critical pore radius in mesoporous silica for fast crystallizing drugs*. International Journal of Pharmaceutics, 2020. **591**: p. 120019.
34. Knapik, J., et al., *Stabilization of the amorphous ezetimibe drug by confining its dimension*. Molecular Pharmaceutics, 2016. **13**(4): p. 1308-1316.
35. Godec, A., et al., *Vitrification from solution in restricted space: formation and stabilization of amorphous nifedipine in a nanoporous silica xerogel carrier*. International journal of pharmaceutics, 2007. **343**(1-2): p. 131-140.
36. Rengarajan, G., et al., *Stabilization of the amorphous state of pharmaceuticals in nanopores*. Journal of Materials Chemistry, 2008. **18**(22): p. 2537-2539.
37. Analytics, O.P.H. *Drugbank*. 2020 07/2020]; Available from: <https://go.drugbank.com/>.
38. Gerber, J., M. Caira, and A. Lötter, *Structures of two conformational polymorphs of the cholesterol-lowering drug probucol*. Journal of crystallographic and spectroscopic research, 1993. **23**(11): p. 863-869.
39. Shen, S.C., et al., *Physical state and dissolution of ibuprofen formulated by co-spray drying with mesoporous silica: effect of pore and particle size*. Int J Pharm, 2011. **410**: p. 188-195.
40. Zhang, Y., et al., *Spherical mesoporous silica nanoparticles for loading and release of the poorly water-soluble drug telmisartan*. J Control Release, 2010. **145**: p. 257-263.
41. Mellaerts, R., et al., *Enhanced release of itraconazole from ordered mesoporous SBA-15 silica materials*. Chemical Communications, 2007(13): p. 1375-1377.

42. Giri, K., et al., *A lysozyme corona complex for the controlled pharmacokinetic release of probucol from mesoporous silica particles*. Biomaterials Science, 2020. **8**(14): p. 3800-3803.
43. Ren, X., et al., *Mesoporous silica nanospheres as nanocarriers for poorly soluble drug itraconazole with high loading capacity and enhanced bioavailability*. Microporous and Mesoporous Materials, 2020: p. 110389.
44. Mehmood, Y., et al., *In-Vitro and In-Vivo Evaluation of Velpatasvir-Loaded Mesoporous Silica Scaffolds. A Prospective Carrier for Drug Bioavailability Enhancement*. Pharmaceutics, 2020. **12**(4): p. 307.
45. Bridges, A., N. Scott, and J. Belch, *Probucol, a superoxide free radical scavenger in vitro*. Atherosclerosis, 1991. **89**(2): p. 263-265.
46. Sheng, L., et al., *Probucol inhibits hydrogen peroxide to induce apoptosis of vascular smooth muscle cells*. Molecular Medicine Reports, 2013. **7**(4): p. 1185-1190.
47. Barnhart, R.L., S.J. Busch, and R.L. Jackson, *Concentration-dependent antioxidant activity of probucol in low density lipoproteins in vitro: probucol degradation precedes lipoprotein oxidation*. Journal of lipid research, 1989. **30**(11): p. 1703-1710.
48. McLean, L.R. and K.A. Hagaman, *Effect of probucol on the physical properties of low-density lipoproteins oxidized by copper*. Biochemistry, 1989. **28**(1): p. 321-327.
49. Kuzuya, M., et al., *Probucol prevents oxidative injury to endothelial cells*. Journal of lipid research, 1991. **32**(2): p. 197-204.

# 5

## Exploring the pharmacological properties of drug compounds released from mesoporous silica for the treatment of neuroinflammation.

### 5.1 Introduction

Endothelial cells play a key role in the development and function of blood and lymph systems. They form the physical barrier between blood and the brain interstitial fluid, playing an important role in restricting the passage of molecules that can cause harm to the brain, while also facilitating the movement of essential nutrients across the blood brain barrier (BBB) [1]. Endothelial cells are also among the first cells to be exposed to pro-inflammatory stimuli such as bacterial or viral pathogens [2]. This stimulus can elicit a strong immunological response in the host cell, increasing the production of reactive oxygen species (ROS) and inflammatory mediators which act as messengers that either activate the host defense mechanisms or recruit professional immune cells to contain and eliminate the pro-inflammatory stimuli. The released ROS is kept within normal physiological concentrations by antioxidants, and participate in many cellular functions including maintaining the integrity of the BBB, immune responses, and controlling the dynamics between cell viability and apoptosis [3].

Cyclooxygenases (COX) are pro-oxidant enzymes, producing the superoxide anion, the main oxidant from the metabolism of arachidonic acid and its conversion to prostaglandins [4, 5]. The superoxide anion, is the primary ROS released from the respiratory transport chain of the mitochondria. It is rapidly converted to the more reactive hydrogen peroxide and peroxy radicals [6]. Inhibition of COX-2, the primary cyclooxygenase involved in inflammation, prevents the production of prostaglandins, thereby reducing inflammation. However, COX-2-independent mechanisms are also known to be relevant in the regulation of pro-inflammatory molecules in neurodegenerative processes of several acute and chronic diseases [7].

Chronic exposure to high doses of pro-inflammatory stimuli can induce excessive cellular oxidative stress and inflammation. In the context of the BBB, cells under oxidative stress produce and release high concentrations of

ROS that affect its integrity due to oxidation of tight junction proteins, leading to cell apoptosis via oxidation of biological membranes, DNA, proteins and lipids [8]. The increase in BBB permeability is a key event in the pathogenesis of neuroinflammatory diseases including Parkinson's, Alzheimer's, and multiple sclerosis [9, 10]. Thus, it is crucial to investigate potential pharmaceutical compounds containing a combination of antioxidant and anti-inflammatory properties that can sustain the integrity of the BBB [11, 12].

One approach is the use of COX inhibitors. The formation of prostaglandin E<sub>2</sub> (PGE<sub>2</sub>) by the COX dependent pathway in endothelial cells has been found to mediate the inflammatory response in immunologically challenged mice with a peripheral injection of lipopolysaccharide (LPS), a bacterial endotoxin that binds to the toll like receptor 4 (TLR4) on the surface of endothelial cells, initiating the production of inflammatory mediators and reactive oxygen species (ROS) [13-16]. Furthermore, PGE<sub>2</sub> is known to disrupt the integrity of the BBB by promoting vasodilation, increase in vascular permeability, and edema [12, 17]. Thus, inhibition of PGE<sub>2</sub> producing COX enzymes has been shown to attenuate the inflammatory response [12, 18, 19].

Indomethacin (INDO) is a nonsteroidal anti-inflammatory drug and a non-selective COX enzyme inhibitor [20]. INDO has been shown previously to be effective in the partial reduction of LPS induced dysfunctions of the BBB, including *in vitro* disruption and *in vivo* impaired amyloid  $\beta$  peptide efflux [11, 18, 21]. In contrast, the diphenolic compound probucol, has been shown to attenuate the increase in activity of the COX-2 enzyme, as well as pro-inflammatory marker expression, leading to decreases in the disruption to BBB integrity in mice under a high saturated fat diet [22-24]. Additionally, PB is a potent free radical scavenger, and is oxidised by free radicals in the formation of stable metabolites, protecting biological molecules and cellular membranes against oxidative damage [25, 26]. However, PB is a highly lipophilic and poorly soluble drug compound requiring a long pre-incubation time of up to 8 hours at a high dosage of 50  $\mu$ M in order for a sufficient amount of drug to be transported into endothelial cells [24]. A lipophilic drug carrier either from a dietary source or in a drug formulation is required to facilitate the absorption of PB from an oral administration, limiting its current application in the treatment of metabolic and vascular diseases, as well as its potential in combating neuroinflammatory diseases.

Mesoporous silica materials with defined pore structures [27-29], tunable pore sizes, and high surface area are known to enhance the solubility of a range of poorly soluble antioxidant and anti-inflammatory drugs including PB [30-35]. The delivery of poorly soluble drugs in the treatment of neurodegenerative diseases has been investigated in the context of enhancing BBB drug transport [36-39]. Shen et al.,[40] have demonstrated the

enhanced delivery of the antioxidant resveratrol (RSV) loaded at very low levels (1.6%wt), using a combination of polylactic acid and low-density lipoprotein receptors coated on mesoporous particles (200 nm average particle diameter, 4 nm pore size) across an *in vitro* BBB endothelial/microglia cell model. The released RSV decreased oxidative stress of lipopolysaccharide (LPS) activated microglia cells, specifically reducing levels of inducible nitric oxide synthase enzyme. The aqueous solubility of RSV is 0.03 mg/mL, whilst that of INDO and PB are 0.0024 mg/mL and 4.18e-05 mg/mL, respectively. Enhancing the solubility profile of these inhibitors of COX enzyme activity, will allow to assess potential therapeutic uses of these compounds and expand the library of potent antioxidants.

In this work, we develop a basic *in vitro* model of neuroinflammation using brain endothelial cells to measure levels of cellular oxidative stress and inflammation caused by LPS, with PB and INDO released from a mesoporous silica material AMS-6. This particular mesostructure is chosen because of its reproducible, scalable and easy synthesis using the amino acid derived anionic surfactant *N*-lauryl-alanine, its spherical morphology and 3-dimensionally connected cylindrical pores which afford a rapid release and dissolution profile of poorly soluble compounds [41-43]. Characterisation of endothelial cell monolayer integrity is performed using transendothelial electrical resistance (TEER) which additionally allows to assess the permeability of the monolayer. The *in vitro* model of BBB using brain endothelial cells allows for a simple and rapid investigation of the pharmacological properties of INDO and PB for the treatment of oxidative stress and inflammation mediated disruption to the BBB integrity, and findings from this work could further add to the discussion on the appropriate pharmacological treatment of neuroinflammation [12, 44].

## 5.2 Materials and method

Tetraethyl orthosilicate (TEOS) and 3-aminopropyl triethoxysilane (APTES) were purchased from Sigma Aldrich (Sydney, Australia). All chemicals and drug compounds were purchased from Sigma Aldrich (Sydney, Australia) and used without further purification. Milli-Q water was used throughout.

### ***Synthesis of AMS-6***

Details of the synthesis for AMS-6 MSP are included in chapter 2, section 2.2.1, pg.44 of the materials and methods.

### ***Scanning electron microscopy (SEM)***

Details of the SEM are included in chapter 2, section 2.6.4, pg.49 of the materials and methods.

### ***Dynamic Light Scattering (DLS)***

Experiments were performed with a Zetasizer ZS (Malvern Instruments, Worcestershire, UK), with a 173° detector angle, at 25 °C with a He-Ne laser (633 nm, 4 mW output power) as a light source. AMS-6 particles (1 mg/ml) were mixed with 1 ml filtered Milli-Q water and filled into disposable folded capillary cell (DTS1070) (Malvern Instruments).

### ***Nitrogen sorption isotherm***

Details of the N<sub>2</sub> sorption isotherm are included in chapter 2, section 2.6.5, pg.49 of the materials and methods.

### ***Drug loading***

Details of the drug loading procedure are included in chapter 2, section 2.4, pg.46 of the materials and methods. Drug loadings at the equivalent loading amount of 30 % w/w (AMS-6PB29.5% and AMS-6INDO28.4%) were chosen for the experiments in this chapter.

### ***Thermogravimetric analysis (TGA)***

Details of the TGA of samples are included in chapter 2, section 2.6.6, pg.51 of the materials and methods.

### ***Differential Scanning Calorimetry (DSC)***

Details of the DSC analysis of samples are included in chapter 2, section 2.6.7, pg.51 of the materials and methods.

### ***Powder X-ray Diffraction (XRD)***

Details of XRD analysis of samples are included in chapter 2, section 2.6.1, pg.46 of the materials and methods.



### ***Drug dissolution and release***

Drug release studies were conducted in simulated intestinal fluid (SIF) containing 0.25% (w/v) CTAB. Size 1 gelatin capsules (ProSciTech, batch: RL042, Queensland) were used to encapsulate both the pure drug and drug loaded mesoporous silica samples. Drug release was assessed under sink conditions (900 ml SIF, pH 6.8) using a UV/VIS spectrometer (Agilent, Cary 60 UV-Vis, Sydney, Australia). The release was carried out in an apparatus II dissolution bath (Agilent, 708-DS, Sydney, Australia) at a stirring rate of 50 rpm, 37°C.

### ***Cells and Cell culture***

Human brain microvascular endothelial cell were cultured in supplemented EBM-2 medium (Lonza, Basel, Switzerland; Cat. No. CC-3156) and grown on plates precoated with rat-tail collagen type I (BD Biosciences, Franklin Lakes, NJ) inside an incubator at 37°C, 5 % CO<sub>2</sub> – humidified atmosphere. Cells of passage between 6 to 8 were used for experiments.

### ***Oxidative stress and cell viability assays***

Details of the Muse® oxidative stress and cell viability assays are included in chapter 2, section 2.7.1 and 2.7.2, pg.53-54 of the materials and methods.

### ***Mitochondria hydroxyl assay***

The Mitochondrial hydroxyl radical detection assay kit (ab 219921, Abcam, Melbourne) was used to detect intracellular hydroxyl radical using the OH580 probe which is cell permeable and reacts with the hydroxyl radical to generate a red fluorescence detected at 540 nm excitation and 590 nm emission wavelengths. The protocol as recommended by the supplier was followed. The results were analysed using a microplate reader (FLUOstar OPTIMA, BMG LABTECH, Victoria, Australia).

### ***Nitric oxide assay***

Details of the nitric oxide assay are included in chapter 2, section 2.7.4, pg.55 of the materials and methods.

### ***Peroxynitrite assay***

Details of the peroxynitrite assay are included in chapter 2, section 2.7.5, pg.56 of the materials and methods.

### ***COX enzyme activity assay***

Details of the COX enzyme activity assay are included in chapter 2, section 2.7.6, pg.57 of the materials and methods.

### ***Prostaglandin E<sub>2</sub>***

Details of the prostaglandin E<sub>2</sub> assay are included in chapter 2, section 2.7.7, pg.58 of the materials and methods.

### ***TNF- $\alpha$ assay***

The human TNF- $\alpha$  ELISA kit (ab181421, Abcam, Melbourne) was used to measure levels of the cytokine in cell culture media following the incubation of endothelial cells for 24 hours with or without the test compounds. The protocol as listed in chapter 2 of the materials and methods was followed.

### ***TEER and FITC dextran permeability measurements***

Details of the TEER and FITC dextran permeability measurements are included in chapter 2, section 2.91 to section 2.9.4, pg.59 to 62 of the materials and methods.

### ***Preparation of Endothelial cells for cellular uptake of probucol***

Endothelial cells were seeded on 24 well plates at a density of  $5 \times 10^5$  cells/well. Confluent cells were treated with 1  $\mu$ g/ml LPS together with either AMS-6PB30% 10  $\mu$ M or PB 10  $\mu$ M for 2,4,6 and 24 hours. After the treatment time, media was removed and discarded, cells were washed three times with 500  $\mu$ l PBS, and cells were solubilised in 300  $\mu$ l solution of 1% NP40 for 30 minutes. After 30 minutes, 700  $\mu$ l of acetonitrile was added, the samples centrifuged for 10 minutes at 10000 rpm, filtered through a 0.45  $\mu$ m filter, and 500  $\mu$ l was transferred to HPLC vials.

### ***HPLC conditions***

Details of the HPLC conditions are included in chapter 2, section 2.10.2, pg.63 of the materials and methods.

### ***Statistical analysis***

Statistical analysis was performed using the paired sample t-test (Excel, Microsoft, USA), and probability values of  $(p) < 0.05$  was considered as statistically significant.

### 5.3 Results and discussion

Structural and porous properties of AMS-6 particles characterised by XRD, SEM and N<sub>2</sub> sorption isotherm are summarised in Figure 5.1. Pharmaceutical drug compounds INDO and PB were loaded into AMS-6 particles and the loading amount (wt%) was determined from TGA. Characterisation of the drug loaded samples are summarised in Table 5.1.

A reduction in surface area and pore volume indicates that drug loading within the pores was achieved. The lack of crystalline endotherm in the DSC traces or diffraction peaks in the high-angle XRD of loaded samples is evidence that the drug is loaded in an amorphous state (Appendix, Figure C1) [45]. As we have reported previously, drug loadings of PB above 30 wt% lead to the complete filling of the mesopore volume of AMS-6, and re-crystallisation of the drug in the exterior of the particles [46]. Therefore, to further explore their antioxidant and anti-inflammatory properties, samples with loading amounts of 29.5wt% and 28.4wt% for AMS-6PB and AMS-6INDO respectively, were chosen.

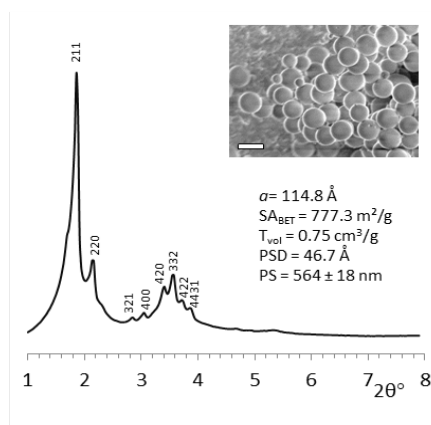


**Figure 5.1.** X-ray diffraction showing mesoscale peaks for calcined AMS-6 mesoporous silica, indexed on the basis of a cubic unit cell. Inset shows a representative SEM images showing the spherical morphology of the particles. Scale bar =500nm. Tabulated parameters include: the unit cell parameters ( $a$ ) obtained from the XRD; BET surface area ( $SA_{\text{BET}}$ ), the total pore volume ( $T_{\text{vol}}$ ) and the pore size distribution (PSD) obtained from nitrogen porosimetry; and the average particle size (PS) from DLS analysis.

	<sup>‡</sup> <i>a</i> (Å)	<sup>*</sup> SA <sub>BET</sub> (m <sup>2</sup> /g)	<sup>‡</sup> T <sub>vol</sub> (cm <sup>3</sup> /g)	<sup>‡</sup> PSD (Å)	<sup>†</sup> D <sub>T</sub> (°C)	T <sub>m</sub> (°C)	ΔH <sub>m</sub> (J/g)
AMS-6	113.2	777.3	0.7	46.7	-	-	-
PB	-	-	-	-	210.4	124.2	54.5
AMS-6 PB(29.5%)	113.9	197.7	0.2	40.3	256.5	-	-
INDO	-	-	-	-	322.8	157.8	78.7
AMS-6 INDO(28.4%)	114.6	369.8	0.3	40.3	410.8	-	-

**Table 5.1:** Physical properties of free probucol (PB) and indomethacin (INDO), as well into loaded AMS-6 particles at loading amounts of approximately 30wt%, including the unit cell parameters (<sup>‡</sup>*a*), BET surface area (SA<sub>BET</sub>), the total pore volume (T<sub>vol</sub>), the pore size distribution (PSD), and the drug decomposition temperature from TGA. The melting endotherm and enthalpy (ΔH<sub>m</sub>) are derived from DSC scans.

Crystalline PB has an extremely low aqueous solubility (~ 5 ng/mL), and dissolution in simulated intestinal fluid is extremely slow, with 20 % of the compound solubilised in 20 hours (Appendix, Figure C2a). In contrast, PB released from AMS-6 in simulated intestinal fluid (SIF) achieved 100 % drug release after 20 hours, with 50 % of the loaded drug released (T<sub>50%</sub>) in 1.6 hours. Whilst less pronounced than INDO an enhancement in the dissolution profile is also observed, with 100 % of the loaded drug dissolved within 1.5 hours, in contrast to 10 hours for the crystalline compound (Appendix, Figure C2b).

To assess the validity of our *in vitro* model of oxidative stress and inflammation in human brain endothelial cells (HBEC), initial studies were conducted to identify the optimal dose of LPS, and incubation time required to generate intracellular ROS and cell death (Figure 5.2). The Muse oxidative stress assay which measures the percentage of cells that are positive for the generation of the primary ROS (the superoxide anion) was utilised. Incubation for 24 hours with 1 µg/ml LPS generated the highest percentage of ROS positive cells (~25.4 %, Figure 5.2a), which was statistically significant (*p* < 0.05) as compared to negative control, whilst at longer incubation times the percentage of cells under oxidative stress decreases. Cells under oxidative stress are exposed to high concentrations of ROS that promote the oxidation of proteins and lipids that induce cellular apoptosis and death. Analysis of cell viability shows a 4 % increase in cell death after incubation of HBECs with 1 µg/ml LPS for 24 hours, compared to the negative control that was not statistically significant (*p* < 0.05) (Figure 5.2b). Further analysis shown in Figure 5.2c (see Materials and Methods for assays) shows significant increases (*p* < 0.05) in the overall levels of ROS species, including levels of hydrogen peroxide, hydroxyl, peroxy, nitric oxide and peroxynitrite in HBEC incubated with 1 µg/ml LPS for 24 hours in comparison to the negative control (cells and media only).

Inflammation markers including the total COX enzyme activity, levels of prostaglandin E<sub>2</sub> and cytokine TNF- $\alpha$  were also higher after incubation in 1  $\mu$ g/ml LPS for 24 hours. These results are consistent with previous *in vitro* reports in the generation of cellular oxidative stress and inflammation in endothelial cells treated with LPS [21]. The presence of high levels of ROS with the absence of pronounced cell death is an optimal cellular scenario to study the ability of PB and INDO to quench ROS production and inhibit the COX-mediated production of inflammatory markers.

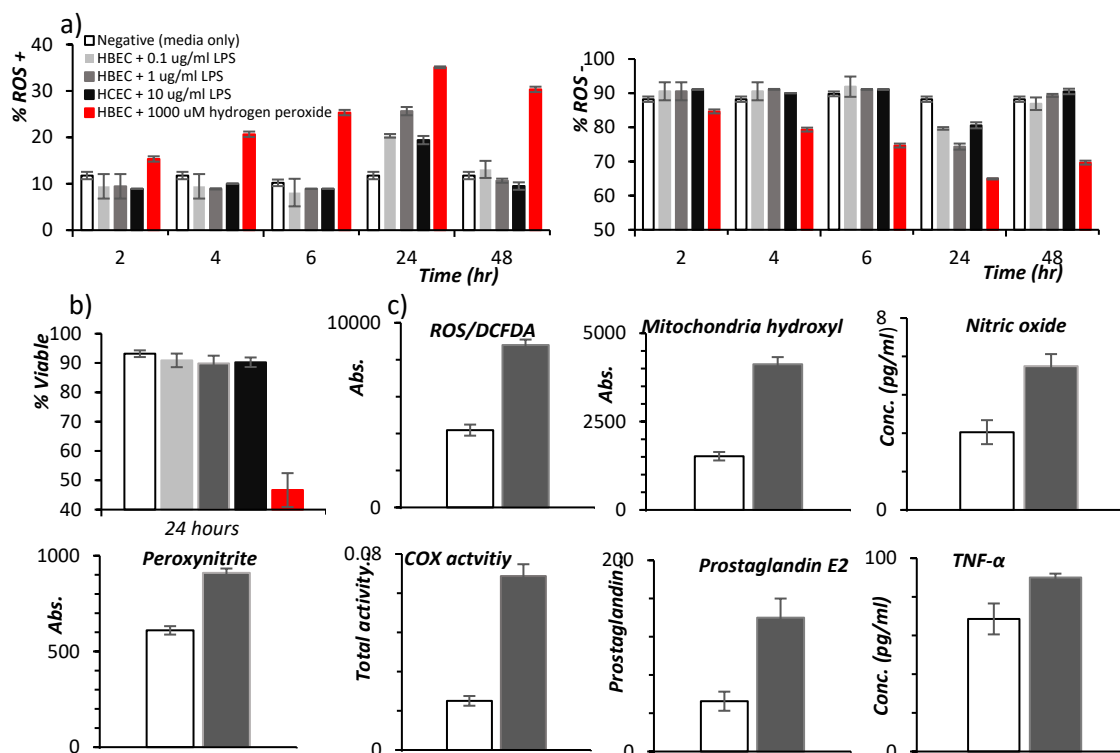


**Figure 5.2.** Percentage of (a) ROS+ and ROS- human brain endothelial cells (HBEC) after incubation with LPS at different test concentrations compared to the negative control (cells with media only) and the positive control (1000  $\mu$ M hydrogen peroxide). (b) Cell viability assay. Production of ROS only causes a relatively small amount of cell death in comparison to the negative control. (c) Analysis of ROS levels using the DCFDA assay suggests an increase of hydrogen peroxide, hydroxyl and peroxy levels; consistent with increases in mitochondrial hydroxyls, nitric oxide and peroxynitrite after incubation of 1  $\mu$ g/ml LPS for 24 hours in HBEC cells compared to negative control (clear bar). Markers of inflammation: COX activity, prostaglandin E<sub>2</sub> and TNF- $\alpha$  levels are also shown.

Test compounds AMS-6PB and AMS-6INDO as well as the respective crystalline compounds were added to HBEC cells at different concentrations together with 1  $\mu$ g/ml LPS and incubated for 24 hours. For comparison, the water-soluble antioxidant compound ascorbic acid was also tested, without a mesoporous particle carrier. Ascorbic acid undergoes rapid cellular uptake in endothelial cells, establishing a high intracellular content [47]. Intracellular ascorbate levels are potent scavengers of ROS including the superoxide anion, hydrogen peroxide and hydroxyl radicals. Figure 5.3a show the concentration dependent effects on the percentage of ROS+ HBEC cells

after incubation with LPS together with the relevant test compounds. The antioxidant properties AMS-6PB are comparable to ascorbic acid and are significantly enhanced ( $p < 0.05$ ) when compared to crystalline PB as evident by a consistently lower number of ROS+ cells at all concentrations studied. The ROS quenching abilities of INDO are not as potent as PB, even when released from the mesoporous carrier, as AMS-6INDO inhibited ROS production to a similar degree than crystalline PB, and comparable to the mesoporous silica particles alone (Appendix, Figure C3a). As would be expected the degree of ROS inhibition by the test compounds correlates well with the degree of cell viability of the LPS treated cells (Appendix, Figure C3b). It is interesting to note that AMS-6PB inhibits the production of mitochondrial hydroxyl radicals, the superoxide anion, and peroxynitrite at comparable levels to ascorbic acid, between 10-100  $\mu\text{M}$  concentrations. Levels of nitric oxide is higher in samples after treatment with AMS-6PB and Ascorbic acid as compared to the other test compounds.

Greater inhibition of total COX enzyme activity and lower levels of COX-dependent release of prostaglandin  $\text{E}_2$  are observed for AMS-6PB and AMS-6INDO compared to crystalline PB, INDO and ascorbic acid (Figure 5.4a-b). Furthermore, there was no significant difference in total COX activity and prostaglandin levels between AMS-6PB and AMS-6INDO at the tested concentrations ( $p > 0.05$ ). Since the COX enzyme resides intracellularly within the lumen of the endoplasmic reticulum and nuclear envelop [48], this is strong evidence for the enhanced transport of PB and INDO within the cell due to their release from the mesoporous carriers. The concentration of  $\text{TNF-}\alpha$  measured increased with concentration for PB and AMS-6PB to higher levels than the positive control but decreased with concentration for INDO and AMS-6INDO and ascorbic acid (Figure 5.4c). Interestingly mesoporous AMS-6 alone induces a decrease in the concentration of  $\text{TNF-}\alpha$  measured, at similar levels to the negative control (Appendix, Figure C4a).

The test compound AMS-6PB achieves a significantly higher concentration of intracellular PB after 24 hours incubation than crystalline PB ( $p < 0.05$ ), as measured from HPLC analysis, with 46.2% of the loaded PB being transported intracellular in contrast to 6.0% for PB alone (Figure 5.4d).

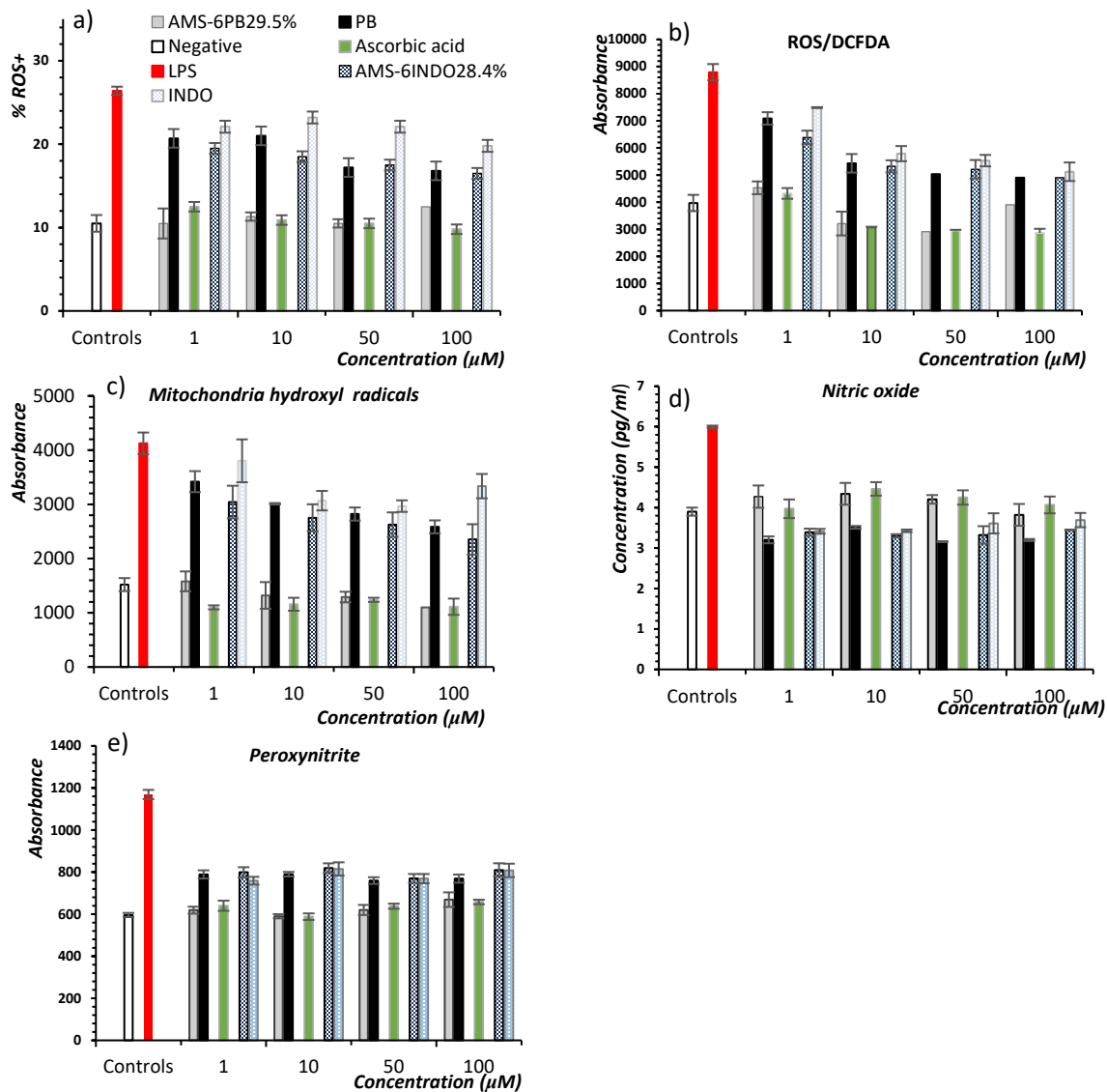


**Figure 5.3.** Concentration dependent effects of test compounds on the production of different ROS species by HEBC cells after 24 hours incubation with 1 µg/ml LPS, as a (a) % of ROS+ cells, (b) analysis of ROS levels using the DCFDA to probe levels of hydrogen peroxide, hydroxyl and peroxy levels, (c) mitochondrial hydroxyl levels, (d) nitric oxide concentration and (e) peroxynitrite. The positive control (red bar) are cells incubated with 1 µg/ml LPS and negative control (white bar) is cells incubated with media only for 24 hours.

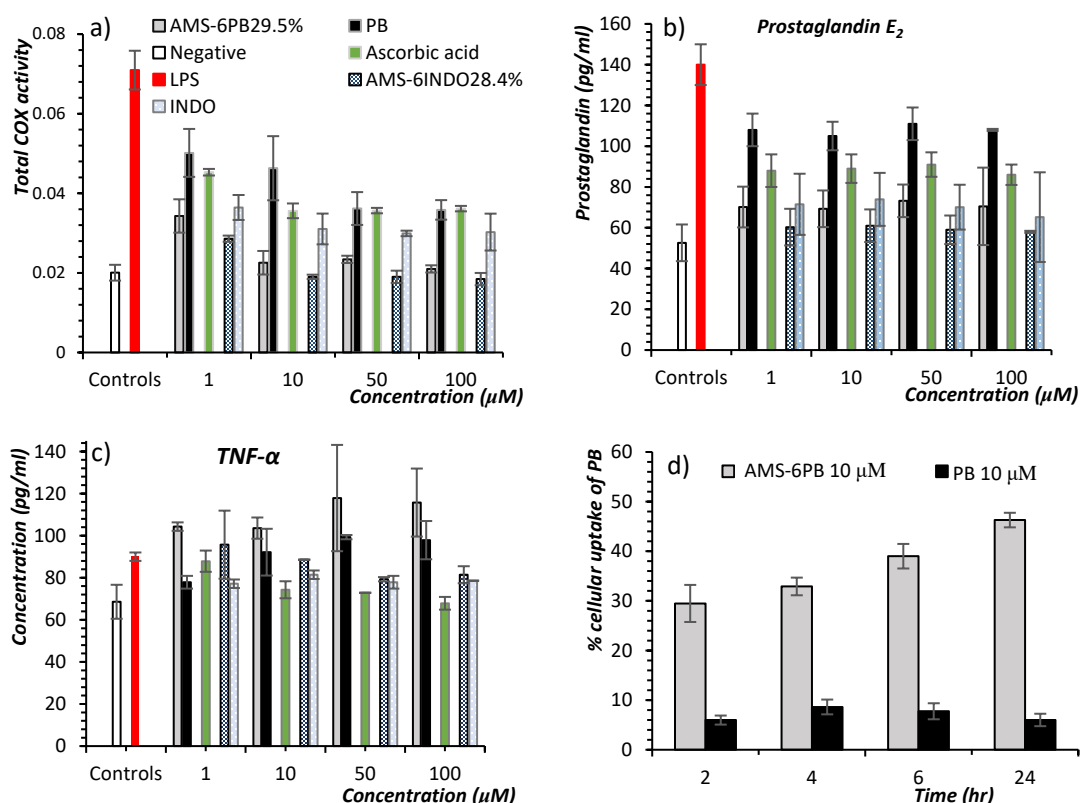


**Figure 5.4.** Concentration dependent effects of test compounds on, (a) the total COX activity; (b) prostaglandin  $E_2$  levels and (c)  $TNF-\alpha$ . (d) Percentage uptake of PB in endothelial cells as measured by HPLC, by HECB cells after 24 hours incubation with 1  $\mu\text{g}/\text{ml}$  LPS. The positive control (red bar) are cells incubated with 1  $\mu\text{g}/\text{ml}$  LPS and negative control (white bar) is cells incubated with media only for 24 hour

To test the effectiveness of the test compounds in maintaining the integrity of a model BBB, an *in vitro* model was established consisting of HECB cultured on the membrane of the transwell insert. LPS (1  $\mu\text{g}/\text{ml}$ ) with or without the test compounds was added and electrical resistance measurements performed using a TEER apparatus, which is a measure of BBB disruption associated with paracellular pathways [49]. For adequate comparison resistance data is normalised to the initial value measured before addition of the LPS, expressed as a percentage. Actual initial resistance values varied between each transwell between 450-510  $\Omega\cdot\text{cm}^2$ . In the negative control, which consisted of brain endothelial cells grown on the transwell membrane in cell culture media, a high TEER value that remained unchanged after 24 hours was measured (Figure 5.5a), which indicate the integrity of the BBB was maintained by tight junction proteins between endothelial cells that restricted paracellular permeability.



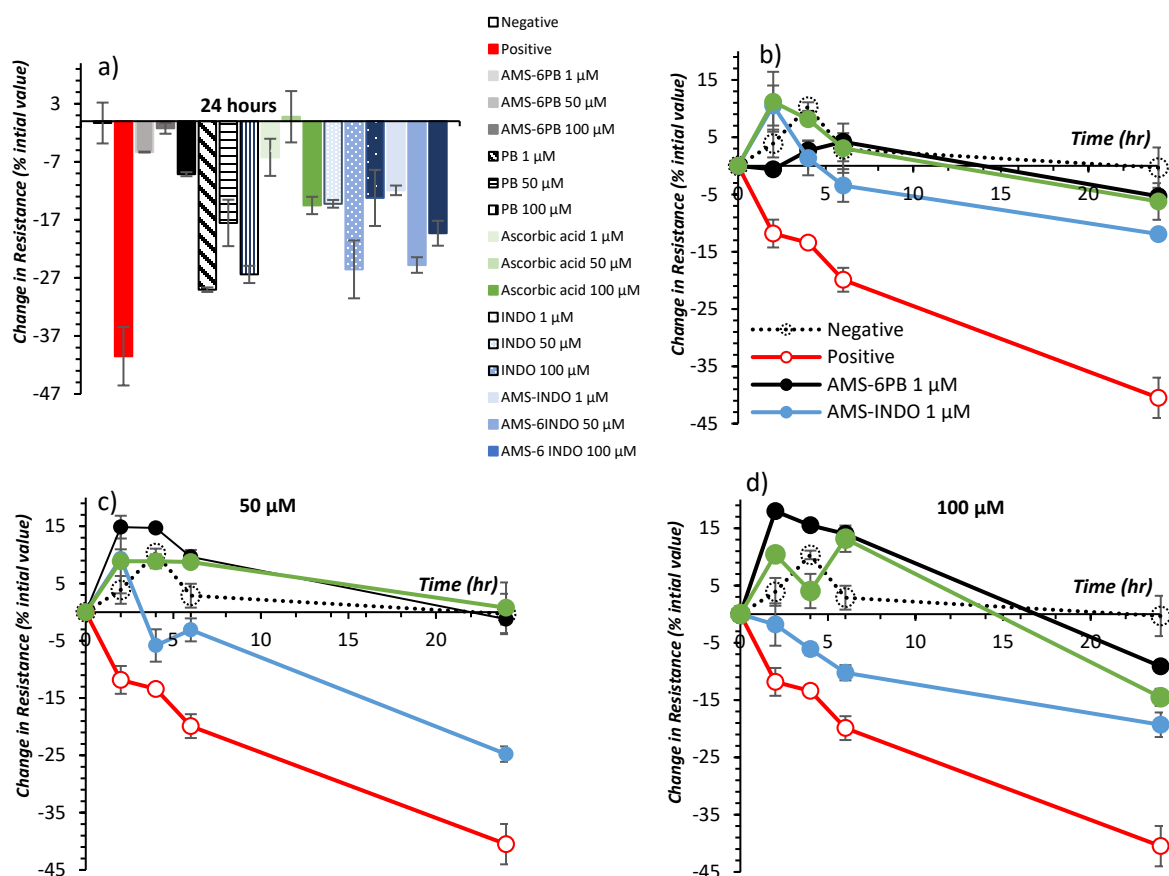


**Figure 5.5.** (a) TEER electrical resistance measurements conducted on monolayers of HEB cells, as a BBB integrity model, incubated with 1 μg/ml LPS and test compounds after 24-hour incubation, expressed as percentage decrease from the initial measured resistance prior to addition of LPS. Time dependent resistance measurements at (b) 1 μM (c) 50 μM and (d) 100 μM for test compounds AMS-6PB, AMS-6INDO and Ascorbic acid compared to controls. For clarity, the error bars for the negative and positive controls have been removed in (c) and (d). For comparison, all data are normalized to the value at 0 hours prior to addition of the LPS and test compounds. Final resistance values for the positive and negative control were 290 and 450 Ω·cm<sup>2</sup> respectively.

Treatment with LPS (Positive control) caused a significant reduction ( $p < 0.05$ ) in TEER in comparison to the negative control (Figure 5.5a). As noted, LPS is known to cause the generation of oxidative stress in endothelial cells that disrupt the integrity of the blood brain barrier through multiple mechanisms including the induction of cellular apoptosis, nitration, and oxidation of tight junction proteins [50]. Mesoporous AMS-6 particles added together with LPS, led to a concentration independent decrease in the resistance per unit area, albeit above the resistance observed for the positive control (Appendix, Figure C5a). All test compounds improved the HBEC monolayer integrity when added together with LPS after 24 hours of incubation in comparison to positive control (LPS alone). Addition of AMS-6PB with LPS led to comparable decrease in resistance as ascorbic acid at 1 μM and 50 μM which was not statistically significant ( $p > 0.05$ ), and a lower decrease at the higher 100 μM concentration after 24 hours of

incubation (Figure 5.5a). Resistance values for AMS-6INDO and INDO alone were lower, indicative of a more disrupted cellular monolayer due to the effects of LPS. The enhanced dissolution properties of PB released from AMS-6 are revealed in the time dependent integrity of the HBEC monolayer (Figure 5.5b-d), where the highest resistance values at 2-hours for the 100  $\mu$ M concentrations, with an 18% improvement in resistance. However, addition of either 50  $\mu$ M of ascorbic acid or AMS-6PB led to the most sustained retention of the HBEC monolayer integrity over the 24-hour period, with very small changes in resistance overall. The COX inhibitor INDO maintains a higher barrier resistance compared to the positive control at all concentrations, with the 100  $\mu$ M concentration showing resistance values above those of the AMS-6INDO sample at the same concentration, at all time points (Appendix, Figure C6).

Membrane permeability to fluorescein isothiocyanate (FITC)-dextran molecules of molecular weight 59000–77000 (approx. size 60 Å) and 3000-5000 (approx. size 14 Å), were used as an indicator of the BBB integrity after 24 hours incubation with 1  $\mu$ g/ml LPS and test compounds. Increased permeability to the larger size FITC-dextran represents broad disruption to the integrity of the endothelial cell monolayer while the smaller size FITC-dextran is a more sensitive marker of BBB disruption [51]. In comparison to TEER, permeability measurements is associated with disruption of the BBB by the transcytotic pathways [52].

As a reference the positive control, LPS at 1  $\mu$ g/ml, induced a 4-fold increase in the permeability rate of the larger size FITC-dextran compared to negative control, and approx. 2.5 times higher permeability than the smaller FITC-dextran (Figure 5.6a-b). This indicates LPS causes a broad disruption to the endothelial cell monolayer involving both paracellular and transcytotic pathways as measured by TEER and permeability measurements [18, 51, 53], consistent with the increase in ROS, PGE<sub>2</sub> levels in LPS treated endothelial cells. Treatment with AMS-6PB and ascorbic acid maintains a significantly lower permeability ( $p < 0.05$ ) to the larger FITC-dextran compared to the other test compounds, confirming that these compounds were most effective in preventing cellular damage associated with LPS. In particular, treatment with AMS-6PB resulted in a significantly lower permeability ( $p < 0.05$ ) to both the small and large FITC-dextran compounds relative to AMS-6INDO. Whilst treatment with AMS-6INDO lead to a reduction in permeability to the smaller FITC dextran, permeability to the larger FITC-dextran was significantly higher than the negative control, suggesting broad disruption to the BBB integrity remained in this sample.

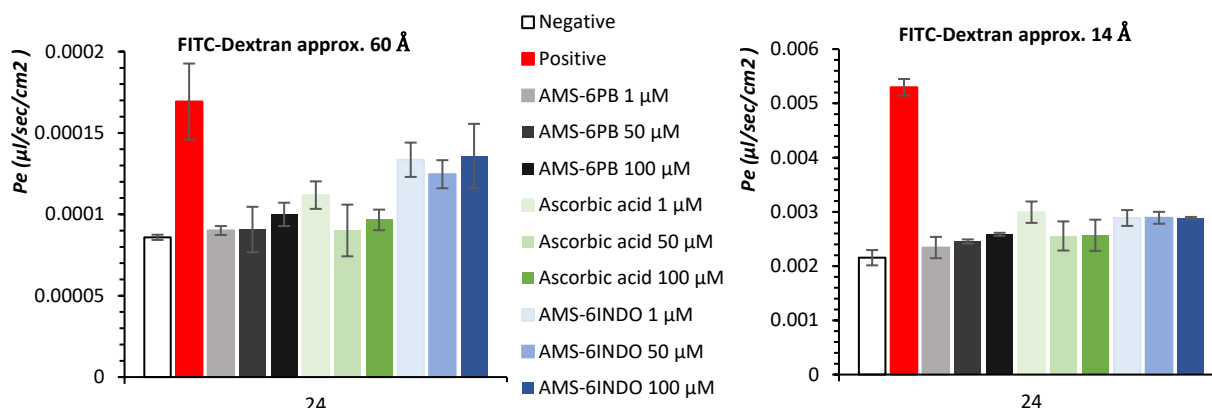


**Figure 5.6.** HEBC permeability measurements to FITC-Dextran molecules of different molecular weight and size, recorded at the end of the 24-hour incubation period with 1 µg/ml LPS and test compounds.

In comparison to the other test compounds, PB released from AMS-6 maintained a high endothelial barrier integrity to a similar degree when compared to ascorbic acid, characterised by a similar reduction in LPS mediated increases in reactive species generation and preservation of nitric oxide levels. PB is known to have some anti-inflammatory properties mediated by the inhibition of NF-κB activation of COX enzyme activity [64][65]. PB's anti-inflammatory properties were shown in our study to be superior to ascorbic acid based on measured COX enzyme activity and PGE<sub>2</sub> levels (Figure 5.4), and this may have contributed to the greater effect on barrier integrity measured at higher doses of 50 and 100 µM in Figure 5.5b and c between 1 and 6 hours. However, the behavior of highly soluble probucol resembles that of a COX-1 specific inhibitor, in as much as that whilst PGE<sub>2</sub> was significantly inhibited, the pro-inflammatory cytokine TNF-α was not.

The pharmacological properties of PB has been previously reported from *in vitro* and *in vivo* models of oxidative stress and inflammation in the context of hypocholesteremia and atherosclerosis administered with organic solvents such as DMSO or together with lipids [66-69]. In this study, the pharmacological properties of PB were significantly enhanced by the encapsulation within AMS-6, and proven to be a viable strategy to reduce LPS induced disruption to endothelial cell integrity via paracellular and transcytotic pathways.

### 5.3 Conclusion

The enhancement in the solubility of PB released from AMS-6 increased the antioxidant properties of the drug as compared to crystalline PB in an *in vitro* endothelial cell model of the BBB. The differences in the

pharmacological properties of PB was likely due to the higher cellular uptake of the drug compound in PB released from MSP as compared to crystalline PB. The antioxidant properties of PB released from AMS-6 was not significantly different to the potent antioxidant ascorbic acid. Furthermore, PB released from AMS-6 and ascorbic acid were significantly superior to INDO and AMS-6INDO in maintaining the integrity of the tight junctions in an *in vitro* BBB model of neuroinflammation, suggesting compounds with potent antioxidant properties are more effective in the treatment of neuroinflammation compared to anti-inflammatory compounds.

## 5.4 References

1. Engelhardt, B. and L. Sorokin. *The blood–brain and the blood–cerebrospinal fluid barriers: function and dysfunction*. in *Seminars in immunopathology*. 2009. Springer.
2. Pober, J.S. and G. Tellides, *Participation of blood vessel cells in human adaptive immune responses*. Trends in Immunology, 2012. **33**(1): p. 49-57.
3. Schieber, M. and N.S. Chandel, *ROS function in redox signaling and oxidative stress*. Current biology, 2014. **24**(10): p. R453-R462.
4. Kukreja, R.C., et al., *PGH synthase and lipoxygenase generate superoxide in the presence of NADH or NADPH*. Circulation research, 1986. **59**(6): p. 612-619.
5. Chan, P.H., *Reactive oxygen radicals in signaling and damage in the ischemic brain*. Journal of Cerebral Blood Flow & Metabolism, 2001. **21**(1): p. 2-14.
6. Beckman, J.S. and W.H. Koppenol, *Nitric oxide, superoxide, and peroxynitrite: the good, the bad, and ugly*. American Journal of Physiology-cell physiology, 1996. **271**(5): p. C1424-C1437.
7. Minghetti, L., *Cyclooxygenase-2 (COX-2) in Inflammatory and Degenerative Brain Diseases*. Journal of Neuropathology & Experimental Neurology, 2004. **63**(9): p. 901-910.
8. Buttke, T.M. and P.A. Sandstrom, *Oxidative stress as a mediator of apoptosis*. Immunology today, 1994. **15**(1): p. 7-10.
9. Zlokovic, B.V., *Neurovascular pathways to neurodegeneration in Alzheimer's disease and other disorders*. Nature Reviews Neuroscience, 2011. **12**(12): p. 723-738.
10. Brown, G.C., *The endotoxin hypothesis of neurodegeneration*. Journal of neuroinflammation, 2019. **16**(1): p. 1-10.
11. Jaeger, L.B., et al., *Lipopolysaccharide alters the blood–brain barrier transport of amyloid  $\beta$  protein: a mechanism for inflammation in the progression of Alzheimer's disease*. Brain, behavior, and immunity, 2009. **23**(4): p. 507-517.
12. Banks, W.A., et al., *Lipopolysaccharide-induced blood-brain barrier disruption: roles of cyclooxygenase, oxidative stress, neuroinflammation, and elements of the neurovascular unit*. Journal of neuroinflammation, 2015. **12**(1): p. 223.
13. Nagyősi, P., et al., *Expression and regulation of toll-like receptors in cerebral endothelial cells*. Neurochemistry international, 2010. **57**(5): p. 556-564.
14. Kawai, T. and S. Akira, *TLR signaling*. Cell Death & Differentiation, 2006. **13**(5): p. 816-825.
15. Engström, L., et al., *Lipopolysaccharide-induced fever depends on prostaglandin E2 production specifically in brain endothelial cells*. Endocrinology, 2012. **153**(10): p. 4849-4861.
16. Li, S., et al., *The febrile response to lipopolysaccharide is blocked in cyclooxygenase-2–/–, but not in cyclooxygenase-1–/– mice*. Brain research, 1999. **825**(1-2): p. 86-94.
17. Jaworowicz Jr, D.J., et al., *Nitric oxide and prostaglandin E2 formation parallels blood–brain barrier disruption in an experimental rat model of bacterial meningitis*. Brain research bulletin, 1998. **46**(6): p. 541-546.
18. de Vries, H.E., et al., *Effect of endotoxin on permeability of bovine cerebral endothelial cell layers in vitro*. Journal of Pharmacology and Experimental Therapeutics, 1996. **277**(3): p. 1418-1423.
19. Wilhelms, D.B., et al., *Deletion of prostaglandin E2 synthesizing enzymes in brain endothelial cells attenuates inflammatory fever*. Journal of Neuroscience, 2014. **34**(35): p. 11684-11690.
20. Craft, J.M., D.M. Watterson, and L.J. Van Eldik, *Neuroinflammation: A potential therapeutic target*. Expert Opinion on Therapeutic Targets, 2005. **9**(5): p. 887-900.

21. Banks, W.A., et al., *Lipopolysaccharide-induced blood-brain barrier disruption: roles of cyclooxygenase, oxidative stress, neuroinflammation, and elements of the neurovascular unit*. J Neuroinflammation, 2015. **12**: p. 223.
22. Takechi, R., et al., *Probucol prevents blood–brain barrier dysfunction in wild-type mice induced by saturated fat or cholesterol feeding*. Clinical and Experimental Pharmacology and Physiology, 2013. **40**(1): p. 45-52.
23. Mamo, J.C., et al., *Probucol prevents blood–brain barrier dysfunction and cognitive decline in mice maintained on pro-diabetic diet*. Diabetes and Vascular Disease Research, 2019. **16**(1): p. 87-97.
24. Kuzuya, M., et al., *Probucol prevents oxidative injury to endothelial cells*. Journal of lipid research, 1991. **32**(2): p. 197-204.
25. Barnhart, R.L., S.J. Busch, and R.L. Jackson, *Concentration-dependent antioxidant activity of probucol in low density lipoproteins in vitro: probucol degradation precedes lipoprotein oxidation*. Journal of lipid research, 1989. **30**(11): p. 1703-1710.
26. Witting, P.K., et al., *Probucol protects against hypochlorite-induced endothelial dysfunction identification of a novel pathway of probucol oxidation to a biologically active intermediate*. Journal of Biological Chemistry, 2005. **280**(16): p. 15612-15618.
27. Terasaki, O., et al., *Structural study of meso-porous materials by electron microscopy*, in *Studies in Surface Science and Catalysis*, O. Terasaki, Editor. 2004, Elsevier. p. 261-288.
28. Wan, Y. and D. Zhao, *On the controllable soft-templating approach to mesoporous silicates*. Chemical reviews, 2007. **107**(7): p. 2821-2860.
29. Atluri, R., N. Hedin, and A.E. Garcia-Bennett, *Hydrothermal Phase Transformation of Bicontinuous Cubic Mesoporous Material AMS-6*. Chemistry of Materials, 2008. **20**(12): p. 3857-3866.
30. Rosenholm, J.M., et al., *Targeting of porous hybrid silica nanoparticles to cancer cells*. ACS Nano, 2009. **3**(1): p. 197-206.
31. Manzano, M. and M. Vallet-Regí, *New developments in ordered mesoporous materials for drug delivery*. Journal of Materials Chemistry, 2010. **20**(27): p. 5593.
32. Rosenholm, J.M., C. Sahlgren, and M. Linden, *Towards multifunctional, targeted drug delivery systems using mesoporous silica nanoparticles--opportunities & challenges*. Nanoscale, 2010. **2**(10): p. 1870-83.
33. Stromme, M., et al., *Mesoporous silica-based nanomaterials for drug delivery: evaluation of structural properties associated with release rate*. Wiley Interdisciplinary Reviews-Nanomedicine and Nanobiotechnology, 2009. **1**(1): p. 140-148.
34. Kjellman, T., et al., *Influence of microporosity in SBA-15 on the release properties of anticancer drug dasatinib*. Journal of Materials Chemistry B, 2014. **2**(32): p. 5265.
35. Wang, Y., et al., *Mesoporous silica nanoparticles in drug delivery and biomedical applications*. Nanomedicine: Nanotechnology, Biology and Medicine, 2015. **11**(2): p. 313-327.
36. Mo, J., et al., *Tailoring particle size of mesoporous silica nanosystem to antagonize glioblastoma and overcome blood–brain barrier*. ACS applied materials & interfaces, 2016. **8**(11): p. 6811-6825.
37. He, L., H. Lai, and T. Chen, *Dual-function nanosystem for synergetic cancer chemo-/radiotherapy through ROS-mediated signaling pathways*. Biomaterials, 2015. **51**: p. 30-42.
38. Karimzadeh, M., L. Rashidi, and F. Ganji, *Mesoporous silica nanoparticles for efficient rivastigmine hydrogen tartrate delivery into SY5Y cells*. Drug development and industrial pharmacy, 2017. **43**(4): p. 628-636.
39. Mendiratta, S., et al., *Multidisciplinary Role of Mesoporous Silica Nanoparticles in Brain Regeneration and Cancers: From Crossing the Blood–Brain Barrier to Treatment*. Particle & Particle Systems Characterization, 2019. **36**(9): p. 1900195.
40. Shen, Y., et al., *ROS responsive resveratrol delivery from LDLR peptide conjugated PLA-coated mesoporous silica nanoparticles across the blood-brain barrier*. J Nanobiotechnology, 2018. **16**(1): p. 13.

41. Garcia-Bennett, A., et al., *Studies of anionic surfactant templated mesoporous structures by electron microscopy*, in *Nanoporous Materials Iv*. 2005. p. 11-18.
42. Garcia-Bennett, A., et al., *Structural investigations of AMS-n mesoporous materials by transmission electron microscopy*. Chemistry of Materials, 2004. **16**(5): p. 813-821.
43. Ulrika, B., et al., *Sustained Release from Mesoporous Nanoparticles: Evaluation of Structural Properties Associated with Release Rate*. Current Drug Delivery, 2008. **5**(3): p. 177-185.
44. Gaillard, P.J., A.B.G. de Boer, and D.D. Breimer, *Pharmacological investigations on lipopolysaccharide-induced permeability changes in the blood-brain barrier in vitro*. Microvascular research, 2003. **65**(1): p. 24-31.
45. Garcia-Bennett, A.E., M. Lau, and N. Bedford, *Probing the Amorphous State of Pharmaceutical Compounds Within Mesoporous Material Using Pair Distribution Function Analysis*. Journal of Pharmaceutical Sciences, 2018. **107**(8): p. 2216-2224.
46. Lau, M., K. Giri, and A.E. Garcia-Bennett, *Antioxidant properties of probucol released from mesoporous silica*. European Journal of Pharmaceutical Sciences, 2019. **138**: p. 105038.
47. Wu, F., et al., *Ascorbate inhibits NADPH oxidase subunit p47phox expression in microvascular endothelial cells*. Free Radical Biology and Medicine, 2007. **42**(1): p. 124-131.
48. Hewett, S.J., S.C. Bell, and J.A. Hewett, *Contributions of cyclooxygenase-2 to neuroplasticity and neuropathology of the central nervous system*. Pharmacology & therapeutics, 2006. **112**(2): p. 335-357.
49. Srinivasan, B., et al., *TEER measurement techniques for in vitro barrier model systems*. Journal of laboratory automation, 2015. **20**(2): p. 107-126.
50. Rao, R., *Oxidative stress-induced disruption of epithelial and endothelial tight junctions*. Frontiers in bioscience: a journal and virtual library, 2008. **13**: p. 7210.
51. Mayhan, W.G. and D.D. Heistad, *Permeability of blood-brain barrier to various sized molecules*. American Journal of Physiology-Heart and Circulatory Physiology, 1985. **248**(5): p. H712-H718.
52. Nag, S., *Blood-brain barrier permeability using tracers and immunohistochemistry*, in *The Blood-Brain Barrier*. 2003, Springer. p. 133-144.
53. Ziylan, Y.Z., P.J. Robinson, and S.I. Rapoport, *Blood-brain barrier permeability to sucrose and dextran after osmotic opening*. American Journal of Physiology-Regulatory, Integrative and Comparative Physiology, 1984. **247**(4): p. R634-R638.
54. Predescu, D., et al., *Constitutive eNOS-derived nitric oxide is a determinant of endothelial junctional integrity*. American Journal of Physiology-Lung Cellular and Molecular Physiology, 2005. **289**(3): p. L371-L381.
55. Bucci, M., et al., *Endothelial nitric oxide synthase activation is critical for vascular leakage during acute inflammation in vivo*. Proceedings of the National Academy of Sciences, 2005. **102**(3): p. 904-908.
56. Kurose, I., et al., *Inhibition of nitric oxide production. Mechanisms of vascular albumin leakage*. Circulation research, 1993. **73**(1): p. 164-171.
57. Heller, R., et al., *L-Ascorbic acid potentiates nitric oxide synthesis in endothelial cells*. Journal of Biological Chemistry, 1999. **274**(12): p. 8254-8260.
58. Westendorp, R.G., et al., *Cyclic-GMP-mediated decrease in permeability of human umbilical and pulmonary artery endothelial cell monolayers*. Journal of vascular research, 1994. **31**(1): p. 42-51.
59. Draijer, R., et al., *cGMP and nitric oxide modulate thrombin-induced endothelial permeability: regulation via different pathways in human aortic and umbilical vein endothelial cells*. Circulation research, 1995. **76**(2): p. 199-208.
60. May, J.M. and Z.-c. Qu, *Nitric oxide mediates tightening of the endothelial barrier by ascorbic acid*. Biochemical and biophysical research communications, 2011. **404**(2): p. 701-705.

61. Han, M., et al., *Ascorbate protects endothelial barrier function during septic insult: Role of protein phosphatase type 2A*. Free Radical Biology and Medicine, 2010. **48**(1): p. 128-135.
62. Wu, F. and J.X. Wilson, *Peroxynitrite-dependent activation of protein phosphatase type 2A mediates microvascular endothelial barrier dysfunction*. Cardiovascular research, 2009. **81**(1): p. 38-45.
63. Squadrito, G.L., X. Jin, and W.A. Pryor, *Stopped-flow kinetic study of the reaction of ascorbic acid with peroxynitrite*. Archives of biochemistry and biophysics, 1995. **322**(1): p. 53-59.
64. Zucoloto, A.Z., et al., *Probucol attenuates lipopolysaccharide-induced leukocyte recruitment and inflammatory hyperalgesia: Effect on NF- $\kappa$ B activation and cytokine production*. European journal of pharmacology, 2017. **809**: p. 52-63.
65. Tikhaze, A., et al., *Antioxidant probucol as an effective scavenger of lipid radicals in low density lipoproteins in vivo and in vitro*. Bulletin of Experimental Biology and Medicine, 1999. **128**(2): p. 818-821.
66. Simon, B.C., C.C. Haudenschild, and R.A. Cohen, *Preservation of endothelium-dependent relaxation in atherosclerotic rabbit aorta by probucol*. Journal of cardiovascular pharmacology, 1993. **21**(6): p. 893-901.
67. Inoue, N., et al., *Probucol improves endothelial-dependent relaxation and decreases vascular superoxide production in cholesterol-fed rabbits*. The American journal of the medical sciences, 1998. **315**(4): p. 242-247.
68. Jiang, J.L., et al., *Probucol preserves endothelial function by reduction of the endogenous nitric oxide synthase inhibitor level*. British journal of pharmacology, 2002. **135**(5): p. 1175-1182.
69. Kita, T., et al., *Probucol prevents the progression of atherosclerosis in Watanabe heritable hyperlipidemic rabbit, an animal model for familial hypercholesterolemia*. Proceedings of the National Academy of Sciences, 1987. **84**(16): p. 5928-5931.



# 6

## Zebrafish as a biological model of oxidative stress for testing the therapeutic properties of drug compounds and mesoporous silica.

### 6.1 Introduction

The aim of this final chapter was to further explore the antioxidant and toxicological properties of the test compounds used in this thesis in an *in vivo* model that is a closer representation of the human physiology. Zebrafish are rapidly becoming an established biological model for biomedical research [1, 2], and was chosen in this thesis as it has a high degree of biological and genetic similarities with humans, along with other advantages. Zebrafish embryos are optically transparent and allow for the visualisation of major organs and tissue development in real time [3]. The high genetic homology (~ 70 %) between zebrafish and humans enable the study of the pathological mechanisms that are relevant in human diseases [4]. Furthermore, large amounts of embryos (approx. 200-300 eggs per day) can be generated every 5 to 7 days, making it readily available for high throughput toxicological or pharmacological screening of drug compounds and materials. Recent advances in the genetic manipulation of zebrafish allow for the development of transgenic fish in the study of the pathogenesis of diseases [5, 6].

The major organs including the cardiovascular, nervous, and digestive systems are highly conserved between zebrafish and humans, making it a relevant model to analyse the ADME (adsorption, distribution, metabolism, and elimination) of drug compounds and materials (Figure 6.1) [7]. For example, the cardiovascular system is highly conserved between humans and zebrafish at the anatomical, cellular and molecular levels, such that many cardiovascular drugs have shown to have identical effects on zebrafish and humans [8].

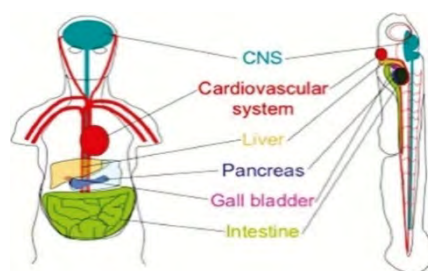


**Figure 6. 1** Conservation of the major organs between zebrafish and humans [9]

Like humans, ROS produced by zebrafish serve as second messengers in normal physiological function, and also in the immune response following exposure to potentially harmful stimuli including environmental pollutants, chemicals, and drug compounds [10-12]. Zebrafish have a range of antioxidant defence mechanisms including enzymes and signalling pathways that detoxify free radicals, and in replenishing levels of small molecule antioxidants [13]. Furthermore, excessive production of ROS is known to cause oxidative damage to the biomolecules of zebrafish including DNA, lipids, and proteins that lead to cell death and destruction [14, 15]. As the major mechanisms of ROS production and function show physiological similarities in humans, zebrafish are a relevant *in vivo* model to study the pathogenesis of diseases mediated by oxidative stress, and to investigate the pharmacological and toxicological properties of drug compounds and materials [16, 17].

Taking advantage of their optical transparency, a range of molecular probes can be used to monitor in real time the production of ROS by zebrafish. For example, the DCFDA probe is typically used to monitor the production of ROS including  $H_2O_2$ ,  $OH^\bullet$ , and  $O_2^{\bullet-}$ , therefore providing a qualitative measurement in the overall levels of reactive species [18]. To determine the antioxidant properties of drug compounds, pre-incubation of zebrafish with the test compounds are performed, followed by exposure to a pro-oxidant, and incubation of the zebrafish with DCFDA [19, 20].

In this chapter, an established zebrafish model of oxidative stress [15] using  $H_2O_2$  as the pro-oxidant was used to determine the antioxidant property of PB released from AMS-6 compared to crystalline PB. In this model, pre-incubation of zebrafish (3dpf) with the test compounds for 24 hours, was followed by treatment with 5 mM hydrogen peroxide for 1 hr, and 25  $\mu$ M DCFDA to monitor the production of ROS as measured by the microplate reader. Consistent with previous chapters, the antioxidant properties of PB was compared to the highly potent water soluble antioxidant ascorbic acid. As an antioxidant, ascorbic acid was shown to have beneficial effects in enhancing the rate of fish growth, cell proliferation and protection against ROS mediated DNA damage and oxidative stress [21, 22].

## 6.2 Materials and methods

### *Synthesis of AMS-6 MSP*

Details of the synthesis for AMS-6 MSP are included in chapter 2, section 2.2.1, pg.44 of the materials and methods.

*Amine-functionalised AMS-6 (NH<sub>2</sub>-AMS-6)* was prepared from the reflux of 1 g of AS-AMS-6 (as synthesised) material at 85 °C in a 500 ml mixture of ethanol/HCl (37%) for a period of 24 hours as previously reported [23]. Extraction of the as synthesised material resulted in the homogenous coverage of propyl amine on the surface of silica, allowing for further coupling with the fluorochrome. The mixture was filtered and the material was washed with ethanol and left to dry at room temperature overnight

*Fluorescein Isothiocyanate (FITC) labelling of silica particles (FITC-AMS-6).* Preparation of FITC-AMS-6 MSPs was achieved by the reaction between NH<sub>2</sub>-AMS-6 with the fluorochrome under alkaline conditions to produce the imminothioester bond, following the protocol previously reported [24]. 1 g of NH<sub>2</sub>-AMS-6 was refluxed in 100 ml ethanol containing the desired amount of fluorochrome, and the pH of the mixture was raised to 11 by the addition of NaOH pellets. The mixture was allowed to reflux at 85 °C for a period of 6 hours. The mixture was filtered and washed with ethanol to dissolve unattached FITC. The sample was dried at room temperature overnight.

### *Characterisation*

#### *Dynamic light scattering (DLS)*

Hydrodynamic diameter and zeta potential measurements were performed by DLS using a Zetasizer ZS (Malvern Instrument, UK) at 25 °C with a He-Ne laser (633 nm, 4 mW output power) as a light source. MSP dispersions (10 µL, 1 mg/mL) were measured in 1 mL in filtered phosphate buffer saline (PBS).

#### *X-ray diffraction*

Details of XRD analysis of samples are included in chapter 2, section 2.6.1, pg.46 of the materials and methods.

#### *Nitrogen sorption isotherms*

Details of the N<sub>2</sub> sorption isotherm are included in chapter 2, section 2.6.5, pg.49 of the materials and methods.

#### *Fourier-transform infrared spectroscopy*

Fourier Transform Infrared Spectroscopy (FTIR) spectra of samples were obtained using a Thermo Scientific Nicolet iS5 FT-IR Spectrometer with iD5 ATR accessory, in transmittance, from 4000  $\text{cm}^{-1}$  to 400 $\text{cm}^{-1}$  was averaged over 32 scans for each curve. All samples were measured without dilution.

#### *Drug loading*

Details of the drug loading procedure are included in chapter 2, section 2.4, pg.46 of the materials and methods.

#### *Thermogravimetric analysis (TGA)*

Details of the TGA of samples are included in chapter 2, section 2.6.6, pg.51 of the materials and methods.

#### *Differential Scanning Calorimetry (DSC)*

Details of the DSC analysis of samples are included in chapter 2, section 2.6.7, pg.51 of the materials and methods.

#### *Zebrafish care and preparation*

Zebrafish were maintained at 28 °C in a 13 hour light and 11 hour dark cycle. Zebrafish embryos were collected by natural spawning and raised at 28 °C in buffer free-E3 solution (E3 solution) following the standard protocol [25]. Experimental protocols were approved by Macquarie University Animal Ethics Committee (Zebrafish models of neural disorders; protocol no. 2012/050; using zebrafish to understand how the central nervous system responds to neuronal stress and death caused by neurodegenerative diseases, 2015/033).

#### *Microscopy images*

Embryonic zebrafish, 2 day post fertilisation (2dpf) were pre-treated with FITC-AMS-6 in E3 solution for 24 hours. Fish were washed three times and transferred to single well sample holders for observation under fluorescent microscope. A tuneable white-light laser was used for excitation of the fluorophore and corresponding filter to image the samples (495/519 Ex/Em wavelength nm). Images were brightness and contrast adjusted for visualisation and illustration.

#### *DCFDA reactive oxygen species assay*

The compound DCFDA (2',7'-dichlorodihydrofluorescein diacetate) was used to monitor ROS production in embryonic zebrafish. DCFDA is cleaved by intracellular esterases, and oxidised by ROS to the fluorescent compound DCF (2',7'-dichlorofluorescein). Embryonic zebrafish (2dpf) were pre-treated with the test compounds dissolved in

E3 solution for 24 hours in an incubator set to 28 °C. At 3 dpf, the embryos were washed three times in E3 solution, and incubated with 5 mM H<sub>2</sub>O<sub>2</sub> for one hour. The embryos were washed three times in E3 solution, and treated with 25 mM DCFDA for 45 minutes, and embryos transferred individually to a black 96 well plate. Fluorescence measurements were obtained using a PHERAstar plate reader (485 excitation, 520 emission wavelength). Data are represented as mean ± Standard deviation. Samples were run in triplicate and values were normalized to the positive control.

### ***Statistical analysis***

Statistical analysis was performed using the paired sample t-test (Excel, Microsoft, USA), and probability values of (p) < 0.05 was considered as statistically significant.

### 6.3 Results and discussion

The structural and textural properties of the mesoporous materials used in this chapter are shown in Table 6.1. Reduction in the pore size and surface area of NH<sub>2</sub>-AMS-6 compared to CAL-AMS-6 was due to the presence of the functional propylamine groups within the internal surface of NH<sub>2</sub>-AMS-6 MSP. Further reduction in pore volume and surface area was observed in the FITC-AMS-6 when compared to NH<sub>2</sub>-AMS-6 indicating the presence of FITC within the mesopores. PB was loaded within CAL-AMS-6 at a loading amount of 29.5% (wt/wt) as determined by TGA. The reduction in pore volume and surface area in the AMS-6PB29.5% sample compared to CAL-AMS-6 suggest PB was loaded within the mesopores as previously described in chapter 4. The AMS-6PB29.5% sample was used in studies comparing the antioxidant properties of PB released from AMS-6 versus crystalline PB.

MSP	$a_o$ , Å	$P_{vol}$ , cm <sup>3</sup> /g	$P_{size}$ , Å	$S_{Area}$ , m <sup>2</sup> /g	$HD_{size}$ , nm (± STD)	$\zeta$ -potential, mv (± STD)
AS-AMS-6	115.3	-	-	-	354.4(160)	36.3(3.0)
CAL-AMS-6	113.2	0.81	47.0	814.2	491(16.5)	-28.5(0.6)
NH <sub>2</sub> -AMS-6	118.8	0.39	37.9	470.5	749(24.1)	29.6(0.8)
FITC-AMS-6	100.7	0.35	36.2	401.5	782 (25.1)	30.8(0.4)
AMS-6PB29.5%	113.8	0.21	40.3	197.7	-	-

**Table 6.1:** Structural and textural data of AMS-6 as utilised in this study. The unit cell parameter,  $a_o$ , was obtained from powder X-ray diffraction. The average pore volume, average pore size and surface area ( $P_{vol}$ ,  $P_{size}$ , and  $S_{Area}$ , respectively) were obtained from nitrogen sorption measurements. The  $HD_{size}$  was measured in PBS buffer, whilst the  $\zeta$ -potential was measured in distilled water. The  $\zeta$ -potential of CAL-AMS-6 was negative due to the presence of surface silanol groups. The NH<sub>2</sub>-AMS-6 MSP showed the highest hydrodynamic ( $HD_{size}$ ) particle size due to particle agglomeration, and a positive  $\zeta$ -potential due to the presence of amine groups.

The presence of amine groups and FITC in NH<sub>2</sub>-AMS-6 and FITC-AMS-6 was further confirmed using FT-IR (Figure 6.1). The absorption bands of the 1000-1200 cm<sup>-1</sup> (Si-O-Si asymmetric stretching), 965 cm<sup>-1</sup> (Si-O stretching) and 801 cm<sup>-1</sup> (Si-O-Si symmetric stretching) is present in all MSP and represent the peaks of the silica framework [26]. The reaction between the amino groups (-NH<sub>2</sub>) on NH<sub>2</sub>-AMS-6 and the isothiocyanate groups (-N=C=S) from FITC is characteristic of the absorption peak attributed to the C-N stretching vibration around 1462 cm<sup>-1</sup> [27]. The symmetrical bending band in 1630 cm<sup>-1</sup> is attributed to the presence of NH<sub>2</sub> groups in NH<sub>2</sub>-AMS-6 and FITC-AMS-6 materials [27].

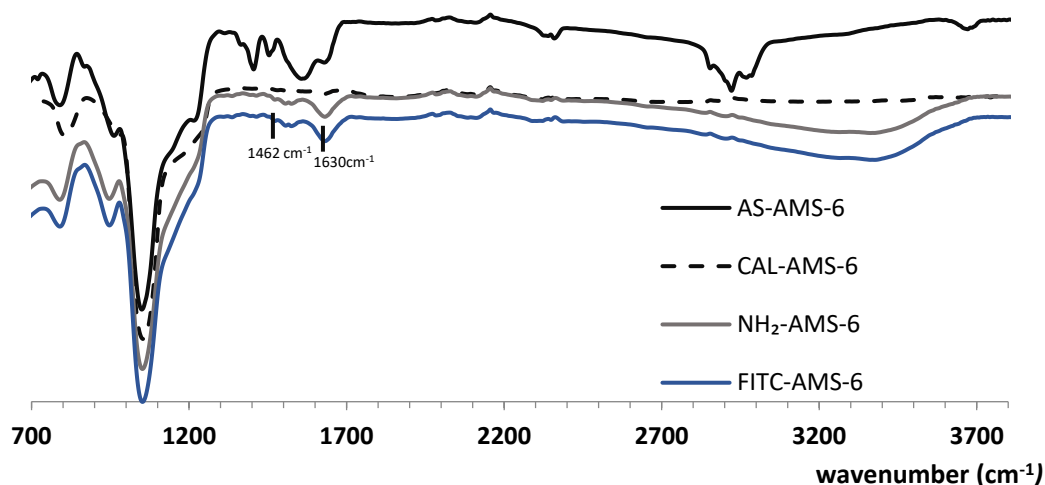


**Figure 6.1:** Infrared spectroscopy of AS-AMS-6, CAL-AMS-6, NH<sub>2</sub>-AMS-6, and FITC-AMS-6 materials. The absorption peak at 1462 cm<sup>-1</sup> is attributed to the reaction between the amino groups (-NH<sub>2</sub>) on NH<sub>2</sub>-AMS-6 and the isothiocyanate groups (-N=C=S) from FITC [27]. The presence of NH<sub>2</sub> groups in NH<sub>2</sub>-AMS-6 and FITC-AMS-6 materials is attributed to the stretching band at 1630 cm<sup>-1</sup> [27]. The broad band between 3200 and 3700 cm<sup>-1</sup> is attributed to the O-H bond stretching of the surface silanol groups and the adsorbed water molecule [28].

Low angle X-ray powder diffraction (XRD) patterns of CAL-AMS-6 show diffraction peaks characteristic of the cubic mesostructured (Appendix, Figure D1) [29]. XRD analysis of NH<sub>2</sub>-AMS-6 material show a similar diffraction pattern to that of the calcined material, suggesting minimal changes in porous structure occurred (Appendix, Figure D1).

### Toxicological properties of CAL-AMS-6

Initial studies were conducted to determine the toxicological profile of CAL-AMS-6 in terms of ROS generation and mortality on the developing embryo at 3dpf. Embryonic zebrafish were exposed in E3 media containing CAL-AMS-6 for a period of 24 hours. At the end of the 24 hours, zebrafish were washed, and incubated in E3 media containing 25 μM DCFDA for 45 minutes to measure ROS production. The fluorescent intensity of DCF in individual zebrafish exposed to different concentrations of CAL-AMS-6 for 24 hours was measured by the microplate reader, and results were normalized to the positive control (fish exposed to 5 mM H<sub>2</sub>O<sub>2</sub> for 1 hour), which has been shown previously to cause oxidative stress in zebrafish [15].

A significant increase ( $p < 0.05$ ) in ROS was observed in fish exposed to CAL-AMS-6 as compared to the negative control (Figure 6.2a). No significant difference ( $p > 0.05$ ) in measured ROS levels was observed between the different doses of CAL-AMS-6 suggesting the increase in ROS was not dependent on the dose of silica. In terms of

viability, no death in fish was recorded in zebrafish after exposure to CAL-AMS-6 at the concentrations used in the study (Figure 6.2b). This suggests the generation of ROS was not associated with significant oxidative damage that would lead to fish death.

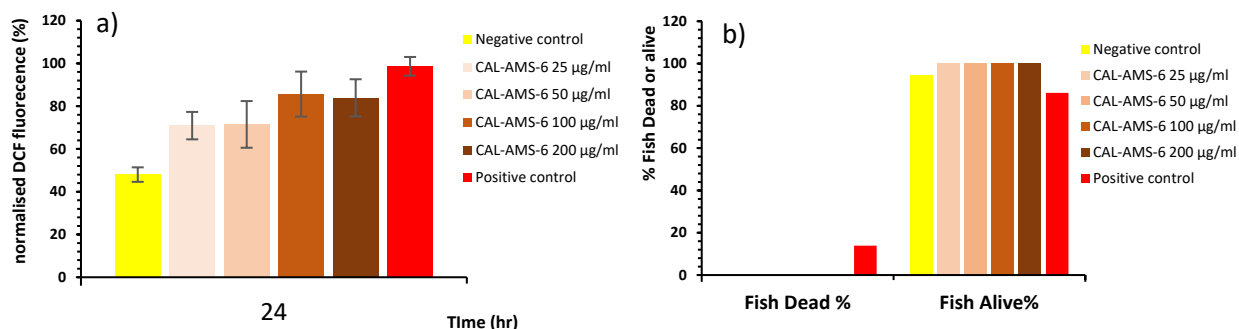


**Figure 6.2:** (a) Zebrafish (3dpf) exposed to different concentrations of CAL-AMS-6 for a period of 24 hours, and measured DCF fluorescence normalized to the positive control (5 mM H<sub>2</sub>O<sub>2</sub>) after incubation for 45 minutes with 25 µM DCFDA probe. (b) Percentage of fish that were either dead or alive as observed under bright field microscopy of the samples.

To determine the uptake and distribution of MSP, zebrafish were exposed to FITC-AMS-6 in E3 media for a period of 24 hours. At the end of the incubation time, zebrafish were washed three times, and observed under microscopy. The majority of the FITC-AMS-6 particles were located in and around the frontal regions of the fish including the heart, yolk sac and mouth, with no obvious accumulation in the brain or other major organs (Figure 6.3). At higher concentrations, an increase in the number of FITC-AMS-6 was observed. Further experiments would need to be conducted to determine whether the particles are internalised or loosely bound to the surface of the fish, and to determine the effect of MSP on embryo development and toxicity.

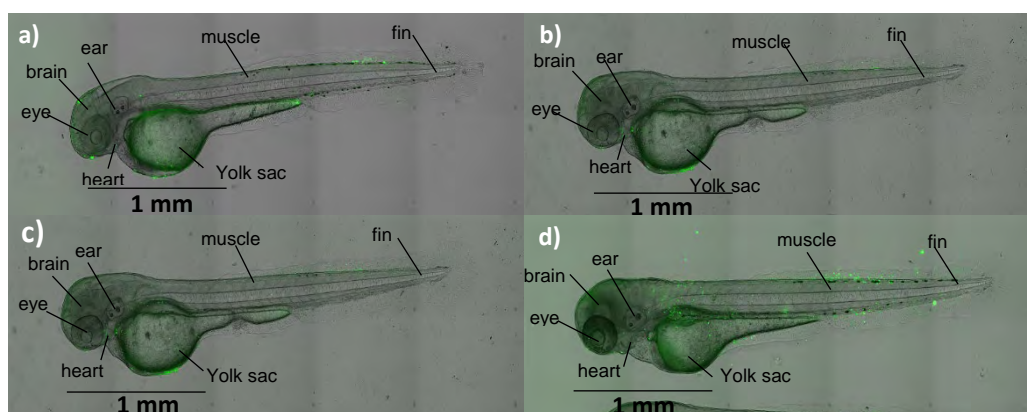


**Figure 6.3:** Images taken of Zebrafish after 24 hours exposure to different concentrations of FITC-AMS-6. The concentration of FITC-AMS-6 are a) 25 µg/ml, b) 50 µg/ml, c) 100 µg/ml, and d) 200 µg/ml.



The particle size, and surface charge of silica particles are key properties that determine its toxicological profile *in vivo* [30-33]. The effect of silica particle size (15 and 30 nm) and *in vivo* toxicity were investigated in freshly fertilised embryonic zebrafish (2 hour post fertilisation - 2hpf). A significant increase in malformations (axial spine curvature, pericardial edema, yolk sac edema) were observed in embryos exposed to 15 nm silica as compared to the exposure at the equivalent concentrations to the larger 30 nm silica. This was associated with the significant increase in the generation of ROS, reduction in antioxidant enzyme activity, and higher silica uptake in embryos exposed to the 15 nm silica, suggesting the malformations were caused by silica induced oxidative stress [33].

High mortality rate (94%) was observed in Zebrafish (20 hpf) exposed to positively charged MSP (POS-MSP,  $HD_{size} < 60$  nm,  $\zeta$ -potential 38.9 mV) as compared to significantly lower mortality in zebrafish exposed to the negatively charged MSP (NEG-MSP,  $HD_{size} < 60$  nm,  $\zeta$ -potential -52 mV) at the equivalent dosage (100  $\mu$ g/ml) [31]. Similar findings were reported in another study where the exposure of zebrafish (8 hpf) to positively charged amine functionalised MSP ( $NH_2$ -MSP, +35.3 mV, 115.8 nm) resulted in 100 % mortality after 48 hours exposure [32]. In comparison, embryonic zebrafish exposed to NEG-MSP (-31.8 mV, 133.8 nm) did not cause a significant increase in mortality and embryos developed normally until the end of the experiment time. Images of zebrafish showed greater penetration and distribution of the POS-MSP in the yolk, tail, intestines and tissues of the embryo as compared to the localisation of NEG-MSP in the intestine with no distinguishable fluorescence in the yolk or tail [31, 32]. The increased mortality in embryos exposed to POS-MSP was likely due to toxicity associated with the increased exposure of the internal organs to MSP, as the positive charge on MSP facilitated greater uptake across biological membrane in comparison to negatively charged MSP of the same particle size.

In comparison to the previous studies, the CAL-AMS-6 MSP used in this study were negative charge particles and had a much larger  $HD_{size}$  (-28.5 mV, 491 nm) (Table 1). Although a significant increase in the production of ROS was observed in zebrafish, further studies would need to be conducted to further explore the toxicological profile such as its effect on embryo's antioxidant levels, cell death and embryo development. Furthermore, the FITC-AMS-6 MSP used for the imaging studies had a positive charge and a much larger  $HD_{size}$  as compared to CAL-AMS-6 (+34.8 mV, 749 nm). The differences in the properties of the materials including particle size and charge and their effect on the toxicity of zebrafish should be further explored in future studies.

## Antioxidant properties of probucol and ascorbic acid

The antioxidant properties of the test compounds were tested in the zebrafish model of oxidative stress. Zebrafish were exposed to the test compounds for 24 hours, followed by 5 mM H<sub>2</sub>O<sub>2</sub> for 1 hour and 25 µM DCFDA for 45 minutes. In the initial experiment, the antioxidant property of CAL-AMS-6 was tested in this model. No significant reduction ( $p > 0.05$ ) in measured ROS was observed with the treatment of CAL-AMS-6 at the different concentrations of MSP when compared to the positive control. A higher percentage of dead fish was actually observed in zebrafish treated with higher concentrations of CAL-AMS-6, which may have been associated with the increase in ROS production observed earlier. This suggests CAL-AMS-6 does not have an antioxidant effect in quenching ROS and may, at higher doses, cause an increase in fish mortality due to an increase in ROS production.

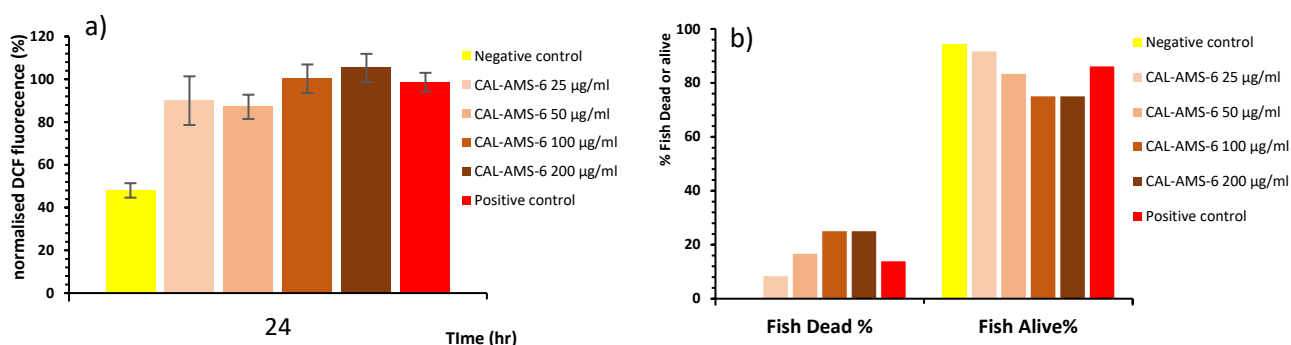


**Figure 6.4:** Treatment with test compound CAL-AMS-6 MSP in zebrafish (3dpf) for 24 hours, followed by 1 hour incubation with 5 mM H<sub>2</sub>O<sub>2</sub> and 40 minutes incubation with 25 µM DCFDA. In Figure a), fluorescence readings of DCF normalised to the positive control (5mM H<sub>2</sub>O<sub>2</sub>), and in b) observation of percentage of fish that were either dead or alive, as observed under microscope.

The test compounds AMS-6PB, PB and ascorbic acid were tested in the zebrafish model of oxidative stress at 25, 50, 100 and 200 µM concentration of the active ingredient. Embryos pre-treated with AMS-6PB29.5% (25 µM and 50 µM) maintained levels of ROS that were not significantly different ( $p > 0.05$ ) to the negative control, suggesting the test compounds protected the embryo from oxidative damage induced by H<sub>2</sub>O<sub>2</sub> (Figure 6.5). Similarly, treatment at high concentrations of ascorbic acid (ASC, 200 µM) also maintained ROS production in embryos at comparable levels to the negative control. This was also reflected with a high percentage of fish that remained alive after treatment with test compounds, with ~91% of fish alive recorded in the AMS-6PB30% 25 µM treatment (Figure 6.5 b). At higher concentrations, AMS-6PB29.5% 100µM and 200 µM caused a significant increase in ROS and % fish death, which was likely contributed by the increase in the silica concentration (Appendix, Figure D2). In comparison,

the production of ROS was significantly higher in embryos treated with crystalline PB (25 and 50  $\mu\text{M}$ ) when compared to the equivalent concentration of PB released from AMS-6 (Figure 6.5).

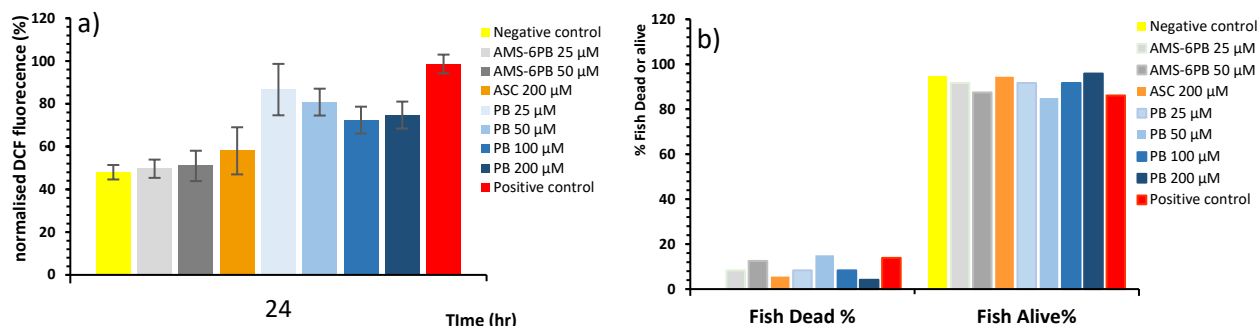


**Figure 6.5:** Zebrafish pre-treated with the test compounds for 24 hours before treatment with 5 mM  $\text{H}_2\text{O}_2$  for 1 hour and 25  $\mu\text{M}$  DCFDA for 45 minutes. a) Measured DCF fluorescence of the samples normalised to the positive control (5 mM  $\text{H}_2\text{O}_2$ ), b) % zebrafish that were either dead or alive after the experiment as observed under microscopy.

The quenching of  $\text{H}_2\text{O}_2$  and other reactive species are likely to account for the reduced ROS production in PB treated zebrafish as compared to the positive control. Furthermore, PB can be incorporated in biological membranes protecting it against  $\text{H}_2\text{O}_2$  mediated oxidative damage and activation of cellular apoptosis [34-36]. Other reported beneficial effects of PB include the increase in antioxidant enzyme glutathione peroxidase (GPx) activity that catalyses the reduction of  $\text{H}_2\text{O}_2$  into unreactive products [37], increase protein expression of thioredoxin- 1 [34], and NAD(P)H:quinone oxidoreductase-1 [38] which are mechanisms that contribute to attenuation of oxidative stress caused by  $\text{H}_2\text{O}_2$ .

The results from these studies suggest the antioxidant properties of PB is enhanced from the encapsulation within AMS-6 as compared to crystalline PB. This enhancement is likely due to the increase in PB solubility from the encapsulation of the drug in the amorphous form within the mesopores, which facilitate greater antioxidant activity in neutralising either intracellular or extracellular  $\text{H}_2\text{O}_2$  present in biological media. Furthermore, the higher solubility of PB released from AMS-6 may have facilitated greater uptake of the drug and incorporation into the biological membranes therefore protecting it against oxidative damage and apoptosis. Further studies would need to be conducted to determine the differences in drug release kinetics in the zebrafish media along with drug concentration in zebrafish to confirm these hypothesis.

Additionally, the antioxidant property of PB released from AMS-6 (at 25 and 50  $\mu\text{M}$ ) was not significantly different to ascorbic acid at 200  $\mu\text{M}$  dosage. As a potent water soluble antioxidant, ascorbic acid can neutralise a range of ROS and RNS present in biological media, and restore the antioxidant activity of other compounds and enzymes *in vivo* [39, 40]. This effect was only observed at high concentrations of ascorbic acid, where the exposure of freshly fertilised zebrafish embryos to ascorbic acid at 100-200  $\mu\text{M}$  was shown to promote an enhancement in embryo development, fish growth, reduced ROS DNA damage, and hatching rate [21]. A high concentration of ascorbic acid is likely required to achieve and maintain high levels of intracellular ascorbate levels required to quench ROS during oxidative stress.

## 6.4 Conclusion

Released PB from AMS-6 resulted in a significant reduction in zebrafish (3dpf) ROS production as compared to crystalline PB at the same concentration of 25 and 50  $\mu\text{M}$  of the active ingredient. The enhancement in solubility of PB released from AMS-6 increased scavenging of  $\text{H}_2\text{O}_2$  and protects against oxidative stress in zebrafish. The antioxidant properties of ascorbic acid (200  $\mu\text{M}$ ) was non-significantly different to AMS-6PB at 25  $\mu\text{M}$  or 50  $\mu\text{M}$ . At this concentration, ascorbic acid is known to protect against oxidative damage by ROS.

## 6.5 References

1. Chakraborty, C., et al., *Zebrafish: A complete animal model to enumerate the nanoparticle toxicity*. Journal of nanobiotechnology, 2016. **14**(1): p. 1-13.
2. Jia, H.-R., et al., *Nanomaterials meet zebrafish: Toxicity evaluation and drug delivery applications*. Journal of Controlled Release, 2019. **311**: p. 301-318.
3. Fang, L. and Y.I. Miller, *Emerging applications for zebrafish as a model organism to study oxidative mechanisms and their roles in inflammation and vascular accumulation of oxidized lipids*. Free Radical Biology and Medicine, 2012. **53**(7): p. 1411-1420.
4. Howe, K., et al., *The zebrafish reference genome sequence and its relationship to the human genome*. Nature, 2013. **496**(7446): p. 498-503.
5. Bradford, Y.M., et al., *Zebrafish models of human disease: gaining insight into human disease at ZFIN*. ILAR journal, 2017. **58**(1): p. 4-16.
6. Zhang, Y., Z. Zhang, and W. Ge, *An efficient platform for generating somatic point mutations with germline transmission in the zebrafish by CRISPR/Cas9-mediated gene editing*. Journal of Biological Chemistry, 2018. **293**(17): p. 6611-6622.
7. Sarmah, S. and J.A. Marrs, *Zebrafish as a vertebrate model system to evaluate effects of environmental toxicants on cardiac development and function*. International journal of molecular sciences, 2016. **17**(12): p. 2123.
8. Asnani, A. and R.T. Peterson, *The zebrafish as a tool to identify novel therapies for human cardiovascular disease*. Disease models & mechanisms, 2014. **7**(7): p. 763-767.
9. Teame, T., et al., *The use of zebrafish (Danio rerio) as biomedical models*. Animal Frontiers, 2019. **9**(3): p. 68-77.
10. Jia, J., et al., *Reactive oxygen species participate in liver function recovery during compensatory growth in zebrafish (Danio rerio)*. Biochemical and biophysical research communications, 2018. **499**(2): p. 285-290.
11. Ko, E.-Y., et al., *The roles of NF- $\kappa$ B and ROS in regulation of pro-inflammatory mediators of inflammation induction in LPS-stimulated zebrafish embryos*. Fish & shellfish immunology, 2017. **68**: p. 525-529.
12. Sullivan, C. and C.H. Kim, *Zebrafish as a model for infectious disease and immune function*. Fish & shellfish immunology, 2008. **25**(4): p. 341-350.
13. Biller, J.D. and L.S. Takahashi, *Oxidative stress and fish immune system: phagocytosis and leukocyte respiratory burst activity*. Anais da Academia Brasileira de Ciências, 2018. **90**(4): p. 3403-3414.
14. Birnie-Gauvin, K., et al., *A comparative and evolutionary approach to oxidative stress in fish: a review*. Fish and Fisheries, 2017. **18**(5): p. 928-942.
15. Formella, I., et al., *Real-time visualization of oxidative stress-mediated neurodegeneration of individual spinal motor neurons in vivo*. Redox biology, 2018. **19**: p. 226-234.
16. Mourabit, S., et al., *New insights into organ-specific oxidative stress mechanisms using a novel biosensor zebrafish*. Environment international, 2019. **133**: p. 105138.
17. Kulkarni, A.A., et al., *An In Vivo Zebrafish Model for Interrogating ROS-Mediated Pancreatic  $\beta$ -Cell Injury, Response, and Prevention*. Oxidative Medicine and Cellular Longevity, 2018. **2018**.
18. Walker, S.L., et al., *Automated reporter quantification in vivo: high-throughput screening method for reporter-based assays in zebrafish*. PloS one, 2012. **7**(1): p. e29916.
19. Sadeghi, S., et al., *Effect of different oxidative stress degrees generated by hydrogen peroxide on motility and DNA fragmentation of zebrafish (Danio rerio) spermatozoa*. Reproduction in Domestic Animals, 2018. **53**(6): p. 1498-1505.

20. Rieger, S. and A. Sagasti, *Hydrogen peroxide promotes injury-induced peripheral sensory axon regeneration in the zebrafish skin*. PLoS Biol, 2011. **9**(5): p. e1000621.
21. Francis, S., R. Delgoda, and R. Young, *Effects of embryonic exposure to  $\alpha$ -lipoic acid or ascorbic acid on hatching rate and development of zebrafish (*Danio rerio*)*. Aquaculture Research, 2012. **43**(5): p. 777-788.
22. Xiang, Q., et al., *Oxidative stress response induced by butachlor in zebrafish embryo/larvae: the protective effect of vitamin C*. Bulletin of environmental contamination and toxicology, 2018. **100**(2): p. 208-215.
23. Zheng, H., C. Gao, and S. Che, *Amino and quaternary ammonium group functionalized mesoporous silica: An efficient ion-exchange method to remove anionic surfactant from AMS*. Microporous and mesoporous materials, 2008. **116**(1-3): p. 299-307.
24. Witasz, E., et al., *Efficient internalization of mesoporous silica particles of different sizes by primary human macrophages without impairment of macrophage clearance of apoptotic or antibody-opsonized target cells*. Toxicology and applied pharmacology, 2009. **239**(3): p. 306-319.
25. Westerfield, M., *The Zebrafish Book: A Guide for the Laboratory Use of Zebrafish *Danio* ("Brachydanio Rerio")*. 2007: University of Oregon.
26. Pereira, C., et al., *Designing novel hybrid materials by one-pot co-condensation: from hydrophobic mesoporous silica nanoparticles to superamphiphobic cotton textiles*. ACS applied materials & interfaces, 2011. **3**(7): p. 2289-2299.
27. Wang, L., et al., *Raman and FTIR spectroscopies of fluorescein in solutions*. Spectrochimica Acta Part A: Molecular and Biomolecular Spectroscopy, 2001. **57**(9): p. 1781-1791.
28. Sae-Ung, S. and V. Boonamnuayvitaya, *Direct synthesis and characterization of amine-functionalized mesoporous silica materials and their applications as formaldehyde adsorbents*. Environmental Engineering Science, 2008. **25**(10): p. 1477-1486.
29. Atluri, R., N. Hedin, and A.E.G. Bennett, *Hydrothermal phase transformation of bicontinuous cubic mesoporous material AMS-6*. Chem Mater, 2008. **20**: p. 3857-3866.
30. Sharif, F., et al., *Mesoporous silica nanoparticles as a compound delivery system in zebrafish embryos*. International Journal of Nanomedicine, 2012. **7**: p. 1875.
31. Liu, T.-P., et al., *Biosafety evaluations of well-dispersed mesoporous silica nanoparticles: towards in vivo-relevant conditions*. Nanoscale, 2015. **7**(15): p. 6471-6480.
32. Paatero, I., et al., *Analyses in zebrafish embryos reveal that nanotoxicity profiles are dependent on surface-functionalization controlled penetrance of biological membranes*. Scientific reports, 2017. **7**(1): p. 1-13.
33. Zhu, B., et al., *The fate and oxidative stress of different sized SiO<sub>2</sub> nanoparticles in zebrafish (*Danio rerio*) larvae*. Chemosphere, 2019. **225**: p. 705-712.
34. Sheng, L., et al., *Probucol inhibits hydrogen peroxide to induce apoptosis of vascular smooth muscle cells*. Molecular Medicine Reports, 2013. **7**(4): p. 1185-1190.
35. Iqbal, M., S.D. Sharma, and S. Okada, *Probucol as a potent inhibitor of oxygen radical-induced lipid peroxidation and DNA damage: in vitro studies*. Redox report, 2004. **9**(3): p. 167-172.
36. Goton, N., et al., *Antioxidant activities of probucol against lipid peroxidations*. Biochimica et Biophysica Acta (BBA)-Lipids and Lipid Metabolism, 1992. **1128**(2-3): p. 147-154.
37. Santos, D.B., et al., *Probucol Protects Neuronal Cells Against Peroxide-Induced Damage and Directly Activates Glutathione Peroxidase-1*. Molecular Neurobiology, 2020.
38. Zhou, Z., et al., *Activation of the Nrf2/ARE signaling pathway by probucol contributes to inhibiting inflammation and neuronal apoptosis after spinal cord injury*. Oncotarget, 2017. **8**(32): p. 52078.
39. Arrigoni, O. and M.C. De Tullio, *Ascorbic acid: much more than just an antioxidant*. Biochimica et Biophysica Acta (BBA)-General Subjects, 2002. **1569**(1-3): p. 1-9.

40. Beyer, R.E., *The role of ascorbate in antioxidant protection of biomembranes: interaction with vitamin E and coenzyme Q*. Journal of bioenergetics and biomembranes, 1994. **26**(4): p. 349-358.

# 7

## Overall conclusions and future directions

The most important and overall conclusion of this thesis is that a significant enhancement in the solubility properties of poorly soluble pharmaceutical compounds (Class II and Class IV), can potentially unlock new therapeutic areas. The consequences of this are large, as it could speed up clinical development and reduce the high attrition encountered for difficult to formulate compounds [1]. As shown in this thesis with several pharmaceutical active ingredients, and in particular probucol, mesoporous silica particles can enable this enhancement. The antioxidant and anti-inflammatory properties of probucol were improved to expand its therapeutic potential in the treatment of conditions associated with oxidative stress.

In Chapter 3, the *Pair Distribution Function* analysis of total scattering data was used to probe the local atomic ordering of drugs loaded within mesoporous silica particles and to characterise how changes in molecular packing affected *in vitro* drug release. The characterisation of the amorphous form is challenging as it is known that pharmaceutical compounds have different crystalline and amorphous states that can affect their physical and chemical properties (polymorphism and amorphism) [2]. *Pair Distribution Function* could differentiate between different amorphous states of the loaded drugs as a function of loading amount, and can complement other characterisation techniques such as TGA, DSC, nitrogen sorption, and conventional XRD techniques that probe more specifically the crystalline state.

In Chapter 4, probucol was loaded into mesostructures AMS-6, MCM-41, SBA-15 to investigate the effect of textural properties of the mesoporous silica, loading amount (wt%) and dose on the physical form of probucol and its drug release profile. The encapsulation of probucol in the amorphous form was achieved by the suppression of crystallisation. A loading of 30 wt% resulted in the optimal release for AMS-6, whilst the presence of crystalline drug material in MCM-41 was detected at 20 wt% loading due to complete pore filling as this material had a lower mesopore volume compared to AMS-6 and SBA-15. The solubility of probucol was significantly enhanced in all particles as compared to the crystalline drug and this was confirmed *in vivo* with pharmacokinetic studies in rodents,



showing an enhancement in oral bioavailability of approximately 7 times for probucol released from AMS-6 after oral administration.

In Chapter 5, the pharmacological properties of probucol were explored further in the context of the blood brain barrier and neuroinflammatory diseases. As neuroinflammation is a complex disease involving both oxidative stress and inflammation, a comparison was made between probucol and a compound with potent anti-inflammatory properties (indomethacin). Furthermore, the antioxidant properties of probucol was compared to ascorbic acid, a potent antioxidant compound. The antioxidant and anti-inflammatory properties of probucol were significantly enhanced in comparison to its crystalline form. Formulations of AMS-6PB and ascorbic acid had superior antioxidant properties in comparison to INDO (and AMS-6INDO), and attenuated LPS induced increases in permeability of the blood brain barrier. Whilst this shows the potential for probucol in the treatment of neurodegenerative diseases associated with oxidative stress and changes in the permeability of the blood brain barrier, it also is strongly suggestive that compounds with antioxidant properties are more effective than anti-inflammatory compounds alone.

In the final Chapter, preliminary work was conducted to investigate the antioxidant properties of probucol released from AMS-6 *in vivo* using a zebrafish model of oxidative stress. Zebrafish were chosen because they have a high degree of genetic homology making them a relevant model to study diseases. Results were also promising as probucol quenched ROS production in zebrafish exposed to the pro-oxidant hydrogen peroxide, at lower concentrations than ascorbic acid (25  $\mu$ M versus 200  $\mu$ M).

## **Future directions**

Future work could be undertaken to expand and explore in further detail on the findings from this thesis. PDF was shown to be a promising tool in probing the local atomic structure of drug compounds loaded within MSP. Further work should be undertaken to systematically evaluate and characterise how the textural properties of MSP can affect molecular ordering and mobility of the loaded drug, and how this can be used to predict the *in vitro* drug release and possibly *in vivo* pharmacokinetics. One such additional technique that could be employed to support total scattering measurements is Dielectric Relaxation Spectroscopy (DRS) as a tool that can probe molecular mobility via the re-orientation motion of dipoles under an applied electrical field. The amorphous state of a compound, stabilised below the critical pore diameter, implies a molecularly disordered arrangement of the drug

within the mesopores. In contrast, a more ordered (crystalline) form of the drug compound, where a dipole motion is fixed at specific sites in the crystal lattice is insensitive to electric field fluctuations [3]. This allows to quantitatively differentiate between the two states, as the silica wall does not respond to the field perturbation, and to probe the molecular mobility of the encapsulated compound through relaxation experiments [4]. Modelling drug release from mesoporous silica is complex. Simulation and experimental evidence reveal a complex scenario for the adsorption of drugs within the mesoporous surfaces, which has limited the amount of systematic modelling studies despite a need to better predict kinetic drug release [5]. The development of a model for drug dissolution within the pores in terms of transient mass balances, considering changes due to amorphisation of the drug, with 3-D complex geometries and variable diffusivities must be developed if these materials are to be generically used as pharmaceutical excipients.

Finally, more *in vivo* studies should be conducted to investigate the pharmacological properties of probucol with enhanced solubility profiles, in disease models such as atherosclerosis, neuroinflammation, or neurodegenerative diseases. The unique antioxidant properties of probucol could generate new therapeutic products, but the toxicological profile of the drug released may also be enhanced and so this should be evaluated too, in particular its potential cardiotoxicity.

## 7.1 References

1. Boyer, S., C. Brealey, and A.M. Davis, *Attrition in Drug Discovery and Development*. Attrition in the Pharmaceutical Industry, 2015.
2. Shalaev, E., et al., *Crystalline mesophases: structure, mobility, and pharmaceutical properties*. Advanced drug delivery reviews, 2016. **100**: p. 194-211.
3. Smith, G., et al., *Dielectric Relaxation Spectroscopy and Some Applications in the Pharmaceutical Sciences*. Journal of Pharmaceutical Sciences, 1995. **84**(9): p. 1029-1044.
4. Brás, A.R., et al., *Amorphous Ibuprofen Confined in Nanostructured Silica Materials: A Dynamical Approach*. The Journal of Physical Chemistry C, 2011. **115**(11): p. 4616-4623.
5. Gignone, A., et al., *Simulation and experiment reveal a complex scenario for the adsorption of an antifungal drug in ordered mesoporous silica*. The Journal of Physical Chemistry C, 2015. **119**(23): p. 13068-13079.

## **8 Appendices**

8.1 Appendix A: Supporting information of Chapter 3.

Supporting Information for:

## **Probing the amorphous state of pharmaceutical compounds within mesoporous material using pair distribution function.**

Alfonso E. Garcia-Bennett,<sup>†‡\*</sup> Michael Lau,<sup>‡</sup> and Nicholas Bedford.<sup>§</sup>

### Table of Contents

**M1.** Synthesis of Mesoporous Materials

**M2.** Characterisation Protocols and Equipment

**M3.** Drug loading and Drug Release

**S1.** Characterisation of mesoporous silica materials

**S2.** Thermogravimetric Analysis of drug loaded mesoporous silica

**S3.** Raw data adsorption isotherms for calcined and drug-loaded samples

**S4.** X-ray Diffractograms of loaded samples

**S5.** Differential Scanning calorimetry curves

**S6.** Scanning and Transmission electron microscopy images

**S7.** Comparison of total scattering profiles for mesoporous loaded samples and crystalline drug

**S8.** Dissolution curves for drug loaded mesoporous silica samples

## M1. Synthesis of Mesoporous Materials

All chemicals, including pharmaceutical drug compounds, were purchased from Sigma-Aldrich (Sydney, Australia) unless stated and used as received without further purification.

The **synthesis of mesoporous material SBA-15** has already been described previously, and is based on the self-assembly of the polymeric surfactant P123 ( $\text{EO}_{20}\text{PO}_{70}\text{EO}_{20}$ ,  $M_{av} = 5800$ ) in aqueous acidic conditions. In a typical synthesis TEOS (8.19 g) was added to a mixture of P123 (4.0 g), HCl (8.0 g, 35 wt%), and deionized water (100 ml) at 40°C. After the mixture was stirred for 24 hrs, the mesostructured product was cured at 100°C for an additional 48 hrs. The products were filtered without washing and dried at ambient temperature and pressure. The surfactant was removed by exhaustive solid-liquid extraction using an HCl (35 wt%)/ethanol solution (ratio 2:8) at 70°C for 24 hrs prior to calcination in order to remove any remaining surfactant by calcination at 550 °C (1 hrs in flowing air), to give the porous material.

The **synthesis of mesoporous material MCM-41** has been reported previously. In this preparation cetyltrimethylammonium bromide (CTAB, 9.4g) were dissolved in 65 g of deionized water under stirring before the addition of trimethyl ammonium hydroxide (TMAOH, 7.0 g). The resulting gel of composition  $\text{SiO}_2:0.27 \text{ CTAB}: 0.19 \text{ TMAOH}: 40 \text{ H}_2\text{O}$  was heated in a sealed stainless steel autoclave at 100°C for hydrothermal treatment for 24 hours. The products were recovered by filtration, washed thoroughly with distilled water and then dried in air. The surfactant was removed by calcination as described previously.

The **synthesis of mesoporous material MCM-48** has been reported previously. In this case sodium silicate is used as the silica source, cetyltrimethylammonium bromide as the surfactant and ethanol as a structure directing additive. Briefly, distilled water and surfactant are stirred at room temperature for 1 hour followed by addition of ethanol. After 30 minutes of further stirring at room temperature the desired amount of sodium silicate is added and hydrothermal treatment is conducted in a teflon autoclave at 100°C for 4 days. The synthesis gel had a molar ratio of 1  $\text{SiO}_2$ : 0.25  $\text{Na}_2\text{O}$ : 0.65  $\text{C}_{16}\text{TMABr}$ : 5  $\text{CH}_3\text{CH}_2\text{OH}$ : 100  $\text{H}_2\text{O}$ . The filtered product was dried in air and calcined as described above.

## M2. Characterisation Equipment and protocols.

### *Material Characterisation*

**Scanning electron microscopy** images were obtained using a JSM-7401F scanning electron microscope (JEOL Ltd., Tokyo, Japan) operating at 1–2 kV with no gold coating.

**Transmission electron microscopy (TEM)** of calcined and extracted samples was conducted with a JEOL-3000F microscope (JEOL Ltd, Tokyo, Japan), operating at 300 kV (spherical aberration: 0.6 mm; resolution 1.7 Å). Images were recorded using a charge-coupled device camera model Keen View, SIS Analysis Specialized Imaging (Olympus Soft Imaging Solutions, Olympus Corporation, Münster, Germany; size: 1024 × 1024; pixel size: 23.5 × 23.5 μm) at 30000–100000x times magnification using low dose conditions on calcined and drug loaded samples.

**Nitrogen adsorption isotherms** were measured at liquid nitrogen temperature (-196°C) using a Micromeritics TriStar II volumetric adsorption analyser (Micromeritics Instrument Corporation, GA, USA). Before the measurements, the samples were outgassed for 3 h at 200°C. The Brunauer–Emmett–Teller (BET) equation was used to calculate the surface area from the adsorption data obtained in the relative pressure ( $P/P_0$ ) range of 0.05 and 0.3. The total pore volume was calculated

from the amount of gas adsorbed at  $P/P_0 = 0.95$ . Pore size distribution curves were derived using the density functional theory method assuming a cylindrical pore model for all samples. Values from the  $t$ -plot analysis are obtained at a thickness range from 3 to 5 Å.

A **thermogravimetric analysis** instrument (TA instruments, TGA-2050, Delaware, USA) was used to determine the loading amount. Analysis was conducted at a heating rate of  $20\text{ }^{\circ}\text{C min}^{-1}$  from 20 to 800  $^{\circ}\text{C}$ . The sample weights varied from 5 mg to 10 mg. The derivative weight loss calculation was performed using TA instruments software (TA instruments, Universal analysis 2000, version 3.0 G).

**Thermal analysis** was conducted using a DSC instrument (TA instruments, DSC-2010, Delaware, USA) at a heating rate of  $10\text{ }^{\circ}\text{C min}^{-1}$  from 20 to 350  $^{\circ}\text{C}$ . The sample weights varied from 5mg to 10mg. Analysis was performed using TA instruments software (TA instruments, Universal analysis 2000, version 3.0 G).

### **M3. Drug loading and release.**

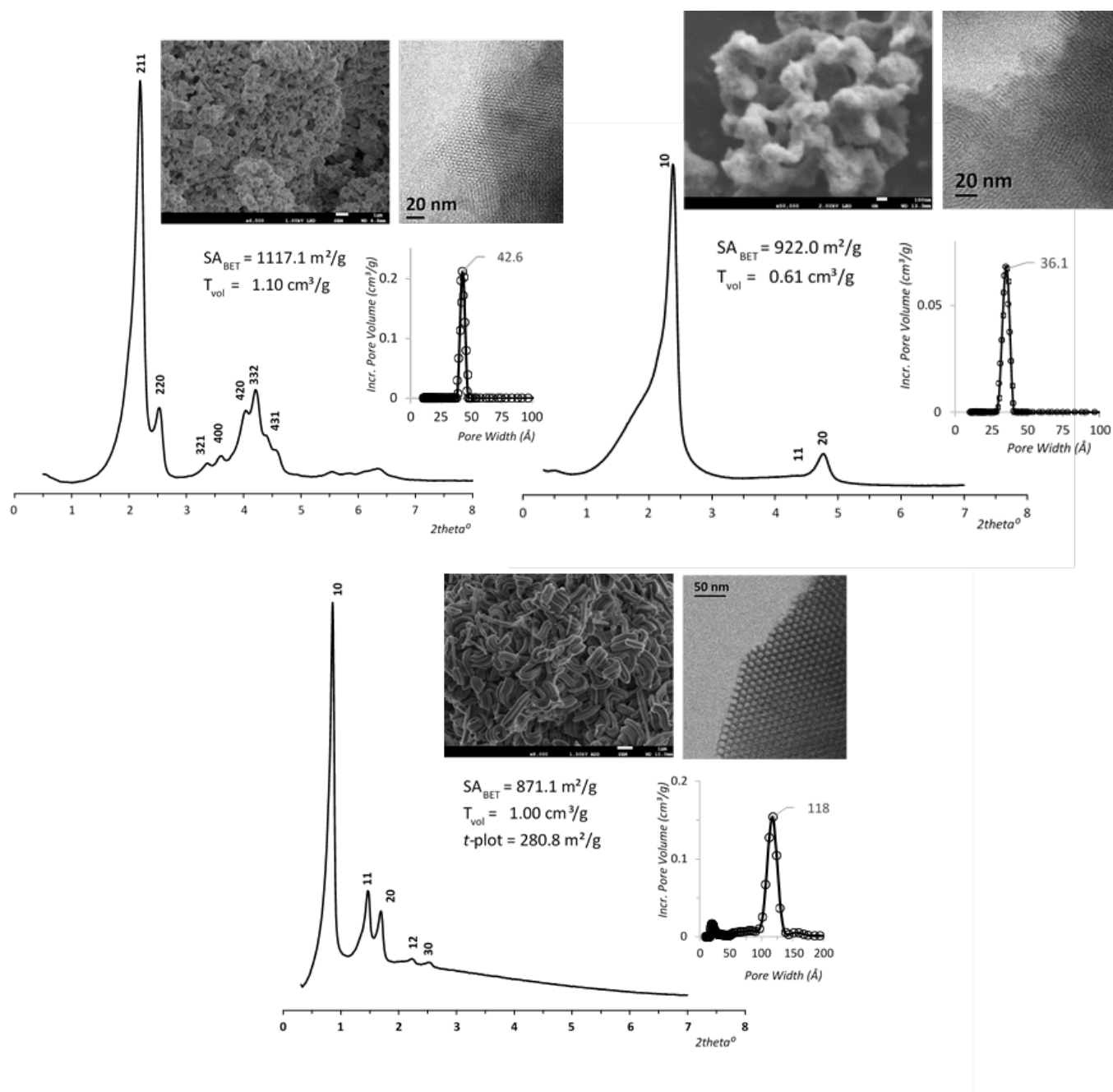
#### *Drug Loading*

Drug loading was achieved via a wetness impregnation method. In brief, a concentrated drug solution in ethanol was mixed with a sample of mesoporous silica (200 mg) and briefly sonicated. The solvent was removed by rotary evaporation at 40 $^{\circ}\text{C}$ . Samples were left to dried and stored in a desiccator until further use.

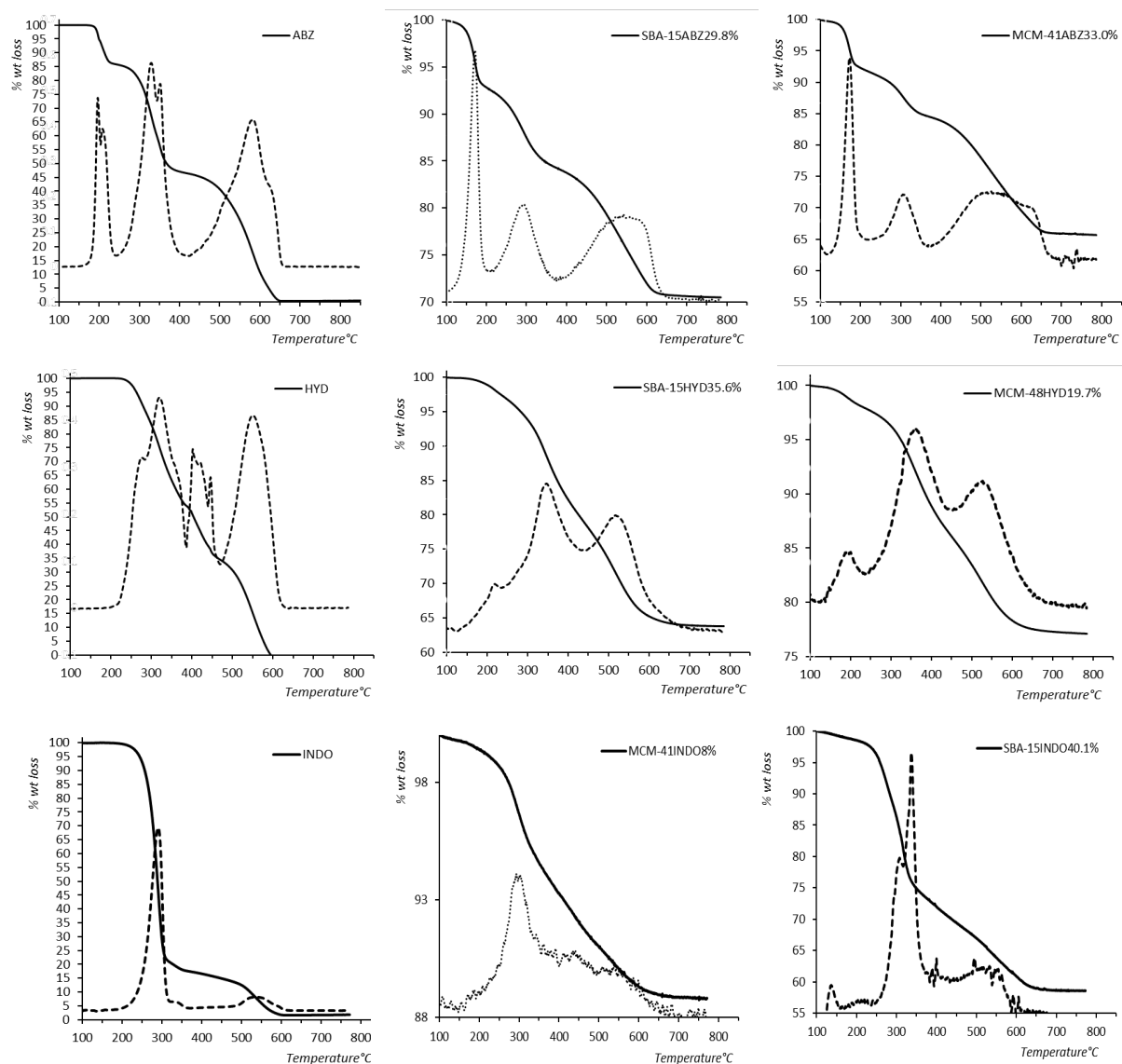
#### *Drug release*

Media preparation: Simulated intestinal fluid (SIF) was prepared by dissolving NaOH (0.896 g) and  $\text{KH}_2\text{PO}_4$  (6.805 g) in purified water (1 L) to give a solution with a pH of 6.8. All chemicals used was purchased from Sigma Aldrich, and purified water (Millipore Reference, Sydney, Australia) was used for the experiment. Size 1 gelatin capsules (ProSciTech, Batch: RL042, Queensland, Australia) were used for both pure drug and drug loaded mesoporous silica samples. Drug release was assessed under sink conditions (900mL SIF, pH 6.8) by UV/Vis absorbance scan (Agilent, Cary 60 UV-Vis, Sydney, Australia). The release was carried out in a dissolution bath (Agilent, 708-DS, Sydney, Australia) at a stirring rate of 50 rpm at 37 $^{\circ}\text{C}$  and data collected typically for 24 hours.

**Figure S1.** Physical and structural characterisation of calcined mesoporous materials MCM-48 (left), MCM-41[2] and SBA-15(bottom). X-ray diffraction spectra of all samples show sharp mesoscale peaks that can be indexed on the basis of hexagonal (for MCM-41and SBA-15) and cubic (for MCM-48) crystal class. Insets show scanning and transmission electron microscopy (TEM), showing highly ordered structures with agglomerated particles for MCM-41 and MCM-48, and rod type particles for SBA-15. The pore size distribution as derived from nitrogen adsorption data is shown for each sample. Together with the textural properties. Note the presence or a certain amount of microporosity (t-plot analysis) for the SBA-15 sample.

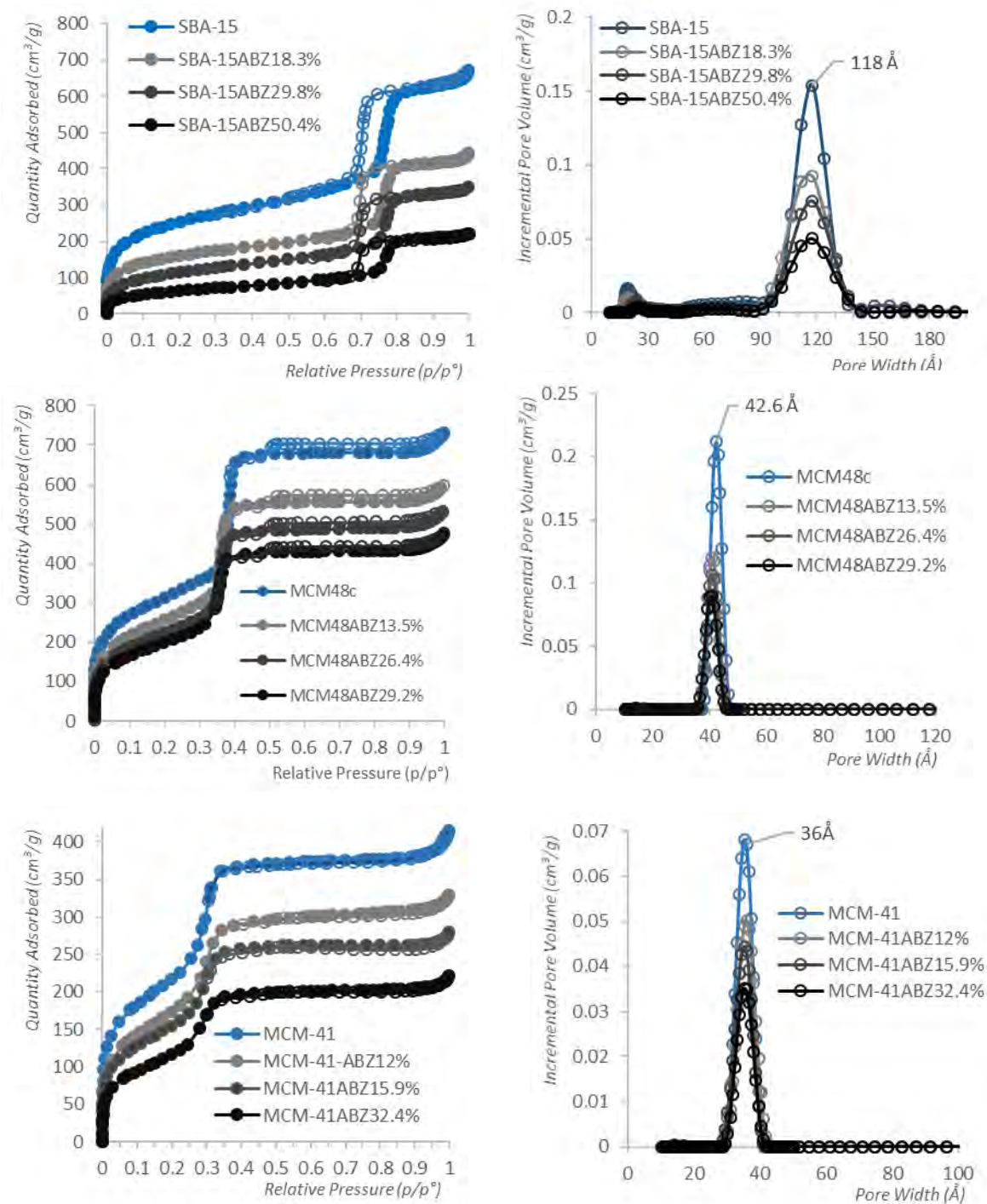


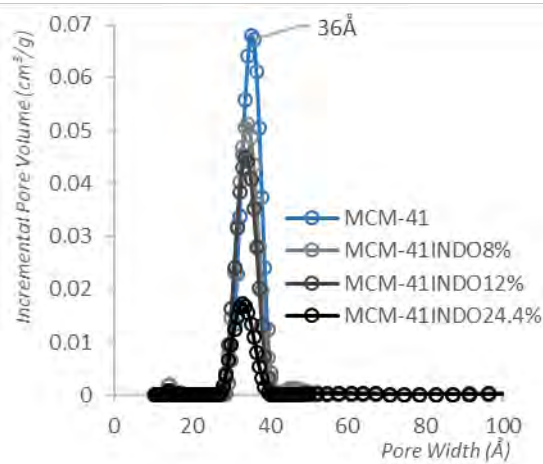
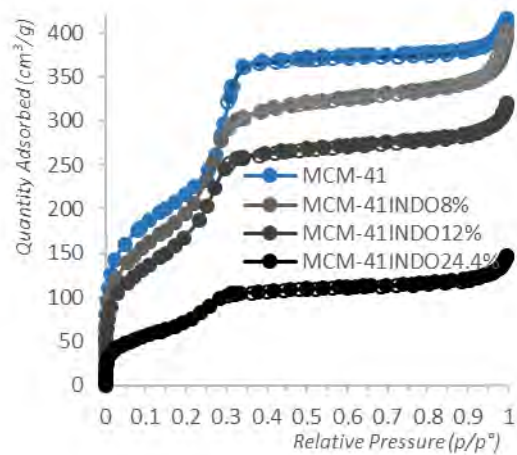
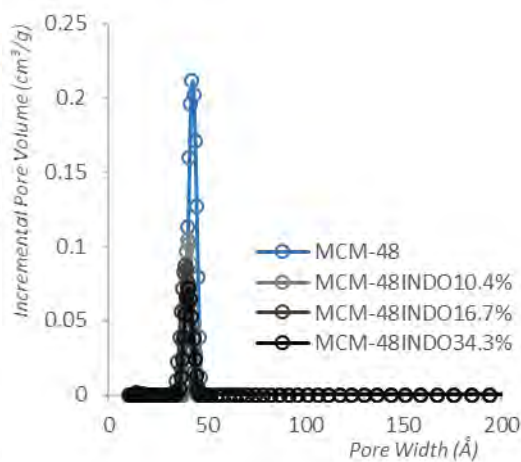
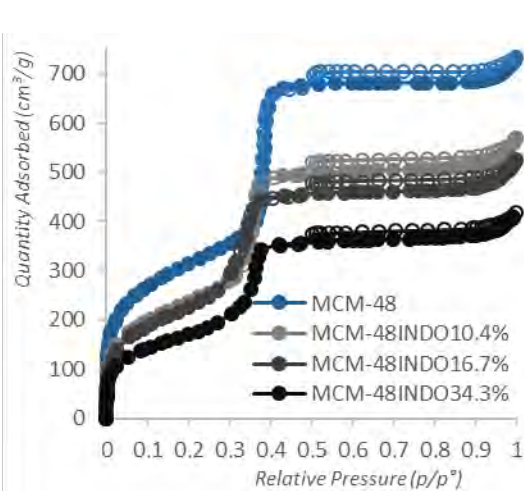
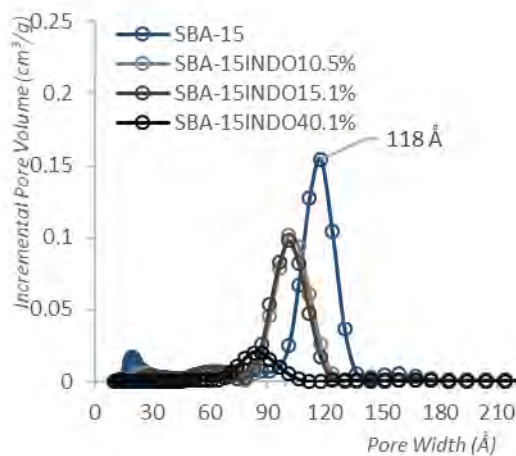
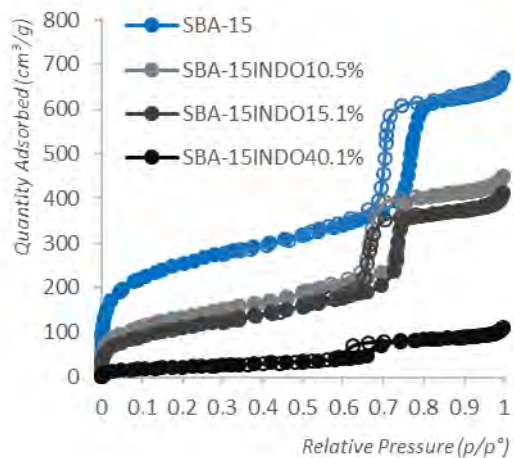
**Figure S2.** Thermogravimetric analysis (TGA) curves and first derivative curves of selected drug-loaded samples showing the variation in decomposition temperatures with respect to loading amount.

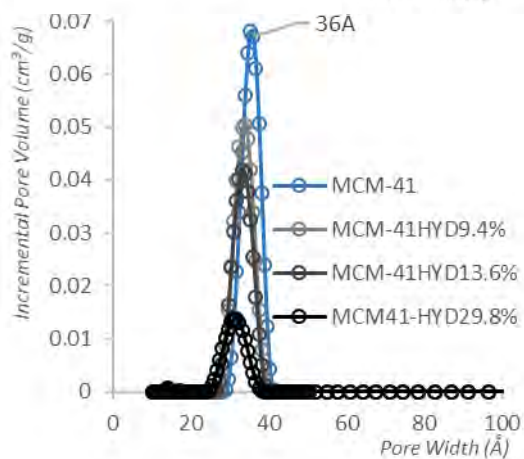
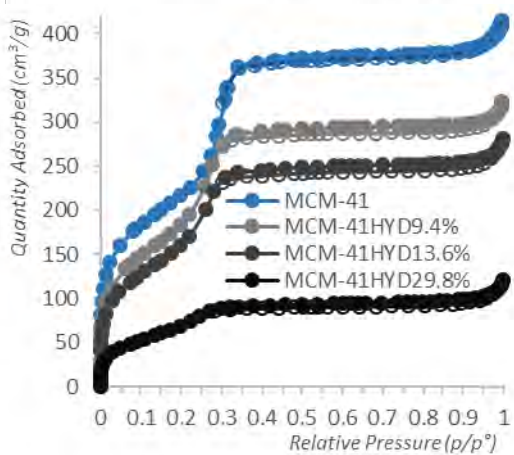
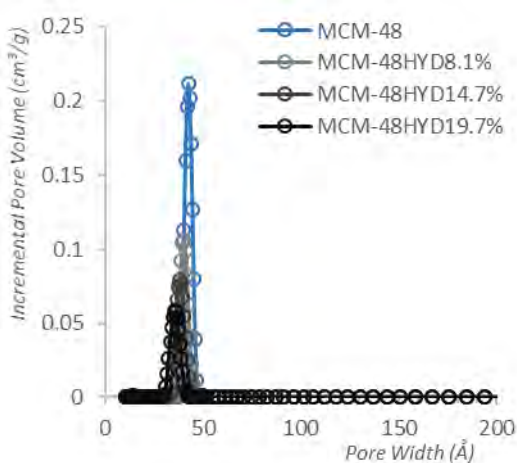
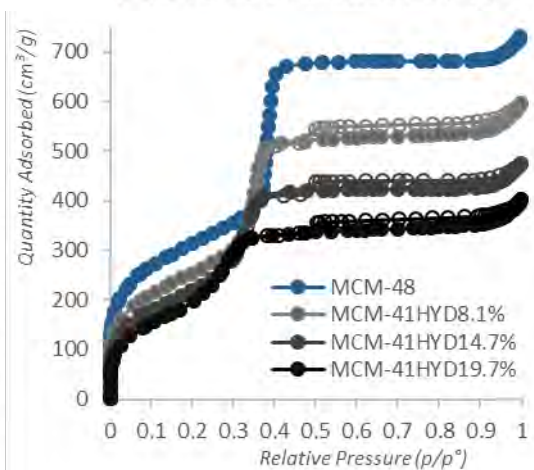
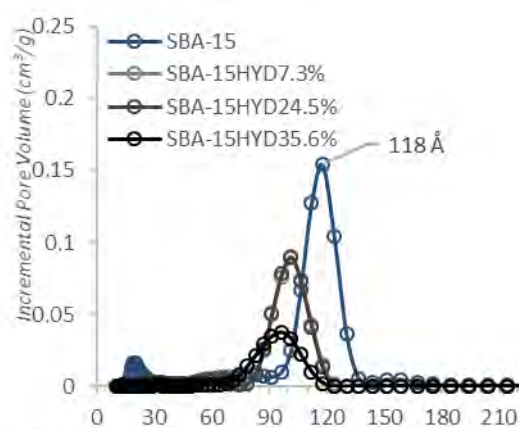
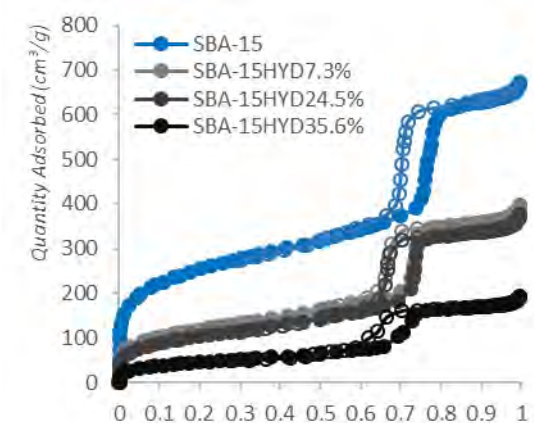




**Figure S3.** Nitrogen adsorption-desorption isotherm curves for calcined and drug-loaded samples, together with the pore size distributions derived from DFT analysis assuming a cylindrical pore.

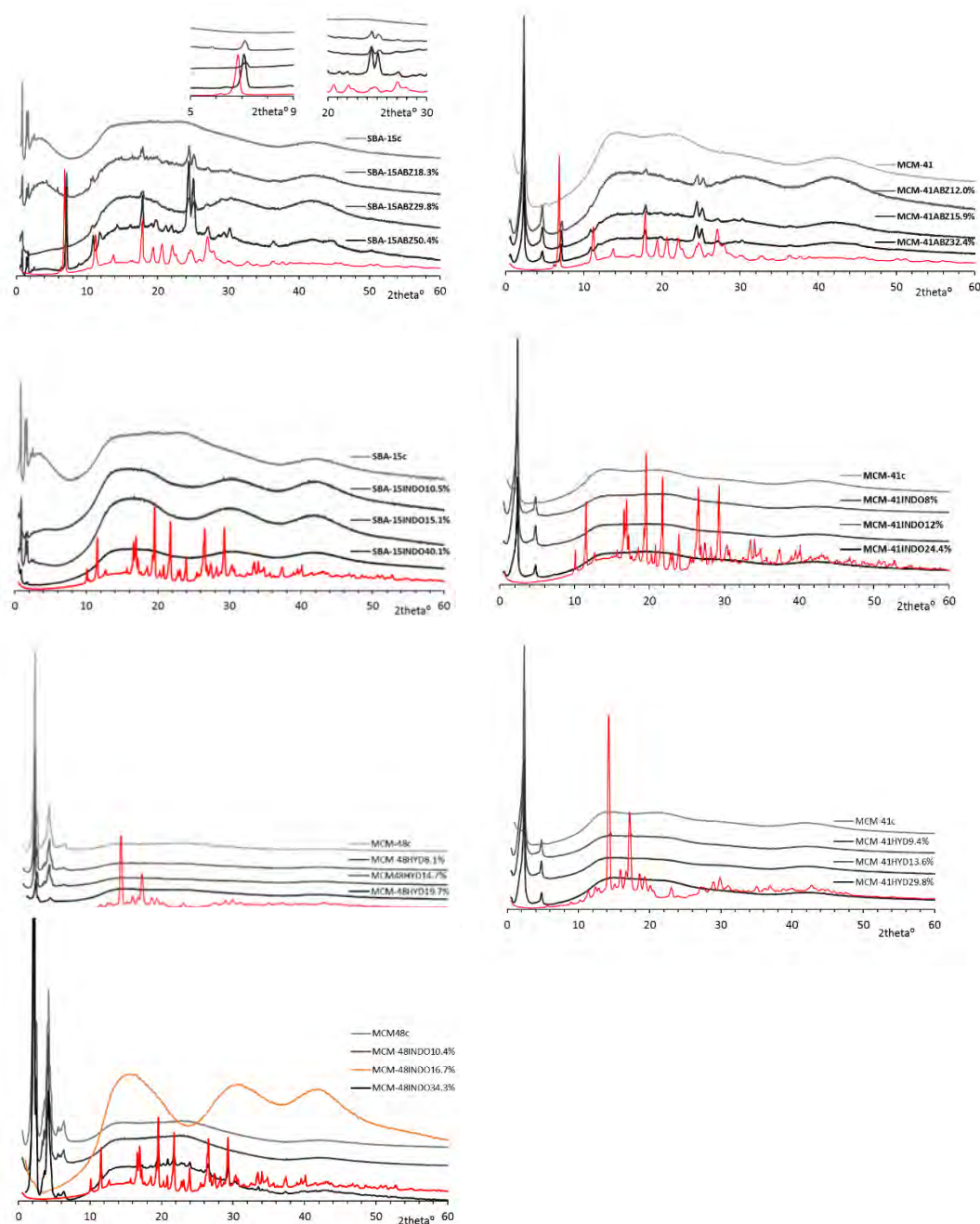




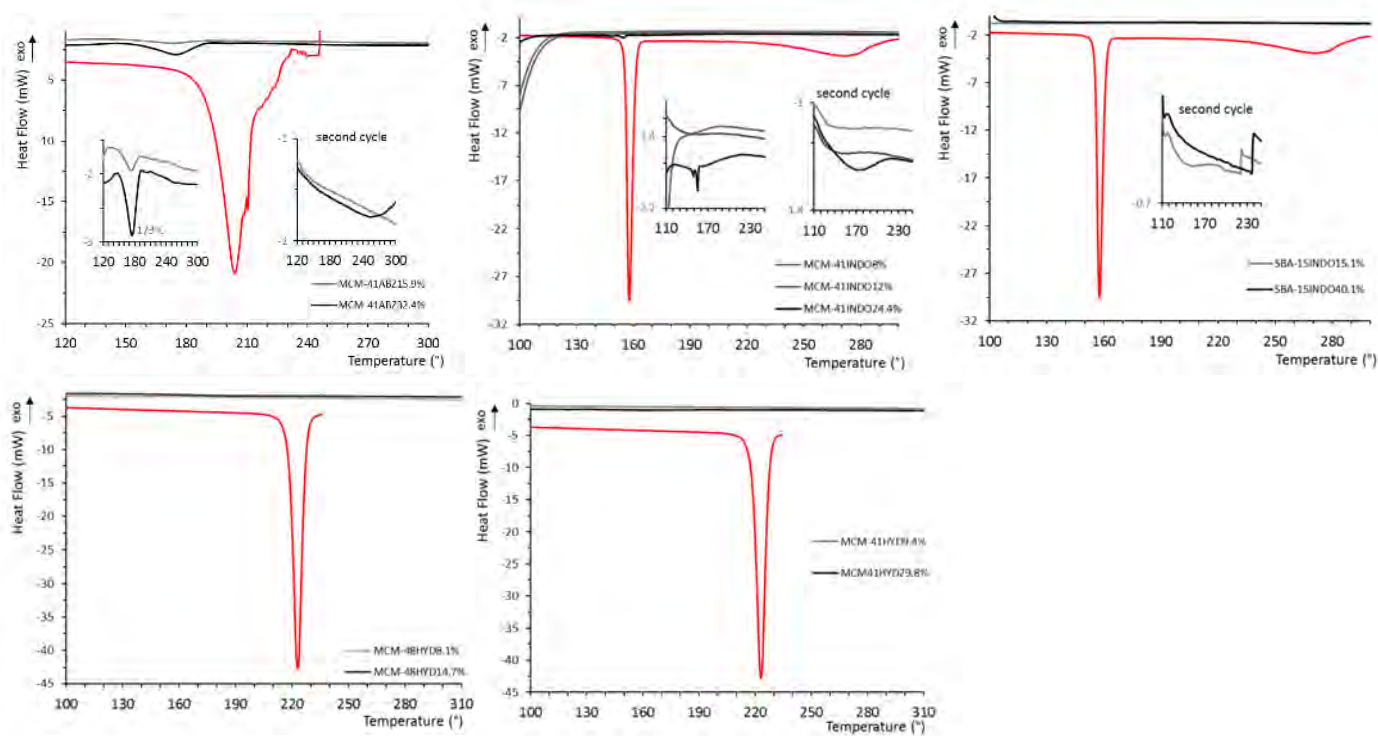




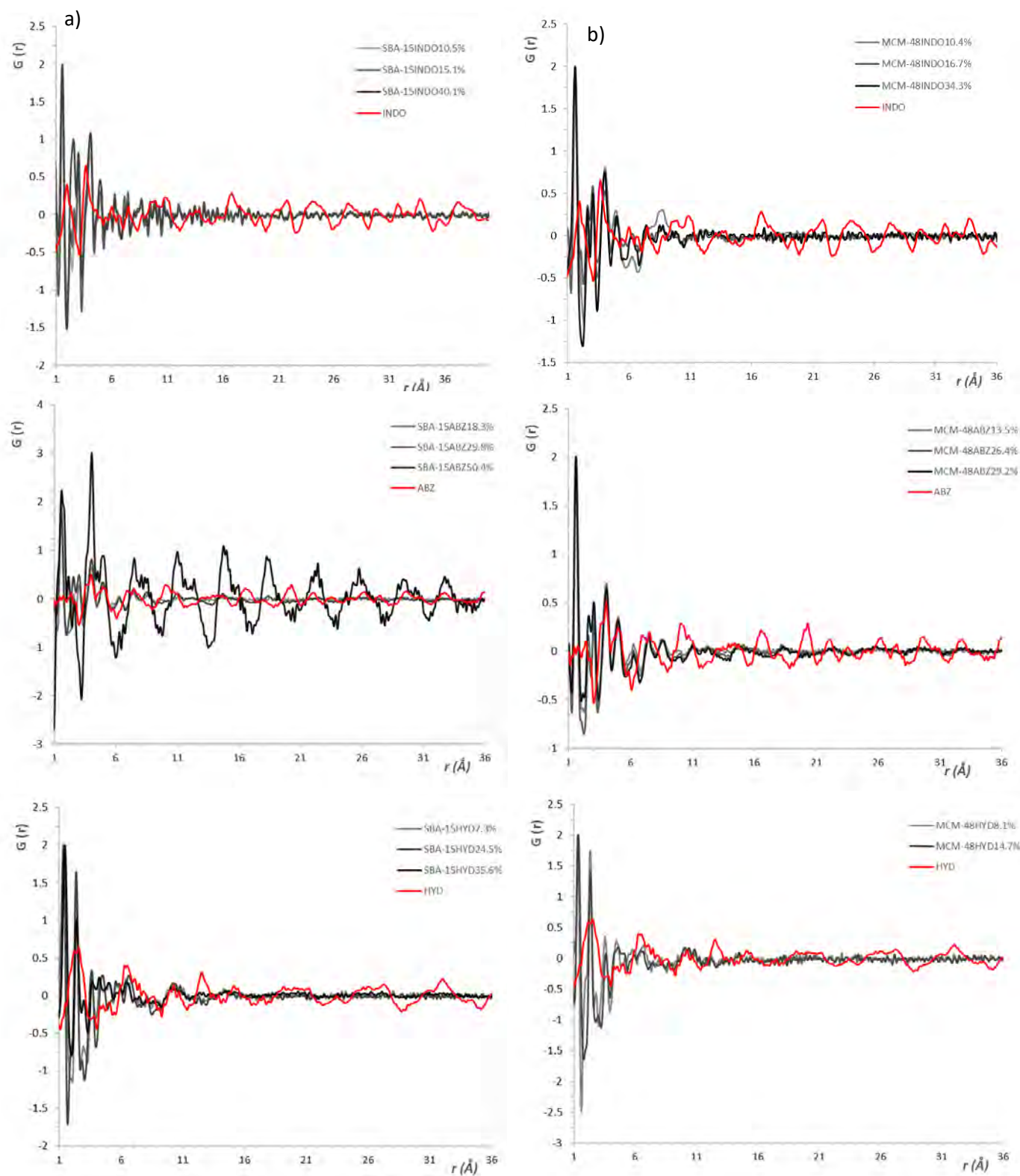
**Figure S4.** Powder X-ray diffraction patterns of mesoporous material ABZ, HYD and IND). Red curves are the respective unloaded drug diffractograms. Insets show regions where scattering peaks can be observed.



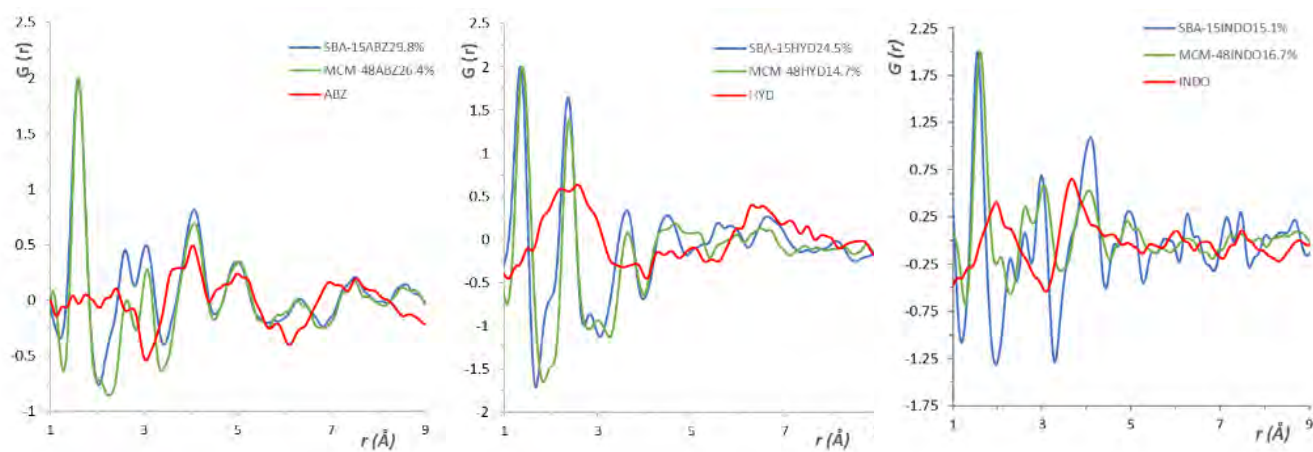
**Figure S5.** Differential scanning calorimetry (DSC) traces of loaded mesoporous silica materials compared to traces for the free crystalline drugs, for INDO and HYD.



**Figure S6.** Comparison of total scattering profiles for mesoporous loaded samples and free crystalline drugs for (a) SBA-15 and (b) MCM-48.

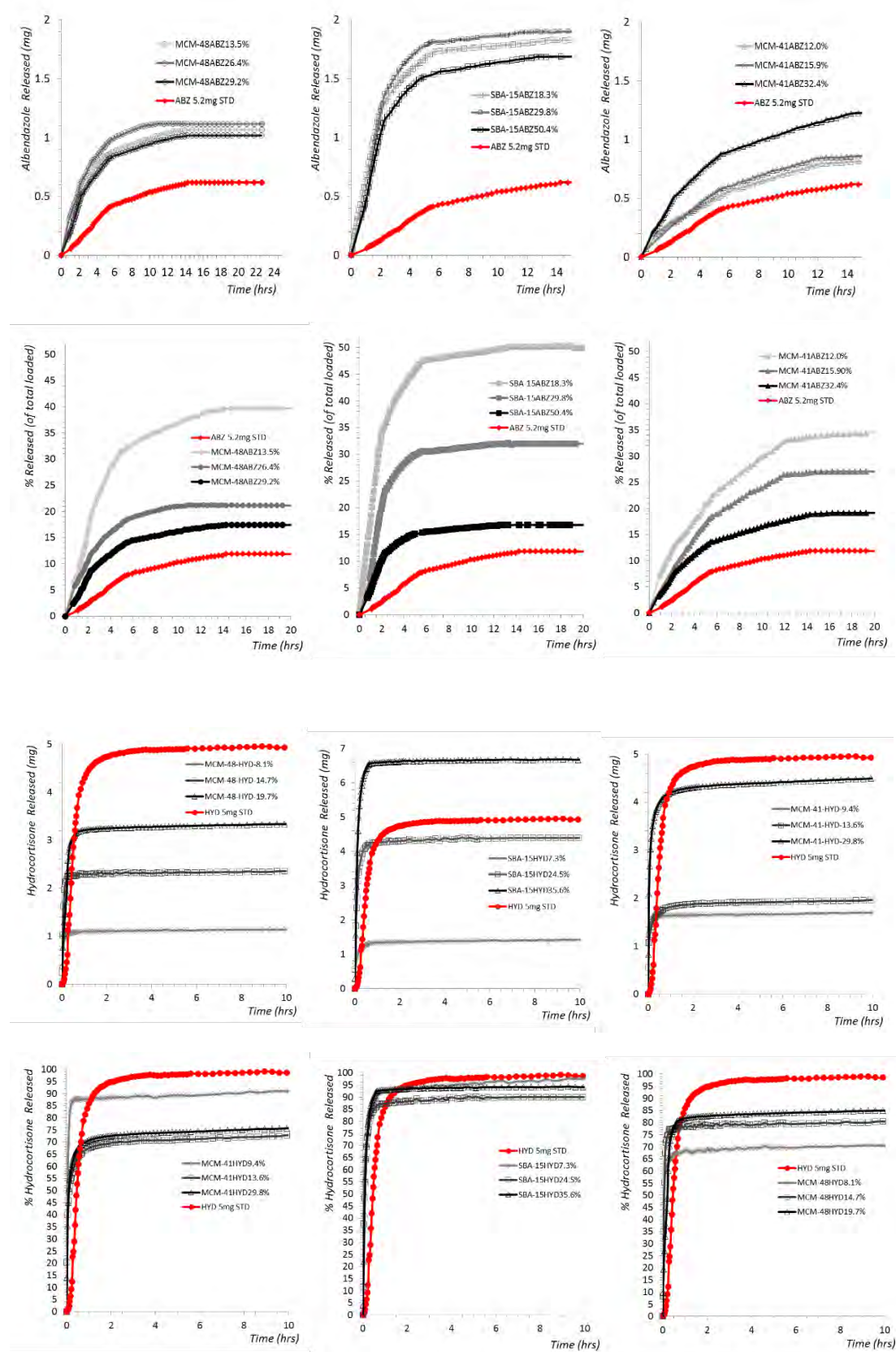


**Figure S7.** Comparison of total scattering profiles for mesoporous loaded samples and free crystalline drugs.

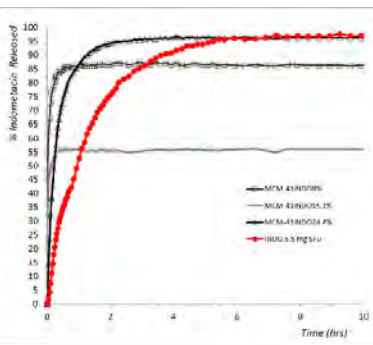
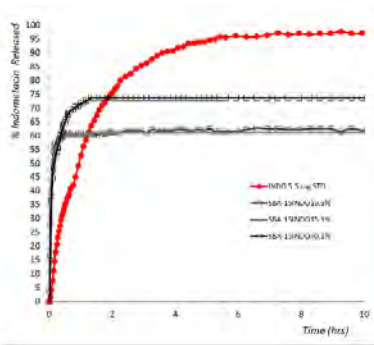
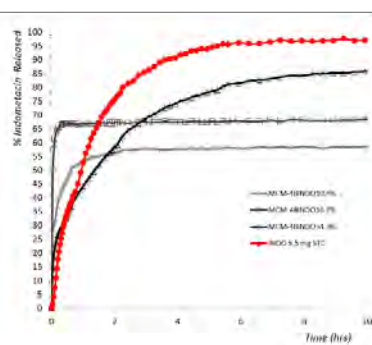
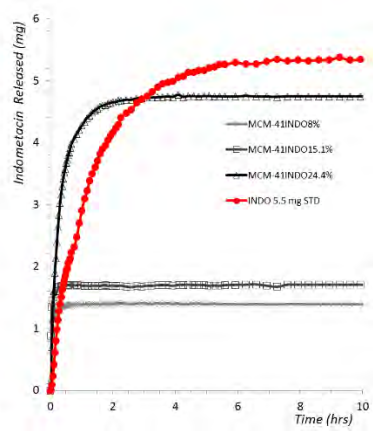
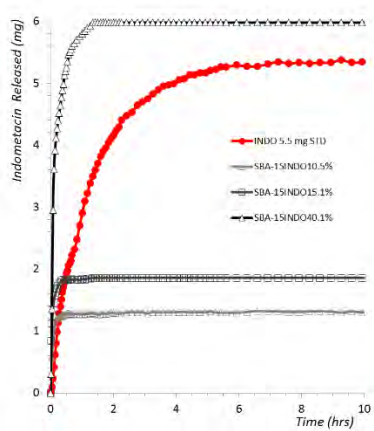
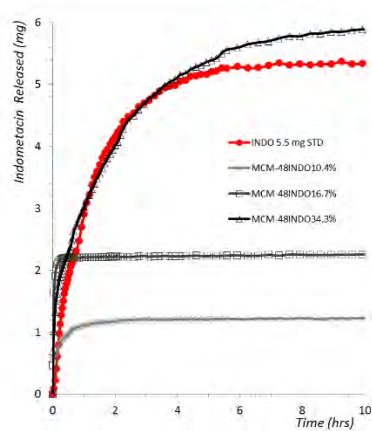




**Figure S8.** Dissolution curves for drug loaded mesoporous silica samples conducted under sink conditions in Simulated Intestine Fluid (SIF).







## 8.2 Appendix B: Supporting information of chapter 4.

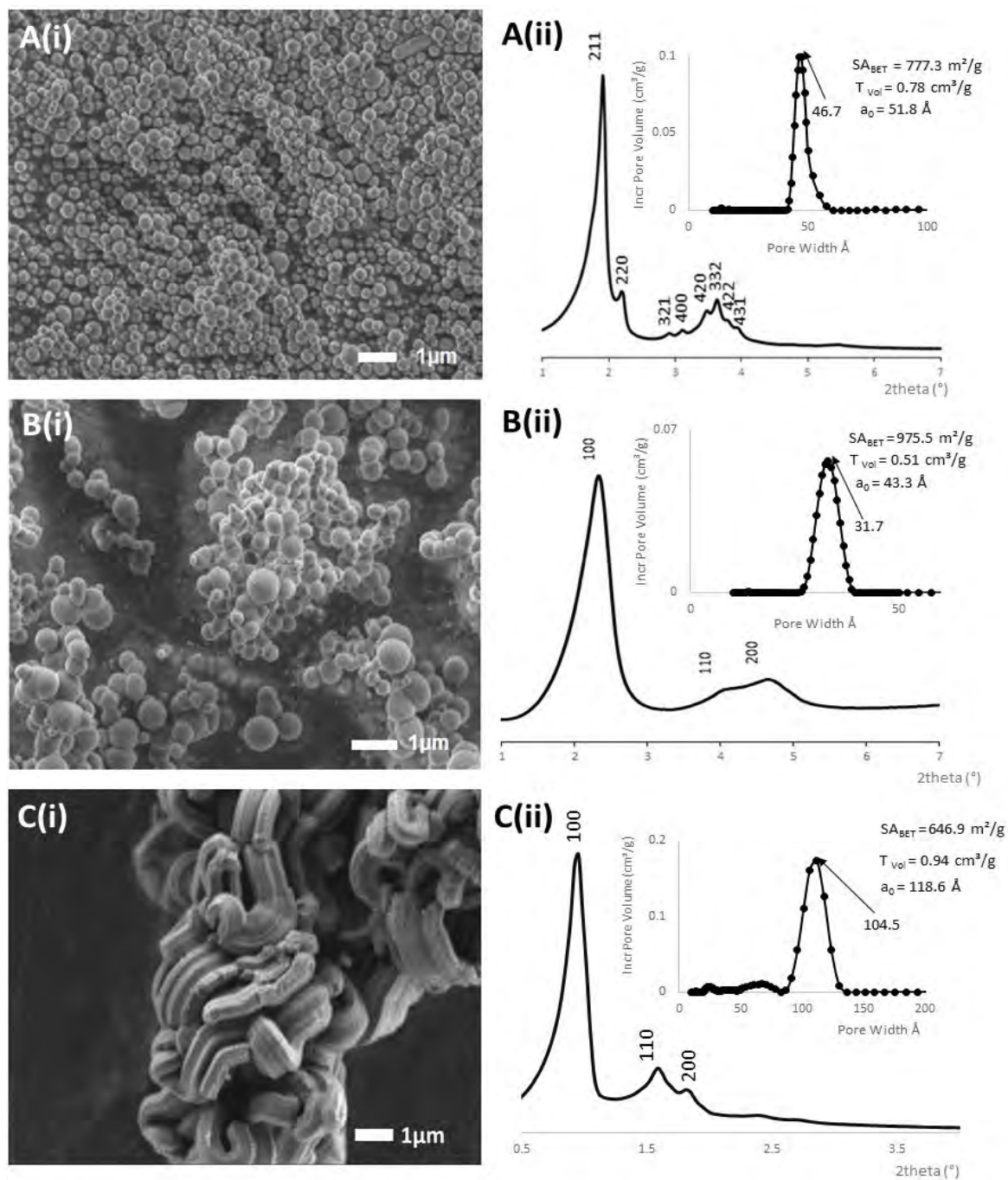
Supporting Material for:  
**Antioxidant properties of probucol released from mesoporous silica**

Michael Lau, Kalpeshkumar Giri, Alfonso E. Garcia-Bennett\*

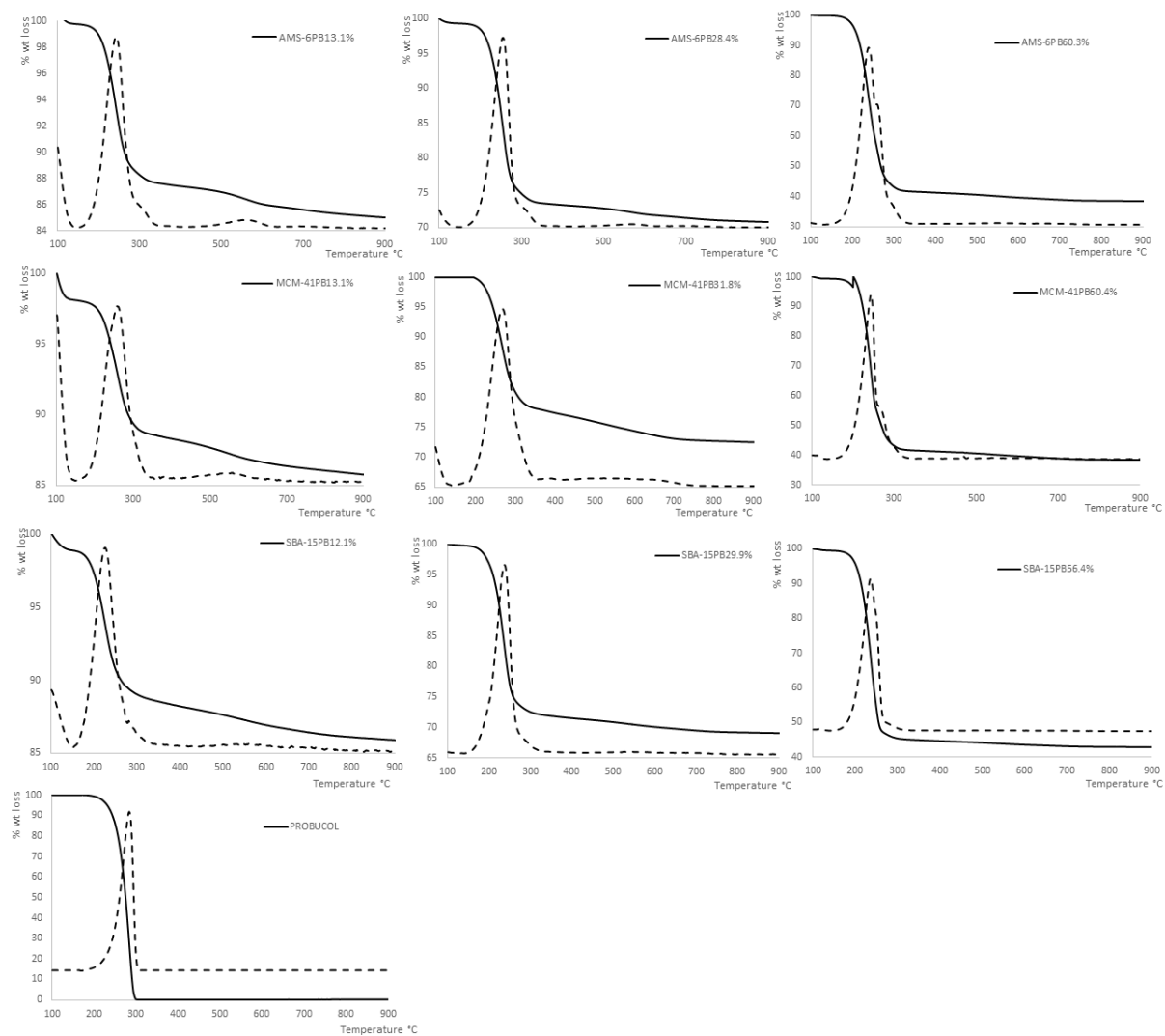
Table of Contents

- S1.** Physical and structural characterization of calcined MCM-41, AMS-6 and, SBA-15
- S2.** Thermogravimetric Analysis of drug loaded mesoporous silica
- S3.** Powder X-ray diffractograms of drug loaded mesoporous materials MCM-41 and SBA-15
- S4.** Differential scanning calorimetry scans of PB and drug loaded mesoporous materials MCM-41, SBA-15, and AMS-6
- S5.** Adsorption isotherms for calcined and drug-loaded samples
- S6.** Kinetic Dissolution curves in SIF for probucol loaded into mesoporous materials AMS-6, SBA-15 and MCM-41.
- S7.** Kinetic Dissolution curves in SIF for probucol with different capsule dose for mesoporous material AMS-6, SBA-15 and MCM-41.
- S8.** Kinetic Dissolution curves in SIF for probucol with different capsule dose for mesoporous material AMS-6, SBA-15 and MCM-41.
- S9.** Percentage reactive oxygen species (ROS) negative cells (hCMEC/D3)
- S10.** Percentage dead and viable cells (hCMEC/D3)
- S11.** Percentage dead and viable cells (microglia)
- ST1.** Pharmacokinetic parameters for PB-loaded mesoporous silica particles.

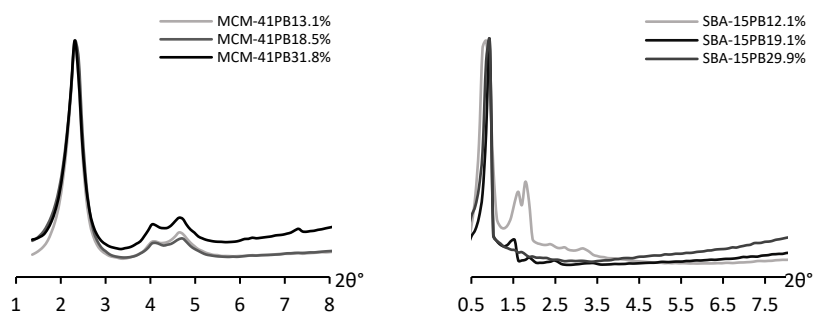
**Fig S1.** Physical and structural characterization of calcined (A) AMS-6, (B) MCM-41 and, (C) SBA-15. Scanning electron microscopy images (i) show agglomerated spherical particles for AMS-6 and MCM-41, rod type morphology for SBA-15. Low angle XRD patterns (ii) can be indexed to cubic (AMS-6) and hexagonal (MCM-41 and SBA-15) mesoporous order. Pore size and porous properties (ii inset) as derived from nitrogen adsorption data are shown for each sample.



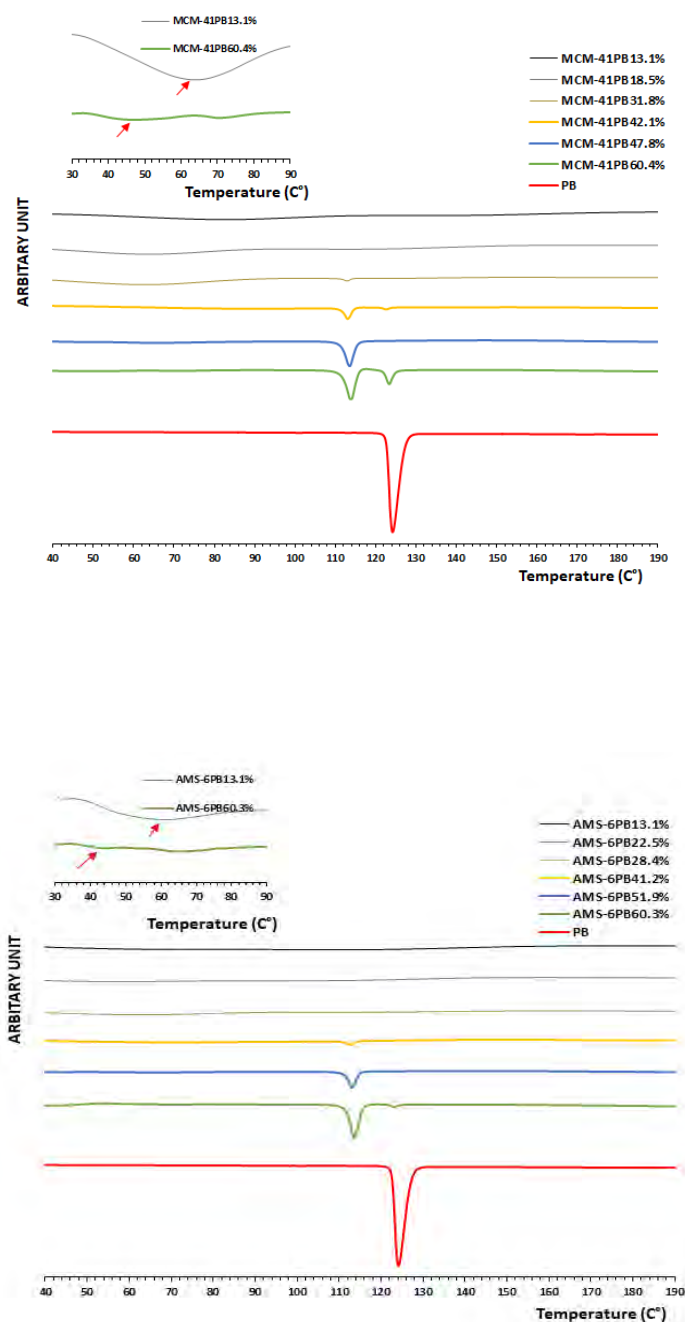
**Fig S2.** Thermogravimetric analysis of drug loaded mesoporous silica for AMS-6, MCM-41, and SBA-15 respectively.



**Fig S3.** Powder X-ray diffractograms of drug loaded mesoporous materials MCM-41 and SBA-15 at low loadings, normalized to the most intense peaks to show that only small changes in peak intensities occur as a function of loading amount. Small changes to scattering intensities observed > 30wt% loading for SBA-15 samples are due to a decrease in the overall amount of mesostructured silica material in the XRD sample.



**Fig S4.** Differential scanning calorimetry scans of PB and drug loaded mesoporous materials MCM-41, AMS-6, and SBA-15 respectively. Curves have been shifted on the y-axis, for ease of interpretation. Inserts show the shift in the water desorption endotherm between the lowest and highest drug loaded samples (red arrows) in MCM-41, AMS-6 and SBA-15 respectively.



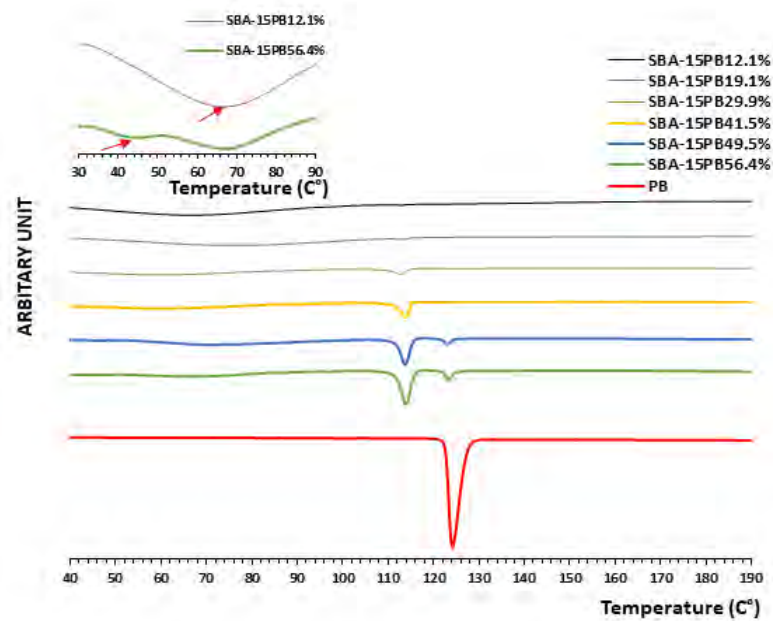




**Fig S5.** Nitrogen adsorption-desorption isotherm curves for calcined and drug-loaded samples, together with the pore size distributions from DFT analysis. Saturation in surface area, and pore volume was observed at drug loadings > 40wt%.

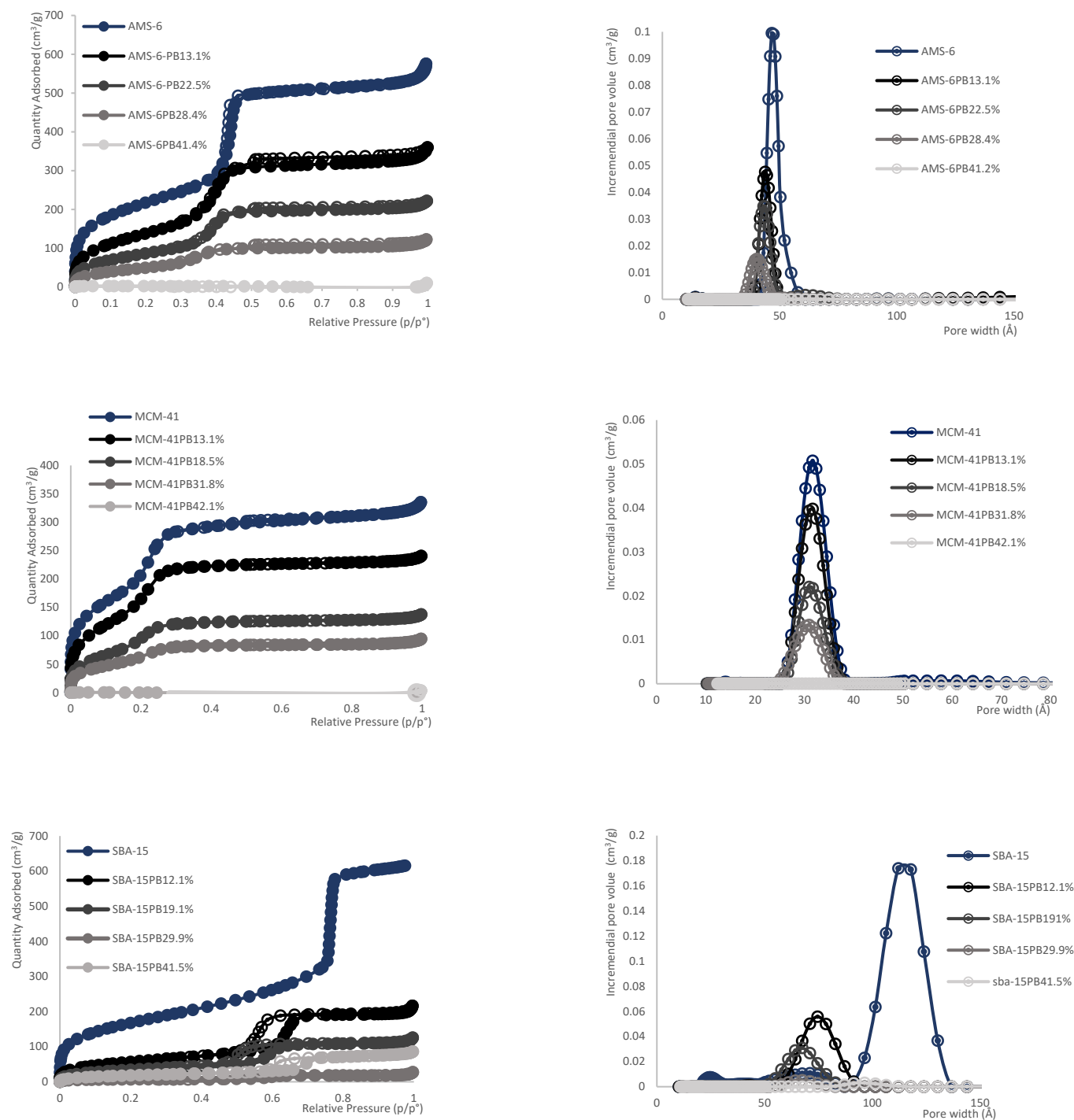


**Fig S6.** Dissolution curves for drug loaded mesoporous samples conducted under sink conditions in simulated intestine fluid (SIF) at 30 mg capsule powder fill weight.

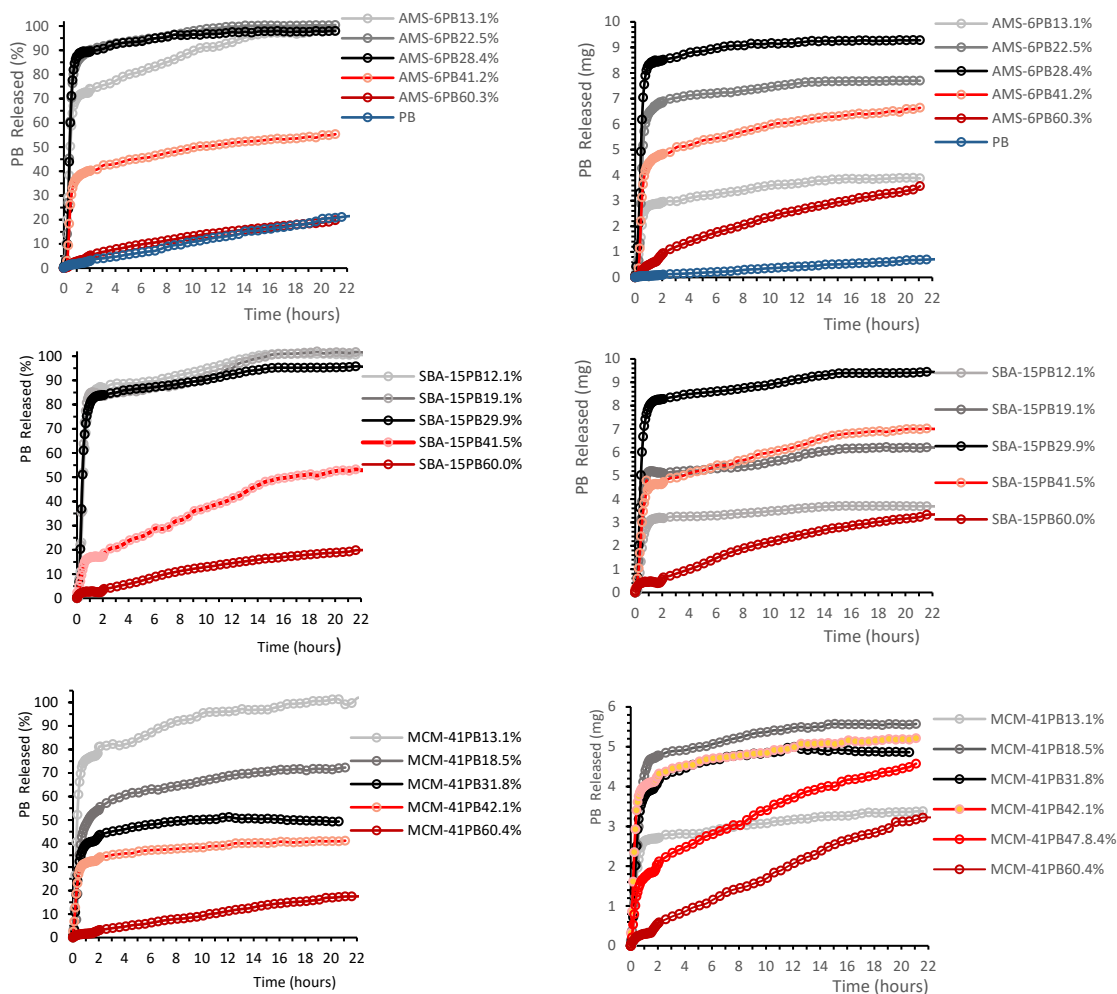


**Fig S7.** Dissolution curves for drug loaded mesoporous samples conducted under sink conditions in simulated intestine fluid (SIF) at capsule dose from 30mg to 100mg.

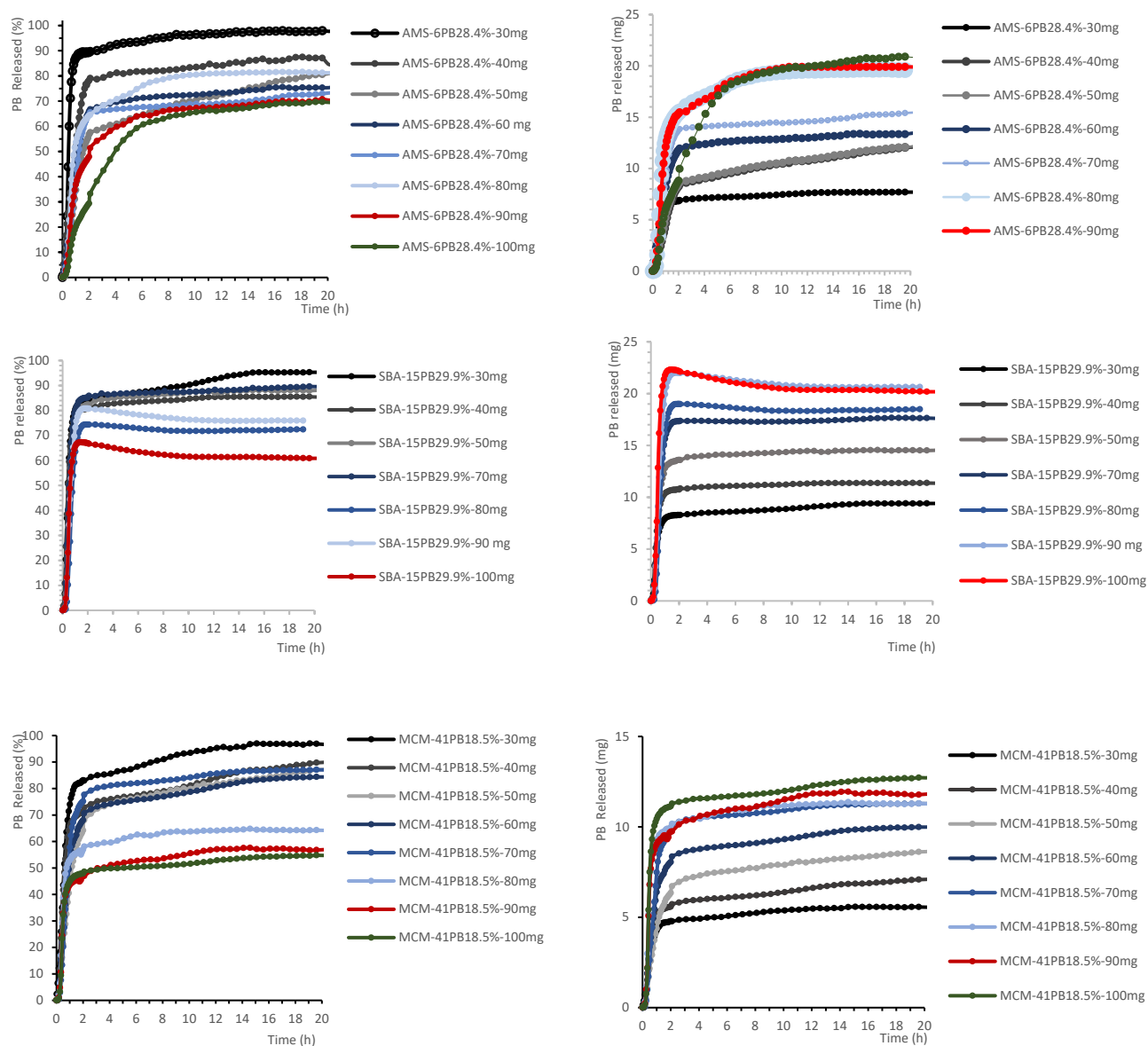


**Fig S8.** Summary of kinetic release measurements of PB loaded into mesoporous silica materials conducted at different doses for AMS-6, SBA-15 and MCM-41. Dissolution curves were conducted under sink conditions in simulated intestine fluid (SIF).

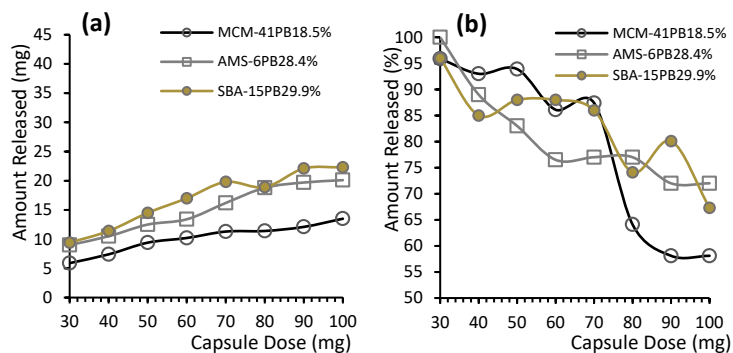


**Fig S9.** (a) %ROS - cells (hCMEC/D3) after 24 h incubation with different concentrations of hydrogen peroxide (500  $\mu$ M to 1500  $\mu$ M) together with the test compounds. The Positive control is hydrogen peroxide by itself whilst the negative control represents normal cell growth with no hydrogen peroxide. (b) Evolution of antioxidant activity of test samples incubated with 1000  $\mu$ M hydrogen peroxide for 2 to 24 h plotted as a function of %ROS – cells (hCMEC/D3).

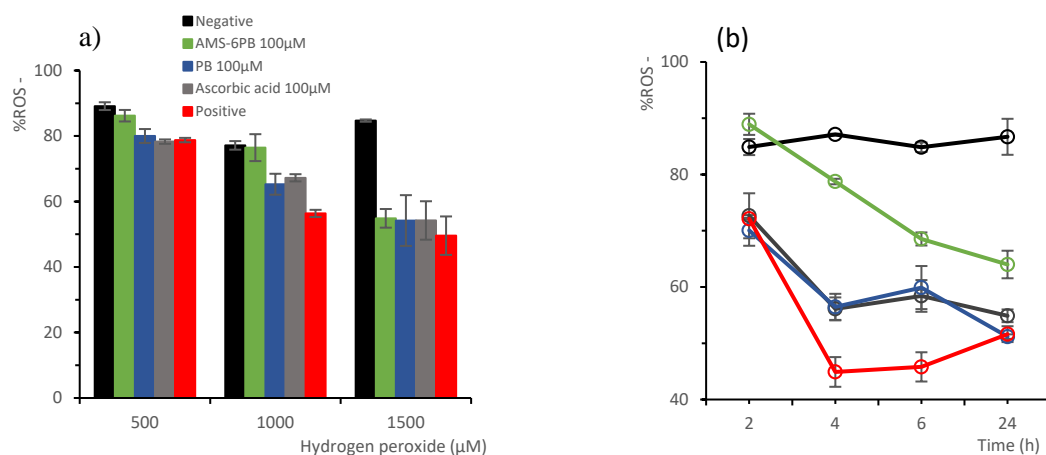


**Fig S10.** (a) %dead cells (hCMEC/D3) after 2 to 24 h incubation with 1000  $\mu$ M hydrogen peroxide and the test compounds. The Positive control is hydrogen peroxide by itself whilst the negative control represents normal cell growth with no hydrogen peroxide. (b) Percentage of viable cells (hCMEC/D3) after 2 to 24hrs incubation at 1000  $\mu$ M hydrogen peroxide together with the test compounds.

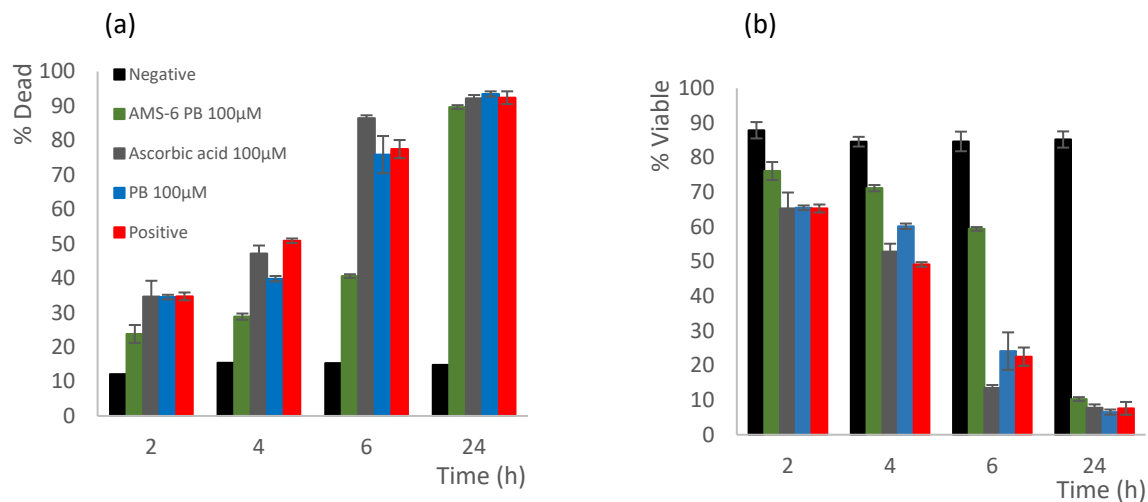


**Fig S11.** (a) % dead cells (microglia) after 2 to 24 h incubation with the test compounds. The Positive control is microglia cells incubated with 10  $\mu\text{g}/\text{ml}$  LPS without addition of the test compounds, whilst the negative control represents normal cell growth without activation by LPS. (b) Percentage of viable cells (microglia) after 2 to 24hrs incubation with the test compounds.

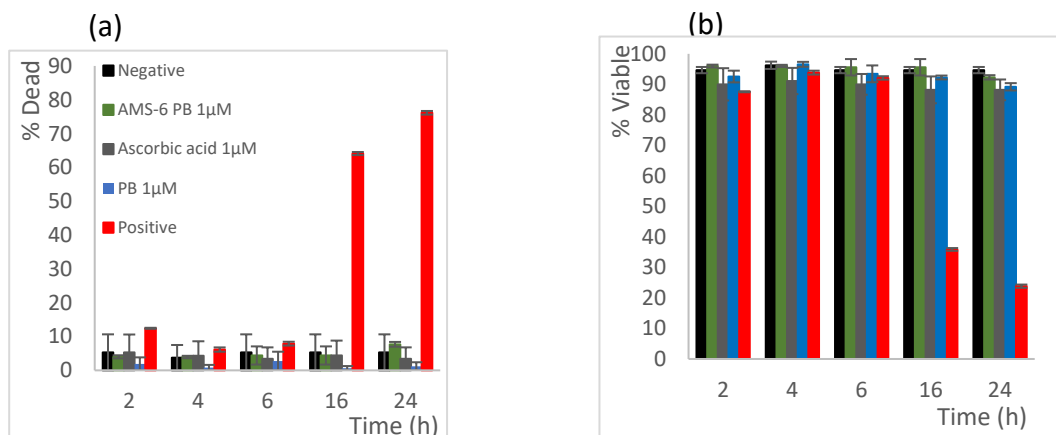


**Table ST1.** Fitted drug release kinetic parameters, using both Higuchi (H) and Korsmeyer-Peppas (KP) model, obtained from dissolution experiments for PB loaded mesoporous silica samples. Crystalline probucol follows zero order rate of release, with 50% of drug release ( $t_{1/2}$ ) > 24 h. PB loadings below complete pore filling resulted in the encapsulated of the drug in the amorphous state, and was shown to have a rapid rate of release as measured by the higuchi rate constant ( $k_H$ ) and 50% drug release of less than 1 h. Drug loadings above complete pore filling resulted in a reduction in the rate of drug release, due to the increase in the recrystallization of PB.

	$R^2$	Zero order ( $k_0$ )	$t_{1/2}$
<b>Probucol</b>	0.98	1.1	>24 hours

	wt%	H $R^2$	$k_H$	$t_{1/2}$ min	KP $R^2$	$k_{KP}$
<b>AMS-6</b>	13.1	0.98	95.9	27.1	0.98	1.6
	22.5	0.96	112.5	26.7	0.98	0.4
	28.4	0.97	123.8	26.8	0.99	0.5
	41.2	0.97	49.3	635.1	0.96	1.6
	51.9	0.97	14.7	-	0.99	0.2
	60.3	0.98	4.1	-	0.99	0.8
<b>MCM-41</b>	13.1	0.97	80.2	26.7	0.95	1.2
	18.5	0.97	71.5	50.1	0.97	0.61
	31.8	0.97	45.5	605.1	0.98	1.6
	42.1	0.94	35.7	-	0.95	0.9
	47.8	0.98	13.3	-	0.97	1.1
	60.4	0.86	2.1	-	0.97	0.3
<b>SBA-15</b>	12.1	0.97	122.4	24.8	0.97	1.39
	19.1	0.98	107.2	25.5	0.97	0.69
	29.9	0.98	99.1	25.5	0.92	0.74
	41.5	0.98	70.3	50.5	0.93	0.64
	49.5	0.96	9.23	-	0.96	0.95
	56.4	0.91	2.77	-	0.91	0.44



### 8.3 Appendix C: Supporting information of chapter 5.

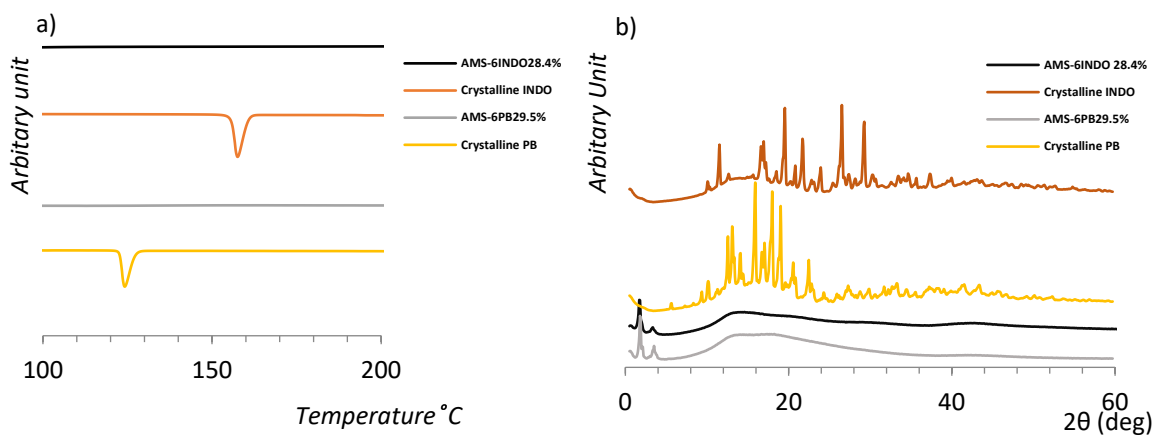


**Figure C1:** a) DSC analysis of Crystalline drug compared to drug loaded in mesoporous silica AMS-6. b) XRD analysis of crystalline drug compared to drug loaded in AMS-6.

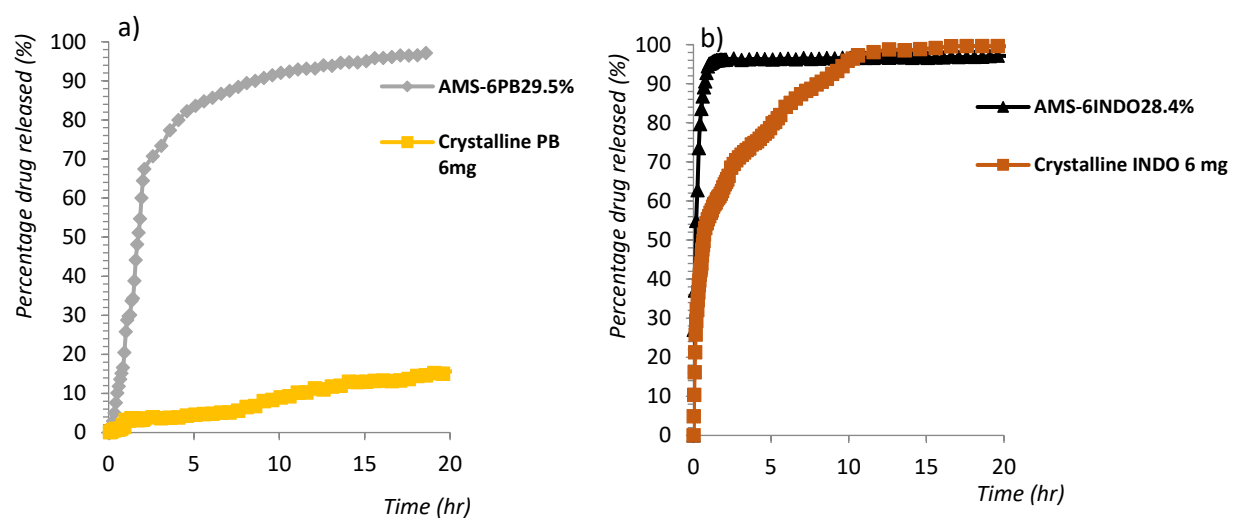


**Figure C2:** Percentage (%) drug released for probucol (a), and indomethacin (b) from *in vitro* dissolution experiments using SIF as the dissolution medium.

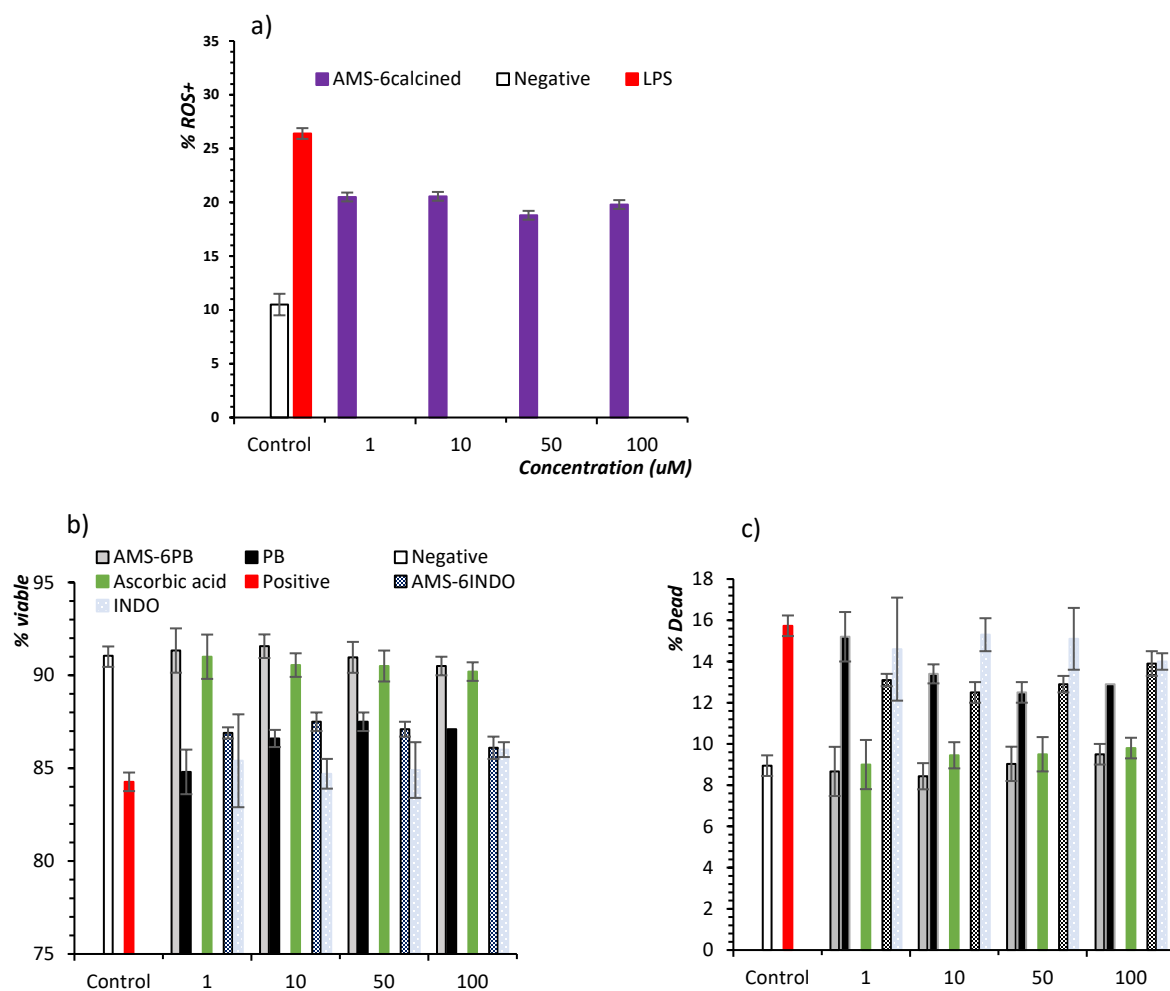


**Figure C3.** (a) Concentration dependent effects of mesoporous silica AMS-6 on the generation of ROS+ HEBC cells after 24 hours incubation with 1 ug/ml LPS. (b) Percentage of viable and dead cells after addition of test compounds after 24 hours incubation with 1 ug/ml LPS. The positive control (red bar) are cells incubated with 1 ug/ml LPS and negative control (white bar) is cells incubated with media only for 24 hours.

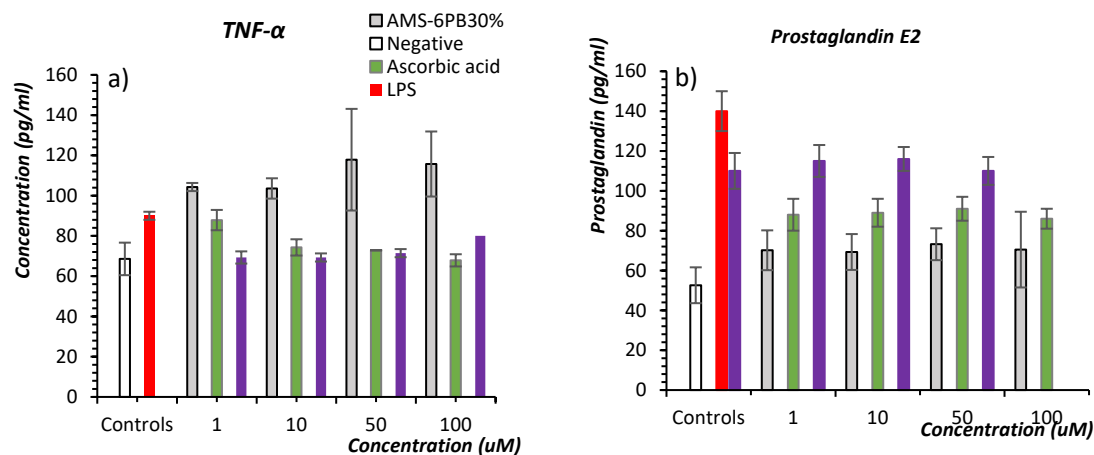


**Figure C4.** (a) Concentration dependent effects of mesoporous silica AMS-6, AMS-6PB, ascorbic acid on the generation of TNF- $\alpha$  in HEBC cells after 24 hours incubation with 1  $\mu$ g/ml LPS. (b) Concentration dependent effects of mesoporous silica AMS-6, AMS-6PB, ascorbic acid on the generation of prostaglandin E<sub>2</sub> in HEBC cells after 24 hours incubation with 1  $\mu$ g/ml LPS. The positive control (red bar) are cells incubated with 1  $\mu$ g/ml LPS and negative control (white bar) is cells incubated with media only for 24 hours.

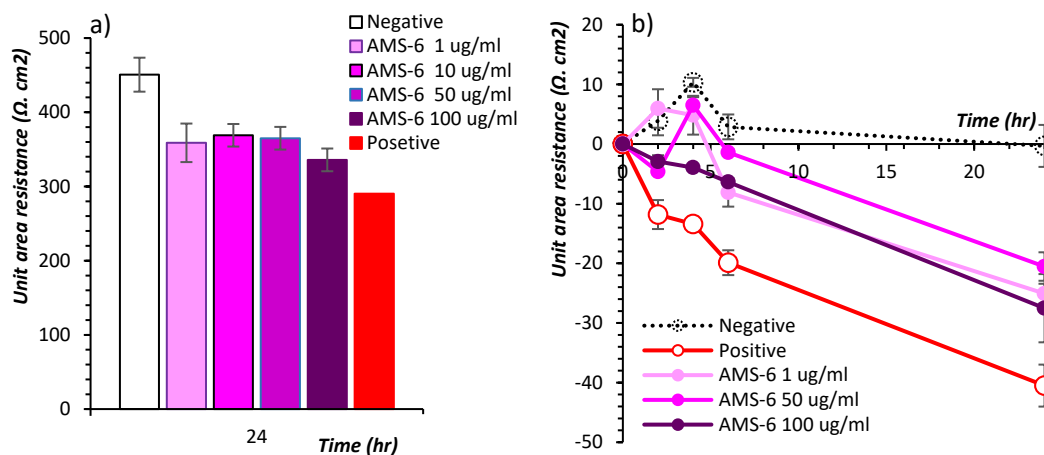


**Figure C5.** (a) TEER electrical resistance measurements conducted on monolayers of HBEC cells as a BBB integrity model incubated with 1  $\mu$ g/ml LPS and mesoporous silica AMS-6 particles alone after 24-hour incubation. (b) Time dependent normalized resistance measurements at 1  $\mu$ M, 50  $\mu$ M and 100  $\mu$ M mesoporous silica particles of AMS-6 alone with 1  $\mu$ g/ml LPS, compared to controls.

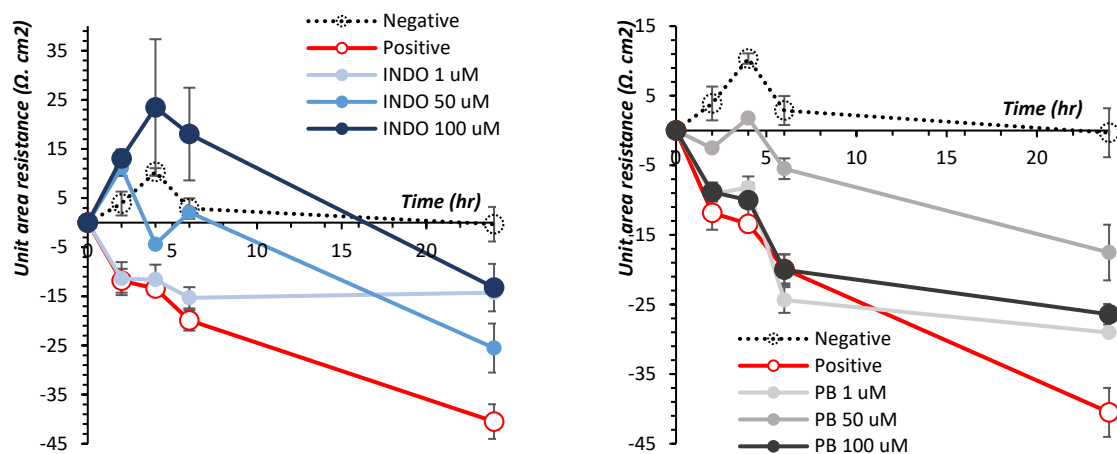


**Figure C6.** Time dependent normalized resistance measurements at 1 $\mu$ M, 50 $\mu$ M and 100 $\mu$ M for test compounds INDO and PB with 1  $\mu$ g/ml LPS, compared to controls.

## 8.4 Appendix D: Supporting information of chapter 6.

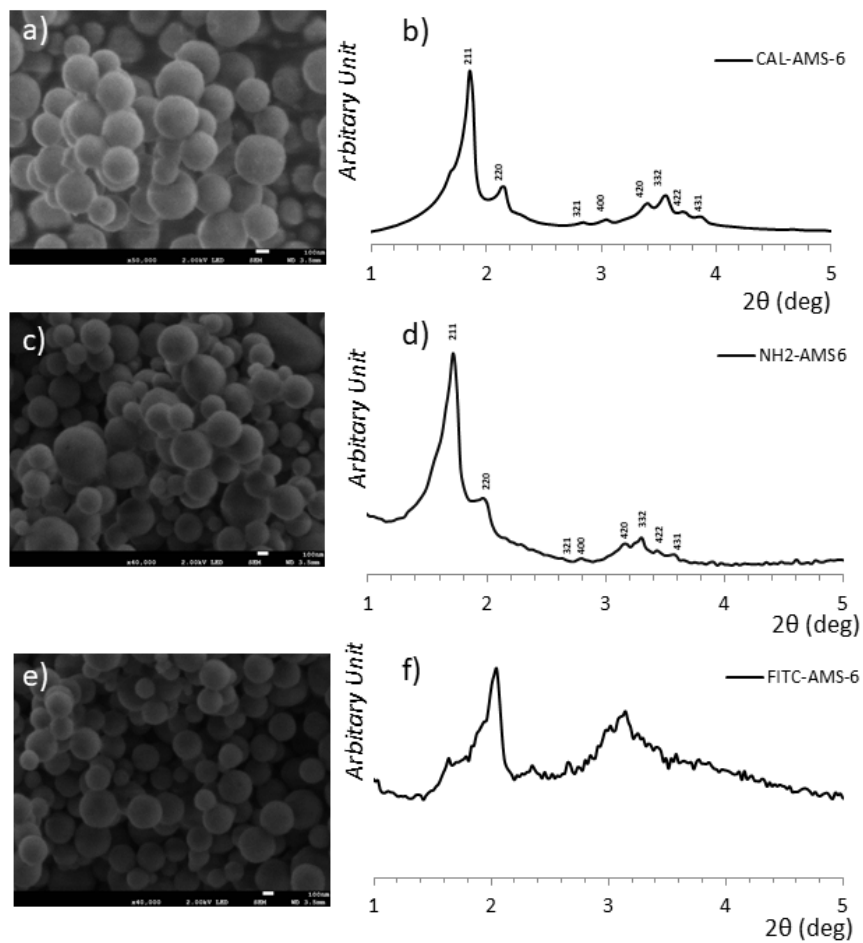


**Figure D1:** SEM and XRD scans of mesoporous materials, (a,b) CAL-AMS-6, (c,d) NH<sub>2</sub>-AMS-6, (e,f) FITC-AMS-6.

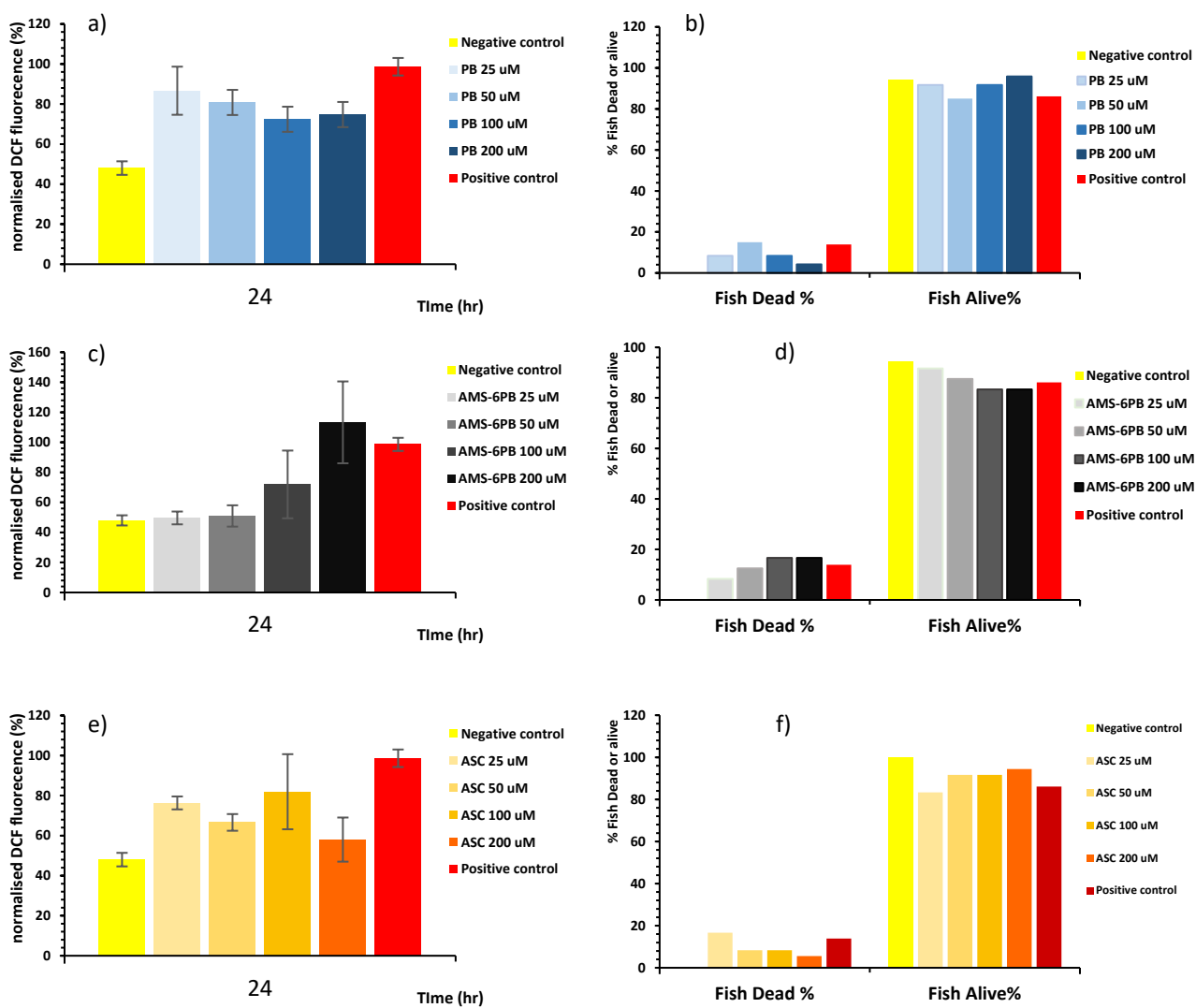


**Figure D2:** Measured DCF fluoresce after 24 hours and percentage of fish death and alive in zebrafish embryo (3dpf) pre-treated with different concentrations of the test compounds, followed by 5 mM H<sub>2</sub>O<sub>2</sub>, and 25 mM DCFDA. (a,b) PB, (c,d) AMS-6PB, and (e,f) ascorbic acid.